NATIONAL UNIVERSITY OF IRELAND GALWAY

Eye modelling for personalised intraocular lens design

by

Matthew Thomas Sheehan

supervisors

Dr Alexander Goncharov and Professor J.C. Dainty

A thesis submitted in partial fulfillment for the degree of Doctor of Philosophy

Applied Optics Group, School of Physics, Science Faculty,
National University of Ireland, Galway

August 2012

Abstract

Approximately 20 million cataract operations are performed per year worldwide[1][1], routinely removing the opaque cataractous lens and implanting an artificial intraocular lens (IOL). Modern technologies used to treat cataract are highly sophisticated and the operation involves remarkable skills; however the IOL power calculation in certain circumstances can be unsatisfactory. Currently the calculation of required IOL power is based on formulas developed from the paraxial geometrical optics equations and/or statistical analysis of retrospective cases. This work aims to improve upon the methodologies currently used to predict required IOL power, particularly for unusual eyes with extreme ocular biometry (e.g. extreme axial length or corneal shape). This work also demonstrates the usefulness of personalized eye models in investigations of IOL designs proposed to correct the higher order aberrations of the eye.

Biometric data was collected on a cohort of subjects undergoing routine cataract surgery with phacoemulsification and *in-the-bag* implantation with an Akreos Adapt AO (Bausch and Lomb) IOL. Anterior corneal topography elevation data using Placido disc technology (Atlas 9000, Carl Zeiss Meditec) and segmented axial length data using optical low coherence reflectometry (Lenstar 900, Haag-Streit) was collected on both eyes of each subject prior to surgery. The same measurements were repeated approximately 3 weeks post-operatively with additional measurements of aberrometry (Zywave, Bausch and Lomb) and autorefraction (ARK-510A, Nidek) to quantify the refractive outcome. *In vitro* IOL metrology was performed on a series of IOLs (Akreos Adapt AO, Bausch and Lomb) immersed in a saline bath, using a Twyman-Green interferometer (FISBA OPTIK μPhase). From the measured ocular biometry and IOL metrology data, personalized eye models were generated and their accuracy in predicting the required IOL power is compared to standard industry formulas applied to the same sample of eyes. The personalized models were also used to study the optimal customized IOL design for an individual eye. This simulation of higher order monochromatic aberration correction allows the retinal image quality to be quantified, which is a preliminary step in investigating the potential visual benefit from customized aberration-correcting IOL designs.

This work concludes that refractive outcomes for cataract patients may be improved by establishing a comprehensive methodology regarding IOL power, design and selection process. Personalised ray tracing eye models are an important tool in this regard and reduce reliance on approximations inherent in the current industry standard formulas.

[1] 2010 data projected from 1995 estimates assuming service levels remain at 1995 levels.

Acknowledgements

Thank you to my funding organisations: Enterprise Ireland (REI996 IR 2008 0014) and Science Foundation Ireland (07/IN.1/1906).

I wish to acknowledge and thank the following people for their support in this research; Alexander Goncharov, Chris Dainty, Eamonn O'Donoghue, Conor Sheil, Hannah Nowitzki, Huanqing Guo, Una Murphy, Henk Weeber, Tim de Jong, Nomdo Jansonius, Carmen Cánovas, Patricia Piers, Sverker Norrby, and Thom Terwee.

To Graeme George - the kind of teacher that makes a difference.

To Chris and Sasha, thank you for creating a research environment with great opportunities to strive for excellence in science.

Thank you to all the members of the Applied Optics group at NUIG.

Thank you to Ollie and all of my family and friends.

Contents

List of Figures

List of Tables

Abbreviations

AC	**A**nterior **C**hamber
ACCC	**A**nterior **C**ontinuous **C**urvilinear **C**apsulorhexis
ACD	**A**nterior **C**hamber **D**epth
BSS	**B**alanced **S**alt **S**olution
CCD	**C**harge **C**ouple **D**evice
CME	**C**ystoid **M**acula O**e**dema
ECCE	**E**xtra **C**apsular **C**ataract **E**xtraction
ELP	**E**ffective **L**ens **P**osition
GRIN	**G**radient **R**efractive **In**dex
HOA	**H**igher **O**rder **A**berration
ICCE	**I**ntra **C**apsular **C**ataract **E**xtraction
IOL	**I**ntra **O**cular **L**ens
LASIK	**L**aser-**as**sisted **I**n situ **K**eratomileusis
LCA	**L**ongitudinal **C**hromatic **A**berration
LCR	**L**ow **C**oherence **R**eflectometry
MTF	**M**odulation **T**ransfer **F**unction
Nd YAG	**Neo**d**y**mium-doped **Y**ttrium **A**luminium **G**arnet
OCT	**O**ptical **C**oherence **T**omography
PCO	**P**osterior **C**apsular **O**pacification
PCI	**P**artial **C**oherence **I**nterferometry
PMMA	**P**oly **m**ethyl **meth**a**c**rylate
poly HEMA	**P**oly **h**ydroxy**e**thyl **meth**a**c**rylate
RD	**R**etinal **D**etachment
RPE	**R**etinal **P**igmented **E**pithelium
SA	**S**pherical **A**berration

SSE	**S**um of the **S**quares of the **E**rrors
SNR	**S**ignal-to-**N**oise **R**atio
TCA	**T**ransverse **C**hromatic **A**berration
UV	**U**ltra**v**iolet
WTW	**W**hite **T**o **W**hite
ZPL	**Z**emax **P**rogramming **L**anguage

Glossary

Aphakic	An eye without a crystalline lens.
Ametropia	A clinically significant refractive error in the eye.
Astigmatism	A refractive state where the dioptric power varies between perpendicular principle meridians of maximum and minimum power.
Biometry	Measurement of the physical parameters of the eye.
Capsulotomy	The surgical incision/removal of part of the capsular bag. Lenticular capsulotomy is typically performed mechanically or by photodisruption.
Cataract	A clinically significant opacity in the crystalline lens.
Clear optic	Diameter of circle concentric with the optical axis of an intraocular lens, containing only features belonging to the optical design.
Emmetropia	No clinically significant refractive error in the eye.
Haptic	Non-optical, generally peripheral, component of an intraocular lens, intended to keep it in place in the eye.
Hyperopia	A refractive state of the eye where either the dioptric power is insufficient, the axial length is insufficient, or both.
In-the-bag	A description of the specific placement of an intraocular lens inside the capsular bag.
IOL body	The central part of an intraocular lens incorporating the optic.
Mesopic	A state of moderate illuminance conditions.
Miosis	A small pupil size, approximately ≤ 2 mm in diameter.
Myopia	A refractive state of the eye where either the dioptric power is excessive, the axial length is excessive, or both.
Personalised	This term is used with two different meanings depending on the context. When discussing industry-standard IOL power calculation formulas, 'personalised' refers to optimisation considering parameters

	unique and consistent to the surgeon, whereas in the context of ray-tracing eye models, 'personalised' refers to optimisation that additionally considers parameters unique to the individual patient.
Photopic	A state of high illuminance conditions.
Phakic	An eye with a crystalline lens.
Phakic IOL	An IOL designed for implantation into a phakic eye.
Phacoemulsification	The emulsification of cataract particles by ultrasound vibration and their extraction from the eye by vacuum forces.
Pseudophakic	An eye with an IOL implanted in replacement of the crystalline lens.
Scotopic	A state of low illuminance conditions.

Symbols

Symbol	Name	Units
a	anatomical anterior chamber depth	meters
P	Intraocular lens power	diopters D (m^{-1})
F	surface power	diopters D (m^{-1})
A	the A constant	diopters D (m^{-1})
V	wavefront vergence	diopters D (m^{-1})
f	focal length	meters
b	distance between the spectacle plane and the corneal plane	meters
l	axial length of the eye	meters
K	corneal power of the eye	diopters D (m^{-1})
d	axial distance from anterior cornea to implanted IOL	meters
r	radius of curvature	meters
s	surgeon factor	meters
n	refractive index	
o	offset	meters

Note: Abbreviations are non-italic, whereas symbols are italicized.

Chapter 1

Background

The eye is a fundamental component of the human visual system and is displayed in transverse section in Fig. 1.1. The crystalline lens is positioned inside the capsular bag, which is suspended around its equator by zonular fibers attached to the ciliary body. The crystalline lens is transparent and flexible, providing a dynamic refractive power to the eye by means of a process called *accommodation*. In middle adult life, the crystalline lens and associated structures gradually lose their accommodative ability. In late adult life, it is typical for the crystalline lens to lose transparency and become opaque. If the loss of transparency is clinically significant the crystalline lens is said to be a cataract (Fig. 1.2). The most common cataracts develop as lens proteins denature due to the oxidative effects of aging and are termed *age-related cataracts*. Other general classifications of cataract by mode of onset include *congenital cataracts* and *acquired cataracts*. Cataracts may also be classified by appearance or location within the nuclei and/or cortical layers of the crystalline lens. Cataracts reduce the transmission of light that would normally pass through the ocular media to form the retinal image. They also scatter light, which further degrades the optical quality of the retinal image, resulting in complaints of blurred vision, reduced contrast and glare difficulties.

Currently the only treatment for cataract is surgical removal. If a cataract causes sufficient visual disability to warrant its removal, the eye will have lost about a quarter of its total refractive power. If the eye is allowed to remain without a replacement for the cataractous lens (aphakia), the refractive correction required to be provided by either spectacles or a contact lens is typically very large: approximately +13 diopters in

the spectacle plane (Fig. 1.3). There are many optical, mechanical, physiological and cosmetic problems with this situation. A preferable solution is to replace the cataractous lens with an intraocular lens (IOL), which is implanted inside the eye (Fig. 1.4). In this approach the optics of the eye can be quite similar to the physiological case and typically most pre-existing ametropia can be corrected, thereafter patients requiring only a mild supplementary refractive aid in the form of spectacles or contact lenses. Modern IOLs are typically composed of an optic providing the refractive power and haptics which maintain positioning and stabilization, although the components may be continuous as in a *one-piece* IOL. Cataract surgical techniques and the associated supporting fields have all accelerated in technology since Harold Ridley performed the first implantation of an IOL in 1949[1] [2]. Although medical issues and surgical risk are still associated with cataract surgery, and they are nontrivial, they are well-controlled with current techniques. Hence our attention is drawn to the more luxurious topic of improving the optical imaging quality of the combined eye-IOL system. Improving the quality of the retinal image may potentially improve the vision of a patient. Currently manufactured IOL designs aim to correct defocus, astigmatism, and, in some cases, spherical aberration. With modern technologies available to the ophthalmology field it is now reasonable to consider the possibility of customized correction of higher-order aberrations (HOAs) of the eye with personalized IOLs.

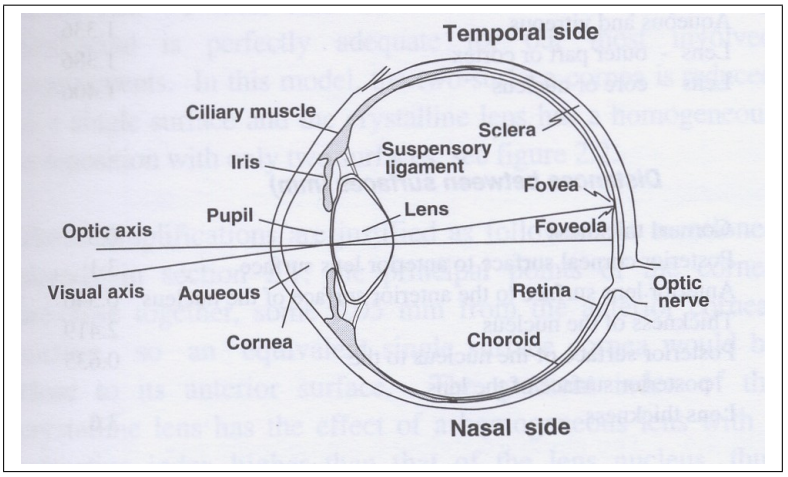

FIGURE 1.1: Schematic of the human eye (*image credit* A H Tunnacliffe & J G Hirst).

The aim of this work was to develop an eye characterization technique providing the required data to produce a personalized eye model. This eye model was simulated on

[1]This was a two part surgery with the second operation involving IOL implantation actually taking place in 1950.

ray-tracing software and used to study customized IOL designs with specific emphasis on incorporating the correction of monochromatic HOAs. Because the personalized eye model was developed on ray-tracing software capable of rapidly performing calculations (regarding the propagation and refraction of many millions of rays through multiple analytical surfaces per second), it is not necessary to restrict the IOL power prediction to a simple two principal meridian defocus calculation, which is the current convention [3]. It is hoped that in the future, manufacturers will produce customized IOLs according to personalized designs and offer such tailored devices to suitable patients. This work shows that personalized eye modelling has the potential to improve IOL power selection for cases that are receiving a standard nominal IOL design (Chapter 3). It is envisaged that personalized eye modelling holds the greatest potential benefit for patients with atypical ocular dimensions requiring cataract surgery. Unusual eyes such as those with extreme axial length or extreme corneal shape (e.g. high hyperopia, previous refractive surgery, previous penetrating keratoplasty, keratoconus) typically exhibit large amounts of HOAs and their required IOL power is often poorly predicted by standard methods.

The hypothesis is that the refractive outcome of cataract surgery may be improved by establishing a comprehensive scientific methodology regarding personalised eye modelling and customized IOL design.

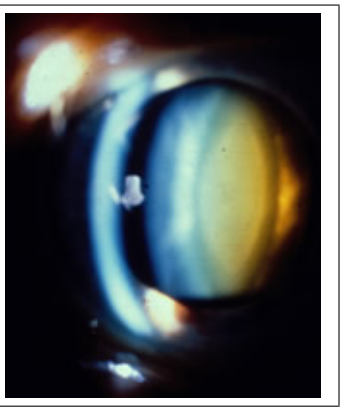

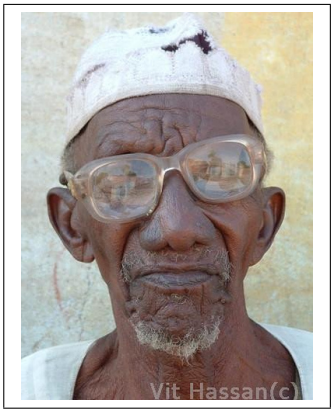

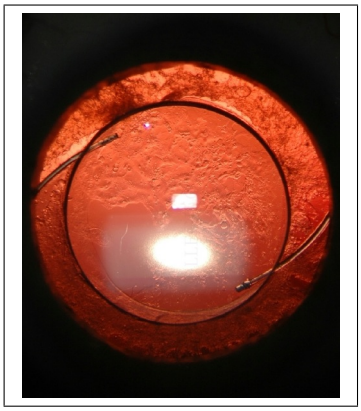

FIGURE 1.2: Sclerotic nuclear cataract (*image credit* Jack Kanski).

FIGURE 1.3: Aphakic spectacle correction (*image credit* Vit Hassan).

FIGURE 1.4: An implanted intraocular lens (*image credit* Michael Kelly).

1.1 Historical treatment of cataract

Historically how were cataracts treated? The desire to remove a cataractous lens from the visual axis needed to be considered against difficulties created by its relatively large size (typically 10 mm diameter). In early times cataract extraction necessitated a large incision, so it was preferable instead to only make a small incision and simply leave the cataractous lens inside the eye after dislodging it from the visual axis. A similar result is achievable by applying a blunt force to the globe. Written records describing this *couching* or *reclination* technique date back to the 6th century BCE and the Indian surgeon Sushruta [4]. *Needling* was another cataract treatment performed in antiquity requiring a procedure similar to couching but with a slight variation in concept - the aim was to manually break the cataract into smaller pieces with a needle, hoping they would be reabsorbed by the eye. Cataract surgery did not progress much from the time of Sushruta until the 18th century brought modern medical concepts [5].

Cataract extraction can broadly be distinguished by three techniques; Extracapsular cataract extraction (ECCE), Intracapsular cataract extraction (ICCE) and Phacoemulsification. The development and popularity of these three techniques overlapped and were *not* chronologically sequential. ECCE was pioneered by Jacques Daviel in 1748, requiring extraction of the cataractous lens without removing the capsule from the eye [4]. The anterior capsule is opened to provide access to the cataract, but importantly the posterior surface of the capsule and the zonules remain intact. An alternative technique, ICCE, was first performed in 1753 by Samuel Sharp [5]. Initially this involved making an incision and then digitating the globe to mechanically force the expulsion of the cataractous lens through the incision. Refinement soon followed and suitable instruments were fashioned to aid in the extraction of the cataract/capsule complex without the need for digitating the globe. Importantly, ICCE results in the removal of the capsule and destruction of the zonules.

In the 1940s, only selective cases were being accepted for cataract surgery. Following extraction of the cataract, the large incision was closed with sutures and the eye thenceforth remained aphakic. In the late 1940s Harold Ridley developed the concept of an IOL after been spurred into action by the comments of a medical student observing him perform cataract surgery [2, 6]. Ridley and other surgeons of the day had already noted the inert properties of poly methyl methacrylate (PMMA) windshield fragments that

had been imbedded in eyes of airforce pilots during World War II. In 1950 following an earlier ECCE procedure, Ridley implanted the first IOL [7]. It was an iris-supported biconvex design and made from PMMA. The IOL had been produced and designed with collaboration from John Pike from Rayner Optical and John Holt from Imperial Chemical Industries. Such pioneering surgery was fraught with risks and complications that required both immediate and long-term management. These risks included those due to IOL implantation in addition to those due to simple cataract extraction and consequentially, some influential members of the ophthalmology profession opposed the use of IOLs [2]. But those ophthalmologists who supported the use of IOLs such as Peter Choyce [8], Cornelius Binkhorst, Edward Epstein and Benedetto Strampelli persevered in their efforts to manage and reduce the risks associated with IOLs [9]. Throughout the 1950s - 1970s it was found that angle-supported and iris-supported IOLs were damaging the internal structures of the eye that they were attached to, or bounced against, during saccades. Particularly at risk of damage was the corneal endothelium and the trabeculae meshwork. The implantation location of the IOL was a major challenge to be solved along with many other difficulties [9].

Throughout the latter half of the 20th century, progress in supporting fields such as instrumentation and pharmacology continued to improve the ICCE and ECCE techniques and their outcomes. The ICCE technique requires a 180 degree incision as the entire cataractous lens, a considerably large element, is removed as a single piece. The capsular bag is extracted along with the cataract and care is required to grasp the capsule and mechanically break the zonules without causing capsular rupture. Although it is no longer performed today, it is worth noting some key milestones in the development of the ICCE technique. In 1957 Joaquin Barraquer was the first to use alpha-chymotrypsin to chemically dissolve the zonules and allow a safer and less vigorous removal [10, 11]. A few years later in 1961 Tadeusz Krwawicz progressed the ICCE technique by introducing a cryoextractor probe to freeze the cataract/capsule structure, which was then dissociated from any zonular remnants and removed from the globe [12]. Visual recovery from ICCE was difficult regardless of whether an IOL was implanted, not least due to the incision size required. Importantly, while removing the cataractous lens from the eye, ICCE additionally removes the capsular barrier and IOL implantation is limited to either iris-supported, angle-supported, or sulcus-supported designs.

During ECCE, the anterior capsule is opened and the firm cataract nucleus is mechanically expressed before the softer cortex fragments are aspirated in a later step. Because the nucleus is smaller than the entire cataract, the incision can be smaller (typically 6 mm) than that required by ICCE, although it may later be widened to allow the implantation of a rigid PMMA IOL. During ECCE the posterior capsule is maintained, this natural barrier separates the vitreous chamber from the posterior chamber, playing a critical role in avoiding disturbance of the vitreous. Apart from the benefit of reducing bulk movement of the vitreous and reducing the risk of retinal detachment (RD) secondary to vitreous loss, retention of the capsule partially restricts the spread of inflammation to the avascular vitreous, which can be difficult to treat. Another substantial advantage of capsular retention is the provision of a minimally harmful location for implantation of the IOL. Throughout the development of the ECCE technique, surgeons observed that if the capsule was maintained and the IOL positioned inside the capsular bag, interaction between the implant and the eye was reduced - the delicate structures of the eye were unlikely to be damaged [9]. This proved to be a significant advance in reducing the risk of many post-surgical complications such as uveitis, RD, Cystoid macula oedema (CME), and Bullous keratopathy [9]. ECCE is still used in some circumstances today even though modern IOL materials are now foldable and insertion of an IOL no longer necessitates the larger incision that ECCE requires. Phacoemulsification techniques are vastly more common in the developed world, however, ECCE may be a preferable technique in the developing world because it requires less-expensive instrumentation, less-expensive consumables, and because cataracts are likely to be more mature at the time of surgery. Phacoemulsification of dense cataract requires higher amounts of ultrasonic energy and puts the retina at greater risk of tearing. Additionally, limited access to ophthalmology services and Neodymium-doped yttrium aluminium garnet (Nd YAG) lasers in the developing world enhances the advantages of a prophylactic surgical posterior capsulotomy allowable with ECCE to avoid posterior capsular opacification (PCO).

ECCE and ICCE incision sizes vary from modest to large (respectively), and hence necessitate sutures to close the wound. The key to reducing incision size lay in development of the phacoemulsification extraction technique and the material science task of producing foldable IOLs. Phacoemulsification was pioneered by Charles Kelman, who adapted ultrasonic dental instruments to perform the first surgery in 1967 [13]. The

cataract is accessed through an opening created in the capsular bag typically 4 to 5 mm in diameter, which was later refined as the *anterior continuous curvilinear capsulorhexis* (ACCC) pioneered by Howard Gimbel [14]. Phacoemulsification allows the cataract to be broken into very small pieces with ultrasonic energy before removal from the eye via vacuum forces. Like ECCE, phacoemulsification preserves the structural capability of the capsule and zonules. Throughout the 1970s improving microsurgery techniques allowed the complete clearance of cataractous material, which combined with better-designed and better-manufactured IOLs, reduced the incidence and degree of inflammation. By the mid 1980s, continuing work and investigations had refined the IOL implantation position to achieve *in-the-bag* implantation, which significantly reduced complications [9]. Today phacoemulsification cataract extraction with *in-the-bag* IOL implantation has attained dominance as the preferred technique in the vast majority of cataract cases in the developed world [15, 16]. It allows most of the capsule to be maintained and a foldable IOL can be inserted into the capsular bag without widening the corneal incision. This means that incisions typically range between 1.8 to 3.2 mm and are structured to self-seal without the need for sutures and without inducing significant corneal astigmatism. Phacoemulsification spurred the development of foldable IOLs and vice-versa, both complementing each other in the development of small incision surgery. As phacoemulsification and foldable IOLs developed they provided advantages of smaller incision size, faster recovery, stronger repair, sutureless healing, and more predictable corneal topography effects (i.e. less astigmatism induction). Phacoemulsification with *in-the-bag* implantation combined with modern surgical technologies has resulted in a refined surgical procedure, which is highly repeatable and highly copied on a worldwide basis.

Table 1.1 broadly summarizes the main complications of cataract extraction and IOL implantation and their key contributory mechanisms. It is presented from a historical perspective and so while these complications are still present in modern cataract surgery, their level of risk is considerably reduced with modern techniques. Table 1.1 also summarizes the strategies developed to reduce these risks; however, they are only a representative selection of the numerous incremental steps which have driven continual refinement of both the surgical procedure and the associated technologies. By analyzing the differences in complications and risks between the various cataract extraction types and implantation locations, Table 1.1 conveys the principal implications borne out

through historical development: complications are best reduced by minimizing both the extent of surgical intervention and the IOL/ocular interaction. With modern technologies this is best achieved by enclosing the IOL (or at least the peripheral aspects of the IOL) inside the capsular bag whereafter capsular fibrosis secures it in place. The logical consequence of this understanding explains why phacoemulsification combined with *in-the-bag* implantation has become the dominant surgical technique where available.

Developing and future IOL designs intending to provide enhanced features such as accommodative function, chromatic aberration correction, and monochromatic aberration correction must improve, or at least maintain, the risk level associated with current standard *in-the-bag* IOL designs. Any IOL designs that evoke increased risks of complications such as those listed in Table 1.1 will be regarded as less-attractive solutions.

1.2 Modern cataract surgery

Modern cataract treatment often follows a typical pathway beginning when a patient notices visual difficulties and is referred to an ophthalmologist if the cataract is clinically significant. The ophthalmologist examines the patient and considers any relevant contraindications to surgery such as poor general health, concurrent ocular infection or inflammation, weak zonules/capsule or predisposition to retinal tearing. After discussing the prognosis, risks and benefits, surgery may be planned with the patient's informed consent. Two important biometry measurements used to predict the required IOL power for implantation will then be performed:

- An axial length measurement of the eye, and
- keratometry measuring the corneal power measurement in two principal meridians.

The measurements are typically performed on both eyes even if only one eye is to undergo surgery, and will usually be repeated several times to ensure reliability. The axial length measurement is often colloquially referred to as an *A-scan* due to the historical association with amplitude-mode ultrasonography. Modern-day measurements are typically performed with a partial coherence interferometer, low coherence reflectometer, or an ultrasonographer (applanation or immersion methods). Corneal power measurements can be performed with numerous types of instruments such as traditional keratometers,

Complication	Description of mechanism	Strategy to reduce risk
Infection	Pathogens may be introduced to the eye by surgical instruments. Static electrical charges on IOLs make them susceptible to attracting foreign matter prior to implantation.	Sterilization of instruments and IOLs. Improved antibacterial agents. Reduced incision size. Reduced traffic insert/remove events and time spent inside the globe.
Glaucoma	Angle-supported IOLs risk mechanical damage to the trabeculae meshwork. Iris-supported IOLs risk mechanical rubbing of pigment from the iris leading to pigmentary dispersion glaucoma. ICCE risks glaucoma secondary to pupil block.	Correctly size the IOL or preferably avoid angle-supported and iris-supported IOL designs. Iridectomy is essential in ICCE to reduce the risk of pupil block.
Luxation and IOL instability	Particularly a problem of iris-supported IOL designs. Largely avoided with *in-the-bag* implantation where the capsular contraction healing response secures the IOL.	Decrease the size and mass of the IOL through optical design and material choice. Avoid iris-supported IOL designs. Development of auxiliary support devices such as capsular tension rings.
Corneal decompensation and bullous keratopathy	Mechanical and thermal stress during surgery causes endothelial cell loss, but this extends into a recurring post-surgery insult if angle-supported and iris-supported IOLs physically bounce off the cornea during saccades.	Modified surgical technique in awareness of endothelial delicacy. Development of viscoelastic agents. Avoid angle-supported and iris-supported IOL designs.
Vitreous loss and retinal detachment (RD)	ICCE generally risks rupturing the vitreous face, thus increasing risk of vitreous loss and subsequent vitreous traction and/or RD. Exacerbated by iris-supported IOLs which increase the inertia effects of the vitreous bulk. Retinal tearing and detachment may also be caused by inappropriate phacoemulsification energy settings.	Avoid ICCE. Avoid iris-supported IOL designs. Conservative patient selection. Prophylactic Argon laser treatment to secure the retina. Improvements in surgical instrumentation.
Inflammation, cystoid macula oedema (CME), and endophthalmitis	General surgical disruption to ocular physiology. Post-surgical interaction between the IOL and the ocular tissue is a major cause. Incomplete extraction of the cataractous matter was an important cause in early ECCE procedures. Risk increased by ICCE because factors responsible for mediating inflammation are unrestricted in the absence of a capsular barrier. Nd YAG capsulotomy risks CME especially if performed too soon after cataract surgery.	*In-the-bag* implantation minimizes IOL contact with ocular tissue. A smooth and biocompatible IOL surface reduces tissue interaction. Irrigate/aspirate capsular polishing allows complete extraction. Avoid ICCE. Allow sufficient recovery time before performing capsulotomy. Improved anti-inflammatory medicines.
Posterior capsular opacification	Remnant cataractous epithelial cells migrate to the central posterior capsule and attempt to grow new lens fibers. These disorganized lens cells aren't transparent. Not applicable to ICCE.	Development of NdYAG laser capsulotomy. Use of phacoemulsification capsular polishing and contact inhibition in IOL designs.
Astigmatism	Large and centrally located incisions risk inducing astigmatism and structural weakness. Especially relevant to ICCE.	Development of small incision phacoemulsification technique and foldable IOL materials.

Table 1.1: Historical overview of cataract extraction and IOL implantation complications.

Placido disc corneal topographers, Scheimpflug cameras, and optical coherence tomographers.

Prior to surgery the patient may be instructed to use topical antibiotics and lid-hygiene products to reduce the natural flora on and surrounding the eye. It is necessary to temporarily discontinue certain ocular and systemic medications in the lead up to surgery and during the post-operative period. On the day of the surgery mydriatic drops are used to dilate the pupil and the patient may be given systemic sedatives. Depending on the specific details of the case, the anaesthetic typically may be administered topically or as a peribulbar or sub-Tenons' injection. Nowadays the use of a retrobulbar anesthetic is relatively infrequent, and very infrequently a general anesthetic is used. A speculum is used to position the eyelids and an incision is made in the cornea or the sclera. The orientation of the incision is typically dictated by access considerations - the patient is supine and therefore a superior or temporal approach is convenient. This orientation may be altered to the steepest corneal meridian in an effort to reduce corneal astigmatism [17]. Balanced salt solution (BSS) is used in conjunction with viscoelastic materials to create a working space in the anterior chamber and to protect the corneal endothelium from mechanical, thermal and sonic damage. The cataract is accessed via an ACCC. Hydrodissection and hydrodelineation separate the cataractous lens from the capsule and then the nucleus is divided into smaller pieces mechanically. The small nuclear fragments are emulsified and aspirated by the phaco-machine. The cortex is softer and is removed next with special care given to protecting the capsule. The ophthalmologist will aspirate as many cataract fragments as possible to reduce the risks of both inflammation and PCO - this may involve a specific irrigation/aspiration tip for *polishing* the capsule. The IOL is introduced into the eye, unfolds inside the capsular bag, and is positioned centrally. If the IOL is toric it will also be rotated to the desired axis orientation. Viscoelastic remnants are aspirated and prophylactic antibiotics are administered. Typically, clear corneal incisions are structured to be self-sealing and the wound doesn't require sutures. Topical antibiotics and steroids are used post-operatively. IOLs are normally implanted with the intention that they will remain in the eye for the life of the patient.

In an uneventful case, the time in theatre for modern phacoemulsification cataract extraction and IOL implantation can be less than ten minutes. There are a multitude

of interdisciplinary technologies that combine in this remarkable surgery: material science (e.g. viscoelastic materials and foldable IOLs), phacoemulsification fluid dynamics, phacoemulsification tip technology, sterilization technology and aseptic techniques, anaesthetics, surgical technique, pharmacology (particularly mydriatic, anti-infective and anti-inflammatory medicines), optics (e.g. operating microscopes, partial coherence interferometers, femtosecond laser capsulotomy), and biological science (e.g. techniques to prevent PCO, biocompatible coatings and filters). All of these technologies contribute to successful and safe cataract surgery with established and controlled complications and risks [18, 19].

1.3 Parameters of the eye

1.3.1 Fundamental anatomical and optical features of the eye

The anatomical and optical features of the human eye are schematically illustrated in Fig. 1.5, with typical values of parameters given in the following background description of function.

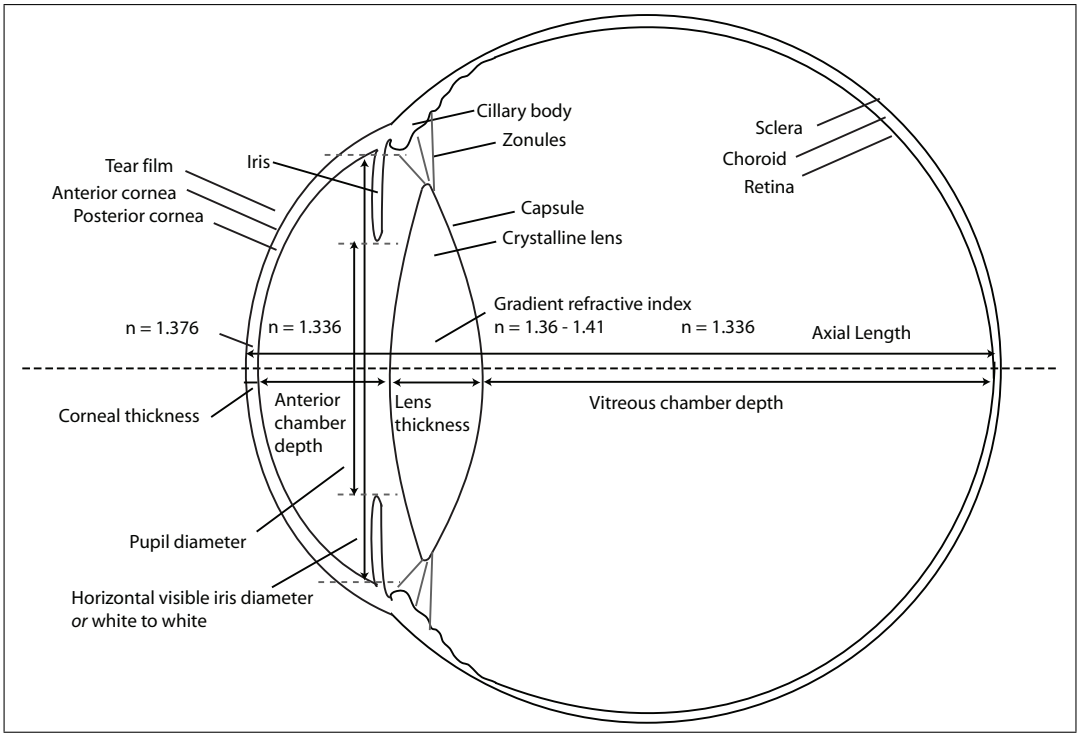

FIGURE 1.5: Schematic depiction and typical parameters of the adult human eye.

The cornea is the transparent, avascular surface at the front of the eye. Together with the tear film it forms the principal refracting surface of the eye and has a typical refractive index of 1.376 [20]. Contributing approximately 3/4 of the total refractive power of the eye, the corneal shape is important in limiting ocular aberrations. Following refractive surgery the cornea may increase in the magnitude of HOAs by one to two orders of magnitude. Typically the cornea has an anterior apical radius of curvature of 7.50 mm to 8.00 mm [21] and a posterior apical radius of the curvature of 6.20 mm to 7.40 mm [20]. It is an aspheric surface with flattening curvature towards the periphery, which helps to reduce spherical aberration in the eye [20]. The cornea has a typical diameter of 11 mm to 12 mm horizontally and 9 mm to 11 mm vertically [21]. Clinically, the corneal diameter is usually represented by the *horizontal visible iris diameter* or the *white to white* parameter. The circumferential edge of the cornea is called the limbus. Corneal thickness typically varies from 0.52 mm at the centre to 0.70 mm at the periphery [21]. The total power of a cornea as approximately +42 D, with the anterior cornea contributing approximately +48 D and the posterior cornea contributing approximately −6 D of power.

Tear film stability and integrity is crucial to imaging in the eye because it forms the principal refracting surface. The tear film has a typical refractive index of 1.336 [20]. Tear film quality and time elapsed since last blink are important factors that dramatically effect the reliability of biometry measurements. Poor tear quality can substantially increase aberrations experienced by a subject and this is a particularly troublesome issue for post refractive surgery patients who commonly suffer reduced tear production following the severing of the corneal nerves, which disrupts the feedback loop responsible for regulating tear production [22]. The tear film is likely to be less stable over any local areas of dramatic topography change, as can occur with pterygiums and in eyes that have previously undergone refractive surgery. Tear quality decreases with age and therefore is a consideration in an aged cataract population.

The anterior chamber is the space occupied between the cornea and the iris and crystalline lens. The typical anterior chamber depth (ACD) is 2.7 mm to 4.5 mm [20]. The posterior chamber is the space occupied between the iris, crystalline lens, and ciliary body. Both chambers are filled with a clear secretion called aqueous humour.

The uveal tract is a pigmented and highly vascular tissue consisting of the iris, ciliary

body, and choroid. Its has many functions including nutrient exchange, production of aqueous humour, accommodation, absorption of scattered light inside the eye, and control of pupil size. Pupil size directly influences the irradiance of the retinal image, diffraction effects and aberration levels [20]. Normal pupil diameters range from 2 mm to 6 mm and are roughly circular in shape. The average pupil diameter is known to decrease with age and is therefore a consideration in an aged cataract population. Various pharmacological agents can both either dilate or constrict the pupil.

Refractive indices of ocular media				
Tear fim	Cornea	Aqueous humor	Lens	Vitreous
1.336	1.376	1.336	1.36 - 1.41	1.336

TABLE 1.2: Refractive indices of ocular media.

The refractive indices of the ocular media are summarized in Table 1.2 although not specified for a reference wavelength. Further reading on this topic is recommended [23, 24, 25].

The primary function of the crystalline lens is to act as a dynamic focussing mechanism. It is biconvex, with the anterior surface being flatter in the unaccommodated eye. The typical relaxed adult crystalline lens has an anterior apical radius of curvature of approximately 10.5 mm and a posterior apical radius of curvature of approximately 6 mm. The average adult lens has an equatorial diameter of 10 mm and an axial thickness of 3.6 mm [20]. The crystalline lens has a gradient refractive index (in both the axial and radial directions) with an optical power *in situ* of approximately 18 diopters. Landmarks of the lens include the anterior pole, posterior pole, lens axis, and the equator. From outermost to innermost the major components of the lens are; the lens capsule, the anterior epithelial layer, and the lens proper (which is often sub-divided in to the cortex and various nuclear layers).

Lens fibers are continuously added throughout life. These cells grow and differentiate from the anterior epithelial layer and must maintain a highly ordered arrangement to maintain transparency. The loss of transparency (cataract development) can occur in any or all layers. In an aged cataract population, the typical lens thickness is significantly thicker than in the average adult eye. It is thought that higher-order aberrations inherent to the crystalline lens may play a role in compensation for corneal aberrations (and vice-versa) in some individuals [26, 27].

The capsule is essentially a transparent elastic bag and shape determinant. It is thinnest at the posterior pole and thickest at the equator. The zonules are a fibrous system that supports the capsule and keep it positioned behind the pupil.

The ciliary body produces aqueous humour, zonular fibers and vitreous hyaluronic acid. It also has a crucial function in accommodation via the action of the ciliary muscle. The ciliary body butts onto the iris and proceeds back to the retina (demarked by the ora serrata). It is a ring of tissue, roughly triangular shape in the long cross section with its base directed anteriorly. The ciliary sulcus is a ring-shaped furrow at the anterior aspect of the ciliary body where the tissue reflexes to continue as the posterior surface of the iris. Attachments to the ciliary body include the scleral spur, the trabecular meshwork, and the vitreous base. The ciliary body consists of two major zones: the pars plicata (the site of aqueous production) and the pars plana (a relatively avascular structure and the origin of the zonules). The elasticity of the ciliary body provides a synchronised movement in an anterior and internal direction with contraction. The zonules are suspensory fibers that hold the crystalline lens in place. They originate at the pars plana (approximately 1.5 mm anterior to the ora serrata) and insert into the crystalline lens at the anterior and posterior marginal zones. In an eye there are approximately 140 bundles of zonular fibers, which are composed of microfibrils having similar properties to elastin.

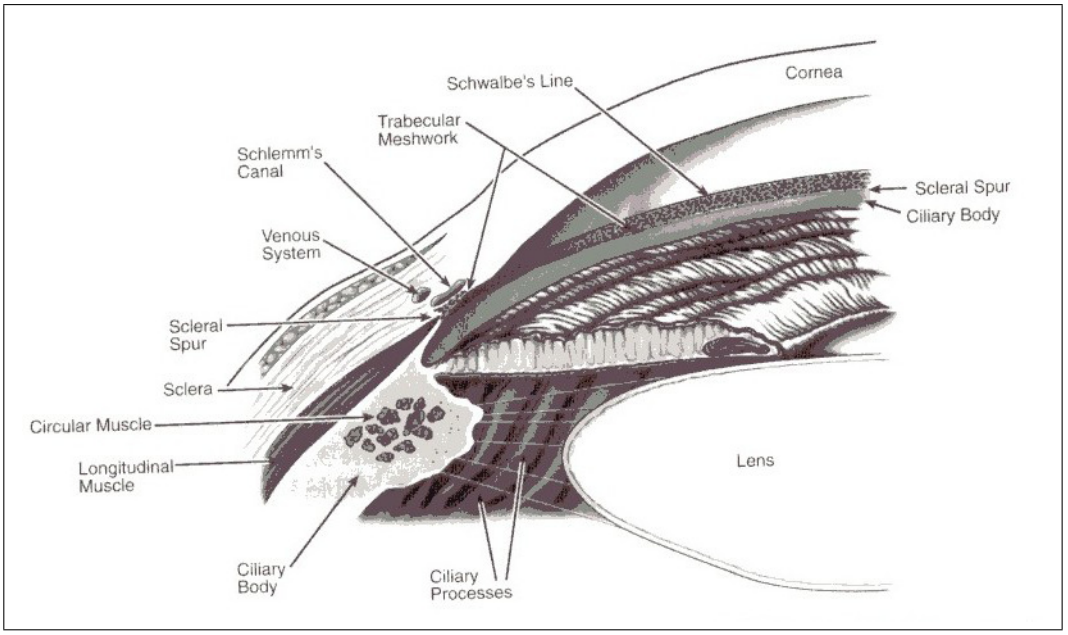

FIGURE 1.6: The anatomy of the angle of the eye (*image credit* W Tasman and E A Jaeger).

The vitreous humor is an avascular gel, which fills the vitreous chamber. It is attached with varying degrees of adhesion to the inner limiting membrane of the retina and the ciliary body. It has a limited metabolic role in the adult eye.

The retina contains the light sensitive photoreceptor cell layer of the eye and its associated neural circuitry, which begins to organise and process the electrical impulses generated by vision, before they leave the globe via the optic nerve. The posterior segment of the eye is called the fundus and clinically there are areas of special distinction; the macula lutea ($\sim$ 5.85 mm diameter), fovea centralis ($\sim$1.85 mm diameter), and the foveola ($\sim$ 0.35 mm diameter) [29]. The photoreceptor cells provide a typical range of sensitivity to wavelengths between 390 nm and 760 nm [20]. The central retina is dominated by cone photoreceptors, which operate optimally under photopic conditions to provide vision with colour perception and both high spatial resolution and high temporal resolution. The peripheral retina is dominated by rod photoreceptors, which operate optimally under scotopic conditions to provide vision with monochromatic perception, and both low spatial resolution and temporal resolution.

Most layers of the sensory retina are displaced sideways at the foveola to create the foveal pit, thus central photoreceptors have unimpeded stimulation from light forming the retinal image. The small cone size, tight cell packing, and 1:1 coupling between cone photoreceptors and Ganglion cells at the fovea increases the spatial resolution of the visual system for on-axis imaging [30].

At the foveola, the cones are packed in a directionally sensitive manner, allowing them to act as waveguides, which is though to be responsible for the Stiles-Crawford effect. This arrangement reduces the effect of aberrations near the pupil edge (see Section 1.3.5). A $1:1$ coupling between cones and ganglion cells exists at the fovea, compared to approximately $100:1$ rod to ganglion cell relationship at the periphery. This difference in coupling ratios exemplifies the low spatial summation at the fovea, which is important for the eye to extract the maximum resolution possible from the retinal image provided by the optics of the eye. The reduced resolution capability of the peripheral retina is economically matched in terms of biological demands to the reduced image quality provided by the eyes optics in the peripheral visual field.

1.3.2 Ocular axes

The optical surfaces of the eye are not rotationally symmetric, additionally these optical surfaces suffer small displacements and tilts with respect to each other, and consequentially the eye has no uniquely defined true optical axis. Instead a collection of different ocular axes and the associated collection of angles formed by the intersection of these axes are used when performing measurements [31]. A selection of the most commonly used axes, angles and landmarks are described below.

- The optical axis is approximated by the line of best fit passing through or near to the centers of curvature of the four optical surfaces (anterior cornea, posterior cornea, anterior lens, posterior lens) of the eye.
- The visual axis is defined by the line connecting the fovea to the fixation target via the eye's nodal points. A ray directed towards the nodal point undergoes no angular deviation by the system and therefore the visual axis is a reference axis for unit angular magnification. The visual axis defines the direction of gaze and a pencil of rays traveling along this axis undergoes no transverse chromatic aberration for a given reference wavelength.
- The line of sight (LOS) is defined by the line connecting the fovea to the fixation target via the centre of the entrance pupil. The LOS defines the path of the principal ray entering the fixating eye.
- The pupillary axis (PA) is defined by the line connecting the center of the entrance pupil with the center of curvature of the anterior cornea, and it therefore intersects the anterior cornea perpendicularly.
- The videokeratoscope axis (VKA) is defined by the line connecting the center of curvature of the anterior cornea with the fixation target, while the eye is fixating (i.e. the fovea is directionally aligned with the fixation target).
- Angle λ is usually denoted as the angle from the PA to the LOS. Average values of +1.4 degrees [32] and +9 degrees [33] in the horizontal direction, where the PA is temporal to the LOS in object space as conventionally defined [31].
- Angle α is usually denoted as the angle from the optical axis to the visual axis. Typically an average value of +5 degrees temporal displacement (i.e. the fovea

is shifted from the optical axis to the temporal retina) is assumed [34]. The visual axis is usually nasal to the optical axis in object space and a range of +17 degrees (nasal object space) to −2 degrees (temporal object space) is normal [34]. Vertically the visual axis is declined relative to the optical axis by 2 to 3 degrees [31].

- Angle κ is usually denoted as the angle from the pupillary axis to the visual axis.

Note the dynamic nature concerning most of these axes and angles. Axes defined by fixation of a target are dependent on the target distance (which may be finite or infinite) and the refractive state of the eye. Apart from typically being decentered (to a much greater extent horizontally than vertically), the pupil is not static, asymmetric dilation and constriction causes fluctuations in the location of axes defined by the entrance pupil center. Although the definition of the visual axis, the videokeratoscope axis, and the line of sight, all contain the fixation target as a reference point, the object distance of the fixation target is not required to be infinite by definition. These means that the three previously listed axes are only parallel in object space if the fixation target of the instrument is conjugated to infinity.

1.3.3 Refractive error and refraction techniques

The lower-order aberrations are typically the overwhelmingly dominant aberrations of the eye and traditionally they are corrected with spectacles, contact lenses or refractive surgery. For the visual system to function well, light from an object of interest must be focussed onto the retina. When this occurs to within clinically measurable limits, the subject is *emmetropic*. When some measurable level of blur exists in the retinal image, the subject is *ametropic*. Ametropia is not the sole requirement for good vision, as the remaining components of the visual system must also function properly, but it is the most common and the most amendable malfunction of the visual system.

Practitioners traditionally quantify ametropia by specifying the refractive error. The refractive error is the dioptric strength of a spectacle lens at the spectacle plane (typically 13 mm in front of the cornea) that is required to remove blur from the retinal image and focus light from an infinite source on the retina while the eye is in an unaccommodated state. Refractive error can be categorized as *myopia* (refractive power

or axial length excessive), *hyperopia* (refractive power or axial length insufficient) and *astigmatism* (varying refractive power with maximum and minimum principle meridians perpendicular to each other, giving rise to two line foci when viewing a point source).

Assuming a normal healthy visual pathway, in the vast majority of eyes if any refractive error present is corrected for defocus and astigmatism, functional and satisfactory vision is achieved. Most people are unaware of any visual degradation attributable to HOAs under normal illumination and a physiological pupil state. Refractive error will change throughout life for various reasons, some of which are known and others unknown. Typically an individual's refractive error will fluctuate across a range of time scales. Higher-order aberrations are likely to fluctuate on various time scales as well [35]. Traditionally, practitioners have only corrected lower-order aberrations with various devices, although modern IOLs currently attempt to correct defocus, astigmatism, and spherical aberration. If higher-order aberrations of the eye are also corrected, there is potential to improve the visual resolution of the subject under certain conditions and likewise the resolution of ocular images (typically, but not limited to, retinal fundus images) [36]. Practitioners determine refractive error (usually limited to the 1st and 2nd order aberrations of tip, tilt, defocus and astigmatism using a sphero-cylindrical approximation) using a variety of tests, which may be either objective or subjective.

Retinoscopy is a partially objective test where the practitioner shines light into the subjects eye and then moves the beam while observing the direction and speed of the reflection from the subjects retina. The apparent motion of the reflex occurs due to vignetting created by the practitioners pupil and the subjects pupil when the retinoscope is moved. It is essentially a Foucault knife edge test. The practitioner rotates the direction of movement of retinoscope beam to eliminate oblique motion in the reflex and then neutralises each principal meridian in turn, resulting in a sphero-cylindrical refraction. The nearer the subjects retina is conjugated to the practitioners pupil by the trial lens, the faster and brighter the reflex appears. When the subjects refractive error is completely neutralised, the reflex's angular motion is infinitely fast and maximally bright. Retinoscopy does not rely on responses from the subject, but it does rely on the skill and interpretation of the practitioner. In addition to refractive error measurement, retinoscopy provides the practitioner with information regarding the internal structures of the eye and media transparency (or lack thereof).

Autorefractors provide an automated and objective estimate of refractive error. This refraction technique typically uses a fixed pupil diameter and samples the eye in at least three meridians before fitting the data to a sinusoidal function. The main components of an autorefractor are the light source (typically infrared), a fixation target, a Badal optometer, and a detector. Early designs of autorefractors were based on an optimal focus principle where the vergence of the ingoing beam is adjusted until the signal through an aperture conjugate to the emmetropic retinal plane is maximised. Modern designs are more commonly based on the Scheiner principle or the Foucault knife edge test [37]. Autorefractors using either the Scheiner principle or the Foucault knife edge test require a synchronisation mechanism between the ingoing beam orientation and the detector.

Subjective refraction relies on responses from the subject and their interpretation by the practitioner. It measures refractive error iteratively and is sometimes ambiguous, relying on the art of the practitioner. When accommodation is present, cycloplegic subjective refraction (where the accommodation ability of the eye is paralysed) is usually considered the most accurate refraction technique. Typically a practitioner prescribes to a precision of ± 0.125 diopters in the sphero-cylindrical approximation.

Wavefront sensing provides the practitioner with greater detailed information compared to traditional refraction techniques. It provides objective information about the optical quality of the eye at high temporal and spatial sampling rates. Even lower-order aberrations measured by wavefront sensors (or *aberrometers*) are potentially more accurate than those measured by autorefractors because they typically possess higher spatial and temporal sensitivity, and they do not use a fixed pupil diameter.

Selecting the most appropriate refraction technique (or combination of techniques) is dependent on each individuals circumstances and prioritising the importance and relevance of the methods available requires the practitioner to have both a technical and clinical knowledge. In this work the refractive outcome of cataract surgery was measured with both an autorefractor and a wavefront sensor.

1.3.4 Aberrations

An ideal imaging system maps light from each point in object space to its respective conjugate point in image space. Optical systems behave ideally in the paraxial approximation, however real systems are expected to operate outside this region and image rays that have large angles of incidence. In real optical systems, even without any manufacturing faults, rays are displaced from their ideal positions in the image plane as predicted by the paraxial approximation. These ray displacements degrade the image quality and give rise to aberrations. The severity in which a system departs from the paraxial approximation is somewhat represented by the f-number because some of the parameters that determine the angle of incidence of the marginal ray are the same parameters that determine the f-number. However, the f-number gives no indication of what type of aberrations we might expect in an optical system. In the image plane, the angular deviations of rays from ideal for each particular field point gives rise to transverse and longitudinal aberrations (Fig. 1.7). Transverse aberrations are measured as the difference between the ray intersection in the image plane (xy) compared to the intersection of the principal ray. Similarly, the deviation along the optical axis gives rise to longitudinal aberrations, which are measured as the longitudinal difference between the ray intersection with the principal ray compared to the intersection of the principal ray with the image plane.

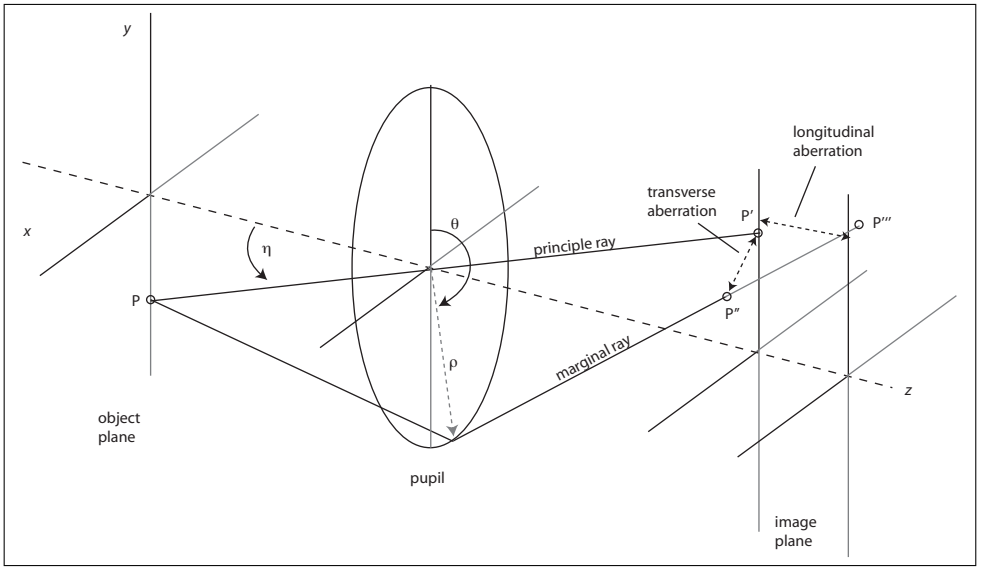

FIGURE 1.7: Longitudinal and transverse monochromatic aberration.

Aberrations may also be described by their effect in the pupil plane where the phase difference between the wavefront and its ideal counterpart gives rise to the wavefront aberration (W). The wavefront aberration is the optical path length along the optical axis between the aberrated wavefront and the reference wavefront (which is arbitrarily constructed as a sphere or plane surface to suit the particular application) and is dependent upon each point on the wavefront surface (ρ, θ) and the field angle (η) (Fig. 1.7).

In $1855-56$ Ludwig Von Seidel described what are commonly called third-order aberrations or Seidel aberrations. This analysis assumes monochromatic light and rotationally symmetric surfaces. The aberration polynomial is derived by considering the contribution of the second term in the sine function identity series $(\alpha^3/3!)$ that would normally be truncated if using the first order paraxial approximation [38]. Equivalently, it may be derived from the $\rho^4/8r^3$ term in the binomial expansion for a spherical surface. When consideration is extended to include off-axis field points, the rotationally symmetric $W(\rho)$ becomes dependent upon a field angle (η) and pupil angle (θ) components as well as the radial component (ρ).

The aberration polynomial, $W\ (\rho, \theta, \eta)$, can be arranged and grouped according to the order of the field angle. Neglecting focus and tilt terms, and removing constant terms, the aberration polynomial may be described using b_n coefficients as

$$W(\rho, \theta, \eta) = b_1\rho^4 + b_2\eta\rho^3 cos\theta + b_3\eta^2\rho^2 cos^2\theta + b_4\eta^2\rho^2 + b_5\eta^3\rho cos\theta \qquad (1.1)$$

This arrangement of terms lends itself to classifying five different aberrations; spherical aberration, coma, off-axis astigmatism, field curvature and distortion. When describing ocular aberrations, Seidel aberration coefficients are not used because the eye is not a rotationally symmetric system. Additionally, the elements of the eye are aspheric and typically decentred. However, vision scientists borrow some Seidel terminology and theory because it forms such a fundamental and widely used optical language. The description of ocular aberrations has recently been standardized using Zernike polynomials [39, 40] although this reporting format also has its own limitations of usefulness when applied to the eye.

Higher order aberrations (HOA) is a term that has only been used routinely by ophthalmologists and optometrists in the last two decades. Until the late 1990s, clinicians

typically grouped all HOAs together and collectively referred to them as 'irregular astigmatism'. Although vision scientists had earlier recognised the academic distinction of the various families of HOAs based on Seidel's aberration theory. Historically there was little clinical relevance in distinguishing, measuring or defining HOAs of the eye correctly, as measurement devices were not practical and there was no remedial treatment for a patient with large amounts of HOAs apart from the use of a rigid gas permeable contact lens (and such a device could be fitted and prescribed without the measurement of HOAs). Typically HOAs have a very low magnitude in a normal eye, especially compared to the lower order aberrations of defocus and astigmatism [41]. In 1994 the work of Liang and colleagues [42] demonstrated a convenient, fast, and objective technique to measure HOAs in the eye. Development of wavefront sensing, correcting devices, and refractive surgery has spurred clinicians and scientists towards the goal of controlling [2] HOAs by refractive surgery [43]. HOAs are particularly important in eyes with unusual corneal shape (e.g. keratoconus, pellucid marginal degeneration, corneal graft, and refractive surgery patients), and especially during tasks when the pupil is dilated (e.g. night driving).

Chromatic aberrations are a consequence of dispersion and they are typically considered separately from monochromatic aberrations. High frequency light undergoes greater refraction at a boundary and the trajectory of these rays depart from those of lower frequency light, which undergo less refraction. It is sometimes convenient to consider the difference in axial foci for the two extreme frequencies at the ends of the bandwidth under investigation. The difference in foci along the optical axis (z) is termed longitudinal chromatic aberration (LCA) while the transverse difference in foci in the image plane (xy) is termed transverse chromatic aberration (TCA) (Fig. 1.8).

The optics of the eye are not perfectly centered - typically the nodal point is not coincident with the centre of the entrance pupil, infact, they are not even coaxial and this has implications for the chromatic aberration in the eye. Ocular TCA varies markedly across subjects and between fellow eyes [44]. Figure 1.9 summarises several experimental reports on the typical longitudinal chromatic aberration of the human eye. It is reasonable to assume approximately 2 to 3 diopters of LCA over the visible spectrum. Howarth *et al.* [45] concluded that ocular LCA is independent of age for human adults, however this

[2] 'controlling' is used to imply both limiting the induction of unwanted HOAs and the purposeful correction of pre-existing HOAs.

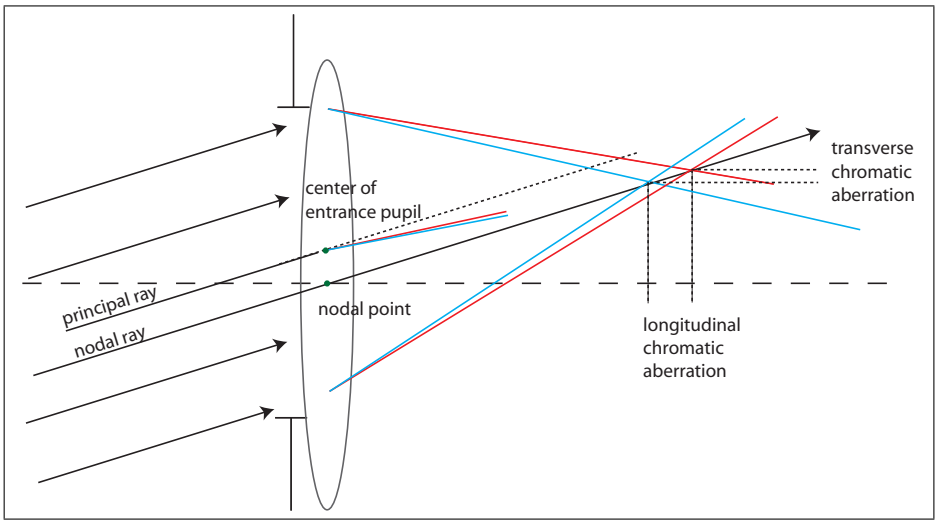

FIGURE 1.8: Longitudinal and transverse chromatic aberration for an off-axis field point imaged by an optical system with a decentered pupil.

was a cross-sectional study and this conclusion has been debated by some researchers [46]. Ocular LCA can be corrected with achromatizing devices or monochromatic viewing and improves visual performance [47, 48, 49]. The correction of LCA in the eye using a diffractive element incorporated into the IOL design has been proposed [50, 51]. Hall's classical technique of combating LCA over a given bandwidth by combining two different media of differing refractive indices into a doublet [52] is seemingly unsuitable for IOL applications. As LCA is thought to be more stable than monochromatic HOAs, perhaps the correction of LCA with a novel IOL design is a more realistically achievable goal compared to the correction of monochromatic HOAs. The potential visual benefit of simultaneously correcting both the monochromatic and chromatic aberrations of the eye has been highlighted by Yoon and Williams [53].

1.3.5 Other optical and psychophysical considerations

There are numerous possible reasons why correcting monochromatic HOAs with a customised IOL design may not result in optimal vision; there may be alignment errors, positioning and rotation errors, faults in manufacturing, or any number of design flaws within the personalised eye model used to determine the prescription. But even if all of these potential errors were removed, the imaging quality of the eye would still be limited other optical phenomena and the visual performance of the subject would still be limited by psychophysical matters. Because vision is a subjective human perception,

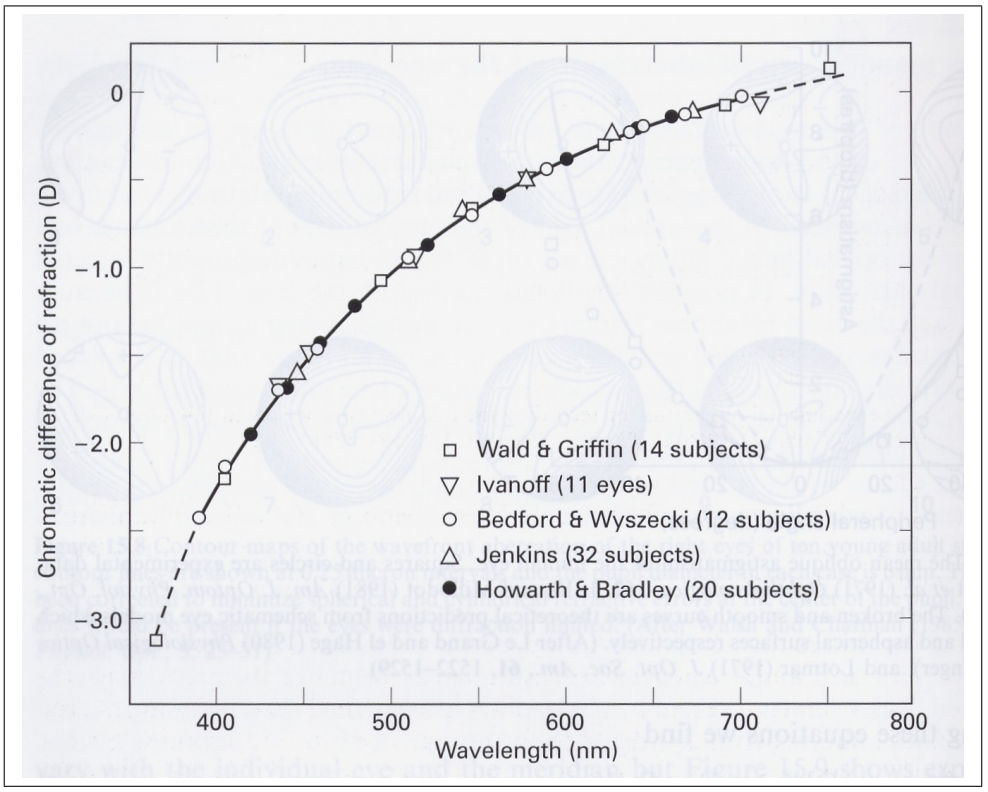

FIGURE 1.9: Longitudinal chromatic aberration in the human eye (*image credit* M H Freeman & C C Hull).

psychophysical issues, including a multitude of associated neural processes that limit (or in some cases enhance) visual performance, must be considered in addition to those that impact on retinal image quality. Psychophysical considerations are complex and include inter-connected topics such as adaptation to pre-existing aberrations, cognition, photopic and scotopic spectral sensitivity, pupil size control and feedback, and receptive field status.

These optical phenomena and psychophysical considerations are typically dynamic in nature because they are influenced by biological processes, such as retinal sampling, pupil size, corneal hydration state, pupil centration, and tear film topography. However, this work does not investigate IOL designs with dynamic capabilities, instead assuming some time-averaged state and this limitation, which applies to any static IOL design, is acknowledged. These optical and psychophysical considerations are vast and only the most fundamental issues are introduced here, further reading is recommended.

Diffraction is a consequence of the wave nature of light and the fact that apertures in an optical system are finite. It describes the bending of light at the edge of an aperture and defines a fundamental limit to the resolution capability of any optical system. The

magnitude of diffraction is dependent upon the wavelength, focal length of the system, and pupil diameter. In a typical human eye, retinal image blur caused by diffraction is negligible when compared to the effects of aberrations for pupil diameters greater than approximately 3 to 4 mm [46, 54, 55]. When the pupil diameter is greater than 4.5 mm, diffraction has little or no effect on visual acuity, as any image blur induced by diffraction is within the resolving power of the foveal cones [56]. The resolution ability improves as pupil diameter increases in a diffraction-limited optical system, as shown in Fig. 1.10 for a model eye. The minimum angular resolution of a diffraction-limited model eye assuming a wavelength of 555 nm and a pupil diameter of 6 mm is approximately 0.4 minutes of arc.

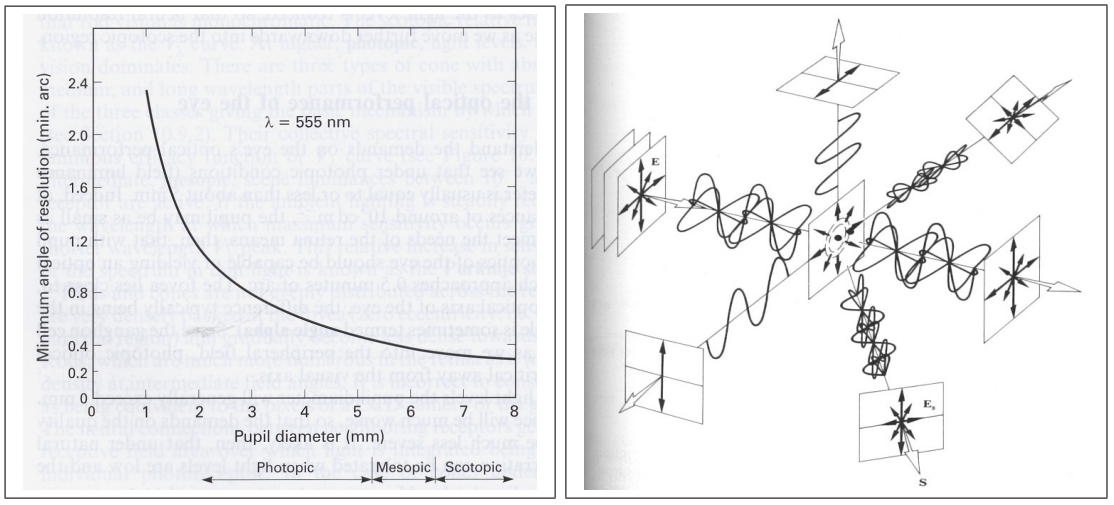

FIGURE 1.10: Resolution of a diffraction-limited model eye (*image credit* M H Freeman & C C Hull).

FIGURE 1.11: Scattering of unpolarised light by a molecule (*image credit* E Hetch & A Zajac).

The factors that influence pupil size in the eye are numerous, but the most fundamental parameters are the amount of ambient light, individual anatomy, and age. In this work concerning cataract patients, the relationship between age and decreased pupil size is important, as a small pupil diameter acts to negate the effects of monochromatic aberrations but diffraction is increased. Any benefit to vision in correcting HOAs will be greatest when diffraction is minimal and aberrations are maximal (i.e. when the pupil is dilated). For a pupil diameter of approximately 3 mm or less, the eye is typically considered diffraction-limited and so correcting HOAs in such a case may provide no advantage. Historically, IOL power calculations have disregarded pupil size, apart from the advisory consideration of suitability for patients receiving a multifocal IOL. The

personalised eye modelling used in this work will consider the individual pupil size of each patient.

Scatter is the deflection of photons by small particles within an optical medium. Particles are excited by the energy of the photon and then re-radiate the portion of the electromagnetic energy that is not absorbed at differing trajectories (Fig. 1.11). This interaction requires various models depending upon the ratio of the particle size to the wavelength of light. In the eye, scatter results in a smeared retinal image and a reduction of contrast, thus degrading the image quality [57]. The eye has numerous anatomical and physiological features that limit the effects of scatter.

In a cataractous eye, extraction of the cataract dramatically reduces absorption and scatter. The next most practical influence we might assert is to control the amount of light scattered by the IOL and the cornea. IOL scatter is reduced primarily by ensuring smoothness of the IOL surface and by using materials with the lowest occurrence of glistening particle formations. Protecting the physiology of a healthy cornea (e.g. avoiding mechanical, thermal and sonic endothelial damage during surgery) will allow the corneal endothelium to maintain stromal hydration at the precisely required level in order to preserve transparency and minimize corneal scatter. Refractive surgery is known to increase corneal scatter, so when modelling any potential refractive improvement that may result from personalisation of IOLs to include HOA correction, for post-refractive surgery patients particular emphasis should be given to the consideration of scatter. An individual's degree of RPE and choroidal pigmentation may also influence whether or not scatter is a limiting consideration for visual performance following HOA correction.

Retinal sampling is another physical consideration relevant to HOA correction and potential improvement in visual performance. Aside from the resolution limit of the eye's optics, the resolution limit of the retina must be considered. At the fovea a 1:1 coupling between ganglion cells and photoreceptors means that the sampling frequency is determined by the photoreceptor size and packing density. In specific situations the neural processing of the visual system can out-perform the Nyquist frequency limit predicted by the Shannon sampling theory, however, for most situations this is a reasonable benchmark to work towards. Apart from considerations of retinal spatial resolution, the temporal resolution of the retina should also be considered. When measuring the effect

of HOAs on vision, most scientists design visual performance tests that include a combination of both spatial and temporal resolution ability, such as a contrast sensitivity function measurement with the target displayed over a brief temporal window.

The eye has a low-pass modulation transfer function (MTF), implying that high spatial frequencies contained in an object will not be transmitted by the optics of the eye to the retina. The high frequency cut-off for the normal human eye is approximately 60 cycles per degree [58]. However, even if a specific spatial frequency is adequately imaged on the retina with sufficient contrast, that spatial frequency is still subject to neural processing throughout the visual pathway and may not necessarily be consciously perceived by the subject. In consideration of neural processing effects in addition to the optical MTF, researchers commonly use the contrast sensitivity function (CSF) as a psychophysical metric of visual performance. The CSF embodies the optical properties of the eye akin to the MTF of an optical system, but also includes all of the neural post-processing up to the level of perception. An example of a CSF is shown in Fig. 1.12 plotting the inverse contrast threshold of a sinusoidal grating pattern that is 'just visible' as a function of spatial frequency. A logarithmic scale is normally used due to the large dynamic range of the visual system [58]. In this work the visual performance of cataract surgery patients was not measured and our experimental results only describe refractive outcome, not visual performance.

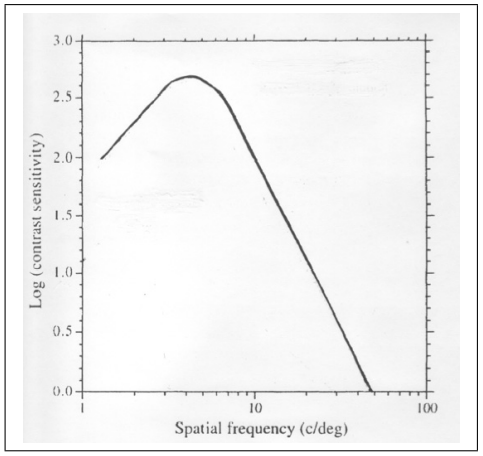

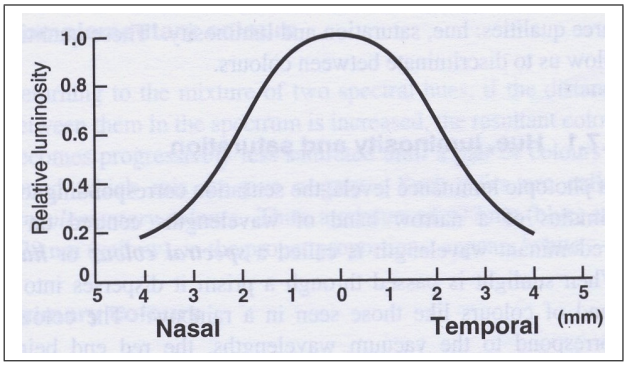

FIGURE 1.12: The contrast sensitivity function of a typical eye (*image credit* adapted from F W Campbell & D G Green).

FIGURE 1.13: The Stiles-Crawford effect, relating the apparent brightness of a ray to its location in the entrance pupil (*image credit* A H Tunnacliffe & J G Hirst).

The Stiles-Crawford effect (SCE) is a consequence of the waveguide nature of the cone

photoreceptors and is thought to limit the deleterious impact that HOAs have on vision. In practical terms the SCE creates an apodised pupil function for relative luminosity in the eye, which is typically centered near the pupil centre. This is illustrated in Fig. 1.13, which plots the relative luminosity for a pencil of rays as a function of location in the entrance pupil. The SCE can be interpreted as, *the closer a pencil of light enters to the centre of the Stiles-Crawford function, the more effective it will be at exciting a photoreceptor.*

In supposing that it is possible to correct the monochromatic HOAs of the eye with a customized IOL, monochromatic aberrations must still be listed as a limiting influence on visual outcome. On first impression this may seem counter-intuitive, however the clarification is that a static correction of HOAs is only appropriate for a given field point and a given set of object and image conjugates. All other field points and conjugates will display *different* monochromatic aberrations. As the human eye can be rotated to fixate an object of interest, this work investigated personalised eye models for correction of monochromatic HOAs over the central field (±5 degrees). Such a model concedes limitations regarding real-life situations where multiple objects of interest are present in the scene simultaneously, or the angular subtense of the object exceeds 10 degrees.

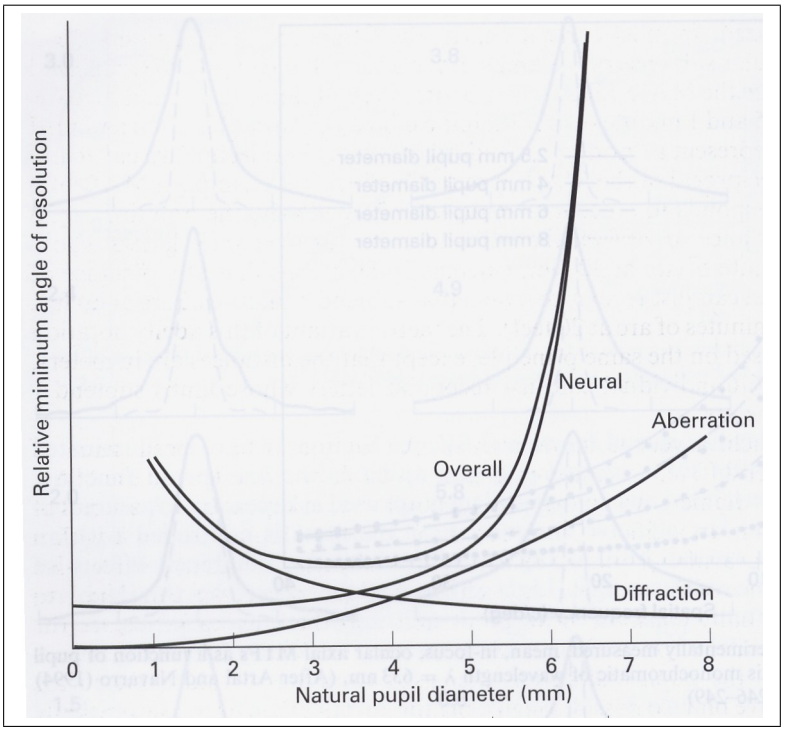

FIGURE 1.14: Phenomena effecting minimum angle of resolution in the eye (*image credit* M H Freeman & C C Hull).

The influence on visual performance from each of the considerations in this section will scale from negligible to significant due to inter-subject variability and the luminance level. Figure 1.14 is a schematic plot of relative minimum angle of resolution verses natural pupil size (note the absence of a scale on the vertical axis). It provides a useful summary to gauge the importance and influence of three key considerations (aberrations, diffraction, and neural processes) and under what conditions they are dominant. Figure 1.14 indicates that diffraction is the limiting factor for angular resolution with small pupils (less than approximately 3 mm diameter), while both aberrations and neural processing factors become the dominant limiting factors for angular resolution with large pupils (greater than approximately 4 mm diameter).

The natural pupil size is the parameter chosen for the horizontal axis because it is as a universal metric, easily relatable to other parameters. For example, as the natural pupil size increases, it is known that spatial and temporal summation (two key neural processes of the retinal receptive fields) also increases and the corresponding illuminance level is scotopic. Conversely, photopic conditions are associated with an abundance of photons, a decreased natural pupil size and decreased spatial and temporal summation of the retinal receptive fields. The natural pupil size itself is determined by a complex interaction between retinal luminance, age, accommodation state, individual anatomy, emotion, and retinal image blur. A summary of the psychophysical limitations to visual performance following correction of monochromatic aberrations are presented by Charman and Chateau [59].

1.3.6 Non-personal eye models

The work presented later in Chapter 3 is based on investigations using personalised eye models created in a ray-tracing software program. To provide a background introduction to this topic, Table 1.3 presents a brief summary of the long history of eye modelling. The eye models listed in Table 1.3 are non-personal in that they are intended to represent a typical eye, however their values for parameters usually originate from the mean value of a data set of actual measurements of real subjects. By contrast, our work in Chapter 3 uses personalised eye models, which correspond to individual patients, not just a realisation from an ensemble data set. Personalised eye models have previously been studied by several researchers [60, 61, 62, 63, 64].

Rather than list of the specifications of each non-personal eye model, Table 1.3 summarizes the characteristics of each model and is largely reproduced from the work of Giovanzana [65]. Some eye models exist in several forms - a full *theoretical* model may also have *simplified* or *reduced* versions, or multiple versions can occur due to an author 'updating' their model. Naturally, each model builds upon the previous generation, with modifications intended to improve accuracy, improve features, and account for experimental data. Some models were generated with a specific purpose or application in mind, for example, to determine the retinal projection from the visual field, or to predict retinal illumination [65].

Model (Year)	Surfaces		Lens	Accom.	Domain		Dispersion	Age	Ametropic
	Spherical	Aspheric			On-axis	Off-axis			
Gullstrand (1909)	6	-	shell	Yes	Yes	-	-	-	-
Le Grand	4	-	-	Yes	Yes	-	-	-	-
Emsley (1952)	1	-	-	-	Yes	-	-	-	-
Lotmar (1971)	3	1	-	-	Yes	Yes	-	-	-
Drasdo & Fowler (1974)	-	4	-	-	Yes	Yes	-	-	-
Kooijman (1983)	-	4	GRIN	-	Yes	Yes	-	-	-
Pomerantzeff *et al.* (1984)	-	2	shell	-	Yes	Yes	-	-	-
Navarro *et al.* (1985)	1	3	-	Yes	Yes	Yes	Yes	-	-
Blaker (1991)			GRIN	Yes	Yes	-		Yes	-
Smith *et al.* (1992)	2	2	GRIN	-	Yes	-	-	Yes	-
Indiana (1992)	-	1	-	-	Yes	Yes	Yes	-	-
Liou & Brennan (1997)	-	2	GRIN	-	Yes	Yes	Yes	-	-
Norrby (2005)	-	4	-	Yes	Yes	Yes	-	Yes	-
Atchison (2006)	-	5	GRIN	-	Yes	Yes	Yes	-	Yes
Goncharov & Dainty (2007)	-	4	GRIN	-	Yes	Yes	-	-	-

TABLE 1.3: Summary of the features for non-personal eye models, based on work by Giovanzana. Accom. is an abbreviation for accommodation.

1.4 Intraocular lens parameters, forms and properties

A typical IOL structure is composed of two main parts: the body (incorporating the optic lens) and the haptics (the struts). IOLs must satisfy specific requirements in terms of optical performance (e.g. dioptric power, resolution efficiency, spectral transmittance), mechanical properties (e.g. compression force, dimension tolerance, dynamic fatigue durability), biocompatibility (e.g. photostability, hydrolytic stability, test for leachables), shelf-life and transportability, labeling and information, clinical investigations, and other fundamental requirements (e.g. sterilization) [66]. The first generation IOLs were made from 'Perspex CQ', which is a trade name for PMMA used by Imperial

Chemical Industries with CQ designating Clinical Quality material of a very high purity level. Since 1949, IOLs have undergone numerous modifications to their materials and form. Not all proposed modifications have proven successful and understandably those providing the lowest complication rates have prevailed. The vast majority of present-day IOL devices are made from foldable materials and are designed for implantation inside the capsular bag. All discussion in this thesis relates to *in-the-bag* designs except where specifically noted otherwise. Figure 1.15 shows a schematic example of two commonly used modern IOL designs with their basic parameters indicated.

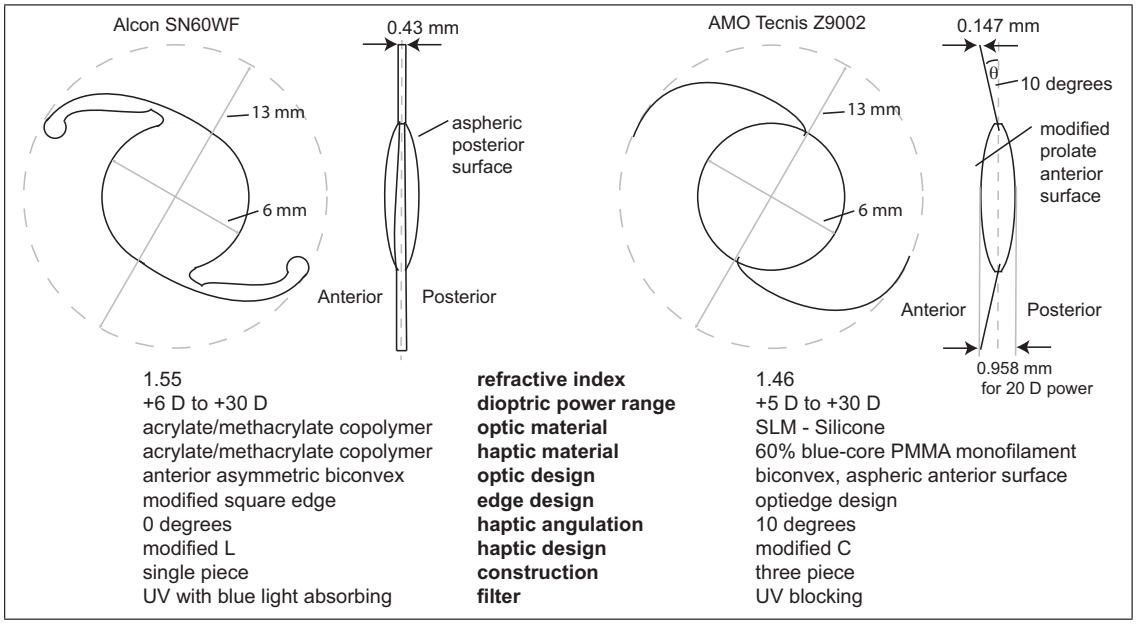

FIGURE 1.15: Schematic drawing of two modern posterior chamber IOL designs with basic parameters indicated. Reproduced from product information leaflets.

1.4.1 Intraocular lens materials and properties

Size and implantation stability

IOL size greatly influences implantation stability. Logically it is desirable to minimize the size of the body to allow insertion of the IOL through a small incision, to reduce mechanical interaction with the iris, and to reduce the demands for physical support required by the body mass. The less bulky and far more manageable haptics may then be suitably sized to obtain an overall diameter which secures the IOL within the sleeve of the capsular bag. Assuming the IOL is well-centered with respect to the pupil, it is unnecessary for the clear optic to exceed the largest expected pupil size. Accounting for typical senile miosis, a 5 to 6 mm optic diameter is a reasonable value

although occasionally edge effects such as reflections and glare may occur in patients with an unusually large pupil or a decentered IOL [67]. A modicum of positioning control inherently exists due to the body diameter being slightly greater than the capsulorhexis diameter, loosely restraining the IOL from moving anteriorly. However, this effect is negligible compared to the role of the haptics in providing positioning and stability. A few days following *in-the-bag* implantation, the IOL placement is quite stable due to capsular fibrosis and the healing response. Even in the event of a minor capsular tear the IOL can often be successfully secured by positioning the haptics approximately perpendicular to the tear. As the peripheral aspects of the haptics should ideally position near the equator of the capsular bag when implanted, unsurprisingly they are sized such that the overall diameter of the IOL (typically 12 to 13 mm) closely corresponds to the typical diameter of the adult crystalline lens.

For angle-supported and sulcus-supported (especially phakic sulcus-supported) designs, stability is critically reliant upon achieving the correct overall diameter sizing for each individual patient and may justify advanced biometry measurements [68]. This is typically not the case for *in-the-bag* designs, which are usually sized accordingly to population statistics. Many IOL designs are produced with only one value for overall diameter, an exception is the Akreos Adapt AO (Bausch and Lomb), which is manufactured in three different overall diameters in recognition that the diameter of the capsular bag generally increases with the axial length of the eye and therefore correlates inversely with required IOL power. Inappropriate sizing of IOLs creates problems of excessive movement, excessive/insufficient vaulting, and undue compressive stress. Both over-sizing and under-sizing is unacceptable, particularly for angle-supported and sulcus-supported IOLs, because it increases risks for glaucoma, corneal decompensation and vitreous loss.

Specific gravity and refractive index

Table 1.4 lists some historically used and modern-day examples of IOL optical materials along with refractive index and specific gravity parameters. Because the density of aqueous humor is similar to that of water, and because IOLs are generally constrained to the same family of biconvex forms, it is typical to use specific gravity of the body material to infer IOL buoyancy [69]. A specific gravity value close to unity is desirable because neutral buoyancy reduces the amount of support required by the optic mass and improves IOL stability. Historically both PMMA and glass materials were employed for

the IOL body, neither of which are foldable and therefore require large incisions for implantation. Glass held advantages over PMMA in terms of surface smoothness, high refractive index, and the ability to be sterilized by autoclaving, but it was only used for a brief period as it suffered buoyancy problems [9]. Further reasons to disregard glass as an IOL material were realized with the development of Nd YAG laser capsulotomy to treat PCO and the unsafe possibility of shattering the IOL *in situ*. The specific gravity of PMMA (1.18) is much closer to unity than that of glass (2.66) and so doesn't suffer the same buoyancy problems. The latter-developed foldable material categories (hydrogel, silicone and acrylic) all display nearly neutral buoyancy.

Properties of historically used[h] and present-day[p] IOL optic materials			
Material	Refractive index	Specific gravity	Attribute
PMMA (Poly methyl methacrylate)[h,p]	1.49	1.18	rigid
Glass[h]	1.62	2.66	rigid
poly HEMA (poly 2-Hydroxyethyl methacrylate)[p]	1.43 to 1.47	1.16 to 1.19	soft
Silicone Rubber (Poly dimethyl siloxane)[p]	1.43 to 1.46	1.14	soft
Acrylate/methacrylate copolymer[p]	1.47 to 1.55	1.15	soft

TABLE 1.4: Properties of historic and present-day IOL optic materials.

Refractive index is dependent on the frequency of light, the reference frequency nominated by standards is $5.4900 \times 10^{14} Hz$, equivalent to a wavelength is 546.07 nm in a vacuum [66]. The refractive index of ocular and IOL media is temperature dependent [70] and is typically quoted for 35° Celsius [66]. The refractive indices of selected optic materials are listed in Table 1.4 and two additional specific examples ($n = 1.55$ and $n = 1.47$) are given in Fig. 1.15. A high refractive index is a desirable property of IOL optic materials as it allows a thinner and flatter profile for a given optical power with subsequent advantages of reduced mass, improved folding/unfolding, easier insertion through a small incision, and decreased the risk of contact with the iris. However, these issues are quite well-controlled by all contemporary *in-the-bag* designs regardless of any nuance of optic material refractive index. The refractive index of the optic material in conjunction with the optical design determines the optical power and resolution. Resolution and other optical performance metrics must satisfy the minimum requirements set out by international standards, which also describe the test protocols that must be used in evaluating the optical performance of IOLs [66]. Chromatic dispersion of IOL body materials is often discussed in association with refractive index as under normal

dispersion these parameters are directly proportional, usually described by Cauchy or Sellmeier dispersion formula [71, 72].

Enhancers, coatings and biocompatibility

All present-day IOL materials filter ultraviolet (UV) light by incorporation of a filter; however some manufacturers also incorporate a yellow tint (often referred to as an *enhancer*) in the optic material to filter violet and blue light. Proponents advocate that clear IOL materials transmit further into the visible spectrum than would occur physiologically due to yellowing of the aging adult crystalline lens [73], and that filtering violet and blue light may act to reduce the risk of photochemical retinal damage [74, 75]. Opponents argue that UV protection is sufficient and need not extend into the visible spectrum, raising concerns that such tints may reduce contrast sensitivity under mesopic conditions and disrupt the circadian rhythm [76]. Recently, IOL materials with light-mediated variable tinting have been investigated [77].

IOL finishing and coating encompasses various manufacturing process that alter material qualities specifically at the surface and is therefore pertinent to biocompatibility and handling qualities. Both hydrophilic and hydrophobic coatings are commonly used in IOLs. The purpose of a coating may be to discourage inflammation, reduce ocular interaction, improve wettability[3], or increase slipperiness. These qualities make the IOL more biocompatible, inert, hydrophilic, and improve the folding/unfolding process.

Both capsular and uveal biocompatibility is essential, regardless of the intended IOL placement [78]. The smoothness of the surface and its wettability contributes to controlling interaction with ocular tissue. IOL materials must remain biocompatible in the event of possible future interruptions such as Argon laser and Nd YAG [79] laser treatments. Another possible future interruption is surgery requiring vitrectomy with silicone oil replacement. It is known that silicone oil strongly adheres to silicone IOLs [80, 81]. Therefore, silicone IOLs are usually avoided in patients with a risk of uveitis, diabetic retinopathy, or retinal detachment, and there is a general trend away from this material.

Biocompatibility is not solely determined by the surface finish of the IOL material or coating - the material bulk plays a role in setting biocompatibility too. The permeability

[3] Wettability is typically described by the contact angle and critical surface tension.

of the optic material to gas and metabolites is most relevant for phakic-IOLs [68] to avoid disturbing the metabolism of the crystalline lens, and this issue is usually not emphasised regarding *in-the-bag* IOLs. Apart from glass, most optical materials (Table 1.4) exhibit at least some degree of permeability. The dry form of poly-hydroxyethyl-methacrylate (poly HEMA) although no longer used, provides a dramatic example of fluid permeability; designed to be inserted into the eye in a compact dehydrated form, the IOL swells to an equilibrium hydrated state by absorbing aqueous humor and BSS [82]. Conversely, note that IOLs must not absorb certain dyes used during ocular surgery [83] such as Trypan blue or bind excessively with ocular drugs, especially those administered via intracameral or intravitreal routes. Beasley *et al.* [84] provide an overview of the factors influencing biocompatibility of the entire cataract extraction and IOL implantation process, including anatomical, etiological, surgical and IOL design considerations.

Intraocular lens body materials

During the mid 1980s, investigations regarding soft foldable materials attempted to take advantage of the small incision allowed by Kelman's phacoemulsification technique, leading to trials of new IOL body materials such as hydrogels [85] and silicone elastomers [86, 87]. Foldability is a key material property that facilitated small incision surgery with ease and safety of IOL insertion [88]. Consequently, research and development has propelled towards soft foldable, rollable, or injectable materials [89]. The task of developing foldable IOL materials required a compromised solution to satisfy competing properties such as rigidity and mechanical strength necessary to avoid distortion or displacement of the IOL. Today, PMMA continues to be a preferred IOL body material under particular circumstances, for example; sulcus-sutured IOLs are typically made from PMMA because it provides overall rigidity and resistance to tilt [90, 91]. However, the use of foldable silicone and acrylic materials is dominant in most circumstances [15, 92]. Modern foldable IOLs employ the use of a hollow *introducer/cartridge* device to inject the IOL into the eye. These devices may be pre-loaded with an IOL for convenience.

Foldable IOL materials are broadly distinguished by three categories; *acrylics* (acrylate/methacrylate copolymer), *silicone elastomers* (poly dimethyl siloxane polymers),

and *hydrogels* (acrylate/methacrylate copolymer) [93]. Both *hydrogels* and *acrylics* categories comprise of acrylate/methacrylate copolymer, the distinction being that hydrogels are specifically composed from poly HEMA, present either as a polymer or co-polymerized with another acrylic monomer. Poly HEMA itself is a hydratable variant of PMMA (a range of water contents are possible), being better tolerated by the eye owing to improved wettability. The *acrylics* category is usually sub-classified into hydrophilic and hydrophobic versions, these properties being determined by the chemistry of the polymer's functional side-groups and measured by the wetting contact angle. The development of novel IOL body materials such as the light-adjustable IOL [94] and the capsular bag refilling technique [95] creates new opportunities and methodologies for refractive correction following cataract extraction. It is beyond the scope of this thesis to discuss the optical, mechanical, biocompatibility, and other physicochemical properties of the diverse range of IOL body materials, further reading is suggested for this purpose [89, 93, 96, 97, 98, 99, 100].

Mechanical stability, manufacturing processes and temperature

The mechanical performance and testing procedures required for IOLs are governed by standards [66]. IOLs must compromise a balance of mechanical features; they should deform sufficiently when a force is applied to avoid damaging ocular tissue (compressibility) and yet they should be resistant enough to avoid warpage and be able to return to their original shape following removal of the force (shape memory). Parameter stability is not solely determined by the material choice alone - the generation and curing processes used during manufacture also significantly influence these properties. IOL components may be manufactured employing a variety of processes including lathe-cut generation, injection moulding, milling, and extrusion processes. Two key process during manufacture are polishing and sterilization.

Polishing creates a smooth surface finish, which improves biocompatibility by reducing interaction between the IOL and the ocular tissue. One-piece IOL designs are particularly well-suited to a tumble polish process, which allows smoothing of relatively inaccessible regions of the IOL. Polishing the optical zones of an IOL also has advantages of improved optical transmission and resolution, and conversely an optically diffuse surface finish around the edge of the IOL is thought advantageous in limiting unwanted edge-reflections and glare.

The importance of the sterilisation process is self-evident. The earliest generation of IOLs underwent chemical sterilisation with Cetrimide (a topical antiseptic). Both gamma irradiation and autoclave processes were used for a period, although not all IOL materials are thermally stable and are therefore unsuitable for autoclaving [9]. Subsequently the industry returned to chemical sterilization with the use of sodium hydroxide. However, ethylene oxide is now compulsorily used following a controversial FDA ruling [9] and is stipulated within the standards [66]. The electrostatic charge of IOL materials is a consideration in regard to controlling the attraction of electrically charged contamination particles.

The effect of temperature on the refractive index of IOL materials has already been mentioned. Temperature also influences the mechanical behavior of acrylics, polymers of acrylics and many other polymers [70, 93]. The glass transition temperature is a parameter used to demarcate a temperature boundary above which the hard and glassy properties of a polymer change to exhibit either viscous flow (linear polymers) or rubbery and elastic behavior (cross-linked polymers) [93]. The glass transition temperature of an IOL material is therefore a critically important parameter, particularly for materials with values within the range of (or close to), those temperatures likely encountered during manufacture, transport, storage, and *in situ*. Additionally, the importance of temperature is highlighted by suggestions that heat control during manufacturing processes plays a role in preventing microvoid formation and subsequent glistening of IOLs [101, 102]. Although to date their effects on visual performance are generally considered inconsequential, there is no known remedy other than IOL exchange if glistenings are believed to be bothersome to the patient [103, 104].

Haptic materials

Many of the mechanical requirements regarding the body material also apply to the haptic material. The haptics must be biocompatible and mechanically stable. Haptic materials should ideally be flexible and thin to allow coiling and insertion through a small incision; they are often coloured to enhance visualization. Historically Nylon (Polyamide) and Prolene (Polypropylene) have been used to create haptic loops. Nylon can be produced by a simple extrusion process, is very smooth, and of a suitable diameter. It is thermoplastic and demonstrates good elasticity at *in vivo* temperatures. It can be attached to the IOL body by friction without requirement of an adhesive [9].

However, biodegradation and inflammation problems lead to discontinued use of Nylon. Prolene exhibits advantages similar to Nylon in terms of producing a continuous smooth filament and is relatively resistant to biodegradation [9]. Prolene has a relatively poor shape memory and deforms easily, happily avoiding exertion of excessive force on the ocular structures, but potentially leading to an unsatisfactory situation where capsular healing forces overcome haptic resistance and misalign the IOL. Prolene is hydrophilic and relatively inert, although it has been shown to stimulate aspects of the complement pathway [105]. Extruded PMMA may also be used as a haptic material. It is more rigid and has better shape memory than Prolene, and is therefore less prone to misalignment problems. PMMA is resistant to biodegradation and also suffers less adherence of bacteria compared to Prolene. Polyimide is a polymer of imide monomers used as a haptic material and it may be formed from a variety of production techniques. It is thermally stable (autoclavable) and can withstand high energy radiation [105]. Poly vinylidene fluoride (PVDF) is a haptic material used on contemporary IOLs, exhibiting very good shape memory [105]. Acrylic (acrylate/methacrylate copolymer) materials are also used to form haptics in many modern IOLs, particularly in the instances of *one-piece* continuous designs and plate haptic designs.

1.4.2 Intraocular lens classes and types

The main classes and types of present-day IOL designs are summarized in Table 1.5 with examples and basic details listed. Here the descriptor *class* groups IOLs by a distinguishing optical feature and is predominantly associated with the IOL optic design, by contrast *type* groups IOLs according to implant location and other surgical circumstances, and is predominantly associated with the haptic design. The type categories are mutually exclusive, whereas the class categories are not; many devices satisfy multiple classes, for example the AT LISA 809MV (Carl Zeiss Meditec) is an aspheric, toric, multifocal, and small incision (1.5mm) IOL. A vast range of IOL devices are available today and only a representative sample are given in Table 1.5, further details of usage and availability of devices can be found elsewhere [106].

Intraocular lens optic designs

Regarding lens shape, historically convex-plano forms were available although today the

Summary of classes and types of modern and developing* intraocular lenses			
Class	**Example Device**	**Manufacturer**	**Principal feature**
Spheric	iSpheric AF-1 (YA-65BB)	Hoya	Defocus correcting
Toric	Staar Toric (AA4203TL)	Staar Surgical	Astigmatism correcting
	Rayner T-flex (573T/623T)	Rayner	Astigmatism correcting
Aspheric	Tecnis (ZA9003/CL Z9002)	AMO	Spherical aberration correcting
	Akreos Adapt AO	Bausch & Lomb	Spherical aberration neutral
	AcrySof IQ (SN60WF)	Alcon	Spherical aberration correcting
Multifocal	ReStor (SN6AD1/SN6AD3)	Alcon	Anterior apodized diffractive
	ReZoom (NXG1)	AMO	Anterior refractive zonal progressive
	AT LISA (809MV)	Carl Zeiss Meditec	Anterior diffractive refractive
	Mplus (LS-312 MF)	Oculentis	Posterior sector-shaped addition
Accommodating (developing* technologies)	Crystalens (AO/HD)	Bausch & Lomb	Flexible and hinged haptics allow translation (z) and flexure of the optic
	Synchrony	AMO	A positive (anterior) and a negative (posterior) lens are joined by a spring allowing a variable separation distance (z)
	Akkommodative (1CU)	Human Optics AG	Flexible junctions within the haptics allow translation (z) and flexure of the optic
	Tetraflex	Lenstec	Angulated ribbon haptics allow translation (z) and flexure of the optic
	NuLens	NuLens	Piston actuation evokes a dynamic change to the optic curvature
	FluidVision	PowerVision	Accommodating forces transport fluids to alter the optic curvature
	Tek-Clear (500)	Tekia	Flexible haptics bow to translate (z) the optic
	Akkolens	AkkoLens International	Two overlapping optics move in opposed transverse (xy) directions based on the Alvarez lens principle
Special	Light Adjustable Lens	Calhoun Vision	Light mediated post-implantation adjustment of the optic curvature
	CT ASPHINA (509M)	Carl Zeiss Meditec	Small incision surgery (1.5 mm)
	Akreos MI-60	Bausch & Lomb	Small incision surgery (1.8 mm)
Type			
In-the-bag	AcrySof (SN60AT)	Alcon	Conventional and routine IOL type
Angle-supported	S122UV/L122UV	Bausch & Lomb	Open-looped and step-vaulted haptics
Sulcus-sutured	SM36530	Aurolab	Modified C-loop haptics with eyelets
Phakic sulcus-supported	Visian ICL	Staar Surgical	Meniscus optic configuration
Phakic iris-supported	Verisyse Artisian	AMO	Meniscus optic configuration. The haptic enclavation mechanism is based on the Worst-claw design
Phakic angle-supported	Kelman Duet (712)	Tekia	Tripod haptic is joined to an independent optic component
Add-on / piggy-back	Sulcoflex (653L)	Rayner	Meniscus optic configuration
Special	Capsular bag re-filling	Nishi Eye Project	Polymer is injected into the capsule bag, which is then plugged to close
	Irismatch (30B)	Morcher	For use in aniridia

TABLE 1.5: Summary of classes and types of modern and developing IOLs.

biconvex form is almost universally used for *in-the-bag* designs. Typically the optic is bent (*asymmetric* biconvex) rather than equi-convex (*symmetric* biconvex), although equi-convex configurations are certainly acceptable. If steeper curvature is employed

on the anterior surface and a flatter curvature on the posterior surface, the resulting Coddington shape factor (q) is between 0 and +1, described by

$$q = \frac{r_2 + r_1}{r_2 - r_1} \tag{1.2}$$

where r_1 is the apical radius of curvature of the anterior surface of the optic (meters) and r_2 is the apical radius of curvature of the posterior surface of the optic (meters).

The optic shape factor effects optical resolution and performance [107, 108, 109]; it is classically used to minimize spherical aberration as discussed later in reference to Eq. 2.7. It also influences glare experienced both by the patient and an external observer [110]. However, there are additional non-optical issues that must also be considered by the optical design due to the interrelated consequences of IOL thickness, clear optic diameter and sagitta with various mechanical behaviors including the folding/unfolding process, the degree of physical contact with ocular tissues, and the compressive and tensile properties of the IOL (particularly at the optic/haptic boundary). A convex shape on the posterior surface of the optic is desirable to ensure contact and adhesion with the capsular bag, and when combined with a sharp edge design, reduced risk of PCO. For these reasons meniscus designs are generally avoided for *in-the-bag* type IOLs, although at least one concave surfaces is compulsory in the rare occasions when an IOL of negative power is required (as all IOL optic materials posses a refractive index value greater than that of aqueous/vitreous humor).

The radii of curvature values used in optic designs are not intended to match the physiological case, although this error was made by Ridley's first IOL, which matched the IOL radii of curvature to the Gullstrand model eye [111] without accounting for the refractive index difference between PMMA and the crystalline lens. The typical eye requires an IOL power of approximately 20 diopters (D), and most IOLs are supplied in dioptric ranges typically from 0 D to +30 D with steps of 0.5 D. Toric IOLs are often supplied with two or three values of cylindrical power. Powers outside the standard dioptric ranges may be available by specific request.

The IOL type as summarized by Table 1.5 is principally determined by the intended implant location, which in turn governs the typical values of various parameters including; optic shape factor (e.g. phakic sulcus-supported IOLs typically require a meniscus configuration), optic material (e.g. sulcus-sutured IOLs are normally made from PMMA),

optic size (e.g. sulcus-sutured IOLs typically employ a larger optic diameter), overall diameter (e.g. iris-supported IOLs necessitate a smaller overall length) and dioptric power range (e.g. angle-supported IOLs require reduced positive power).

Spherical designs incorporate rotationally symmetric spherical surfaces and intend to correct defocus. They are the simplest, oldest, and typically least-expensive IOL class. Their power is typically selected to provide a *best sphere* refraction, if the pseudophakic eye is approximated as a sphero-cylindrical system, this makes the circle of least confusion conjugate with the retina. Generally the spherical aberration (SA) of a spherical IOL is proportional to its dioptric power. Toric designs are designed to correct the astigmatism of the eye in addition to defocus. The rotation position of these IOLs (about the z axis) is aligned by the ophthalmologist at the time of implantation. Aspheric designs intend to control spherical aberration in addition to correcting defocus/astigmatism. Based on assumptions that the average adult cornea has $+0.275\,\mu m$ of SA over a 6 mm diameter [112], three different approaches to SA control have been adopted and are summarized below.

- Aim to fully correct the spherical aberration of the *typical* cornea. This methodology is used by Tecnis (AMO), which incorporates $-0.27\,\mu m$ of SA over a 6 mm diameter, intending to leave the typical pseudophakic eye with zero SA.
- Aim to partially correct the spherical aberration of the *typical* cornea. This methodology is used by AcrySof IQ (Alcon), which incorporates $-0.20\,\mu m$ of SA over a 6 mm diameter, intending to leave the typical pseudophakic eye with $+0.075\,\mu m$ of SA.
- Aim to impart a neutral effect on the spherical aberration of the cornea. This methodology is used by Akreos Adapt AO (Bausch and Lomb), which incorporates zero spherical aberration, intending to leave the pseudophakic eye with whatever amount of corneal SA is present.

The three different methodologies offer different advantages and disadvantages in performance regarding contrast sensitivity, visual acuity, depth of focus, and tolerance to IOL misalignment and tilt [113, 114, 115]. Currently, manufacturers do not supply IOLs with a customizable value for SA, although a particular IOL design may be supplied with an

option for multiple modalities, for example the CT ASPHINA (Carl Ziess Meditec) is supplied in both SA correcting (model 509M) and SA neutral (model 409M) designs.

To provide patients with the ability to focus on objects of interest at different distances from the eye, three different methodologies are used; monovision, multifocal IOLs, and accommodating IOLs.

Monovision aims for an emmetropic outcome in one eye (typically the dominant eye) and a myopic outcome in the fellow eye (typically the non-dominant eye) [116, 117]. Monovision is widely successful with contact lenses [116] and produces similar optical outcomes when used with IOLs. As monovision only requires IOLs of spheric, toric, or aspheric designs, it is less expensive than the multifocal and accommodating methodologies.

Multifocal IOLs use either diffractive, refractive, or combined surfaces, aiming to provide a static simultaneous range of focal powers either in a discrete or continuous manner. As an aside, the correction of longitudinal chromatic aberration (LCA) has been proposed with the use of diffractive IOLs, similar to that as in contact lenses. To correct LCA with IOLs, the use of diffraction is thought more practical than the classical doublet technique of Hall [52].

Accommodating IOLs aim to provide a dynamic focusing ability. Their mechanism of action may or may not mimic physiological accommodation, although all designs intend to replicate its visual outcome. Accommodating IOLs are arguably the most complex class, usually requiring moving and flexible components and materials. Most designs rely on intact zonules and capsular structure to transfer the variable accommodative forces from the ciliary muscle to the IOL, which then effects a change in the optic position and/or shape. Note that the change in the optic position encompasses the possibilities of, translation along the z axis, transverse movement in the xy plane, and rotation about z axis. I consider accommodating IOLs to currently be in a developmental or experimental stage.

A detailed discussion of IOL classes, their relationship to choice of materials, and their influence on vision quality is beyond the scope of this thesis, further reading is recommended for this purpose [18, 89, 117, 118].

Intraocular lens haptic designs

The primary purpose of haptics is to provide stability of positioning. The haptic design should be easily foldable, rollable, or coiled to enable small incision surgery. They must position the optic reasonably well-centered, without difficulty, and with minimal tilt. Haptic design is mainly influenced by the implant location, which dictates the required haptic size (IOL overall diameter) and the degree of angulation or vaulting. Haptic forms can be broadly classified as closed loop, open loop, and plate. If the IOL is manufactured by combining two separate haptic components with the body then the design is referred to as *three-piece*, whereas if the haptics are formed from the same continuous substrate as the optic body then the design is called *one-piece*.

The compressibility of the haptic material is a particularly important parameter because it characterizes the balance between important competing interests; the haptic should compress sufficiently to avoid damaging ocular tissues while at the same time it should be resistant enough to avoid distortion and displacement of the IOL, especially relevant in the days immediately subsequent to surgery as the capsular bag contracts and fibroses. The haptic design must ensure that when the IOL is compressed, it does not vault in either the anterior or posterior direction in any unintended way.

Stability regarding rotation about the z axis is particularly important for toric IOLs. It is surgically convenient if the haptic design of a toric IOLs allows rotation in both clockwise and counter-clockwise directions. Although once the desired rotation position is achieved, the haptics (and any plate fenestrations) should then restricting any further rotation. Some toric IOLs incorporate frosted plate haptics with larger fenestrations claiming this increases capsular bioadhesion [119], although conventionally the use of frosted surfaces is restricted to the optic edge in concern of exacerbating the inflammation process.

Haptic angulation is usually between 0 to 10 degrees and may be produced with angulation, dished, or offset haptic arrangements [105]. Haptic angulation is used to minimize unacceptable contact between the IOL and the iris, as abrasion of the posterior surface of the iris can cause pigmentary dispersion glaucoma. Angulation also acts to promote apposition between the posterior IOL and the posterior capsule, a feature that complements other techniques intended to limit PCO (see Section 1.4.2). It is preferable for the haptics to slightly stretch the posterior capsule such that a smooth drape is formed

over the IOL and reduces the chance of PCO. However, this consideration is moderated by risk of the haptics stretching the bag too aggressively, which can lead to capsular distention.

Modern *in-the-bag* IOLs commonly use open loop or plate haptic configurations. The current trend is towards modified versions of C loop and L loop, and Fig. 1.15 shows an example of each of these designs. Due to their low usage compared to *in-the-bag* designs, the haptic design requirements for angle-supported, iris-supported, sulcus-supported and sulcus-sutured IOLs may be considered relatively specialized. The comparatively infrequent use of these types of IOLs is now mainly reserved for situations when there is insufficient capsular and/or zonular integrity to position the IOL *in-the-bag* in the pseudophakic case, and for myopic refractive surgery in the phakic case [90, 91].

Early angle-supported IOLs with closed loop haptic designs posed unsatisfactory risk of corneal decompensation due to excessive vaulting and mechanical damage to endothelium [9]. These eyes also risked secondary glaucoma due to synechia formation in the angle that typically enveloped the haptic. These risks were improved somewhat by progressing from closed loop to open loop designs [9]. The development of the open loop haptic arrangement was led by Kelman, it allowed easier insertion through a small incision and was therefore better suited to phacoemulsification surgery than closed loop designs. Open loop haptics were developed in various configurations of J loop, Y loop, C loop, L loop, and modified versions of each.

Iris-supported haptic designs risk iris erosion and inflammation. They must mechanically brace the iris and so are configured using clips or closed loops rather than the more common open loop and plate haptic design of modern conventional *in-the-bag* IOLs. Historical examples of haptic designs for iris-supported IOLs include Epstein's 'collar-stud' and 'maltese cross' designs, Copeland's design, Binkhorst's iris-clip, and Worst's iris-claw [9].

Modern sulcus-supported phakic IOLs often employ a plate haptic design, while sulcus-sutured pseudophakic IOLs often employ an open loop configuration with eyelets.

Discouraging posterior capsular opacification and dysphotopsia

Following cataract surgery, remnant cataractous epithelial cells can migrate from the

equator and proliferate across the posterior capsule. Because these cells have a disordered arrangement, they are opaque and can effectively negate the visual improvement initially gained by removing the cataract. Posterior capsular opacification (PCO) can be discouraged by the following techniques; total clearance of cataractous debris and capsular polishing, contact inhibition by incorporating a sharp edge profile in the IOL design, constraining the optic shape factor to ensure a convex posterior surface, haptic angulation to promote apposition between the posterior optic surface and the posterior capsule, and use of anti-mitotic agents (although the latter is not widely favored).

The use of a sharp barrier is particularly relevant to the posterior edge of the IOL and contact inhibition should ideally be maintained throughout 360 degrees, even at the haptic/optic junction. A sharp square edge design is thought to reduce risk of PCO although this may inadvertently increase glare and edge reflections in comparison to a smooth rounded edge. In this way a design compromise exists between the desire to prevent PCO and yet avoid dysphotopsia [18, 88].

In further consideration of dysphotopsia, a frosted or diffusely textured optic edge surface may slightly reduce glare [120]. Manipulation holes and other fenestrations are another important potential source of unwanted reflections and their use and placement in a design should be carefully considered. Certain IOL materials possess an innate defense against unwanted reflections due to their absorption properties that arguably creates a GRIN-like effect at surface of the optic [119]. The causes of dysphotopsia are not completely understood and further discussion on this subject can be found elsewhere [67, 110, 120, 121].

If PCO does occur, it can be treated by Neodymium-doped yttrium aluminium garnet (Nd YAG) laser capsulotomy. This treatment causes photodisruption to the epithelial cells using a 1064 nm wavelength pulsed laser operating in Q-switched mode [122]. The treatment was first performed by Daniele Aron-Rosa in 1979 and although it effectively constitutes no infection risk, it is associated with other various complications such as inflammation (e.g. CME) and the risk of pitting the IOL surface. The risk of damaging the IOL is increased for soft optic materials and if proper care is not taken to accurately focus the laser [79]. Pitting damage to the optic surface is thought to increase scatter and potentially disturb vision. Another possible consequences of Nd YAG laser damage to the IOL is the potential release of toxins from the IOL material. Due to this latter

concern, chromophores and other constituents are combined with the IOL material using specific methods that avoid toxicity. Further reading is recommended for discussion of the issues associated with PCO [84, 123, 124, 125].

1.5 Intraocular lens power calculations

1.5.1 Geometrical optics formula

Compared to the sophisticated technologies and surgical skills involved in performing cataract surgery, the methods used to select the required IOL power are remarkably rudimentary. The numerous IOL power prediction formulas currently used are remnants of a past era when the limiting factor of visual outcome was generally not the power prediction formula, but rather some dominating clinical issue. Efforts during that period were justly directed toward addressing the overriding concerns such as controlling the risk of infection, corneal decompensation, CME, and RD, reducing the rate of PCO, positioning the IOL in a stable and safe location, reducing the required incision size, improving biometry instrumentation, etc. In previous times, the prediction formulas were satisfactory given the overriding priority of the surgical and medical issues. However, today the limiting factor on visual outcome is likely to be significantly influenced by factors such as, the care taken by clinicians performing biometry, IOL power selection methodology, the IOL manufacturing quality, the IOL design, the surgical skill of the ophthalmologist, and the accuracy of the measurement of the stabilized post-surgery refractive error [126].

Historically, there have been two main approaches to IOL power calculations, based on a geometrical optics solution and/or linear regression analysis of retrospective cases. A third approach based on ray-tracing [61] is now gaining awareness amongst the industry and is the technique used in this work (see Chapter 3). Although the first IOL was implanted in 1949, it took until 1967 before the first two-surface, thin lens geometric optics equation was published [127], and the first publication on this topic in English was not until 1973 [128]. Prior to 1967 the required IOL power was determined by a rule of thumb using

$$P_e = 18 + 1.25\,R_o \tag{1.3}$$

where P_e is the IOL power required (iris-supported design) for emmetropia (diopters) and R_o is pre-existing refractive error (diopters) [129]. This delay in formalising a simple geometrical optics formula until 1973 provides insight into how unimportant the IOL power calculation was compared to the surgical and medical considerations of the time.

Between 1967 and 1976 IOL power calculation formulas were published by Thijssen [130], Colenbrander [128], Fyodorov [131], van der Heijde [132], and Binkhorst [133]. All of these formulas can essentially be regarded as algebraic rearrangements of the same[4] equation,

$$P_e = \frac{n_v}{l-d} - \frac{n_a}{(n_a/K)-d} \tag{1.4}$$

where P_e is the required IOL power for emmetropia (diopters), n_a and n_v is refractive index of the aqueous humor and vitreous humor respectively, l is axial length (meters), K is the corneal power (diopters), and d is the axial depth from the cornea to the IOL (meters), later commonly called the effective lens position (ELP). Equation 1.4 can be derived by using thin lens geometrical optics approximations and a step-through vergence equation, treating the eye-IOL system simply as two refracting surfaces and an image plane [3].

To implement Eq. 1.4 in practice, the refractive indices are assumed from the literature ($n_a = 1.336$ and $n_v = 1.336$) without regard for chromatic dispersion. Initially the ELP was assumed constant for all patients and its value was only dependent on the implant location of the IOL; posterior chamber, iris-supported, or angle-supported. The eye was approximated as a paraxial sphero-cylindrical system, and because a 'best sphere' defocus-only correction was the norm until the introduction of toric IOLs in the 1990s, the value used for corneal power was taken as the mean apical corneal power of the two principal meridians. Since the advent of toric IOLs, for the prediction of required IOL power, Eq. 1.4 and its analogous successors were then applied separately to each principal meridian in turn.

The calculation of corneal power itself, regardless of meridian, historically relied upon assumed values of the central corneal thickness, and the ratio between the anterior and posterior corneal curvature. Determination of corneal power required this ratio because

[4]The formulas published differ slightly with each author suggesting slightly different constants to account for retinal thickness and the location of the IOL plane. Notably Binkhorst's formula also differs from his colleagues by using a value of 4/3 for n_e, n_v, and n_a. See Appendix C

the curvature of the posterior cornea was not measured directly, but rather estimated from the anterior corneal curvature value, and conventionally was accounted for by using an *equivalent* value of the corneal refractive index. Under this approximation the corneal power calculation can be simplified into an expression with the same form as the paraxial spherical surface power equation:

$$F = \frac{n' - n}{r} \tag{1.5}$$

where F is the power of a single spherical surface (diopters), r is the radius of curvature of the surface (meters), n is the refractive index of the first media, and n' is the refractive index of the second media. Further details concerning the approximation of corneal power are explained in Appendix A. Over time the instrumentation available for measuring the two key biometry parameters of axial length and corneal curvature have improved, including technologies that now allow direct measurement of the posterior corneal shape. Concurrently, the formulas used to calculate required IOL power also improved, although it can be argued that some proposed ad-hoc modifications lacked scientific merit.

Even for a data set obtained with state-of-the-art biometry instruments, any predictions of required IOL power using Eq. 1.4 would still be constrained by various limitations listed in Table 1.6.

The last five issues listed in Table 1.6 partially concern instrumentation limitations rather than solely relating to the IOL power calculation formula and methodology. Apart from the influence that assumptions regarding refractive index for various media have on determining axial length and corneal power, biometry data suffers other uncertainties particular to the specific technology of each instrument - these issues are discussed later (see Section 1.7).

1.5.2 The effective lens position

The geometrical optics formula (Eq. 1.4) was used in its several guises [128, 130, 131, 132, 133] from 1973 until 1980, and its greatest limitation during that time was the use of a constant value for the ELP for each patient, which was only varied according to IOL type (i.e. angle-supported, iris-supported, or posterior chamber IOLs). The value for the ELP, was called the *ACD constant*, and for a specific manufacturer and IOL

Approximations associated with industry-standard IOL power calculations
The ELP is very difficult to predict and the estimation of this highly sensitive value is considered critical for accurate prediction of required IOP power.
The various axes and angles of the eye are not considered.
Chromatic dispersion is ignored, directly by Eq. 1.4, but also indirectly by the combination of biometry data collected from instruments operating with multiple different wavelengths.
The eye is approximated as a paraxial, sphero-cylindrical system.
The IOL is approximated as a paraxial, sphero-cylindrical system.
The pupil size is disregarded, assumed negligible by the paraxial assumption.
The refractive indices of the aqueous humor and vitreous humor are assumed from the literature.
The post-surgery value for corneal power is assumed equal to the pre-surgery value.
The calculation of corneal power requires an assumed value for corneal refractive index from the literature.
The *time of flight* measurement performed by an interferometer (e.g. PCI or LCR) is converted to an axial length value by the instrument software, which requires assumed values of refractive indices for the cornea, aqueous humor, cataractous lens, and vitreous humor. If the device only measures the location of the retinal plane relative to the anterior cornea and not the intermediate segments, then calculation also requires an assumed ratio of segmental lengths (e.g. ACD : cataractous lens thickness : vitreous depth).
The *time of flight* measurement performed by ultrasonography is converted to an axial length value by the instrument software, which requires assumed values of acoustic impedance for the cornea, aqueous humor, cataractous lens, and vitreous humor. If the electronic gating of the ultrasonography instrument only measures the location of the retinal plane relative to the anterior cornea and not the intermediate segments, then calculation also requires an assumed ratio of segmental lengths (e.g. ACD : cataractous lens thickness : vitreous depth).

TABLE 1.6: Approximations associated with the implementation of geometrical optics formula for IOL power prediction.

model is defined as the post-surgical axial distance from the anterior corneal vertex to the IOL plane in an average eye. Since the 1980s, modifications to the geometrical optics formula (see Section 1.5.4) have recognised inter-subject variation in the value for ELP. In this work, we distinguish between the *ACD constant* (d_o), which is the ELP value of a particular IOL in an average eye, from the patient-specific modified ELP value (d_m), which considers biometry values specific to an individual patient for a particular IOL.

Gross variation in ELP is dictated by the implantation location (e.g. angle-supported, iris-supported, sulcus-supported, or *in-the-bag*), and beyond that, secondary issues effecting ELP can be separated into three general areas as follows;

- *Surgeon-specific and instrument-specific idiosyncrasies of the surgical technique.*

For example, the incision type (corneal or scleral), size, and structure; the capsulorhexis size, construction (manual or automated), and configuration; the manipulation of the IOL during implantation.

- *Patient-specific anatomical and physiological factors.* For example, the strength and distribution of fibrotic and contractive capsular forces, the magnitude of various ocular dimensions, the patient age, gender, and ethnicity.

- *IOL design-specific configuration details.* For example, optic shape factor, compressibility of materials, haptic angulation, which effect the physical/geometrical position of the IOL.

Concerning this final point, within the literature the optical shape factor is often discussed in regard to its effect on the position of the 'optical plane of the IOL' as though it is a consequence of optical theory, and distinct from the physical plane of the IOL. However, this is a misunderstanding, as when applying formulas such as Eq. 1.4 (and others subsequently developed from it), that are based on thin lens assumptions, by definition the principal planes and the vertex planes of the IOL are conceptually coincident and hence no distinction is possible between the physical location and the 'optical plane.' Acknowledgment that IOL power prediction is influenced by the IOL optic configuration (i.e. shape factor) implies that the IOL should in fact be modeled as a thick lens and this conclusion is neglected by some authors. This issue emphasizes the central tenet of this work: exact ray-tracing should be used to model the pseudophakic eye, rather than a thin-lens or thick-lens geometrical optics approximation.

The ELP is a very sensitive parameter in IOL power calculation and unfortunately it is also difficult to accurately predict. Determining exactly what axial depth an implanted IOL will acquire as its position stabilizes and the eye heals is a difficult task. Most researchers approach this issue by relying on correlation between ELP and one or more pre-surgery biometry measurements (typically anterior chamber depth (ACD), axial length, corneal power, and white to white (WTW) are used), and the estimation of ELP remains a major source of uncertainty in IOL power prediction [126]. Suggested methodologies propose that the ELP will coincide with the equatorial plane of the cataractous lens [134] or at some sagittal ratio of the central cataractous lens thickness. However, obtaining accurate biometry of these locations and distances is extremely challenging. Here the importance of the axial position of the IOL has been emphasized.

The IOL position in all dimensions of *xyz* space (these degrees of freedom are colloquially referred to tip, tilt, decentration, and rotation) are also important in determining the optical performance of the pseudophakic eye.

1.5.3 Linear regression formula

In 1980 the first linear regression IOL power calculation known as the SRK formula [135] was published:

$$P_e = A - 2.5\,l - 0.9\,K \tag{1.6}$$

The authors collected post-surgical refraction data from over 2500 eyes and after adjusting the value of the implanted power to account for residual refractive error, the revised data set of IOL power required for emmetropia (P_e) (diopters) was modeled using least-squares linear regression of two biometry variables measured pre-surgery; axial length (l) (millimeters) and corneal power (K) (diopters). The SRK formula represents a purely statistical approach, perhaps best highlighted by the formula's use of incongruous units. No optical laws are used in its derivation. To calculate the post-operative refractive error, they authors again apply regression analysis to a large data set and derive the following rule of thumb

$$R_t = 0.67\,(P_e - P_i) \tag{1.7}$$

where P_i is the implanted IOL power, P_e is the predicted IOL power for emmetropia, R_t is the targeted post-surgery refractive error, and all variables have units of diopters. A discussion of this topic is given in Appendix B and use of Eq. 1.7 is cautioned as providing an approximation only.

The SRK formula avoids some of the criticisms of the approximations associated with the geometrical optics formula listed in Table 1.6, simply by avoiding an optical framework in preference for a statistical solution. However, the use of a statistical approach is bound to produce results governed by central tendency. That is, the more common the parameters of an eye are, the more accurate the prediction should be. By contrast, the more uncommon the parameters of an eye, the more inaccurate the prediction should be. Arguably the most influential contribution the SRK formula brought to IOL power calculation was the concept of *personalisation* of the A constant. In some respects, the A constant was initially regarded to act primarily as a proxy for the influence of the IOL

design on ELP (and hence in some respects is equivalent to the ELP parameter of the geometrical optics approach). However, over time the concept of personalisation of the formula was extended to encompass all prevailing conditions including; the particular surgeon and all features of their surgical technique, the particular clinician measuring biometry data, the particular biometry instruments used, the particular IOL manufacturer, the particular IOL design, etc. After performing an initial series of surgeries using the manufacturer-nominated A constant value, the biometry data set (comprising of pre-surgery axial length, pre-surgery corneal power, implanted IOL power, intended refractive error, and observed post-surgery refractive error) is analyzed using Eq. 1.6 to find the refined value for the A constant that produces a mean difference of zero between the intended refractive error and the observed post-surgery refractive error. This methodology is repeated and eventually after multiple retrospective analyses of data sets obtained within a consistent clinical and surgical setting, and by applying linear regression techniques to those data sets, the A constant becomes *personalised* bringing improvements to IOL power prediction.

It is considered good practice to continually refine and update the A constant value, even if the clinical and surgical setting is thought to be unchanged. The advantage of retrospective analysis of data sets and including a parameter in the IOL power prediction formula, which can be adjusted accordingly, is that the regression technique acts to minimise the effects of any bias consistent at the inter-subject level, regardless of wherever throughout the entire process the bias originates from. The concept of the A constant was also popular because it offered a simple method for reworking IOL power calculations *on the fly* during surgery in the event of insufficient capsular/zonular support. If such complications forced the implant location of the IOL to be changed, the surgeon simply determined the difference between the A constant used in the original power calculation and the A constant of the reserve IOL. Because the A constant has a 1:1 ratio with IOL power, the IOL power is simply adjusted by the same value. In comparison to the various geometrical optics formulas (Eq. 1.4), the SRK formula predicts a greater value of emmetropic IOL power for longer than average eyes and a lesser value for shorter than average eyes [3]. A typical A constant value for *in-the-bag* placement of a biconvex IOL is 117.8 to 118.8 [3].

1.5.4 Modified geometrical optics and linear regression formulas

Neither the geometrical optics formula or the SRK formula proved overly accurate. This was particularly true when applied to eyes with unusually short or long axial lengths and eyes with unusually steep or flat corneas. The geometrical optics formula (Eq. 1.4), was initially implemented with a constant value for ELP, varying only by the implant location category; angle-supported, iris-supported, or posterior chamber-supported. Throughout the 1980s various modifications were made to both the geometrical optics formulas and to the linear regression formulas, and so began a series of ad-hoc adjustments to both methodologies.

In 1981 Hoffer proposed modifying the geometrical optics formula (Eq. 1.4) to adjust the ELP (d) in a linear relationship with axial length (l) according to

$$d_m = d_o + 0.292\,l - 6.87 \tag{1.8}$$

where d_m is the modified value, d_o is the initial value (known as the *ACD constant*), and all units are millimeters. Hoffer also pointed out the convenience of treating the term for corneal power (K) in the geometrical optics formula as $(K + R_t)$ where R_t is the targeted post-surgical refractive error (see Appendix B).

In 1982 Shammas also proposed modifications to the geometrical optics formula, including adjustments to the value for axial length (l) by 0.1 mm for every millimeter variation in axial length lesser or greater than 23 mm, as expressed by

$$l_m = 0.9\,l_o + 2.3 \tag{1.9}$$

where l_m is the modified value, l_o is the initial value, and all units are millimeters. Shammas hoped to improve calculations in long and short eyes by this modification of axial length that had a similar effect on the predicted IOL power that others achieved by varying the ELP value.

Other proposed variations in methodology concerned the determination of corneal power - a preliminary step before the geometrical optics formula (Eq. 1.4) can be evaluated. Like Binkhorst, Shammas promoted using a value of 4/3 for the equivalent corneal refractive index (n_e) rather than the conventionally used value of 1.3375 when estimating

the corneal power (K) from Eq. A.10 (see Appendix A). Shammas and Binkhorst argued the choice of a lower value for equivalent refractive index is beneficial in anticipation that the post-surgical corneal power will be less than the pre-surgical value as a result of the relatively large corneal incisions required by the surgical techniques of the day [3]. Olsen also argued for using a lower value than the conventional value of 1.3375 for equivalent corneal refractive index, by applying a thick lens formula in accordance with Gullstrand's exact schematic eye, proposing that a value of 1.3315 should be applied [136] (see Appendix A). Use of a lower value for equivalent corneal refractive index is supported by Purkinji-imaging and Scheimpflug-imaging studies [137, 138], which suggest the mean ratio of corneal curvature is actually even lower than the Gullstrand value of 6.8/7.7. Happily the use of population averages for these parameters is now unnecessary as modern instruments readily allow clinical measurement of pachymetry and posterior corneal shape of an individual patient.

Various authors have suggested the addition of a *retinal thickness* constant to the axial length measurement. This modification mainly applies to the geometrical optics formulas and is considered unnecessary in the regression formulas where the variation in the measurement of axial length is embodied within the personalised A constant. Axial length measured by applanation ultrasound devices are prone to artificially low values due to inadvertent corneal compression. When comparing applanation to immersion measured values, Shammas suggests the addition of 0.24 mm. Similarly, when the mean axial length of the Binkhorst (applanation) and Hoffer (immersion) studies are compared, a differential value of 0.20 mm is observed [3, 139]. Axial length measurements performed with interferometry (commonly PCI and LCR devices) are thought to measure the signal reflection from the retinal pigmented epithelium. While ultrasound devices are thought to measure the signal reflection from the hyaloid face, and therefore produce values that are generally lesser. Accordingly, ultrasound-measured values are often compared to interferometry-measured values by the addition of a constant.

Similar to the modification of Hoffer, in 1984 Binkhorst published modifications to the geometrical optics formula (Eq. 1.4) proposing to adjust ELP (d) in a linear relationship with axial length. An example of this modification is given in Eq. 1.10 for a posterior chamber IOL where d_m is the modified value, d_o is the initial value (known as the *ACD constant*), axial length (l) is constrained to be less than 26 mm, and all units are

millimeters.

$$d_m = d_o \cdot \frac{l}{23.45} \tag{1.10}$$

In 1988 the SRK II formula was published, it was based on the original SRK linear regression formula (Eq. 1.6) except with the following conditions added

$$\begin{aligned} \text{if} \qquad l \geq 24.5 \text{ mm} \quad &\text{then} \quad \alpha = -0.5 \\ 22 \text{ mm} \geq l < 24.5 \text{ mm} \quad &\text{then} \quad \alpha = 0 \\ 21 \text{ mm} \geq l < 22 \text{ mm} \quad &\text{then} \quad \alpha = 1 \\ 20 \text{ mm} \geq l < 21 \text{ mm} \quad &\text{then} \quad \alpha = 2 \\ l < 20.0 \text{ mm} \quad &\text{then} \quad \alpha = 3 \end{aligned} \tag{1.11}$$

where axial length (l) has units of millimeters and α is a constant with units of diopters.

In regard to a targeted post-surgical refractive error (R_t) calculated with the SRK II formula, the term for corneal power (K) is not simply replaced with ($K + R_t$) as it can be when approximated by the geometrical optics formula (see Appendix B), instead another set of adjustments are stipulated, which can be summarized with the following boolean statement

$$\begin{aligned} \text{if} \qquad & A - 2.5\,l - 0.9\,K + \alpha > 14 \\ \text{then} \qquad & P_a = A - 2.5\,l - 0.9\,K + \alpha - 1.25\,R_t \\ \text{else} \qquad & P_a = A - 2.5\,l - 0.9\,K + \alpha - R_t \end{aligned} \tag{1.12}$$

where P_a is the predicted IOL power for ametropia required to produce the targeted post-surgical refractive error (R_t), and all units are diopters. To apply the SRK II formula for a desired emmetropic IOL power (P_e), simply set $R_t = 0$ when evaluating Eq. 1.12.

From the 1980s through to the 1990s, many aspects of cataract surgery were improving. New interferometric devices [140, 141] and corneal topographers provided more accurate measurements of axial length and corneal shape [142]. Phacoemulsification was becoming dominant and in the developed world ICCE was rarely performed past the mid 1980s. The choice of IOL placement was now firmly favoured to be *in-the-bag* and techniques

to both prevent, and if necessary treat, PCO were maturing. All of these advances provided impetus to address the limitations of the IOL power calculations.

1.5.5 Modern formulas

During the 1980s many of the adjustments to IOL power calculations were aimed at improving the estimate of ELP. Proposals were made to modify the ELP value in a linear relationship with axial length (Eqs. 1.8, and 1.10), and as the SRK formula does not include a parameter for ELP, its suggested modifications were based on subgrouping intervals of axial length (Eq. 1.11). The next layer of ad hoc adjustment to the geometrical optics formula was to modify the ELP value in a relationship dependent on both axial length and corneal power (or analogously, corneal radius of curvature). These adjustments were published during in the 1990s, they are currently the industry norm and are often referred to as *modern formulas*. The most well-known and widely used modern formulas are summarized in this section.

Understanding and comparing the modern IOL power calculations is not straight forward. Some scientific discomfort arises because the modifications are ad hoc in nature, born out of clinical experience and empirical data. At times, the various authors of the modern formulas rely on arbitrarily defined parameters that apply uniquely to their own model and are not relevant to the approach of others. Perhaps most frustrating, these newly introduced variables representing some physical parameter, are not directly measured, but instead estimated by a combination of variables that are already present in the IOL power prediction formula (i.e. axial length and corneal power or anterior corneal radius of curvature). Many publications in the field contain typographical errors, omissions and inconsistencies, and when combined with the use of confusing and conflicting nomenclature and definitions, their interpretation is often ambiguous. In this work, where technically accurate, redundant terminology between the various authors has been consolidated and formulas have been rearranged to improve legibility and typographical errors of the original publications have been corrected.

Each of the modern formulas actually contain multiple equations and most merge statistical regression techniques with a geometrical optics framework. Most modern formulas are essentially based on the idea of improving the estimate of ELP by first performing regression analysis on retrospective cases. Importantly, as many variables as possible are

controlled in the cases selected for analysis. It is recognized that consistency is essential regarding the surgeon, surgical technique, IOL manufacturer and design, biometry instrumentation, medicine regimes, etc. The modified ELP value is then applied to future cases by evaluating the geometrical optics formula in its three-lens form (see Eq. B.9), although the exact expression used is often re-arranged algebraically and often simplified by assumptions (such as $n_v = n_a$) and default values (such as $b = 12$ mm).

Holladay I and II formulas

Both the Holladay I and Holladay II formulas are commonly used today, even though specific details of the Holladay II formula remain unpublished [139]. Holladay and colleagues were the first to articulate the common sense idea of applying a formally defined data screening procedure. The everyday reality of clinical practice is that compulsory data screening compels a deeper consideration for the reliability of biometry data and reduces mis-measurement. Holladay's formal data screening compares biometry measurements of fellow eyes and flags significant levels of asymmetry, as well as improbable values, and improbable combinations of values (e.g. a combination of a short axial length with low corneal power). This procedure has been universally adopted by biometry instruments and computer programs performing IOL power calculations. Holladay's biometry screening criteria regarding axial length (l), mean corneal power (K_m), calculated emmetropic IOL power (P_e), and mean emmetropic IOL power (P_n) are given in Table 1.7 where the first row declares the monocular criteria and the second row declares the binocular criteria.

Biometry data screening criteria		
Axial length	Corneal Power	IOL power
$l < 22.0$ mm or $l > 25.0$ mm	$K_m < 40$ D or $K_m > 47$ D	$\lvert P_e - P_n \rvert > 3$ D
$\lvert l_{OD} - l_{OS} \rvert > 0.3$ mm	$\lvert K_{OD} - K_{OS} \rvert > 1$ D	$\lvert P_{OD} - P_{OS} \rvert > 1$ D

TABLE 1.7: Holladay I biometry data screening criteria to identify atypical results. Mean emmetropic IOL power (P_n) is specific for each IOL style, calculated with a personalised formula constant and values of $K_m = 43.81$ D and $l = 23.5$ mm, intended to represent a typical eye. The subscripts OD and OS represent the right eye and left eye, respectively.

The Holladay I formula defines the ELP value as the sum of the *anatomical anterior chamber depth*[5] (AACD) and the *surgeon factor* as given in Eq. 1.13 where all variables

[5]Distinct from the *anterior chamber depth constant* (d_o) previously defined in Section 1.5.2.

are in units of millimeters.

$$d = a + s \tag{1.13}$$

The AACD (a) is defined as the axial distance between the anterior corneal vertex and the anterior iris plane for the pseudophakic eye. The surgeon factor (s) is defined as the axial distance from the anterior iris plane to the optical plane of the IOL. These parameters are schematically displayed in Fig. 1.16 along with the *corneal height* (h) and *offset* (o) parameters of the SRK/T formula for comparison.

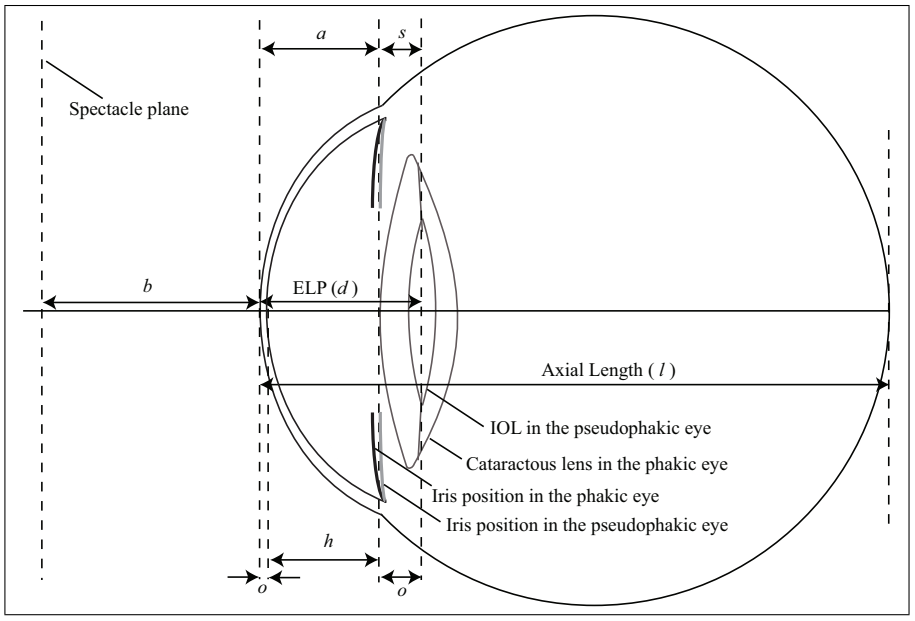

FIGURE 1.16: Schematic representation of the anatomical anterior chamber depth (a) and surgeon factor (s) as defined by the Holladay formula I, as well as corneal height (h) and *offset* (o) as defined by the SRK/T formula.

The AACD definition specifies a pseudophakic state, essentially demarked posteriorly by the plane of the iris root, but while the eye is phakic it is not a trivial dimension to measure owing to iris bow and interaction with the crystalline lens. Neither the AACD nor the surgeon factor are measured directly although they are real physical distances that could theoretically be measured in a pseudophakic eye. Instead the Holladay I formula proposes to estimate AACD (a) from the axial length (l) and mean anterior corneal radius of curvature (r_m) using Eq. 1.14 where all units are millimeters.

$$a = 0.56 + r_m - \sqrt{r_m^2 - \frac{l^2}{14.077504}} \tag{1.14}$$

with conditions that the value used for r_m is confined to be not less than 7 mm and l is confined to be not greater than 25.326 mm. Equation 1.14 bears a strong resemblance to the expression for corneal height (Eq. E.5) and is this topic is discussed in Appendix E.

Holladay I specifies an axial length measurement by ultrasonography (l) and a modified axial length (l_m) is used in Eqs. 1.16 and 1.17 according to

$$l_m = l + 0.2 \tag{1.15}$$

where all units are millimeters.

Holladay *et al.* [139] argue the distance represented by the surgeon factor is consistent from patient to patient, provided the IOL manufacturer and model, and all other surgical parameters are unchanged. In a method similar to the personalisation of the A constant from the SRK group of formulas, the Holladay I formula uses retrospective analysis of selected typical cases to personalise the surgeon factor. By personalising the surgeon factor, it accounts for any consistent bias, no matter where it comes from in the entire process. However, the surgeon factor is most adept at representing bias in the ELP - this is a subtle improvement over the A constant, because it attributes the retrospectively observed error directly to the ELP, which is where most uncertainty is though to arise from, rather than allocating it to a dioptric constant term. The ELP is a key parameter most likely to be influenced by surgical technique and IOL design, and within the geometrical optics formula it is the parameter most difficult to predict. As with all surgical techniques, it is reasonable to expect variations (due to factors such as tiredness, dexterity, age, experience, etc.) and therefore continual re-assessment of the personalisation constant (e.g. the surgeon factor) is necessary to ensure consistency in the refractive outcome.

Unlike the A constant of the SRK formulas, there is no assumption of a 1:1 ratio between IOL power and surgeon factor, instead the observed post-surgery refractive error is used to personalise the surgeon factor according to geometrical optics laws. But, as a series of cases are considered, the laws of statistical regression are also applied. The surgeon factor is personalised by solving a series of cases using the implanted IOL power (P_i) (diopters), resultant post-surgery refractive error (R_r) (diopters), modified pre-surgery axial length (l_m) (meters), pre-surgery mean corneal radius of curvature (r_m) (meters),

the distance between the spectacle plane and the corneal plane (b) (meters), refractive index of the aqueous (n_a) and effective refractive index of the cornea (n_e).

$$
\begin{aligned}
q_1 &= n_e - 1 - R_r(bn_e - b - r_m) \\
q_2 &= R_r(l_m bn_e - l_m b - r_m l_m + r_m bn_a) - l_m n_e + l_m - n_a r_m \\
q_3 &= R_r(bn_a r_m - bl_m n_e + bl_m + l_m r_m) \\
q_4 &= l_m n_a r_m - R_r l_m b r_m n_a - \frac{n_a(n_a r_m - l_m n_e + l_m - q_3)}{P_i} \\
s &= \frac{-q_2 - (q_2^2 - 4q_1 q_4)^{1/2}}{2q_1} - a
\end{aligned}
\tag{1.16}
$$

The five expressions in Eq. 1.16 are just a rearrangement the geometrical optics equation (Eq. B.9), given the relationship expressed in Eq. 1.13 and solving for surgeon factor (s). If Holladay's recommended default values $b = 0.012$ m and $n_e = 4/3$ are applied, then these expressions simplify to

$$
\begin{aligned}
q_1 &= 1/3 - R_r(0.004 - r_m) \\
q_2 &= R_r(0.004\, l_m - r_m l_m + r_m bn_a) - l_m/3 - n_a r_m \\
q_3 &= R_r(bn_a r_m - 0.004\, l_m + l_m r_m) \\
q_4 &= l_m n_a r_m - R_r l_m b r_m n_a - \frac{n_a(n_a r_m - l_m/3 - q_3)}{P_i} \\
s &= \frac{-q_2 - (q_2^2 - 4q_1 q_4)^{1/2}}{2q_1} - a
\end{aligned}
\tag{1.17}
$$

Note that when solving Eqs. 1.16 or 1.17 for surgeon factor, the targeted post-operative refractive error and the predicted IOL power for emmetropia are irrelevant, but rather the resultant post-operative refractive error and the implanted IOL power parameters are required for the calculation. To personalise the surgeon factor, Eq. 1.17 is evaluated for a large data set collected under consistent clinical conditions, and the mean value of s is found.

Prospectively, the personalised surgeon factor influences the prediction of IOL power for future cases through the geometrical optics framework according to

$$
P_a = \frac{n_a(n_a r_m - l_m/3 - R_t(bn_a r_m - bl_m/3 + l_m r_m))}{(l_m - d)[n_a r_m - d/3 - R_t(bn_a r_m - bd/3 + r_m d)]} \tag{1.18}
$$

which is simply a rearrangement of geometric optics equation (Eq. B.9). Equation 1.18 relies on the assumption that $n_v = n_a$ and its derivation from the geometrical optics equation is given in Appendix D. Note that in Eqs. 1.18 and 1.19 the mean radius of curvature is specified to be consistent with the original Holladay I publication and accordingly the R_r parameter in Eqs. 1.16, 1.17 and the R_t parameter in Eq. 1.18 should be interpreted as *best sphere* (defocus only) refractive errors. If considering power calculations for a toric IOL, the Holladay formula just like all others, may be applied to each principle meridian in turn.

For the case of an emmetropic goal, Eq. 1.18 simplifies to

$$P_e = \frac{n_a(n_a r_m - l_m/3)}{(l_m - d)(n_a r_m - d/3)} \tag{1.19}$$

Note that if we allowed $n_e = n_a = n_v = 4/3$, as Binkhorst does, Eq. 1.19 becomes equivalent to Binkhorst's arrangement of the geometrical optics equation (Eq. C.5).

The surgeon factor can be negative (implantation in the anterior chamber) or positive (implantation in the capsular bag) in value with typical values ranging from -0.5 to 1.7. For a particular surgeon and condition set, it is possible to convert between the surgeon factor (s), the A constant used by the SRK group of formulas, and the *ACD constant* (d_o) using normalised expressions (Eq. 1.20) where s and d_o are in units of millimeters and A is in units of diopters. It should be emphasized that the expressions given in Eq. 1.20 are a conditional equality and not an identical equality, in other words this relationship is a correspondence and not a definition.

$$\begin{aligned} s &= \quad 0.5663\,A - 65.6 \\ s &= \quad 0.9704\,d_o - 3.595 \end{aligned} \tag{1.20}$$

Holladay I uses a series of retrospective empirical results to find the mean value of surgeon factor for the data set, using Eq. 1.17 in conjunction with Eqs. 1.14 and 1.15. This mean value for surgeon factor is then applied in all future cases, implementing Eqs. 1.13, 1.14, 1.15, and 1.18. Although the Holladay II formula is unpublished, it has become widely used and accepted. It attempts to improve the estimate for the ELP by not only using axial length and corneal radius of curvature variables, but also parameters

of white-to-white corneal diameter, phakic ACD, cataractous lens thickness, pre-surgery refractive error, and age.

SRK/T formula

SRK/T is an acronym for each of the authors of the original SRK formula, but with the additional letter 'T' used to denote the consideration given to the *theoretical* geometrical optics solution in combination with regression techniques. The SRK/T is another modern formula that implements a geometrical optics solution after using preliminary regression analysis of an empirical data set to optimize parameters. Like the Holladay I formula, the SRK/T formula uses regression analysis to optimize the prediction of the ELP, however the SRK/T formula extends this concept further to also include the optimization of axial length (specifically retinal thickness) and equivalent corneal refractive index. The SRK/T formula was developed by optimizing these three parameters interactively undergoing numerous iterations, although unfortunately a detailed description of this process is not provided by the authors.

The SRK/T formula defines the ELP (d) as the sum of the corneal height (h) and the *offset* (o)

$$d = h + o \tag{1.21}$$

where all units are meters. The corneal height and *offset* are schematically displayed in Fig. 1.16. The corneal height parameter was introduced by Fyodorov and was also used by Olsen (and essentially used by Holladay too, but renamed AACD). It is the axial distance between the cornea and the pseudophakic iris plane, and like the AACD of the Holladay I formula, it is calculated from the axial length and corneal radius of curvature values, rather than being measured directly. However, the corneal height doesn't include the central corneal thickness, whereas by contrast the AACD parameter does.

The *offset* is the axial distance from the estimated pseudophakic iris plane to the IOL plane, and conceptually is similar to the surgeon factor used by the Holladay I formula, although note the SRK/T definition of *offset* includes the central corneal thickness. The term *offset* was coined by Olsen, hypothesizing that the distance it represents is consistent for a particular IOL manufacturer and type. Likewise the SRK/T formula also postulates that the implanted IOL lies at a constant distance from the calculated iris plane, that is, for a specific surgeon and specific IOL manufacturer and type, the

offset value is constant with negligible inter-patient variation. The *offset* term facilitates personalisation of the formula, it is primarily dependent upon the IOL design, the biometric, clinical and surgical conditions, but is largely patient-independent.

Corneal height is derived by considering the cornea as a section of a thin-walled sphere, then by employing Pythagorus' theorem and the general solution for a quadratic equation (see Appendix E) giving

$$h = r_m - \sqrt{r_m^2 - \left(\frac{w}{2}\right)^2} \tag{1.22}$$

and the solution given in Eq. 1.22 is the definition used by the SRK/T formula. Although the corneal width (w) is a real physical distance and readily measurable clinically as WTW, the SRK/T formula instead predicts a corneal width value as a function of axial length (l) and mean corneal power (K_m) according to

$$\begin{aligned}
&\text{if} && l \leq 24.2 \\
&\text{then} && w = 0.098\,K_m + 0.58412\,l - 5.41 \\
&\text{if} && l > 24.2 \\
&\text{then} && w = 0.098\,K_m + 0.58412\,(-0.0237\,l^2 + 1.715\,l - 3.446) - 5.41
\end{aligned} \tag{1.23}$$

where units for l and w are millimeters, and units for K_m are diopters.

To optimize the *offset* value for the SRK/T formula, the authors analysed their data set and found a mean value for corneal height (h) of 3.336 mm,

$$\overline{h} = 3.336 \tag{1.24}$$

and although not a unique solution, by solving Eq. 1.22 and 1.23 for $h = 3.336$ mm we can extrapolate that the SRK/T data set satisfies estimated mean population values for mean corneal power of ~ 44.18 D and axial length of ~ 23.45 mm.

The *offset* value of an IOL is calculated as the difference between the *ACD constant* of that particular IOL and the mean sample value of the corneal height (h) as shown in Eq. 1.25

$$\begin{aligned}
o &= d_o - \overline{h} \\
o &= d_o - 3.336
\end{aligned} \tag{1.25}$$

For example, if the SRK/T formula is applied considering a specific IOL with an *ACD constant* of 4.00 mm (historically defined), then the nominal *offset* value for this IOL would be 0.664 mm. Having determined the *offset* value, concerning future cases the ELP of an individual patient receiving this specific IOL implant could be determined by evaluating Eqs. 1.23, then 1.22, then finally 1.21. However, it is recommended to personalise the *offset* value, which is achieved via personalisation of the A constant as described below.

Like all modern IOL power calculation formulas, the SRK/T formula incorporates both the advantages and the disadvantages of maintained compatibility with legacy parameters. The nominal *offset* value is calculated using the ACD constant of a specific IOL in Eq. 1.25, or alternatively it can be calculated using the manufacturer-nominated A constant value of a specific IOL by evaluating Eq. 1.31 and then 1.25. This later method is preferred because it allows personalisation of the formula if instead of using the manufacturer-nominated A constant value, a surgeon-specific personalised value is used. To this purpose, the SRK/T authors suggest using the SKT II formula to first personalise the A constant for each individual surgeon, but with some subtle variations in the re-declared conditions,

$$\begin{aligned}
\text{if} \qquad l &\geq 24 \text{ mm} \quad \text{then} \quad \alpha = -0.5 \\
22 \text{ mm} \leq l &< 24 \text{ mm} \quad \text{then} \quad \alpha = 0 \\
21 \text{ mm} \leq l &< 22 \text{ mm} \quad \text{then} \quad \alpha = 1 \\
20 \text{ mm} \leq l &< 21 \text{ mm} \quad \text{then} \quad \alpha = 2 \\
l &< 20.0 \text{ mm} \quad \text{then} \quad \alpha = 3
\end{aligned} \tag{1.26}$$

and P_a is found with this boolean expression

$$\begin{aligned}
\text{if} \quad & A - 2.5\,l - 0.9\,K + \alpha > 16 \\
\text{then} \quad & P_a = A - 2.5\,l - 0.9\,K + \alpha - \beta\,R_t \quad \text{and} \quad \beta = 1.25 \\
\text{else} \quad & P_a = A - 2.5\,l - 0.9\,K + \alpha - \beta R_t \quad \text{and} \quad \beta = 1
\end{aligned} \tag{1.27}$$

Equation 1.27 is suitable for use when predicting the required IOL power of future cases, however, to optimise the A constant, the formula can be re-written to account for any inaccuracy in the prediction of post-surgery refractive error for a large empirical data set. Let us define the targeted post-operative refractive error that was desired (R_t), the resultant post-operative refractive error that was actually observed (R_r), the generic manufacturer nominated A constant (A_g), and the personalised A constant (A_p). For a large data set collected under consistent clinical conditions and with IOL power calculated according to Eq. 1.27 using A_g, these variables are related in the following way, where the over bar symbol represents the mean data set value.

$$A_p = A_g + \overline{\beta(R_r - R_t)} \tag{1.28}$$

after substituting for A_g and expanding becomes

$$A_p = \overline{P_i + 2.5l + 0.9K - \alpha + \beta R_t + \beta R_r - \beta R_t} \tag{1.29}$$

which simplifies to

$$A_p = \overline{P_i + 2.5l + 0.9K - \alpha + \beta R_r} \tag{1.30}$$

The A constant can be personalised for a particular surgeon and clinical conditions by evaluating Eq. 1.30 and in most circumstances a *best sphere* (defocus only) approach to refractive error, IOL power, and mean corneal power is used for practical reasons.

Returning to the SRK/T formula, remembering the description of personalisation of the A constant (which essentially implements the SRK II formula) was given above because the SRK/T makes use of the A constant. In this way the historical legacy linking the SRK/T with the SRK II and the SRK is evident, although this occurs in all modern equations usually through their definition of the ELP itself, or through the conversion between the various constants (ACD constant, *surgeon factor*, A constant, *offset*, and Hoffer's *phakic ACD*). Just as Eq. 1.20 states relationships of correspondence between the various constants as determined specifically from the Holladay data set, the authors of SRK/T state relationships of correspondence between the ACD constant, A constant, and *offset* as determined specifically from their data set (Eq. 1.31).

Once a surgeon has personalised their A constant according to Eq. 1.30, within the SRK/T formula the ACD constant then functions as an intermediary to convert the personalised A constant into a personalised *offset* value by evaluating Eq. 1.31 (d_o has units of millimeters and A has units of diopters) and then Eq. 1.25.

$$d_o = 0.62467\,A - 68.747 \tag{1.31}$$

Having determined the personalised *offset* value, in future cases the ELP of an individual patient receiving this specific IOL implant is determined by evaluating Eqs. 1.23, then 1.22, then finally 1.21. However, these multiple steps can be condensed into a single expression

$$d = r_m - \sqrt{r_m^2 - \left(\frac{w}{2}\right)^2} + 0.62467\,A - 72.083 \tag{1.32}$$

where w is defined as in Eq. 1.23 and the use of A_p is preferred rather than A_g. As in all equations relating to the SRK group of formulas, the units disobey scientific convention, d, r_m and w are in units of millimeters and A has units of diopters.

The SRK/T determination of ELP and personalisation of the *offset* seems slightly more convoluted compared to personalisation of the surgeon factor for the Holladay I, mainly because personalisation of the surgeon factor remains within the geometrical optics framework, so less equations are necessary and more repetitious terms can be used.

The SRK/T formula uses two different values for effective corneal refractive index. It uses $n_e = 1.3375$ when converting measurements of corneal power into anterior radius of curvature, a term used in both Eqs. 1.22 and 1.34. This is reasonable if the instrument used to measure corneal power also employed a value of $n_e = 1.3375$ in its initial conversion, however this can not be ensured and there is no compensatory mechanism within the formula in consideration of the alternative case. Simply by directing that raw biometry data be recorded as radius of curvature instead of corneal power could avoid this issue.

When evaluating the geometrical optics equation (Eq. 1.34), the SRK/T formula uses an effective corneal refractive index of $n_e = 1.333$. The authors report that after heuristically testing values for effective corneal refractive index ranging from 1.330 to 1.338, they elect to use $n_e = 1.333$ because it provided good accuracy and corresponding values of *ACD constant* that were harmonious with historical values. Unfortunately, the

description of this 'optimisation' process is vague and the decision to promote a value based on agreement with historical values for the *ACD constant* suggests the investigation was not a true optimisation, because this criteria serves only to reinforce whatever value of effective corneal refractive index was inherited when manufacturers originally derived the nominal value for *ACD constant* for the IOL.

The SRK/T was developed using axial length data from applanation ultrasound devices. Ultrasonic axial length values are typically underestimated by two processes previously mentioned. Firstly, the reflection of the ultrasonic wave is thought to be strongest at the vitreous/retinal interface, which is anterior to the photoreceptor layer. Secondly, the technique of the clinician can significantly effect the value for axial length depending on how gently they couple the ultrasound probe with the cornea. It is easy to accidentally compress the ACD during measurement and create an artificially reduced value for axial length. A third issue effects short eyes and long eyes differently, it concerns the fact that the measured *time of flight* is converted to axial length using an average acoustic impedance value, which itself is dependent on assumptions of the typical ratio of segmental distances (cornea : anterior chamber : crystalline lens : vitreous body). In a short eye, the crystalline lens usually contributes a greater proportion toward the overall axial length and vice-versa in a long eye the crystalline lens usually contributes a lower proportion towards the overall axial length. Because ultrasound devices use a typical segment ratio to determine the average acoustic impedance, this artificially inflates the reported axial length value of a long eye and artificially diminishes the reported axial length value of a short eye. The result of this third issue is that for long eyes, it partially counter-acts the two issues described previously, whereas in a short eye, it exacerbates the two previously described issues. The combined result of these three issues should therefore produce a model of modified axial length showing decreasing disparity from the original value with respect to axial length, over a range typical values, as demonstrated by the SRK/T model for axial length values up to $l_o = 32.3785$ mm (Eq. 1.33). The implications of this third phenomena are reversed when light based interference devices (PCI and LCR) are considered because light travels slower through the crystalline lens compared to the aqueous and vitreous. The opposite occurs for sound, which travels faster through the crystalline lens compared to the aqueous and vitreous. For cases where axial length data is measured with light based interferometry devices, the suitability of the model described in Eq. 1.33 becomes questionable, as this

situation is more accurately modeled by a modified axial length of increasing disparity from the original value with respect to axial length, over a range of typical values.

Acknowledgement of the second issue (compression of the ACD by excessive coupling force) is absent in the SRK/T publication, perhaps because their data set was collected using applanation ultrasound devices that are prone to this source of error while largely avoided by the use of immersion ultrasound technology. The first (stronger signal from the vitreoretinal interface) and third (use of an average acoustic impedance value) issues are described by the SRK/T publication, which proposes to modify axial length to account for these considerations using the following equation where l_m is the modified value, l_o is the original value, and all units are in millimeters. This modification is often referred to as a correction for *retinal thickness*.

$$l_m = 0.97971\, l_o + 0.65696 \tag{1.33}$$

Once the personalised *offset* value has been calculated, in future cases the ELP value for an individual patient is estimated and the SRK/T formula uses the following geometrical optics solution to predict the required IOL power

$$P_a = \frac{n_v[n_a r - 0.333 l_m - R_t(n_a r b + l_m r - 0.333 l_m b)]}{(l_m - d)(n_a r - 0.333 d) - R_t(n_a r b + d r - 0.333 d b)} \tag{1.34}$$

which is simply a partially evaluated version of the geometrical optics equation (Eq. D.12) as derived in Appendix D requiring the assumption that $n_v = n_a$. The SRK/T authors recommend default values of $b = 12$ mm and $n_a = n_v = 1.336$.

Hoffer Q formula

Hoffer initially proposed modifications to the geometrical optics equation to refine the ELP in a linear relationship with axial length (see Section 1.5.4). In 1993 he altered his opinion, arguing that the relationship between ELP and axial length is non-linear, and presented the Hoffer Q formula [143]. Like all modern formulas, the Hoffer Q formula proposes that ELP can be estimated in an improved approach by using regression techniques on a large data set collected under consistent clinical conditions (so called *personalisation*), combined with an individual's measured value for axial length and

corneal power. Unlike the Holladay I and SRK/T formulas, Hoffer doesn't use Fyodorov's corneal height parameter. Instead, Hoffer's method was to make conjecture and experiment with different mathematical formulas relating axial length and corneal power to ELP until he found an equation that resembled his speculation of the relationship between these parameters (Eq. 1.37). Hoffer literally acknowledges the derivation of his formula was based on 'speculation' and a 'trial and error' approach - a more honest description than the 'heuristic' terminology used by the SRK/T authors when reporting their own 'optimisation' processes concerning corneal refractive index and axial length.

Rather than relying on the manufacturer's nominal *ACD constant*, which is intended to represent the ELP value of a specific IOL in an average eye, Hoffer promotes that each surgeon should personalize their own ACD constant to represent the ELP value of a specific IOL in an average eye under the clinical conditions associated with that particular surgeon. This exercise is conceptually similar to personalizing the *surgeon factor* for the Holladay I formula, except that Hoffer doesn't combine this process with the use of a corneal height parameter.

Let,

$$R_{rm} = \frac{R_r}{1 - 0.012R_r} \tag{1.35}$$

so that the resultant refractive error at the corneal plane (R_{rm}) can be used as a shorthand notation instead of the resultant refractive error at the spectacle plane (R_r), assuming a default value of 12 mm between the spectacle plane and the corneal plane. The *personalised ACD constant* is found by solving the geometrical optics equation for ELP and then calculating its mean value for a large data set collected under consistent clinical conditions. Hoffer rearranges Colenbrander's form of the geometrical optics equation (Eq. C.2) to solve for d as described in Eqs. 1.35 and 1.36. The full derivation of Eq. 1.36 is given in Appendix F .

$$d = \frac{l + \dfrac{1.336}{K + R_{rm}} - \sqrt{\left(l - \dfrac{1.336}{K + R_{rm}}\right)^2 + \dfrac{4 \cdot 1.336[(1.336/(K + R_{rm})) - l]}{P_i}}}{2} - 5 \cdot 10^{-5} \tag{1.36}$$

Using Eq. 1.36 a value for d is retrospectively calculated for each patient in the data set, and the mean value of all patients is called the personalised ACD constant (d_p).

In the Hoffer Q formula, the ELP prediction is based on the *personalised ACD constant* along with other terms that act to increase ELP with axial length over a range of typical values, however outside this range (for very short or very long eyes) the variation on ELP is moderated. The formula also modifies ELP to increase with increasing corneal power and finally it also requires the addition of a constant. The individual's ELP is calculated according to

$$d_i = d_p + 0.3(l - 23.5) + \tan^2 K + 0.1\gamma(23.5 - l)^2(\tan 0.1(\epsilon - l)^2) - 0.99166 \qquad (1.37)$$

where axial length (l) is in units of millimeters, and

$$\begin{aligned} &\text{if} \quad l \leq 23 \quad \text{then} \quad \gamma = +1 \quad \text{and} \quad \epsilon = 28 \\ &\text{if} \quad l > 23 \quad \text{then} \quad \gamma = -1 \quad \text{and} \quad \epsilon = 23.5 \end{aligned} \qquad (1.38)$$

with restrictions that d_i is constrained not to be greater than 6.5 mm or less than 2.5 mm.

As one might expect of an expression genesised from speculation, Eq. 1.37 applies the tangent function improperly, which should act upon an argument with units of radians to produce a dimensionless value. Instead, to interpret this expression sensibly, we must suppose the intention of Hoffer was that the argument K be converted from diopters to degrees using a 1:1 ratio, and that the argument $0.1(\epsilon - l)^2$ be converted from meters squared to degrees using a 1:1 ratio. For the sake of a complete discussion, it should also be pointed out that the tangent function is discontinuous with a period of π radians. Luckily for Hoffer, it is extremely unlikely that an eye would ever possess biometry values that would reach the first discontinuity of the expression (occurring when $K = 90$ D and also when $l = 53.5$ mm).

For prospective cases, to predict the required IOL power Colenbrander's arrangement of geometrical optics formula is used with the individual's predicted ELP (d_i) substituted in place of the *ACD constant*, and with Hoffer's modification to satisfy cases targeting

an ametropic outcome as follows;

$$P = \frac{n_v}{l - d_i - 5 \cdot 10^{-5}} - \frac{n_a}{\frac{n_a}{K + R_{tm}} - d_i - 5 \cdot 10^{-5}} \tag{1.39}$$

with default values of $n_v = n_a = 1.336$ and with

$$R_{tm} = \frac{R_t}{1 - 0.012R_t} \tag{1.40}$$

so that the target refractive error at the corneal plane (R_{tm}) can be used as a shorthand notation instead of the target refractive error at the spectacle plane (R_t), assuming a default value of 12 mm between the spectacle plane and the corneal plane. Along with publishing the Hoffer Q formula, Hoffer compared alternative methods to predict the ELP, verifying an improved result when the technique combines a personalised (IOL-dependent and surgeon-dependent) parameter and individual (patient -dependent) biometry parameters. He also compared the refractive outcomes of the SRK/T, Holladay I and Hoffer Q formulas, which were generally found to perform similarly, for short, medium, long, and very long eyes. These modern formulas were superior to the SRK II and SRK formulas. In a final area of investigation, Hoffer found no benefit in personalising formula constants (e.g. *ACD* constant, *surgeon factor*, *offset*, *A* constant) according to subgroups of axial length.

Olsen formula

The Olsen formula differs from other modern formulas in four main areas. Firstly Olsen recommends using an effective corneal refractive index of $n_e = 1.3315$, as derived in Appendix A when converting measured corneal curvature into corneal power [136]. Secondly Olsen considers the main difficulties associated with axial length measurement by ultrasound, as previously described:

- A stronger signal from the vitreoretinal interface, which is anterior to the photoreceptor layer.
- The potential for ocular compression by accidental excessive coupling force with the applanation technique.

- The use of an effective acoustic impedance value based on the average eye.

From regression analysis, Olsen proposes that the crystalline lens thickness (t_l) can be estimated from the axial length (l_o) by

$$t_l = -0.082\, l_o + 6.44 \tag{1.41}$$

where all units are millimeters. As the *time of flight* value is simply the sum of the *time of flight* through the individual segments of the eye, and because the velocity of sound in vitreous humor is considered equal to that in aqueous humor, and assuming the contribution of the corneal thickness to the overall *time of flight* is relatively small, the modified axial length (l_m) can be calculated as

$$l_m = \left(\frac{l_o}{\upsilon_e} - \frac{t_l}{\upsilon_l} \right) \upsilon_a + t_l \tag{1.42}$$

when evaluated with the typically used values for effective velocity (υ_e = 1550 m/s), lenticular velocity (υ_l = 1640 m/s), and aqueous velocity (υ_a = 1532 m/s). Modern optical interferometry devices have neutralized the first and second issues bulleted above; however such devices are not universally available and often in cases of moderate to dense cataract, an insufficient optical SNR means that ultrasound technology continues to be necessary and widely used. Concerning the third bulleted issue, a conceptually similar adjustment as in Eq. 1.42 may be applied to data from optical interferometry devices. Technologies that measure each segment length individually (e.g. ultrasound devices and the Lenstar LCR device), have the potential to largely avoid this issue and avoid the use of *effective* acoustic impedance, or *effective* refractive index. However, the accuracy of such segmented *time of flight* data is still limited by the accuracy of the individual acoustic impedance values or refractive indices assumed for each segment. The use of an *effective* impedance value based on the average eye was likely borne out of convenience and has persisted because, even though computing the *time of flight* data in segmental form is not onerous, the signal at the posterior boundary of a moderately dense cataract is often ill-defined and this episodic potential error may outweigh any generalized improvement resulting from the segmental calculation of axial length.

The third and fourth topics emphasized by Olsen, the prediction of ELP and the IOL configuration are interrelated. Rather than use geometrical optics to back-calculate the ELP (which is the theoretical position of the second principle plane of the IOL), Olsen instead performs ultrasound measurements on the post-surgery eye to physically measure the actual IOL position and its axial depth (d_r). Olsen then attempts to estimate this distance using multiple regression analysis of parameters measured in the pre-surgery phakic state; the sample mean ACD by ultrasonography (t_{am}), corneal height by calculation (h) (see Appendix E), ACD (t_a), crystalline lens thickness (t_l) as derived from Eq. 1.41, and axial length by ultrasonography (l_m).

$$d_r = t_{am} + 0.12\,h + 0.33\,t_a + 0.3\,t_l + 0.1\,l_m - 5.18 \tag{1.43}$$

The crystalline lens thickness and modified axial length values are both derived by linear expressions (Eqs. 1.41 and 1.42) from the one original axial length measurement (l_o) and therefore these parameters are likely to be highly correlated. The decision to include both of them in the multiple regression analysis seems erroneous as they are closely related and not measured independently. The corneal height is calculated from the solution of a spherical segment as derived in Appendix E.

The final issue regards the necessity of knowing the IOL configuration and it naturally follows the decision to model the actual physical depth of the IOL (d_r) instead of the ELP. Olsen promotes modelling the IOL with the thick lens Gaussian approximation rather than the thin lens approximation, consistent with his approach of treating the cornea as a thick lens (see Appendix A). Olsen suggests calculating the location of the principle planes of each IOL power in a series, and reports that manufacturers are willing to disclose the apical radii of curvature, refractive index, and central thickness data required for such calculation. In our experience, manufacturers are unwilling to disclose such information, making implementation of a formula that models the actual IOL configuration as a dioptrically varying series along with its actual physical depth a labour intensive task to perform the IOL metrology, at least in the first instance.

The topics emphasized by Olsen illustrate a desire to reduce the use of approximations and fudge factors within IOL power calculations and refreshingly his work isn't cluttered with arbitrarily defined parameters or equations of correspondence to legacy parameters inherited from formulas of previous generations. His contentions represent progress

towards the ray-tracing methodology, which to be successful, requires greater amounts of unadulterated physically true biometry data and IOL metrology data.

Haigis

The Haigis formula, like the Holladay I, SRK/T, Hoffer Q, and Olsen formulas, is based on the geometrical optics equation. Like Olsen, Haigis promotes using a value of 1.3315 for the effective refractive index of the cornea based on the thick-lens geometrical optics approximation of Gullstrand's exact schematic model eye, as derived in Appendix A. Haigis supports the idea of extending thick-lens calculations to the IOL too, although pragmatically he reverts to a thin-lens approximation for the IOL power citing the unwillingness of manufacturers to disclose the necessary data (apical radii of curvature, central thickness, and refractive index) required to perform these calculations.

Where the Haigis formula differs from others is that personalisation process for a specific IOL (for a specific surgeon and clinical conditions) generates three values, which are used to predict the ELP. Haigis argues that when relating the ELP to the biometry parameters, the model itself should be dependent on the IOL specifications. On the other hand, Holladay I, SRK/T and Hoffer Q formulas personalise a constant that is added to the function for predicting ELP, which is the same regardless of the IOL characteristics. Haigis' personalisation creates two coefficients (α_1, α_2) and a constant (α_0), which means that the function is not simply translated by a constant, but the shape of the function itself is also altered by the value of the coefficients. Haigis uses two pre-surgery measured biometry parameters, ACD (t_a) and axial length (l) to predict ELP (d) according to

$$d = \alpha_1 \, t_a + \alpha_2 \, l_m + \alpha_0 \tag{1.44}$$

To personalize the values of α_1, α_2 and α_0, firstly the ELP value for each case in a large data set gathered under consistent clinical conditions is found using the geometrical optics formula

$$d = \frac{P_i l + P_i \eta - \sqrt{\left(-P_i l - P_i \eta\right)^2 - 4 P_i \left(n l - n \eta + P_i l \eta\right)}}{2 \, P_i} \tag{1.45}$$

which is equivalent to the solution of Eq. F.19 derived in Appendix F after dividing both the numerator and denominator on the right hand side of Eq. 1.45 by the term P_i and making use of the abbreviation defined by Eq. F.2.

Next, multiple regression analysis of Eq. 1.44 is used to personalise the values of $\alpha_1, \alpha_2,$ and α_0. Personalisation of these three parameters requires a larger data set than is necessary for personalisation of other formulas, and special attention must be given to ensuring a broad range of eyes are included in the sample (e.g. short eyes and long eyes). By way of acknowledging the reluctance and/or inability of surgeons to perform such a task, Haigis suggests default coefficient values of $\alpha_1 = 0.4$ and $\alpha_2 = 0.1$, and if used in this default setting the Haigis formula reverts to being conceptually similar to the other modern formulas personalized by a single constant. To solely personalise the value for α_0, the regression analysis of the data set is performed with $\alpha_1 = 0.4$ and $\alpha_2 = 0.1$, equivalently Haigis suggests adjusting the value of α_0 to satisfy Eq. 1.46 for a large data set (as is done for the Holladay I, SRK/T and Hoffer Q formulas) such that the mean difference between the best sphere (defocus only) resultant refractive error R_r and the best sphere (defocus only) targeted refractive error R_t equals zero. The resultant refractive error is measured when stable post-operatively, while the targeted refractive error is the value predicted from Eq. B.13 (although note that Haigis algebraically rearranges this expression).

$$\overline{R_r - R_t} = 0 \tag{1.46}$$

In satisfying Eq. 1.46, the optimisation process is susceptible to the possibility that consistently positive errors for one extreme of axial length are balanced by consistently negative errors at the other extreme of axial length, instead of the ideal random spread of positive and negative errors over the domain. All modern formulas are susceptible to this, but if all three parameters of the Haigis formula (α_1, α_2 and α_0) are personalised, the Haigis formula offers some defense against this issue, particularly regarding IOLs with significantly different shape factors than those used in the data sets of authors when originally deriving the Holladay I and SRK/T formulas.

To provide a legacy connection to the ACD constant (d_0), the default mode of the Haigis formula can be used to calculate a value for α_0 according to

$$\alpha_0 = d_0 - 0.4\overline{t_a} - 0.1\bar{l} \tag{1.47}$$

where the mean ACD ($\overline{t_a}$) is 3.37 mm and the mean axial length ($\bar{l}$) is 23.39 mm, both are mean ultrasound population values. Further correspondence to the historical SRK

A constant is given by

$$\alpha_0 = 0.62467A - 72.434 \tag{1.48}$$

Even in the default mode, the Haigis formula might perform slightly better than other formulas. Haigis attributes this partially due to the age of the other formulas, derived from data sets regarding now discontinued IOL designs, whereas the Haigis formula was derived using more recent IOL designs, and of particular importance is the shape factor of the IOL design. The Haigis and the Olsen formulas both use the pre-surgery phakic ACD as a parameter in the prediction of IOL position, thus requiring extra biometry compared to other formulas. However, this measurement is conveniently facilitated by modern PCI and LCR instruments.

Other formulas

In the last decade, many formulas have been suggested to address the inaccuracies of IOL power prediction in unusual eyes, especially those eyes that have previously undergone refractive surgery. By 2007, Savini [144] counted as many as 25 formulas and/or methods for this purpose. A good summary of these formulas is given by Hoffer [145]. The seemingly endless modifications and variations have the advantage that by examining the spread of predictions for IOL power, outliers may be avoided. However, the sheer number of formulas may act in part to muddy the waters and make it difficult for the industry to both identify and acknowledge through implementation, a single universal optimal method, essentially a gold standard. Such a formula/method must be robust and suitable for use on eyes with both normal and exotic dimensions. Achieving this goal requires developing new formula, so in the intervening period the number of formula options will continue to increase, unfortunately adding to the sense of confusion regarding suitability and use.

It is widely accepted that improved accuracy in IOL power prediction for unusual eyes will require highly accurate biometry data including post-surgery measurement of refractive state, excellent surgical technique, customized and highly accurate IOL manufacturing, and a more complex model of the pseudophakic eye than that provided by the geometrical optics approximation. Concerning this final topic, momentum towards industry acceptance of a raytracing solution is increasing as evidenced by the work of Preussner [61, 146] and Okulixe.

Concluding remarks regarding IOL power calculation

In an effort to collate the IOL device documentation (specifically the A constant, ACD constant and *surgeon factor*), Jack Holladay published the International IOL registry in 1999 [147]. Revisions were published annually in the January issue of the Journal of Cataract and Refractive Surgery until 2004, and the current registry is available electronically [148].

Pragmatically one can appreciate that at the time the formulas were published, given the limitations of surgery, IOL manufacturing tolerances, and the available technologies for biometry measurements, the formulas deserve fair merit. The modern formulas for IOL power calculations are sufficient for their purpose in a clinical setting with a typical eye of normal corneal power and normal axial length. In this regard they are workable and hold in agreement, even if the litter of fudge-factors and unscientific treatment of parameters is disappointing. Two key applaudable advances that the formulas have brought are the concepts of a formalised data screening process and personalisation of the formula using retrospective analysis of empirical data.

Unfortunately, the formulas do not agree in their prediction of IOL power when extreme values of axial length and corneal power are encountered. In a short eye with a flat cornea, the modern formulas disagree by up to 2 diopters. In a long eye with a steep cornea, they disagree by up to 1.3 diopters [3]. The fact that an ophthalmologist may compare numerous formulas when considering an atypical case highlights the area that needs improvement - the formulas are too simplistic to deal with extreme values of axial length, corneal power, and large amounts of HOAs.

The development, acceptance and implementation of a suitable raytracing-based IOL prescription methodology is interlinked with the capabilities of biometry instrumentation, IOL manufacturing, and surgical techniques. Mutual progress in all of these fields is necessary in order to realize improvement in the refractive outcome following cataract extraction and IOL implantation. An opportunity exists to contribute to the development of an improved method of IOL power calculation and remove many of the historically applied approximations and assumptions.

1.6 Zernike polynomials

Zernike polynomials (Z_i) are a set of polynomials defined over the unit circle and commonly used by the optics community [149]. In recent years, vision scientists have standardised the description of ocular aberrations by using Zernike polynomials [39, 40]. Zernike polynomials are used because of certain properties they have over the unit radius circle. Two features of Zernike polynomials should be highlighted. Firstly, they are a more general set of basis functions than the Siedel polynomials; the Zernike polynomials allow the description of any arbitrary surface shape, whereas the Siedel polynomials directly relate to consideration of a rotationally symmetric optical system. The second feature of Zernike polynomials is that each polynomial is defined in such a way as to posses minimum variance. This is often demonstrated by the *balancing* of higher-order polynomials that contain terms resembling their lower-order relatives. The spherical-like polynomial $(6\rho^4 - 6\rho^2 + 1)$, which contains a proportional amount of the defocus polynomial $(2\rho^2 - 1)$ is an often-cited example [150].

If a wavefront $W(\rho, \theta)$ is continuous and sufficiently smooth, it may be completely described by an infinite series of weighted polynomials [151].

$$W(\rho, \theta) = \int_i^\infty \alpha_i \, Z_i(\rho, \theta) \tag{1.49}$$

where α_i represents the weighting coefficients and the unit circle is constrained by

$$0 \leq \rho \leq 1 \quad \text{and} \quad 0 \leq \theta \leq 2\pi \tag{1.50}$$

Each Zernike polynomial is orthogonal,

$$\int_0^1 \int_0^{2\pi} Z_i(\rho, \theta) \, Z_j(\rho, \theta) \, \rho \, \mathrm{d}\rho \, \mathrm{d}\theta = \pi \delta_{ij} \tag{1.51}$$

meaning that each describes a function that can not be replicated by any linear combination of its fellow polynomials. As such, the fitting variance of any Zernike polynomial term to an arbitrary wavefront is independent of its fellow polynomials. Each Zernike polynomial can be normalised to have a mean of zero and unit variance

$$\frac{\int_0^1 \int_0^{2\pi} Z_i(\rho, \theta) \, Z_i(\rho, \theta) \rho \, \mathrm{d}\rho \, \mathrm{d}\theta}{\int_0^1 \int_0^{2\pi} \rho \, \mathrm{d}\rho \, \mathrm{d}\theta} = 1 \tag{1.52}$$

which simplifies total wavefront root mean square (RMS) calculations because the average value for the cross terms then becomes zero [151]. In practice, a finite number (k) of polynomials are used to fit the wavefront and Eq. 1.49 becomes

$$W(\rho,\theta) = \sum_{i}^{k} \alpha_i Z_i(\rho,\theta) \tag{1.53}$$

The Zernike polynomials contain an azimuth component (a trigonometric function) where m is the angular frequency of the azimuth component

$$\begin{cases} \cos(m\,\theta) & \text{if} \quad m > 0 \\ \sin(m\,\theta) & \text{if} \quad m < 0 \\ 1 & \text{if} \quad m = 0 \end{cases} \tag{1.54}$$

a normalisation component

$$N_n^m = \sqrt{\frac{2(n+1)}{1+\delta_{m0}}} \quad \begin{cases} \delta = 1 & \text{if} \quad m = 0 \\ \delta = 0 & \text{if} \quad m \neq 0 \end{cases} \tag{1.55}$$

where δ_{m0} is the kronecker delta function, and a radial component

$$R_n^m(\rho) = \sum_{s=0}^{\frac{n-|m|}{2}} \frac{(-1)^s (n-s)!}{s!(\frac{n+m}{2}-s)!(\frac{n-m}{2}-s)!} \cdot \rho^{n-2s} \tag{1.56}$$

where n is the radial order. Equations 1.54, 1.55, and 1.56 combine to give the Zernike circle polynomial

$$Z_n^m(\rho,\theta) = N_n^m\, R_n^m(\rho) \cdot \begin{cases} \cos(m\,\theta) & \text{if} \quad m > 0 \\ \sin(m\,\theta) & \text{if} \quad m < 0 \\ 1 & \text{if} \quad m = 0 \end{cases} \tag{1.57}$$

Values for the radial order n are derived from

$$n = \text{ceiling}\left[\frac{-3+\sqrt{9+8(q-1)}}{2}\right] \tag{1.58}$$

where the ceiling function is equivalent to rounding towards positive infinity and q is the polynomial number ($q = 0, 1, 2, 3, 4, 5, \ldots$ and so on). Values for the angular frequency

m are derived from

$$m = q - \frac{n(n+1)}{2} - 1 \tag{1.59}$$

Contour maps of the first four orders of Zernike polynomials are shown in Fig. 1.17. The plane contour map at the apex of Fig. 1.17 represents piston (0th order), which is not a relevant (or measurable) consideration in ocular wavefront sensing. The 2nd and 3rd rows are contour maps of the 1st and 2nd order (low order) Zernike polynomials. The 4th and 5th rows are contour maps representing the 3rd and 4th order Zernike polynomials, and along with all other orders these are referred to as higher order.

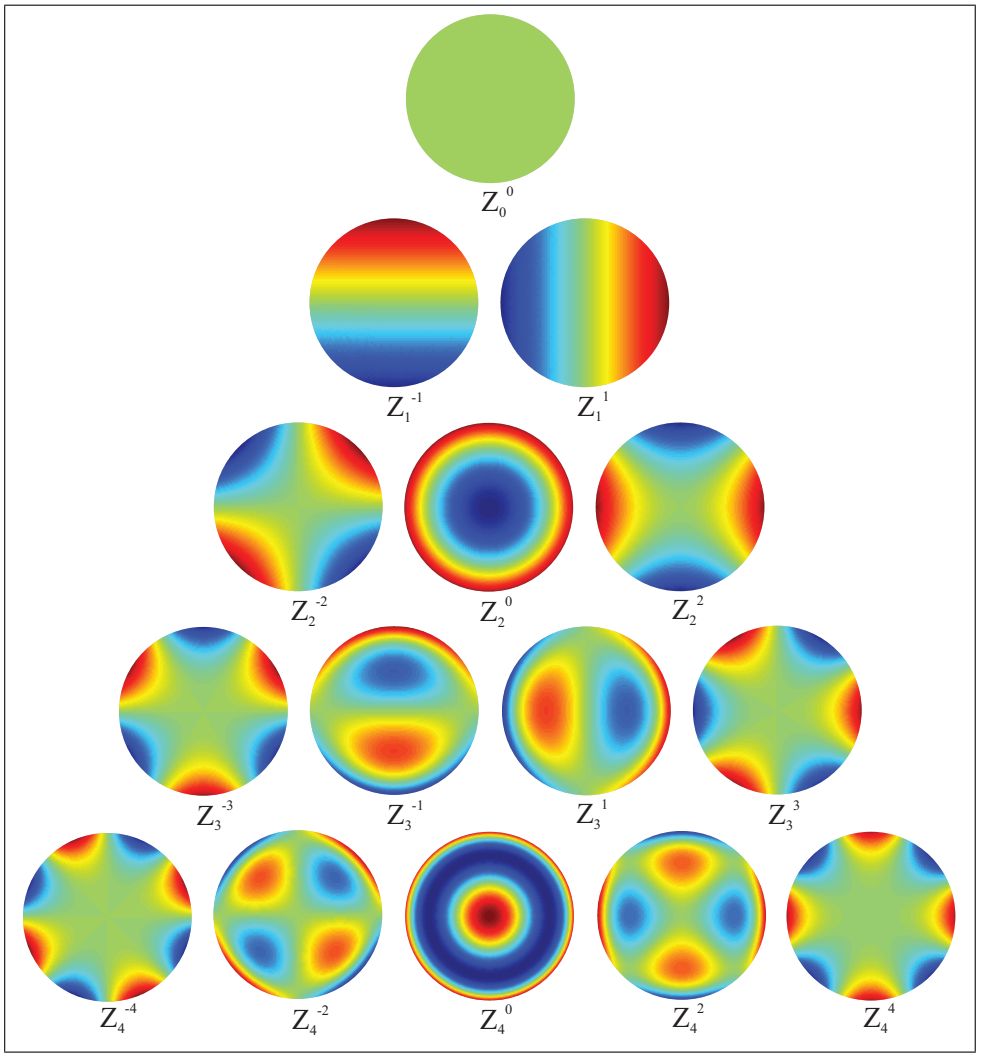

FIGURE 1.17: Zernike polynomials colour contour map.

The first five Zernike polynomial orders in standard ophthalmic double indexing format using a right-handed polar coordinate system are listed in Table 1.8. Some of the polynomials are given a descriptive name based on loose similarities shared with traditional

Seidel aberrations. Zernike polynomials are commonly used by the broader optical community as they are well-suited for describing traditionally encountered optical surfaces. However, Zernike polynomials lack any biological or anatomical basis to be applied to the eye, it is simply mathematically convenient to use them [152]. Interpretation of Zernike coefficients requires particular care, for example, orthogonality of Zernike modes in the pupil plane should not be misinterpreted as independence of optical consequences at the image plane (the retina).

The complex interaction between multiple Zernike modes is not instinctively interpreted, especially when presented in a numerical format. The phase error (either positive or negative) for a certain Zernike coefficient may be neutralised across a large proportion of the pupil by the combined phase of several other modes, or alternatively, the combination of Zernike modes may exacerbate the phase error. The interactions between multiple modes are necessarily complex, required to describe potentially very complicated surfaces. A clinician may prefer to interpret ocular wavefront data using a single-value description: the total wavefront RMS. This condensed summary of data looses the intricate details contained in the description of the wavefront, but many clinicians use this single-value descriptor because it is simpler to manage. As in all variance relationships, the total wavefront variance is equal to the sum of the individual variance values for each mode. The total wavefront RMS is equal to the square root of the sum of the squares of the individual Zernike coefficients.

$$\text{total wavefront RMS} = \sqrt{{\alpha_1}^2 + {\alpha_2}^2 + {\alpha_3}^2 + {\alpha_4}^2 \cdots + {\alpha_k}^2} \tag{1.60}$$

The calculation required to evaluate the total wavefront RMS is straightforward because the definition of the Zernike modes has been contrived though the normalisation of the Zernike coefficients. Similarly, the Zernike coefficients of modes describing the lower order aberrations may be used to generate a lower order wavefront RMS value and the Zernike coefficients of modes describing the higher order aberrations may be used to generate a higher order wavefront RMS value.

Standards [39, 40] recommend that ocular aberrations be described by Zernike polynomials fitted to the wavefront conjugate to the entrance pupil, with the origin and axis defined along the line of sight, reported from the observers point of view while facing the subject. Positive values represent a phase-advanced wavefront region and negative

values represent a phase-retarded wavefront region. The coordinate system is illustrated in Fig. 1.18. The standards do not define a specific pupil diameter over which aberrations should be reported, nor is there a specific wavelength recommended for reporting aberrations. Although higher order aberrations may not differ significantly across the visible spectrum [153, 154], defocus is certainly dependent on wavelength. Given the typical peak of the relative luminous efficiency spectral function for the standard photopic observer, 555 nm would seem a reasonable selection for a standard wavelength and this would require a conversion from the red and infrared wavelengths used by most wavefront sensors.

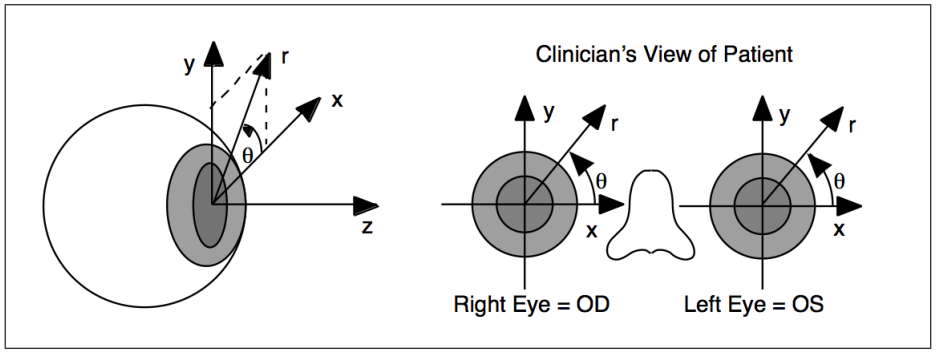

FIGURE 1.18: Conventional right-handed coordinate system for the eye in Cartesian and polar forms (*image credit* L N Thibos *et al.*).

Zernike Polynomials (ophthalmic standard format)				
Z_n^m	Order (n)	Freq. (m)	Polynomial	Description
Z_0^0	0	0	1	Piston
Z_1^{-1}	1	-1	$2\rho\sin\theta$	Tilt about x axis
Z_1^1	1	1	$2\rho\cos\theta$	Tilt about y axis
Z_2^{-2}	2	-2	$\sqrt{6}\rho^2\sin 2\theta$	Astigmatism 45/135
Z_2^0	2	0	$\sqrt{3}(2\rho^2-1)$	Defocus
Z_2^2	2	2	$\sqrt{6}\rho^2\cos 2\theta$	Astigmatism 0/90
Z_3^{-3}	3	-3	$\sqrt{8}\rho^3\sin 3\theta$	Trefoil (base on x axis)
Z_3^{-1}	3	-1	$\sqrt{8}(3\rho^3-2\rho)\sin\theta$	Coma along x axis
Z_3^1	3	1	$\sqrt{8}(3\rho^3-2\rho)\cos\theta$	Coma along y axis
Z_3^3	3	3	$\sqrt{8}\rho^3\cos 3\theta$	Trefoil (base on y axis)
Z_4^{-4}	4	-4	$\sqrt{10}\rho^4\sin 4\theta$	
Z_4^{-2}	4	-2	$\sqrt{10}(4\rho^4-3\rho^2)\sin 2\theta$	
Z_4^0	4	0	$\sqrt{5}(6\rho^4-6\rho^2+1)$	Spherical aberration
Z_4^2	4	2	$\sqrt{10}(4\rho^4-3\rho^2)\cos 2\theta$	
Z_4^4	4	4	$\sqrt{10}\rho^4\cos 4\theta$	
Z_5^{-5}	5	-5	$\sqrt{12}\rho^5\sin 5\theta$	
Z_5^{-3}	5	-3	$\sqrt{12}(5\rho^5-4\rho^3)\sin 3\theta$	
Z_5^{-1}	5	-1	$\sqrt{12}(10\rho^5-12\rho^3+3\rho)\sin\theta$	
Z_5^1	5	1	$\sqrt{12}(10\rho^5-12\rho^3+3\rho)\cos\theta$	
Z_5^3	5	3	$\sqrt{12}(5\rho^5-4\rho^3)\cos 3\theta$	
Z_5^5	5	5	$\sqrt{12}\rho^5\cos 5\theta$	

TABLE 1.8: List of Zernike polynomials in right-handed polar coordinate system.

1.7 Biometry considerations

1.7.1 Instrumentation

This section provides a brief overview of the possible methods for performing biometry, as required for personalised eye modelling of cataract surgery.

Keratometry

Keratometers describe anterior corneal curvature in two perpendicular principle meridians, typically over the central 3 mm diameter zone. There are two main types of manual keratometers, classified by their method used to alter the image size, either by variable doubling or by variable size of the mire (the test object). Manual keratometers are still widely used today, although increasingly, automated keratometers are incorporated with autorefraction instruments and also with optical interferometers capable of measuring axial length. The IOLMaster (Zeiss) and Lenstar (Haag-Streit) are examples of the later, these instruments allow all biometry measurements necessary for current industry-standard IOL power formulas to be performed on a single platform.

Placido disc corneal topography

The Placido disc is a concentric arrangement of black and white rings, this mire (test object) is reflected by the tear film and its virtual image is analysed to determine radial magnification. This longstanding method of characterizing anterior corneal topography was ideally suited to automation and quantification made possible by the development of CCD and personal computer technologies in the 1980s. Like Keratometers, Placido disc corneal topographers analyse the magnification of the 1st Purkinji image, treating the corneal surface, specifically the tear film, as a specular reflector. Measurement is limited to the anterior cornea and analysis is limited to radial meridians as tangential curvature is not measured directly. Similar to automated Keratometers, Placido disc instruments do not alter or adjust the image size of the mire.

Modern Placido disc instruments (Fig. 1.19(a)) capture an *en face* two-dimensional image that is analyzed to produce a three-dimensional elevation data map of the anterior

corneal surface. They provide vastly improved spatial sampling than traditional keratometers, typically measuring anterior corneal curvature at hundreds of data points, in numerous meridians, over a much larger 10 to 12 mm diameter zone.

Scanning slit and Scheimpflug photography

Placido disc and Scheimpflug technologies are based on distinctly different principles. Scheimpflug technologies treat the cornea and other ocular tissue as scattering layers - the eye itself is the object that is imaged, there is no reflected mire image. This fundamental difference explains why Placido disc technology is more sensitive to detecting tear film changes and irregularities compared to Scheimpflug based technology. For anterior segment imaging, the scanning slit method may be viewed as a precursor to rotating Scheimpflug instruments, both methods allow tissue layers deeper than the anterior cornea (e.g. the posterior cornea, iris and crystalline lens) to be imaged and measured.

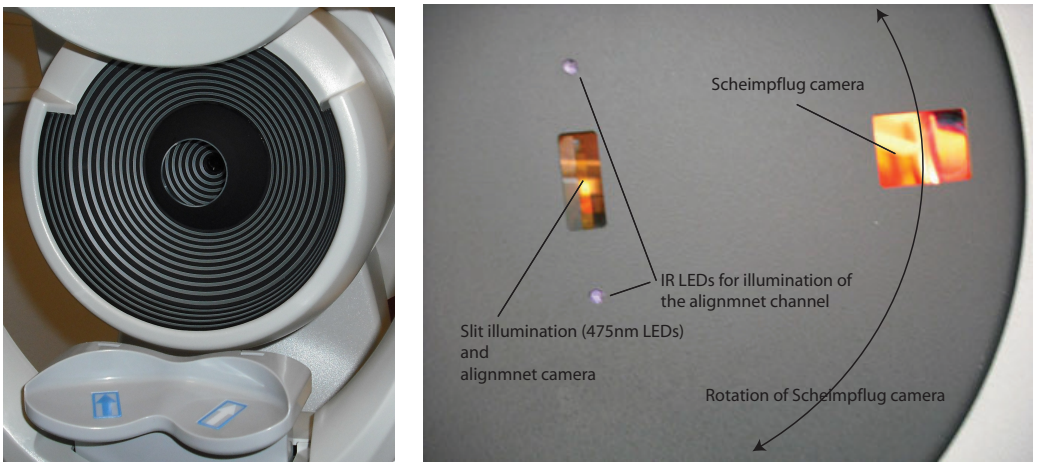

(a) Subject's view of the Atlas (b) Subject's view of the Pentacam

FIGURE 1.19: Commercial instruments capable of providing corneal topography data.

The scanning slit method illuminates the eye with a narrow slit of light, which is then imaged by a camera at an oblique angle, capturing a meridional two-dimensional sectional image along the z axis. By transversely sweeping the illumination and/or observation arms across the eye, typically in an arc-shaped path, a series of sectional images are captured and then registered together to create a three-dimensional volumetric data set [155].

Scheimpflug photography is based on imaging an object at an oblique angle, rather than capturing *en face* image. Under normal photography arrangements this results in an image with a depth of field problem (Fig. 1.20(a)) as some points of the object are closer to the camera while other points of the object are further away from the camera. By tilting the objective lens or detector plane relative to each other, such that their planes intersect at the same location along the illumination axis, it is possible to make the entire field appear correctly focussed (Fig. 1.20(b)), even though the object extends along the z axis [156].

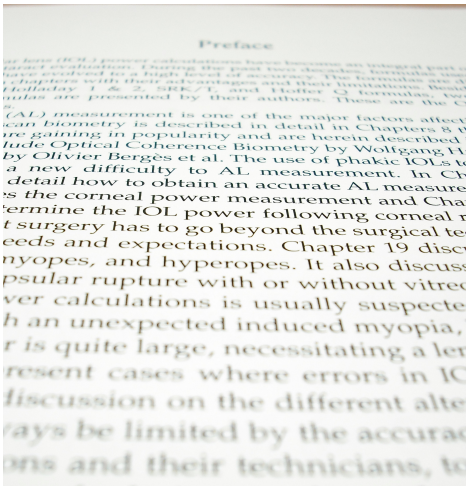

(a) Depth of field issue

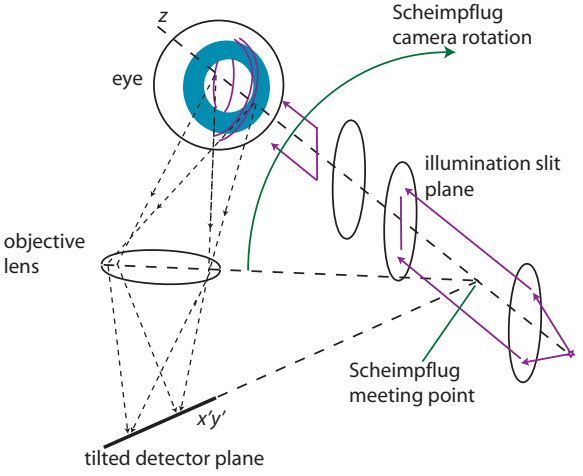

(b) Scheimpflug arrangement

FIGURE 1.20: Scheimpflug photography motivation and arrangement.

Rotating Scheimpflug photography supersedes earlier scanning slit techniques primarily because its optical layout maintains a more consistent relationship between the eye and the illumination and observation arms during measurement. It also benefits from potentially more accurate image registration as a common landmark (the apex) is imaged in each meridional section. Both the scanning/rotation movement of components makes instrument alignment and calibration a challenging task for the manufacturer. Registering a series of meridional two-dimensional images into a three-dimensional volumetric data set relies on accurate and consistent alignment of the moving instrument components, it also relies on accurate alignment of a cooperative patient, able to maintain a stable eye position during the measurement time, usually lasting a few seconds.

Figure 1.19(b) shows the subject's view of a commercial rotating Scheimpflug instrument. The central slit illumination is generated by a strip of 475 nm LEDs. Two infrared LEDs are positioned directly above and below the slit window providing illumination for

the alignment system. The camera is positioned at an angle of approximately 45 degrees with a working distance of approximately 75 mm. The thin slit illumination penetrates through a depth along the z axis of approximately 5 mm - from the anterior cornea to the anterior crystalline lens. In some subjects, particularly those with large pupils, the central region of the posterior crystalline lens is detectable although it is not the norm.

Scheimpflug images suffer from geometric and optical distortion that must be corrected to obtain real surface depth information from the apparent surface depth [157]. Geometric distortion occurs due to the oblique angle between the observation and illumination arms, correcting for this effect is relatively straight forward provided the specifications of the optical layout are known. Optical distortion occurs because the scattered light that has passed through intervening refractive surfaces before reaching the Scheimpflug camera. All surfaces must be corrected for geometrical distortion, whereas all surfaces apart from the first (anterior cornea) must be corrected for optical distortion.

In correcting optical distortion of a Scheimpflug image, the illumination wavelength and associated refractive index of preceding media must be known. Due to cumulative effects, any error in the refractive index values, will impart greater noise on the estimation of depth for each successive surface, with the most posterior surface being the least accurately known (assuming adequate contrast at all interfaces).

In a related topic, the intensity of scattered signal in the Scheimpflug technique is significantly dependent on wavelength, as shown by Raleigh's model. The cornea preferentially scatters shorter wavelengths, whereas longer wavelengths penetrate deeper generating increased signal from the crystalline lens.

$$I = I_0 \frac{N\, 8\pi^4 \alpha^2}{\lambda^4 R^2} (1 + \cos^2 \theta) \tag{1.61}$$

where N is the number of scatterers, α is the polarizability, R is the distance from the scatterer, I_0 is initial irradiance, I is the observed irradiance, and assuming that the scattering particles have a small size parameter.

Optical coherence tomography

Like rotating Scheimpflug photography, optical coherence tomography (OCT) is capable

of anterior segment imaging and providing biometry data, but with the benefit of improved resolution associated with optical interferometry. Both rotating Scheimpflug and OCT instruments provide substantially more anatomical information in addition to anterior corneal surface topography. These additional measurements include; pseudo-images of the tissue to allow visual inspection of the edge detection software, pachymetry, posterior corneal surface topography, anterior chamber depth, anterior chamber angle, limbal position, crystalline lens position, crystalline lens densitometry, pupil center and edge positions, and pupil size [158]. Many of these additional measurements are potentially useful in personalised eye modelling for cataract surgery.

OCT employs optical interferometry to capture one-dimensional axial (z axis) information. By transversely scanning the beam in two dimensions in the xy plane, a series of one-dimensional axial measurements are recorded and then registered together to form a three-dimensional volumetric data set. The first generation of instruments relied on physical movement of the reference arm mirror and are said to operate in the *time* domain, whereas later instruments make use of a spectrometer, thereby avoiding movement of the reference mirror and improving temporal resolution, these instruments are said to operate in the *frequency* domain [158, 159, 160].

The axial resolution of an OCT instrument is primarily determined by the bandwidth of source, as such, SLDs are a popular choice of source due to their moderate coherence properties. The transverse spatial resolution of an OCT instrument is primarily determined by the scanning method, field size, and the mirror scanning speed. The typical scanning methodology employed means that temporal resolution has a differential in the xy plane, with maximum and minimum directions of sensitivity occurring perpendicular to each other. Temporal resolution may be considered generally consistent along the z axis. Like Scheimpflug-based instruments, OCT instruments must address issues of image registration, and both geometrical and optical distortion. In balancing considerations of dynamic range and resolution, OCT instruments are dedicated solely to measurement of either the anterior segment or the posterior segment. Current commercial technologies are not capable of simultaneous OCT imaging over the entire depth of the eye (typically ~ 23 mm) [161].

Partial coherence interferometry and low coherence reflectometry

Ocular axial length can be measured using optical interferometry, essentially this is a

one-dimensional counterpart of an OCT measurement. The two most widely accepted commercial instruments, the IOLMaster (Zeiss) and Lenstar (Haag-Streit), are based on similar technologies known respectively as partial coherence interferometry (PCI) and low coherence reflectometry (LCR). The IOLMaster employs a laser source with a wavelength of 780 nm while the Lenstar uses an SLD source with a peak wavelength of 820 nm. Both instruments measure along the visual axis. The Lenstar measures axial length data segmentally and it is often capable of detecting the IOL axial position in a pseudophakic eye. These two key advantages of the Lenstar over the IOLMaster provide very useful information for personalised eye modelling of cataract surgery.

Ultrasonography

Ocular ultrasonography requires topical anesthesia and is separated into two methods; *applanation*, possibly requiring a drop of coupling fluid on the probe tip, and *immersion*, necessarily requiring an eyebath. The advantages and disadvantages of these two methods, as well as other general considerations of ocular ultrasonography have previously been discussed. Historically ultrasonography was the most reliable and clinically suitable technology for measuring ocular axial length, until the first commercial PCI instrument became available in the late 1990s [140], providing improved accuracy and resolution. Today, ultrasound instruments are smaller, less expensive and more portable than PCI and LCR instruments. Ultrasonography remains an essential reserve technique for occasions when the maturity (e.g. dense nuclear sclerotic cataracts) or location (e.g. posterior subcapsular cataracts) of cataract prevents adequate SNR for optical measurement. In these cases, ultrasonography is often more reliable. Personalised eye modelling for cataract surgery requires flexibility to utilize ultrasound axial length data in these circumstances. To provide the most reliable data possible in such cases, where the option exits, protocol should insist that the immersion method be used in preference to the applanation method.

Ultrasonography principles can be extended from the one-dimensional application of axial length measurement (traditionally referred to as *amplitude mode* operation) to the three-dimensional application of anterior segment imaging and biometry [162]. Like with Scheimpflug and OCT techniques, a wide range of anterior segment parameters are measurable, albeit at an inferior resolution than optical techniques. The most prominent commercial instrument in this field describes the technology as *high-frequency ultrasound*

biomicroscopy and its ability to image behind optically opaque structures such as the iris could be helpful for measuring the peripheral crystalline lens profile, a task not possible with optical techniques. A more complete knowledge of the crystalline lens topography in a cataract patient may provide an advantage in predicting the post-surgery IOL position.

Optical interferometry

Optical interferometry forms the underlying principle of operation for the PCI, LCR, and OCT techniques described above. It is also used in this work to perform metrology on IOLs as described in Chapter 2. Optical interferometry is a fundamental metrology technique, especially suited to measuring high spatial frequencies and low amplitude aberrations. It's high sensitivity means that it is prone to vibrational noise and is becomes especially difficult when testing large beam diameters [163]. Additionally, the interpretation of interferograms requires sophisticated software. For these reasons and because many other suitable alternative technologies exist (see paragraph below), optical interferometry is not commonly used as an ocular refraction technique.

Ocular wavefront sensing

Accurate measurement of the post-surgery refractive outcome is critical part of the biometry required for personalised eye modelling of cataract surgery and IOL power prediction. Various techniques for measuring the ocular refractive state have already been introduced in Section 1.3.3, including retinoscopy, subjective refraction, autorefraction, and wavefront sensing. Of these techniques, only wavefront sensing is capable of measuring the higher order monochromatic aberrations of the eye, and so this method was selected for assessing the post-surgery refractive outcome of cataract patients, as part of the experiment reported in Chapter 2.

Due to the importance of wavefront sensing in evaluating personalised eye modelling of cataract surgery, this section extends the description of the numerous ocular wavefront sensing techniques, although not all technologies listed below have been developed into clinical instruments. Ocular aberrations can be measured using interferometry or ray-tracing techniques. WFSs are typically categorised as either subjective or objective and may also be categorised depending on whether the wavefront is subdivided into samples

before the first pass into the eye or after the second pass out of the eye [164]. Ocular aberrometry techniques include;

- Tscherning's aberroscope [165] with modifications by Howland [166], then further modifications [167, 168], and more recent clinical embodiment [169, 170].
- The works of Ivanoff [171] and Smirnov [172] that were developed as the spatially resolved refractometer [173].
- Laser ray tracing [174, 175, 176].
- Curvature wavefront sensing [177].
- Pyramid wavefront sensing [178, 179].
- Skiascopy [180, 181].
- Hartmann-Shack aberrometry [182] that was first used in ocular applications by Liang *et al.* [42].
- A novel method described by Neil *et al.* [183].

Most commercial ocular WFSs are based on Hartmann-Shack (HS) technology. Comparison studies between HS wavefront sensing and other aberrometry techniques have been made by many researchers including Salmon *et al.* [55] and Liang and Williams [36]. Various limitations remain in the current designs of commercial WFSs. Their measurements are only concerned with monochromatic light and they involve an unnatural viewing field for the subject. They do not provide information regarding chromatic aberration in the eye, scatter in the eye, subjective preference and acceptance, or the binocular vision status of the subject. Measurements are sensitive to accommodation-induced fluctuations of aberrations. Many of these limitations affect autorefraction technology and may be addressed in similar ways that autorefractors have attempted to address them (e.g. by using a fogging technique) [37]. Just as autorefractors can give inaccurate results in the presence of media opacities, corneal irregularities, or poor tear film quality, so too can WFSs. Ginis and colleagues [184] outline areas where practitioners should be careful in interpreting results from WFSs such as re-scaling procedures, pupil edge determination, pupil centre determination, and noise levels.

1.7.2 The biometry parameter space

This section discusses what biometry data is required for personalised eye modelling of cataract surgery. A suggested *ideal* list of biometry parameters relevant to simulating the personalised eye model is given below.

- anterior and posterior corneal topography
- corneal pachymetry
- some pre-surgery parameter/s capable of predicting the stabilized IOL position
- segmented axial length of the eye
- retinal topography (especially the macula region)
- pupil size and location (consider various lighting conditions)
- refractive index of the cornea, aqueous, crystalline/cataractous lens (GRIN estimate) and vitreous
- refractive state (especially post-surgery)

In the above list it is desirable that the biometry data have excellent accuracy, repeatability, and the measurement technique be minimally invasive. For personalised eye modelling of cataract surgery to be realistically considered for widespread adoption, the biometry parameter space must be clinically convenient and economically justified. When selecting the biometry parameter space various scientific, financial and practical issues must be considered. Personalised eye modelling will undoubtedly have to suffice with only a selection of the above *ideal* list of biometry parameters. Practical issues demand that the time required to collect the biometry data must not be onerous for either clinician or patient. The potential benefit of improved accuracy associated with individually measuring each parameter uniquely for each patient must be considered against the convenience of using a nominal population typical value. The inter-subject variation of some of the above listed parameters may be very low, therefore the use of a nominal population typical value may prove to exert insignificant influence over the personalised eye model. For some of the above listed parameters, measurement in a clinical environment may be so challenging that only very noisy data would result,

and therefore accuracy may be gained with the use of a laboratory-measured nominal population typical value rather than a clinically measured individual value.

In general, the more parameters that can be measured on a single instrument platform, the better. This holds practical advantages of reduced patient movement, a smaller collective instrument footprint, and potentially reduced data registration demands. The seemingly trivial task of relocating an elderly patient with reduced mobility from one instrument to another can be very time consuming and exceed the constants of a busy clinical environment. This task is especially frustrating as duplication of patient data entry is required for multiple instruments. For eye modelling, it is advantageous to avoid numerous instruments during biometry data collection as all data must be exported, converted into compatible formats, and then registered with respect to each other. Each instrument uses different; data formats, measurement wavelengths, coordinate systems, reference axes, assumptions, and reference surfaces. Restraining the biometry protocol to collect as much biometry data from as few instruments as possible will help manage these challenges. The development of a single-platform instrument capable of performing ray-tracing analysis of personalised eye models for customized IOL power calculation, in addition to performing all required biometry measurements should be a future industry goal.

Listed below are the relevant state-of-the-art commercial technologies capable of providing biometry data, with examples of relevant manufacturer and model names. Each technology possesses its own advantages and disadvantages.

- Rotating Scheimpflug technology (Oculus Pentacam)
- Scanning slit technology (Bausch and Lomb Orbscan II)
- Anterior segment optical coherence tomography (Zeiss Visante)
- High-frequency ultrasound biomicroscopy (Paradigm UBM)
- Corneal topography (Zeiss Atlas)
- Placido disk and dual rotating Scheimpflug combined (Ziemer Galilei)
- Placido disk and optical coherence tomography combined (Zeiss Omni)
- Partial coherence interferometry (Zeiss IOLMaster)

- Low coherence reflectometry (Haag-Streit Lenstar)
- Immersion ultrasonography
- Abbe refractometry
- Wavefront sensing / aberrometry (Wavefront Sciences COAS)
- Corneal topography and aberrometry combined (Abbott iDesign)

A significant effort was dedicated to evaluating the commercial instruments listed above in regard to suitability for use in providing biometry data for personalised eye modelling. Not all of the instruments listed above were available and so investigation concentrated primarily on the following instruments, Pentacam (Oculus), Atlas (Zeiss), IOLMaster (Zeiss), Lenstar (Haag-Streit), iDesign (Abbott), Zywave (Bausch &Lomb), and ARK-510A (Nidek). One key issue considered was the export capabilities and data format used by the instrument, and how this data might be converted into an acceptable structure for the ray-tracing software. The biometry data structure had several key considerations. Firstly, the format must be compatible (or able to be made compatible) with the Zemax and MatLab software programs use for simulating the eye model. Secondly, wherever possible the data should be exportable without requiring screen capture and manual transcribing of data. Manual transcribing steps should be avoided if at all possible to reduce the risk of human error. Finally, the data format must be suitable for the particular application of personalised eye modeling for cataract surgery, including the modelling of unusual eyes. For example, data must be reported at appropriate resolution if exported as discrete data points, or if exported after the instrument's internal software has fitted analytical functions to summarize the data, the appropriateness of this procedure must be considered (e.g. zonal fitting, Fourier series fitting, and Zernike polynomial fitting will not perform equally when attempting to describe the surface topography of a post-refractive surgery cornea).

Calibration techniques were investigated for the available instruments. It is necessary to calibrate and verify the results of a commercial instrument in order to gain confidence in understanding how the measurements are analysed and reported by the software of each instrument. Due to the propriety nature of commercial instruments and the complex way in which data can be reported, it is important to ensure that the biometry data output is not mis-interpreted. Verification against a known surface (or more appropriately, an

artificial eye with multiple known surfaces and distances) provides reassurance in this issue. These studies were intended to reveal how data is processed by the instrument and to understanding the exported data structure (including the coordinate system, image registration, data resolution, etc). Even after these investigations, often the finding was one of relative confidence in understanding, rather than absolute knowledge of the internal workings of an instrument.

Selected technologies

The following decisions regarding the biometry parameter space selected for personalised eye modelling of cataract surgery are summarize here. For axial length measurement, the Lenstar was selected in preference to the IOLMaster for two capabilities thought crucial - segmented axial length measurement and the ability to measure IOL axial position in the pseudophakic eye. The decision regarding corneal topography measurement was composite with the issue of aberrometry. The iDesign offered the advantage of synchronised corneal topography and aberrometry on a single platform, the Pentacam offered the advantage of posterior corneal topography and ACD measurement, while the Atlas offered the advantage of a long-standing and widely used instrument. The iDesign and Pentacam both were preferenced above the Atlas, however while planning the clinical measurements of the experiment described in Chapter 2, the iDesign and Pentacam instruments both became unavailable for use. By default, the Atlas was then selected for use and consequently aberrometry measurement was required from a separate instrument. The Zywave wavefront sensor was selected for this and due to the age of the instrument resulting in temperamental operation, it was decided that measurement with the ARK-510A should also be included in the protocol, particularly for its autorefraction capability. To generate ray-tracing eye models, the Zemax software program was selected in preference to the Lensforge software program owing to its superior range of features, particularly regarding optimisation. The Matlab software program was also required by the protocol to take exported data from the instrument and create a file suitable for input into the Zemax program.

1.7.3 Ancillary biometry investigations

Following the instrument selection decisions and changed availability of the Pentacam and iDesign instruments, several preliminary studies performed thence became irrelevant

to the main body of work. These preliminary studies are reported here with brief summary descriptions below.

The iDesign and Pentacam were studied regarding topics of; test re-test repeatability of measurements on real and artificial eyes on short and medium time scales, temporal and spatial sampling features, deduced CCD specifications, data sampling rate, spatial distribution (density) of sampling and relationship to the SNR distribution of the image, areas of repeated sampling, meridians of greatest and least sampling, the potential risk of aliasing, the potential risk of fitting errors of analytical functions in the presence of localised topography features, techniques for correcting for intra-measurement patient movement, techniques for registration of a measurement series.

In work performed in collaboration with Hannah Nowitzki, the IOLMaster was studied regarding the following topics; test re-test repeatability of real eyes and artificial eyes on short and medium time scales, off-axis measurements, decentered measurements.

In work performed in collaboration with Conor Sheil, surface metrology was performed on a series of IOLs under dry conditions. Measurements were performed with the FISBA interferometer and data was analyzed with Zemax ray-tracing software.

Various materials and coatings of test surfaces and artificial eyes were investigated for potential use in a comparative calibration study of Placido disc and rotating scheimpflug instruments. It was considered advantageous to devise a method of comparison that employed the same artificial eye for calibration of both Placido disc and rotating scheimpflug instruments. Of the numerous coatings that were investigated to enhance either scattering or reflective qualities of the test surfaces, the best compromise was achieved with a 2-surface rubber artificial eye - used without modification during measurement by the rotating Scheimpflug method and irrigated with isopropanol just prior to measurement by the Placido disc method. A test re-test repeatability study comparing the Atlas and Pentacam instruments was performed with this technique and also on a sample of real eyes.

Scheimpflug spectral modification

The Pentacam Scheimpflug camera uses a blue (peak $\lambda = 475$ nm) slit beam illumination, selected for its preferential scattering properties, which vary inversely with wavelength raised to the 4th power (see Eq. 1.61). Other biometry instruments perform

measurements using a variety of wavelengths, for example the IOLMaster (λ = 780 nm), Lenstar (λ = 820 nm), Zywave (λ = 785 nm) while IOL resolution and optical testing is performed with green light (λ = 546 nm). Data registration between these various measurements is made potentially more difficult due to the chromatic dispersion error arising from assumptions of refractive index values for the ocular media across the various wavelengths employed by different biometry instruments. This error primarily effects registration of the ACD parameter and the crystalline lens surfaces. Personalised eye modelling of cataract surgery may potentially benefit if this source of noise could be minimized by obtaining all required biometry data with similar wavelengths, allowing consistency in the assumed refractive index values for ocular media.

As most biometry instruments operate in the red and infrared bandwidth of the spectrum, Scheimpflug photography of the anterior segment was studied to investigate if sufficient tissue scatter was possible using a red (λ_{peak} = 660 nm) illumination source. A Scheimpflug camera with a variable colour slit beam was constructed, capable of performing photography with white, red, or blue illumination. Spectroscopy was performed to characterize the spectral content of the various colour settings of the illumination source. Scheimpflug photography using white, blue and red slit beam illumination was performed on both eyes of 2 male subjects aged 31 years and 33 years.

The results demonstrated that Scheimpflug photography using both red or white illumination produced sufficient scatter from both the corneal tissue and the crystalline lens to provide acceptable Scheimpflug images (as judged acceptable by overall image contrast and edge contrast) with modest irradiance (addressing concerns of patient comfort and safety) and with exposure times of less than 1 second (addressing concerns of patient comfort and sufficient temporal resolution to avoid patient movement noise). The penetration depth was comparably equivalent between all three trials (blue, white, and red illumination). Edge resolution also was comparable between all 3 trials. The SNR obtained was abundant in all 3 trials, suggestive that faster temporal sampling and lower irradiance settings than those used may still produce Scheimpflug images of satisfactory quality.

Scheimpflug enhanced scattering modification

The origin of the 1st Purkinje image analyzed by Placido disc technology is well-defined, it is the air-tear interface and is the principle refractive surface of the eye. By contrast,

it is ambiguous, which corneal ultrastructure layer is responsible for the peak scatter signal detected by Scheimpflug photography, and how closely this layer matches the topography of the tear film. Furthermore, it unknown if the scattering properties of the corneal tissue were sufficiently discrete and if the resolution of the instrument is sufficiently high enough, to enable the scatter signal to be related to a discrete interface on the ultrastructure scale. It was hypothesised that instilling sodium fluorescein (NaFl) in the tear film would increase the SNR (effectively the contrast) of the anterior layer of a Scheimpflug image, which may improve the accuracy of edge detection analysis for that boundary and verify the origin of the signal is the tear film. It was difficult to predict the effect this may have on repeatability of the anterior corneal topography measurement. If edge detection accuracy improved, it was anticipated that repeatability of the anterior corneal topography measurement may also improve. Alternatively, repeatability may decrease if an increased sensitivity to the dynamics of the tear film resulted, replacing a sensitivity that might normally be tuned to the more static underlying tissue topography.

A study was performed on the right eye of five subjects (2 females aged 24 and 26 years, 3 males aged 27, 28 and 31 years) with 50 meridional Scheimpflug images captured for each measurement. Ten measurements were performed on each subject with a 30 second rest period and instrument realignment between each measurement. Sodium fluorescein (NaFl) was then instilled into the tear film and the same eyes were measured a further ten times. With NaFl instilled in the tear film, a dramatic increase in contrast of the first scattering layer was observed compared to a natural tear film measurement, verifying that this signal arises from the tear film, at least under this modified technique. The higher contrast gave better edge detection accuracy but two difficulties were associated with this modification.

It is known that the tear film thickness comprises less than 2% of the total corneal thickness, however Scheimpflug images captured under this modified technique show a brighter signal covering almost 50% of the apparent thickness. A proposed explanation of this effect is that the increased scatter was excessive, with particles illuminated by the slit not only scattering light back to the camera, but also scattering light transversely (xy) through the tear film. This effectively broadens the meridional section and each sample becomes a parallelepiped 3-dimensional volumetric image, instead of the thin 2-dimensional section desired. In addition to this issue, in a small percentage of images (approximately 10%), the instillation of NaFl confused the edge detection software

specifically for the posterior cornea location. It is advised that any use of this modified technique should guard against these two issues, perhaps avoidable with a smaller dosage of NaFl while still preserving the beneficial effects of improved edge detection accuracy.

Chapter 2

Experiment

2.1 Experiment rationale and hypothesis

Refractive surgery encompasses numerous different surgeries including; radial keratectomy, photorefractive keratectomy (PRK), laser in situ keratomileusis (LASIK), laser sub-epithelial keratomileusis (LASEK), and conductive keratoplasty. Conventional refractive surgery, although successful at correcting defocus and astigmatism of the eye, typically induces large amounts of higher order aberrations (HOAs). Customised refractive surgery attempts to correct both low order and higher order aberrations. Customized surgeries, such as *wavefront guided* and *wavefront optimized* LASIK have been modestly successful in limiting induction/exacerbation of HOAs, especially spherical aberration, but thus far rather less successful in correcting the already relatively small pre-existing HOAs in a typical virgin eye [185].

The popularity of each specific refractive surgery has varied over time and across regions. Some surgery types have largely been abandoned, however, on the whole, the popularity of refractive surgery has increased significantly since the 1980s. Due to this trend over the last three decades, a growing percentage of patients possess unusual biometry parameters. Typically formerly myopic, these patients often have a long axial length, a flattened central corneal surface and a large amount of corneal HOAs. As this demographic ages, patients from this subgroup are now requiring cataract surgery in increasing numbers. Current industry standard IOL power calculation formulas and IOL designs often give unsatisfactory results in these cases.

This work is motivated by the opportunity to improve upon standard IOL power calculations and standard IOL designs, acutely highlighted by the growing subgroup of cataract patients who have previously undergone refractive surgery. IOL power calculations based on geometrical optics approximations and the use of IOL designs only customizable in regard to a sphero-cylindrical prescription, fail to meet the challenges arising from the refractive surgery era.

The aim of this work is to address limitations of the industry-standard IOL power calculations as previously discussed (see Section 1.5). The foremost potential solution is to develop personalised eye modelling of cataract surgery on ray tracing software that can model any desired analytical surface and is not limited to sphero-cylindrical approximations or the paraxial domain. If such modelling indicates that attempted correction of HOAs is likely to be beneficial, then manufacturers might progress toward creating customized IOL designs. If modeling suggests that attempted correction of HOA would likely provide insignificant benefit, or indeed perhaps worsen the refractive outcome, the ray-tracing framework may yet still demonstrate improved IOL power prediction compared to industry standard formulas when considering a nominal non-customized IOL design of sphero-cylindrical prescription. Personalised eye modelling of cataract surgery with ray tracing software is currently being developed by several groups [61, 64, 146, 186, 187].

The hypothesis is that the refractive outcome of cataract surgery may be improved by establishing a comprehensive scientific methodology regarding personalised eye modelling and customized IOL design. Personalised eye modelling of cataract surgery and customised IOL designs will likely demonstrate greatest potential benefit in patients with unusual eyes (such as patients with irregular corneal shape or extreme axial length) and least potential benefit in eyes with typical biometry values. However, the solution must be suitable for all cataract patients, regardless of subgroup. The first step in investigating the hypothesis is to study a group of typical eyes, without any history of previous ocular surgery, undergoing phacoemulsification cataract extraction and receiving a nominal non-customized defocus-correcting IOL implanted in the capsular bag. The performance of personalised eye modelling should be compared with the industry standard formulas for this group of typical eyes. If personalised eye modelling is proven statistically equal to or better than industry standard formulas for this group of typical eyes, progress can then be made toward future studies of unusual eyes (such as those

with a history of previous refractive surgery) undergoing cataract surgery receiving a nominal non-customized defocus-correcting or possibly astigmatism-correcting IOL design. If these primary and secondary investigations demonstrate superior accuracy and reliability of personalised eye modelling compared to industry standard formulas, and if modelling suggests that a subject is likely to benefit from customization of an IOL design prescribed to correct HOAs, then manufacturers might be persuaded to produce the required technologies to facilitate tertiary investigations regarding IOL designs customized for HOA correction.

2.2 Intraocular lens metrology

Introduction

Modelling the pseudophakic eye with ray tracing software requires knowledge of the IOL shape, central thickness and refractive index. These parameters are only partially disclosed by manufacturers and so a preliminary step in the experiment was to measure the IOL surface shape and central thickness *in vitro* of a dioptric series of IOLs (Akreos Adapt AO, Bausch and Lomb). This type of IOL material is hydrophilic, necessitating the IOL remain hydrated by use of a saline bath during measurements. Various measurement protocols were investigated with the assistance of Conor Sheil; the final selected methodology offered a compromise between achieving a full gamut of specifications and practicality. The results generally show excellent reliability and repeatability. An interferometer (FISBA OPTIK μPhase HR) was used to measure the apical radius of curvature, central thickness, and residual surface deviation (from a spherical reference) in single reflection at normal incidence. Measurements were repeated 10 times for each IOL orientation (anterior and posterior) and the apparent distance values were analysed with Zemax ray tracing software to determine real distance values.

Apparatus and error level

The basic manufacturer-stated specifications of the IOL are given in Table 2.1 [188].

The FISBA interferometer employs a Twyman-Green configuration and a five step phase-shifting technique for phase unwrapping. It uses a Helium-Neon laser ($\lambda = 632.8$ nm) and is mounted on a micrometer stage with a smallest ruled division of 0.01 mm. The

Summary of IOL (Akreos Adapt AO, Bausch and Lomb) specifications	
material	26% hydrophilic acrylic co-polymer with UV absorber
manufacturing method	lathe cut
specific gravity	1.21g/cm^3
refractive index	1.458 (when in the eye at 35°C)
	1.459 (when wet at 20°C)
optic	biconvex aspheric
optic size	6 mm diameter
haptics	single-piece, 4 loops, 0 degree angulation
overall diameter	11.0 mm from 0.0 D to 15.0 D
	10.7 mm from 15.5 D to 22.0 D
	10.5 mm from 22.5 D to 30.0 D
diopter range	0.0 D to 9.0 D in 1.0 D increments
	10.0 D to 30.0 D in 0.5 D increments
feature	zero spherical aberration
nominal constant values	*ACD* 4.96 mm
	surgeon factor 1.22 mm
	A constant 118.0 (ultrasound)
	A constant 118.5 (IOLMaster SRK II) 118.3 (IOLMaster SRK/T)

TABLE 2.1: Summary of IOL (Akreos Adapt AO, Bausch and Lomb) specifications.

error associated with determination of each measurement position is therefore ±0.005 mm, while the error associated with parameters dependent on the difference between two positions (including central thickness values and apical radius of curvature values) is ±0.007 mm to a first order approximation regarding apparent distance. Raytracing analysis shows that the micrometer position error associated with these parameters in terms of the real distance value is slightly increased - for the central thickness parameter the error is ±14 μm, and for the radius of curvature parameter the error is ±13 μm. These values were calculated for a 21.5 D power IOL and may be considered representative for other powers.

The accuracy of a surface figure measurement (deviation from spherical or plane reference) is primarily determined by the interferogram, the specifications of the CCD used to capture the interferogram and the software used in its analysis. To a first order approximation, the resolution of an interferogram is on the order of $\lambda/2$ peak to valley. The optical layout of the interferometer is an important consideration, in reflection mode the SNR of surface figure effectively doubles in comparison to operation in transmission mode.

The interferometer allows attachment of various objective lenses, each possessing a different numerical aperture (NA). For consistency, only one objective lens was used throughout all measurements. The arrangement consisted of a beam expander producing a collimated 10 mm diameter beam, which then passed through the objective (focal length 43 mm and objective diameter 15 mm), forming a converging beam with approximately a 19 degree full angle in air, equivalent to a NA of 0.16.

Protocol

The interferometer was calibrated at the start of each session by arranging a concave spherical calibration surface, of 10 mm radius of curvature and 0.04 reflection coefficient, in the confocal position (Fig. 2.1). The confocal position is deemed achieved when the interferogram displays the null fringe condition. The peripheral interferogram data was masked by an electronic virtual circular aperture to avoid unwanted edge diffraction effects and artifacts. The calibration surface has a figure error of $\lambda/20$ RMS and measurement of the calibration interferogram allows the interferometer to account for any internal aberrations owing to its own optical system in subsequent measurement of test surfaces.

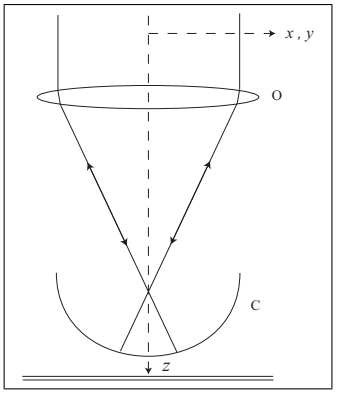

FIGURE 2.1: Calibration position of the interferometer using a spherical reference surface (C). The objective lens is shown (O) while the remaining optical layout of the interferometer is omitted.

The experimental procedure was based on the measurement of successive cat eye and autocollimation positions by translating the interferometer along the z axis with a micrometer stage. At each measurement the micrometer position was recorded and the difference between successive positions allows determination of apparent distances. By analyzing the apparent distances in Zemax ray-tracing software and assuming a value for the refractive index of saline from the literature, the real distances were then found.

Figure 2.2 shows the four measurement positions used in the experiment. In the cat eye position the beam is focused on the surface apex. In the autocollimation position the beam is incident normal at the surface. The autocollimation position assumes a spherical surface. Although the IOL surface is known to be aspheric, it is reasonable to approximate it as spherical for the purpose of this measurement. In this approximation the IOL surface asphericity acts to elongate the range of positions (z axis) over which the operator observes the null fringe condition and in our experience this was a minor error. Once the autocollimation position is found, an interferogram is recorded and analysed, allowing the surface deviation from spherical to be found.

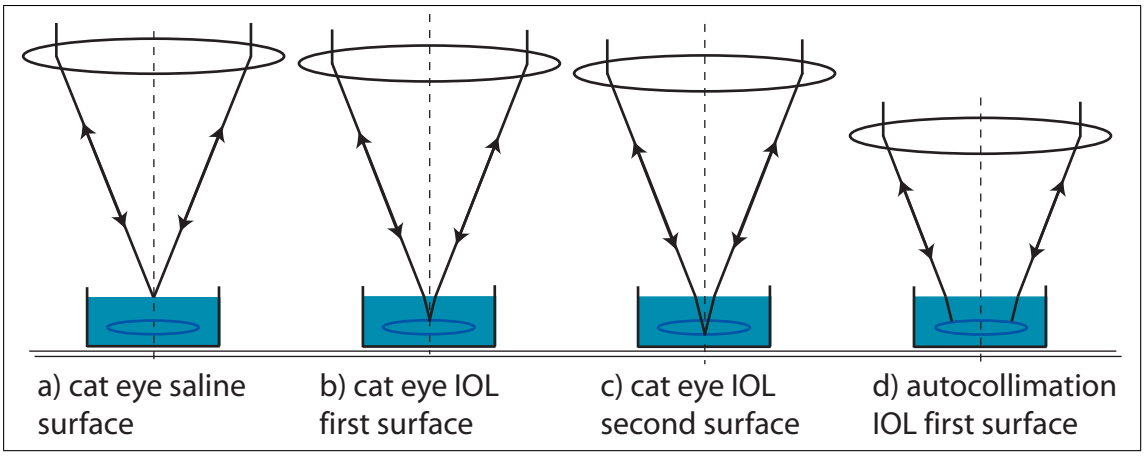

FIGURE 2.2: The four measurement positions used during IOL metrology. The IOL is immersed in a saline bath. The objective lens is shown while the remaining optical layout of the interferometer is omitted.

Preliminary testing of the method was performed on 3 convex glass hemispheres with radii of curvature values (6.15 mm, 8.00 mm and 9.65 mm) of a similar range to those expected to be encountered during IOL metrology. The experiment results gave radius of curvature values identical to the known values (nominally quoted to 0.01 mm) for all 3 test surfaces of differing curvature. Having gained confidence regarding measurements of a dry rigid glass surface, progress was made to develop a protocol regarding the vastly more challenging measurement of a wet, soft, IOL surface.

Once the vial containing the IOL was opened, the IOL was rapidly transferred to the saline bath, being exposed to the atmosphere for only a few seconds. The IOL was grasped with non-toothed tweezers by the haptics only. Care was taken to ensure a minimal amount of handling while positioning the IOL in the center of the bath. A pipette was used to adjust the volume of saline in the bath to achieve the optimal level ($\sim$ 2 mm central coverage above the top surface of the IOL) and to ensure the IOL

was fully submerged. The bath was mounted to a stage with 5 degrees of freedom to allow alignment of the IOL with the interferometer - xy translation, and tilt about the x, y, and z axes. The interferometer was mounted to a micrometer stage that allowed translation along the z axis - this 6th degree of freedom was varied to achieve the four measurement positions (Fig. 2.2) and verify correct alignment in all. Once the IOL was aligned with the interferometer, the bath stage controls were locked and only translation along the z axis was varied during a measurement.

The operator viewed the interferogram and recorded the null fringe state corresponding to the three cat eye and one autocollimated positions. Interpretation of the interferogram is a learnt skill and experience gained through preliminary investigations proved a significant advantage during this experiment. Each trial measured all 4 positions independently. The stage translation direction was reversed after each trial to help avoid bias. At each measurement point, the null fringe condition was found using a localized staircasing method. Ten trials were performed in each orientation, therefore for each IOL the sample size was 10 for the radius of curvature parameters and 20 for the central thickness parameter. The experiment was exposed to numerous sources of noise (discussed in the following section), however the vast majority of these issues were anticipated and many details within the protocol were designed to control and minimize these sources of error.

Limitations in data collection

First, metrology of dehydrated IOLs was investigated because it offered advantages of simpler apparatus and the ability to measure the vertex focal length of most IOL powers. This measurement, corresponding to the confocal position, is not possible in the hydrated state because the lower refractive index differential creates a longer focal length, exceeding the dynamic range of the micrometer stage for the selected objective lens, for all but a very limited range of high IOL powers. Testing confirmed that metrology of either *dry* or *drying* IOLs was unreliable and inappropriate. For an IOL exposed to the atmosphere, the interferograms rapidly fluctuated preventing assessment, only stabilizing after periods greater than 40 minutes - coinciding with complete dehydration of the IOL. Although the parameters of a hydrated, partially hydrated, and dehydrated IOL are highly correlated, determining the relationship between the two states in any case requires hydrated measurements and therefore it is logical to simply perform only

hydrated measurements that are directly representative of the *in situ* case, and forego measurement of the vertex focal length (a compromise imparted by the limited range of the micrometer stage).

Mounting the IOL inside a cuvette was avoided due to complications of introducing multiple interceding surfaces between the interferometer and the IOL. Various alternative methods for mounting the IOL in the saline bath were investigated, including a method to support the IOL from underneath with an annulus 6 mm in diameter. Such a method avoids any physical contact with the central optic. However, preliminary testing indicated that mounting the IOL by directly resting the second surface against the floor of the bath and making physical contact was an acceptable compromise. With suitable care the risk of damaging the optic was low and indeed no damage was observed throughout the experiment. In hindsight, perhaps a supportive gel bedding would have provided an improved mounting arrangement.

Another concern regarded potential sagging of the haptics without direct contact support due to the action of gravity. It was possible that haptic sagging might cause strain on the IOL optic, altering shape of the surface undergoing measurement. In this event the curvature of the IOL surface under measurement would steepen, artificially reducing the radius of curvature value. This effect was also not observed in results and is thought negligible owing to the combined influences of the 0 degree haptic angulation, the low mass of the haptics, and the near-neutral specific gravity of the haptic material.

The optimal depth of the saline bath was determined through preliminary testing. To preserve as much dynamic range of the micrometer stage as possible and to provide maximum possible beam coverage in the autocollimated position, the saline depth should be minimal. A saline depth of 1 to 3 mm was found to limit vignetting and total internal reflection effects, providing the best possible interferogram contrast. These considerations are balanced against the need to ensure that the IOL remains fully submerged throughout an entire trial, which sometimes exceeded 50 minutes, and with consideration given to the rate of evaporation. The saline bath also needs to be sufficiently deep to avoid the air/saline surface from being influenced by the underlying IOL. The optimal saline level was achieved with an initial depth of approximately 2 mm centrally above the top surface of the IOL at the start of a trial.

Surface ripples and splashing of the saline bath was avoided by minimizing vibration - a gentle and smooth operation of the micrometer stage is paramount. The air/saline surface is treated as plane although it is recognized that in reality the surface is not perfectly flat. Around the perimeter of the bath, meniscus effects induce a concave shape in the saline surface. These effects were combated by using a large bath diameter, which decreased the ratio of the scale between the local meniscus height and the global bath diameter, meaning that the meniscus distortion occurs far from the central area. The metal bath walls were lined with a wettable plasticine layer and by pre-wetting this lining just prior to the start of each measurement series, the surface tension around the bath perimeter was reduced, lowering the meniscus height. Even in the ideal scenario of a plane saline surface, this interface still complicates data analysis because in a convergent beam path, even a plane interface induces spherical aberration. Additionally, refraction at the plane air/saline interface slows the beam and hence reduces beam coverage of the IOL surface in the autocollimated position.

Rather than counteracting evaporation of the saline bath through complicated humidity controls and hooded apparatus, it was decided to simply perform the experimental measurements as quickly as possible and under a stable and cool temperature (approximately 22°C). Measurements were never paused during a session and only essential people were allowed inside the laboratory during a experiment session. Sessions were performed at the same time of day to improve temperature stability, that said, the IOL parameters measured (apical shape and central thickness) are not thought to be particularly vulnerable to temperate variation of this magnitude (< 10°C). By measuring all 4 positions independently for each trial, and by reversing the stage translation direction after each trial, the saline thickness (apparent) is known for both the start and finish of each trial. When calculating the real saline thickness and other IOL parameters, the mean evaporation rate over the trial is taken into consideration and a mean saline thickness value is used. A time-averaged mean saline thickness is deemed acceptable because when the measurement sequence was timed on multiple occasions, the interval between the recording of each measurement position was consistently evenly spaced by a quarter period to within a few seconds. Ensuring that the bath suffered no leakage flaws was straightforward.

One of the most important protocol details concerns the choice of the objective lens. It was desirable to select an objective lens that would be suitable for a broad range

of IOL powers. A low NA objective lens provides improved accuracy, the ability to measure over an increased dynamic range (particularly regarding low IOL powers), but with reduced sampling area (beam coverage of the IOL in the autocollimation position). By contrast, a high NA objective lens suffers diminished accuracy, a reduced dynamic range (particularly regarding low IOL powers), but provides improved coverage in the autocollimation position. The focal length of the objective lens in conjunction with the range of the micrometer translation stage determines the dynamic range of IOL radius of curvature measurement. The selected objective lens had a focal length of 43 mm and diameter of 15 mm, forming a converging beam with a 19 degree full angle in air (equivalent NA 0.16). Preliminary investigations attempted to increase the beam coverage of the IOL in the confocal position by coupling various microscope objectives to the interferometer. These tests were unsuccessful; the 3rd party microscope objectives produced a far greater amount of spherical aberration than those objectives supplied by the interferometer manufacturer[1]. The final apparatus set up was such that the separation distance between the objective lens and the IOL was unrestricted in the maximum direction (allowing measurement of high positive powered IOLs) but restricted in the minimum direction (preventing measurement of low positive powered IOLs).

Vibration sensitivity is a well-known issue when performing interferometry. Practical steps to minimize vibrations included limiting laboratory access to essential personnel only, restricting all but essential movement in the vicinity, and taking care to perform all micrometer stage movements with a smooth technique. Rarely during a measurement trial the IOL would become misaligned and if this occurred the trial was aborted. The IOL would be realigned rapidly (to limit evaporation) and measurement would resume by repeating all measurements of the aborted trial. In general, all measurements were performed as rapidly as possible to decrease the risk of a misalignment event (e.g. somebody entering the laboratory), to minimize evaporation, and to minimize dust contamination of the saline bath. After initial alignment, the typical time required to perform each trial (4 measurement positions) was approximately 5 minutes. Controlling dust contamination also required a fresh saline bath every 10 trials or so.

Limitations in data analysis

The experiment was based on measurement of apparent distances. As the surfaces

[1] It is likely that these objectives were designed for microscopy to compensate spherical aberration of the slide coverslip.

concerned are not plane, the apparent distance values can not be converted into real distance values simply by multiplying with the refractive index, as in the commonly cited example concerning a parallel plate. Curvature of the interceding IOL surface means that accurate conversion requires ray tracing analysis for the calculation of both the central thickness and radius of curvature parameters. Ray-tracing analysis was evaluated independently for each trial data set, as opposed to just once only based on the mean of the 10 trials for each IOL orientation. Accordingly, analysis required a large amount of time, but in doing so, the most accurate data possible is obtained. Only after conversion into real distance values is the data set summarized by calculation of mean, standard deviation, and standard error of the mean.

The residual surface deviation measurements obtained from the autocollimation position are converted from interferograms into phase elevation maps and fitted with Zernike polynomials by the internal FISBA software. The Zernike polynomial coefficients are exported but must be processed further with ray tracing software before they can be interpreted. The first issue to consider in the analysis is the *incomplete* and *variable* beam coverage of the IOL surface in the autocollimation position. The incomplete beam coverage means that the periphery of the IOL surface is not measured and any extrapolation of topography data is inherently unreliable. Beam coverage and therefore the diameter over which the Zernike coefficients are referenced to, varies with the radius of curvature of the IOL surface. Therefore, to make the aberration coefficient values easily comparable across an IOL range, the coefficients must be re-scaled, preferably to the largest common diameter measured. Secondly, the saline thickness also varies across trials and this is an important component of the ray tracing model as previously described because the plane air/saline interface induces spherical aberration in the wavefront.

Measurement of the residual surface deviation was not possible on all IOL surfaces due to the temperamental nature of capturing an interferogram. Usually failure was attributable to low contrast and/or image instability. Of those measurements possible, only Zernike coefficients relating to rotationally symmetric functions (e.g. defocus and spherical aberration) should be considered reliable. The interpretation of all other coefficients remains ambiguous in the current study because unfortunately the mounting of the IOL proved inadequate regarding rotation (tilt about the z axis) prevention. Although a consistent orientation was applied to the initial positioning of the IOL, by the end of a series of 10 trials the IOL was often observed to have rotated by amounts

exceeding 90 degrees. Unfortunately, this issue was not noticed until the concluding stages of data collection. As previously mentioned, in hindsight perhaps a gel bedding could have improved the IOL mounting and avoided this problem.

Beam coverage of the IOL surface in the autocollimated position was measured at the end of each measurement series by translating the bath stage in the x meridian and recording the micrometer value corresponding to when the beam was exactly tangential to the edge of the IOL optic. By repeating the same measurement in both the positive and negative x directions, and by knowing the IOL optic diameter (6 mm), the beam coverage was calculated. However, to determine exactly when the beam was tangential to the IOL optic, the observation angle was unavoidably very oblique due to the physical arrangement of the apparatus as schematically illustrated in Fig. 2.3. In consideration of this, it is preferable to use the well-known parameters of the objective lens in the ray-tracing model to theoretically estimated the beam coverage values.

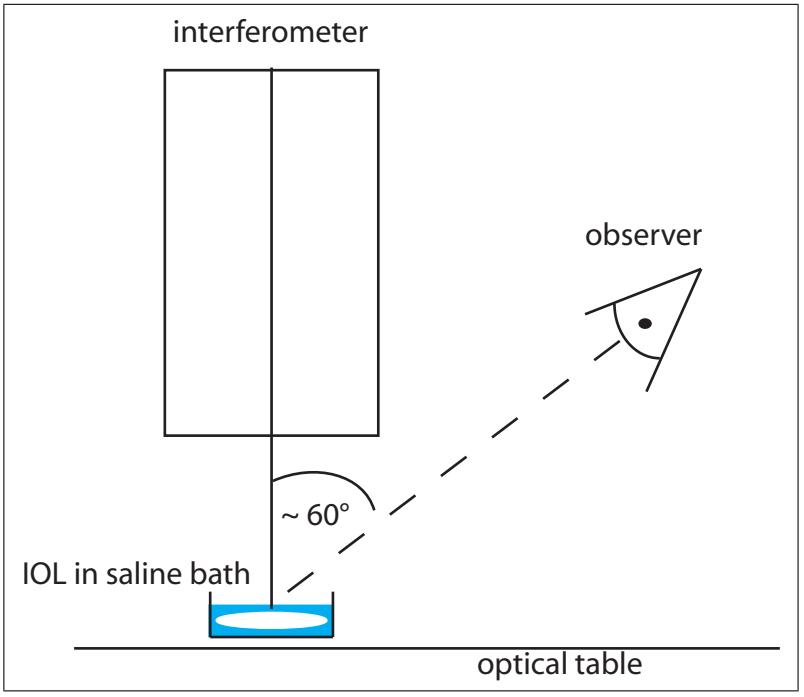

FIGURE 2.3: Schematic depiction of the parallax error caused by the oblique angle of the observer viewing the interferometer beam incident on the IOL.

Analysis of the apparent distance data required modelling parameters of the saline bath on ray-tracing software. These estimated specifications are a source of error. The air/saline surface is assumed approximately plane and the refractive index of the saline is assumed to be 1.333 relative to the interferometer measurement wavelength ($\lambda = 632.8$ nm). The refractive index estimation is based on the following considerations; the

temperature of the saline bath was typically near 22 degrees Celsius and the NaCl concentration in the saline was relatively low (0.67%). Without readily accessible data regarding the refractive index of saline, it is reasonable to estimate this value based on similarity with distilled water. After considering the literature describing the refractive index of water [189, 190, 191] and taking into account the temperature and wavelength conditions, it was decided to use an estimated saline refractive index of 1.333. As an aside, note the use of preserved saline as the bath medium was a secondary preference. Although preserved saline and balanced salt solution (BSS) have similar physicochemical properties, they are not identical solutions and it would be preferable to use BSS to better mimic the *in situ* environment.

Data analysis with ray tracing software assumed a refractive index value of 1.4585 for the IOL material. Any error in this assumption only effects calculation of the central thickness parameter, not the radius of curvature parameter. The refractive index value for the IOL material was taken as the mean of the manufacturer-stated values given in Table 2.1 given that the temperature of the IOL bath was typically near 22 degrees Celsius. Arguably as 22 degrees is much closer to 20 degrees than 35 degrees, a refractive index value of 1.459 also would also have been acceptable. Note that the reference wavelength specified by standards regarding the measurement of IOL dioptric power is 546 nm [66]. Although not explicitly declared, it is fair to assume that manufacturers also describe refractive index values relative to the 546 nm wavelength, which is reasonably similar to the interferometer measurement wavelength of 632.8 nm.

Results

Table 2.2 shows the mean and standard deviation of the anterior radius of curvature, central thickness, and posterior radius of curvature for all IOLs measured. The labelled dioptric power ranges from 6.0D to 30.0 D. For some powers (18.5 D, 20.0 D, 29.0 D and 30.0 D), multiple samples of 2 to 3 IOLs were measured and were used to study reproducibility in manufacture. Financial constraints precluded a larger sample size. Unfortunately, due to the small sample sizes these results were inconclusive and are not reported.

Figure 2.4 presents a summary of the metrology data from Table 2.2, displaying nearly all parameters measured in the one graph. The anterior radius of curvature, posterior radius of curvature, and central thickness are plotted against the labelled effective focal

IOL (Akreos Adapt AO, Bausch and Lomb) metrology data summary							
Serial No.	Labelled	Anterior radius of curvature		Central thickness		Posterior radius of curvature	
	power (D)	mean (mm)	SD (mm)	mean (mm)	SD (mm)	mean (mm)	SD (mm)
1633502/014	6.0	32.792	0.242	0.678	0.0129	46.533	0.248
1821118/043	12.5	17.002	0.048	0.625	0.0134	21.869	0.029
1821702/037	13.5	16.059	0.034	0.657	0.0084	20.313	0.056
1707208/088	14.0	15.197	0.036	0.643	0.0100	20.051	0.030
1711707/015	14.5	14.902	0.026	0.686	0.0093	19.131	0.032
1633508/041	15.0	14.266	0.014	0.717	0.0058	18.534	0.035
1634105/011	15.5	13.989	0.049	0.723	0.0164	17.795	0.020
1627514/059	16.0	13.245	0.020	0.736	0.0233	17.199	0.028
1631113/006	16.5	12.872	0.019	0.750	0.0060	16.733	0.017
1700804/075	17.0	12.538	0.011	0.773	0.0077	16.215	0.010
1701013/069	17.5	12.212	0.024	0.805	0.0064	15.626	0.023
1705130/052	18.0	11.556	0.047	0.821	0.0058	16.106	0.065
1635304/039	18.5	11.605	0.012	0.838	0.0062	15.091	0.017
1712210/026	18.5	11.681	0.009	0.816	0.0112	15.038	0.020
1810627/029	19.5	10.976	0.013	0.859	0.0058	14.460	0.018
1703801/007	20.0	10.555	0.010	0.865	0.0121	14.096	0.012
1719007/004	20.0	10.811	0.052	0.867	0.0090	14.040	0.285
1800217/021	20.0	10.912	0.013	0.904*	0.0087	14.151	0.020
1719113/045	21.5	9.979	0.013	0.908	0.0081	13.038	0.017
1719422/011	22.0	9.631	0.017	0.921	0.0044	12.757	0.017
1811215/063	22.5	9.454	0.009	0.903	0.0053	12.617	0.017
1706003/047	23.0	9.344	0.011	0.916	0.0114	12.285	0.026
1710723/075	24.0	8.865	0.013	0.938	0.0054	11.750	0.013
1716613/027	25.0	8.488	0.005	0.979	0.0050	11.219	0.010
1702909/082	25.5	8.335	0.015	0.993	0.0057	10.956	0.025
1702914/070	26.0	8.265	0.017	1.022	0.0074	10.750	0.013
1631902/024	27.0	7.900	0.004	1.043	0.0049	10.466	0.008
1813812/069	28.0	7.624	0.011	1.078	0.0142	10.082	0.006
1704803/025	28.5	7.529	0.010	1.086	0.0053	9.887	0.009
1627501/003	29.0	7.367	0.016	1.118	0.0053	9.636	0.007
1627501/001	29.0	7.364	0.021	1.139*	0.0044	9.708	0.005
1630414/007	30.0	7.176	0.005	1.132	0.0112	9.318	0.013
1630414/008	30.0	7.162	0.008	1.130	0.0071	10.686*	0.013

TABLE 2.2: Summary of IOL metrology results. Radius of curvature parameters refer to the apical region. SD is standard deviation. Sample size is 10 for radius of curvature measurements and 20 for central thickness measurements. The standard error of the mean for each parameter may be found by dividing the standard deviation by the square root of the sample size. Three values marked with an asterisk* are considered outliers.

length. For all parameters, the error bars indicate ± 2 standard deviations. In many instances, for anterior and posterior radius of curvature values the associated error bars are not visible as the values are below the point size used to plot the data point. By contrast, a dramatically larger spread of values relative to the range measured is observed for central thickness measurements.

Data relating to IOL serial number 1633502/014 although thought reliable, is not plotted in Fig. 2.4 for the sake of obtaining a practical scale on the graph. Figure 2.5 re-plots the same data as Fig. 2.4, this time including data relating to IOL serial number 1633502/014. The revised scale is useful in modelling IOL powers between 6.0 D and 12.5 D, although interpolation over such a broad range is cautioned. Three values marked with an asterisk* in Table 2.2 were considered outliers and are excluded from further

data analysis, including the fitting of analytical functions (Eqs. 2.1 to 2.6). The three outlier data points are omitted from Fig. 2.4 but are displayed in 2.5 for completeness.

For the 12.5 D to 30.0 D data range as shown in Fig. 2.4, the IOL parameters may be modeled by fitting analytical functions. Figure 2.4 suggests that it is appropriate to use linear regression to fit the radius of curvature data trend and a power function to fit the central thickness data trend. The fitted analytical expressions are

$$r_1 = 0.21433511f - 0.02268 \qquad R^2 = 0.9985 \tag{2.1}$$

$$t_c = 11.783752408f^{-0.669924619} \qquad R^2 = 0.9897 \tag{2.2}$$

$$r_2 = 0.27059735f + 0.43978 \qquad R^2 = 0.9977 \tag{2.3}$$

where r_1 is the anterior radius of curvature, t_c is the central thickness, r_2 is the posterior radius of curvature, f is the vertex focal length and all units are in millimeters. The associated square of the sample correlation coefficient (R^2) values are all greater than 0.98, indicating high correlation between the fitted expressions and the metrology data. Concerning IOLs with a labelled power within the 12.5 D to 30 D range, Eqs. 2.1 to 2.3 can be used to estimate likely values for the IOL parameters. For example, within the data collection a 20.5 D IOL was not measured, however an IOL of this power may still be simulated in a personalised pseudophakic eye model (see Chapter 3), by evaluating Eqs. 2.1, 2.2 and 2.3. Furthermore, this method is used to simulate all IOLs within the 12.5 D to 30.0 D range, regardless of whether the specific IOL power was directly measured during the experiment. In this way, the estimation becomes more accurate, benefiting from the trend across the dioptric series and the increased sampling.

For convenience, both the anterior and posterior radius of curvature values are reported with the same sign in Figs. 2.4 and 2.5 and in Eqs. 2.1, 2.3, 2.4, and 2.6. When optical calculations are performed, a trivial change of sign is required to one of these parameters when both surfaces are combined to create a *biconvex* lens. Most typical coordinate systems would designate the posterior radius of curvature as a negative distance.

These expressions are derived from metrology data solely concerning one particular IOL model (Akreos Adapt AO, Bausch and Lomb) and are not valid for any other IOL model. Similarly, outside the range of 12.5 D to 30 D, Eqs. 2.1, 2.2 and 2.3 are not valid and should not be used. The 6 D to 12.5 D range was analysed separately due to the

large interpolation required and the associated uncertainty of results. If it is necessary to model IOLs in the 6 D to 12.5 D range, linear regression fitting of the radius of curvature parameters still seems to be an appropriate choice for the model as shown in Fig. 2.5. However, the use of a power function (as in Eq. 2.2) drastically underestimates the central thickness for focal length values greater than 80 mm and it is not suitable. This effect should be interpreted with caution as it is due to the influence of one single data point. Given a priori knowledge regarding IOL mechanical issues, in the range 6 D to 12.5 D it is perhaps sufficient to simply use a constant value of 0.65 mm to estimate IOL central thickness. Alternatively, an exponential decay function such as that given in Eq. 2.5 is also a reasonable postulation.

$$r_1 = 0.19662590f + 0.84392 \qquad R^2 = 0.9961 \tag{2.4}$$

$$t_c = 0.95^{(f-20)} + 0.62 \qquad R^2 = 0.8659 \tag{2.5}$$

$$r_2 = 0.27676076f + 0.13460 \qquad R^2 = 0.9992 \tag{2.6}$$

The symbols and units used in Eqs. 2.4 to 2.6 and the same as those used in Eqs. 2.1 to 2.3.

Refractive index verified by model agreement with labelled dioptric power

Because the IOL manufacturer does not disclose values for apical radius of curvature or central thickness, these parameters were measured experimentally. By contrast, the manufacturer does report the IOL material refractive index and initially it was hoped this value might be indirectly verified by measuring the vertex focal length relating to the confocal position. This data, when combined with the other measured parameters, would have allowed the refractive index to be indirectly calculated. However, as previously described, preliminary testing demonstrated the confocal position arrangement was not possible due to the limited range of the micrometer stage.

The manufacturer-stated refractive index is slightly ambiguous, mainly because this extremely sensitive parameter is only reported to a precision of 4 significant figures. Additionally, the influence of temperature is another consideration as highlighted by the two values reported in Table 2.1. For these reasons, and the inability to perform confocal measurements, it was decided to verify what refractive index value provides best agreement to the labelled power. It is reasonable to assume that the labelled power

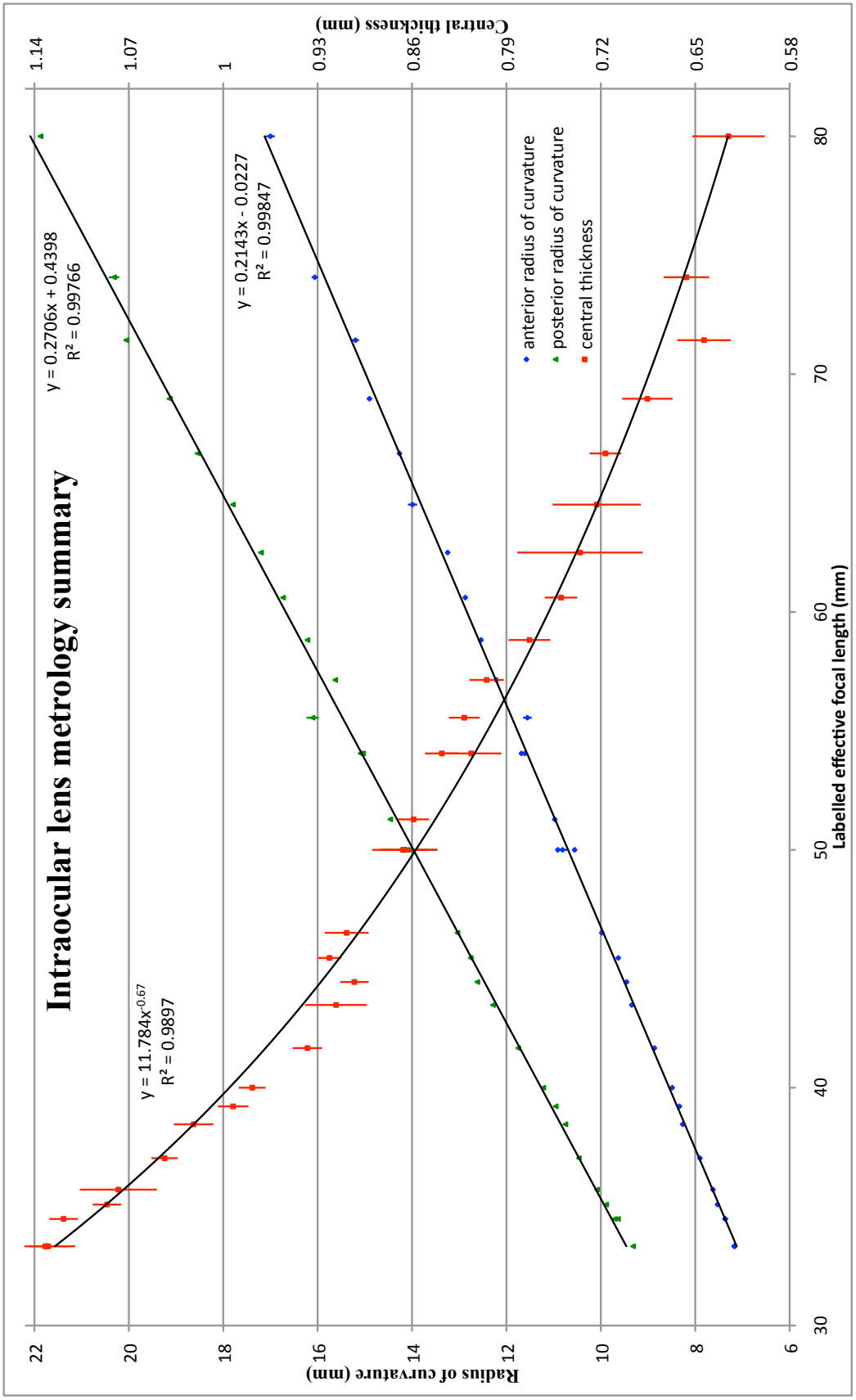

FIGURE 2.4: Summary of IOL metrology results. Error bars represent ±2 standard deviations for all parameters. Anterior radius of curvature (blue diamonds) and posterior radius of curvature (green triangles) are plotted against the left vertical axis. Central thickness (red squares) is plotted against the right vertical axis.

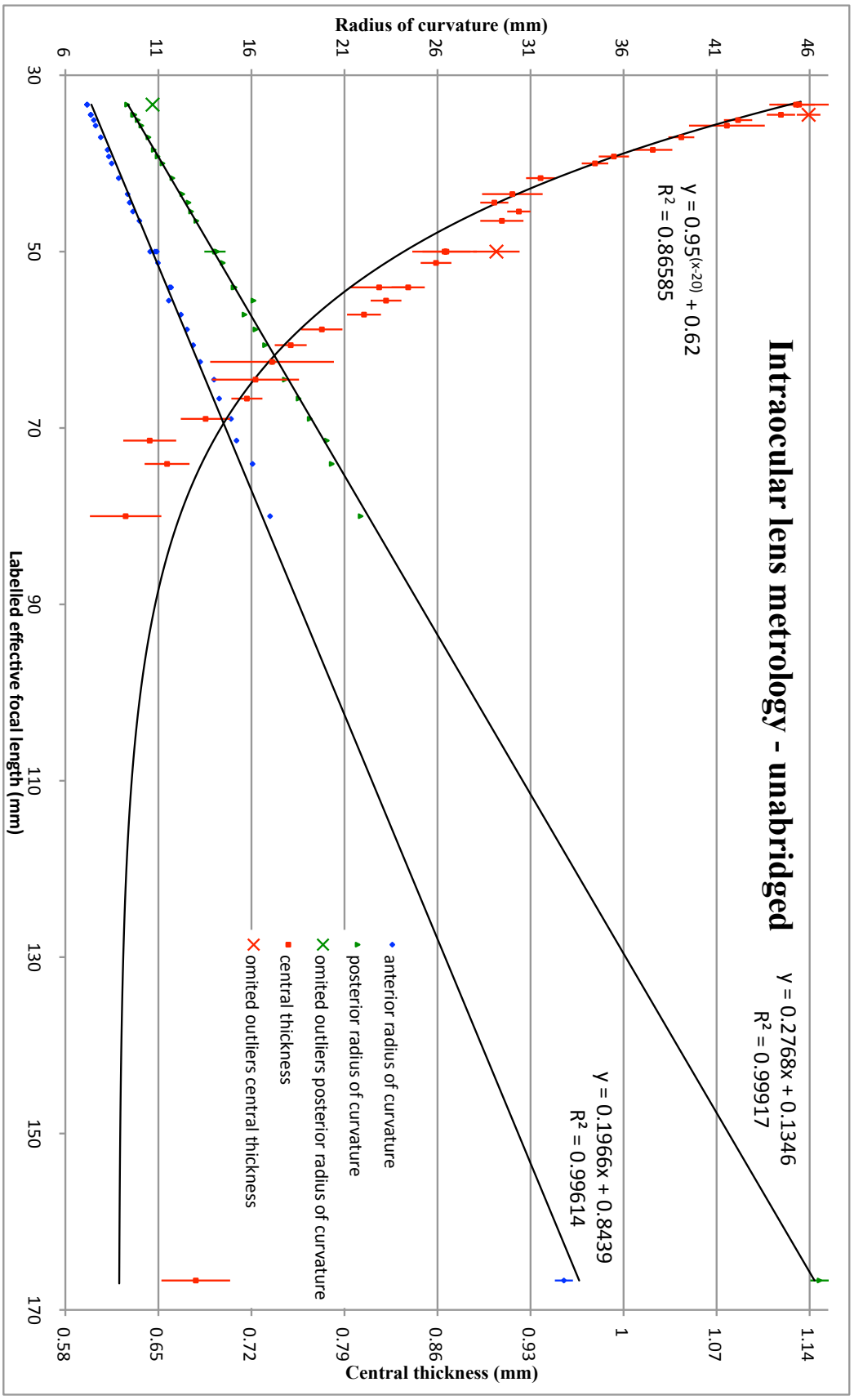

FIGURE 2.5: Unabridged IOL metrology results. Error bars represent ±2 standard deviations for all parameters. Anterior radius of curvature (blue diamonds), posterior radius of curvature (green triangles), and omitted posterior radius of curvature (green cross) are plotted against the left vertical axis. Central thickness (red squares) and omitted central thickness (red cross) are plotted against the right vertical axis.

value is generally accurate, and therefore the refractive index value providing the best agreement over the data set is a suitable estimate.

Following determination of the anterior and posterior radius of curvature, and central thickness parameters, the IOL was modelled in ray tracing software to determine the effective focal length. The IOL was simulated in aqueous humor media with a refractive index value of 1.336 at 546.07 nm and 35° C. The entrance pupil of a collimated beam was defined by an aperture diaphragm of 5 mm diameter and this beam was incident on the IOL. Each IOL was modeled in 3 different scenarios using refractive index values of 1.4580, 1.4585, and 1.4590 for the IOL material. The results are displayed in Table 2.3, with the trend of mean difference between modelled and labelled power being lowest for a refractive index value of 1.4580. Accordingly, we elect to use this value when generating personalised pseudophakic eye models (see Chapter 3). The accuracy of this estimated value is dependent upon the accuracy of the labelled power, which itself is described according to a standard temperature 35°C ± 2°C, wavelength 546 nm ± 10 nm, in aqueous humor of refractive index 1.336 [66].

Our results support the use of a refractive index value of 1.4580 (see Table 2.3) when the IOL is modelled at standard temperature 35°C ± 2°C, wavelength 546 nm ± 10 nm, in aqueous humor of refractive index 1.336 - in agreement with the manufacturer's reported value. Although our metrology experiment was carried out at approximately 22°C, that does **not** imply that best modelled agreement with the labelled dioptric power should be expected with a refractive index value of 1.4590 (the manufacturer's reported value at 20°C - see Table 2.1). Our metrology experiment only measured the physical shape and central thickness, parameters that are stable over the relevant temperature range (22°C - 35°C). It is the refractive index value that varies over this temperature range. As the metrology experiment made no direct or indirect measurement of refractive index, there is no reason to expect disagreement between the modelled and labelled power using the manufacturer's reported value (1.458) even though the metrology was performed at a non-standard temperature.

Repeatability in metrology

By repeating the trial measurements (each trial consisting of 4 measurement positions) 10 times independently in each orientation (anterior and posterior orientation) for each IOL, the spread of the data can be analyzed. The standard deviation (SD) provides an

Comparison of labelled and modelled IOL parameters											
Serial No.	Effective focal length (mm)				Effective power (D)				Difference in power (D)		
	Labelled	Modelled refractive index			Labelled	Modelled refractive index			Modelled - Labelled		
		1.4580	1.4585	1.4590		1.4580	1.4585	1.4590	1.4580	1.4585	1.4590
1633502/014	166.667	157.787	157.144	156.505	6.0	6.34	6.36	6.39	0.34	0.36	0.39
1821118/043	80.000	78.511	78.191	77.873	12.5	12.74	12.79	12.84	0.24	0.29	0.34
1821702/037	74.074	73.619	73.319	73.021	13.5	13.58	13.64	13.69	0.08	0.14	0.19
1707208/088	71.429	70.968	70.679	70.392	14.0	14.09	14.15	14.21	0.09	0.15	0.21
1711707/015	68.966	68.779	68.499	68.221	14.5	14.54	14.60	14.66	0.04	0.10	0.16
1633508/041	66.667	66.196	65.926	65.659	15.0	15.11	15.17	15.23	0.11	0.17	0.23
1634105/011	64.516	64.313	64.051	63.791	15.5	15.55	15.61	15.68	0.05	0.11	0.18
1627514/059	62.500	61.457	61.207	60.958	16.0	16.27	16.34	16.40	0.27	0.34	0.40
1631113/006	60.606	59.761	59.517	59.276	16.5	16.73	16.80	16.87	0.23	0.30	0.37
1700804/075	58.824	58.087	57.851	57.616	17.0	17.22	17.29	17.36	0.22	0.29	0.36
1701013/069	57.143	56.323	56.094	55.866	17.5	17.75	17.83	17.90	0.25	0.33	0.40
1705130/052	55.556	55.290	55.064	54.841	18.0	18.09	18.16	18.23	0.09	0.16	0.23
1635304/039	54.054	53.915	53.695	53.477	18.5	18.55	18.62	18.70	0.05	0.12	0.20
1712210/026	54.054	54.027	53.807	53.588	18.5	18.51	18.59	18.66	0.01	0.09	0.16
1810627/029	51.282	51.290	51.081	50.874	19.5	19.50	19.58	19.66	0.00	0.08	0.16
1703801/007	50.000	49.619	49.417	49.217	20.0	20.15	20.24	20.32	0.15	0.24	0.32
1719007/004	50.000	50.210	50.005	49.803	20.0	19.92	20.00	20.08	-0.08	0.00	0.08
1800217/021*	50.000	50.654	50.448	50.243	20.0	19.74	19.82	19.90	-0.26	-0.18	-0.10
1719113/045	46.512	46.486	46.297	46.110	21.5	21.51	21.60	21.69	0.01	0.10	0.19
1719422/011	45.455	45.138	44.954	44.772	22.0	22.15	22.24	22.34	0.15	0.24	0.34
1811215/063	44.444	44.451	44.270	44.090	22.5	22.50	22.59	22.68	0.00	0.09	0.18
1706003/047	43.478	43.657	43.479	43.303	23.0	22.91	23.00	23.09	-0.09	0.00	0.09
1710723/075	41.667	41.575	41.406	41.238	24.0	24.05	24.15	24.25	0.05	0.15	0.25
1716613/027	40.000	39.773	39.611	39.451	25.0	25.14	25.25	25.35	0.14	0.25	0.35
1702909/082	39.216	38.969	38.810	38.653	25.5	25.66	25.77	25.87	0.16	0.27	0.37
1702914/070	38.462	38.473	38.316	38.161	26.0	25.99	26.10	26.20	-0.01	0.10	0.20
1631902/024	37.037	37.077	36.926	36.777	27.0	26.97	27.08	27.19	-0.03	0.08	0.19
1813812/069	35.714	35.766	35.620	35.476	28.0	27.96	28.07	28.19	-0.04	0.07	0.19
1704803/025	35.088	35.218	35.075	34.933	28.5	28.39	28.51	28.63	-0.11	0.01	0.13
1627501/003	34.483	34.412	34.272	34.133	29.0	29.06	29.18	29.30	0.06	0.18	0.30
1627501/001*	34.483	34.517	34.377	34.238	29.0	28.97	29.09	29.21	-0.03	0.09	0.21
1630414/007	33.333	33.420	33.284	33.150	30.0	29.92	30.04	30.17	-0.08	0.04	0.17
1630414/008*	33.333	35.336	35.193	35.051	30.0	28.30	28.41	28.53	-1.70	-1.59	-1.47
						MEAN all data included			0.01	0.10	0.18
						MEAN outliers* omitted			0.08	0.16	0.24

TABLE 2.3: Comparison of labelled and modelled IOL parameters of effective focal length (mm) and effective power (D) as a method to estimate the refractive index of the IOL material in consideration of *in situ* conditions. Three IOLs marked with an asterisk* are considered outliers.

indication of test-retest repeatability in metrology. In an alternative metric of repeatability, the standard deviation is divided by the mean and then multiplied by 100 to give a percentage expression. The standard error of the mean (SEM) describes the likely variation between the sample mean estimate and the true population mean. These 3 indices are reported for the anterior radius of curvature ($n = 10$), central thickness ($n = 20$), and posterior radius of curvature ($n = 10$) parameters of each IOL in Table 2.4. The SD and SEM values in Table 2.4 compare well to the previously described precision limit determined by the micrometer scale of approximately 14 μm for all parameters (21.5 D representative case).

In the measurement of dioptric power, a repeatability level of 0.5% of the power is typical [66]. By way of comparison, if the 21.5 D (serial number 1719113/045) representative case is modelled with mean errors of 0.19%, 1.04%, and 0.21% for anterior radius of curvature, central thickness, and posterior radius of curvature, respectively. In a worst case scenario when the effects of the errors are cumulative, the modelled effective power is 21.55 D compared to the true value of 21.51 D. This is equivalent to a repeatability level of 0.19% and demonstrates an improved typical repeatability in metrology about twice that considered typical by industry [66].

The three outlier data points illustrate the sensitivity of dioptric power to noise in the radius of curvature parameter and its relative insensitivity to noise in the central thickness parameter. In Table 2.3, for IOL serial number 1630414/008, the error in the posterior radius of curvature causes a drastic difference between the modelled and labelled power, whereas IOLs suffering central thickness errors (1800217/021 and 1627501/001) exhibit negligible effect on the modelled power, generally indistinguishable from the global variation exhibited by the entire group. The outlier data points were discriminated with respect to their mean values, metrics of their constituent data spread itself (e.g. standard deviation) may be quite unremarkable, and this is why the outliers do not greatly influence the repeatability analysis in Table 2.4.

Within the data set, the measurement of various labelled powers (18.5 D, 20.0 D, 29.0 D and 30.0 D) was intentional replicated to investigate *reproducibility in manufacture* of IOL parameters. Unfortunately, the sample size for each subgroup ($n = 2, 3, 2$, and 2 respectively) is too small for any meaningful analysis.

Repeatability of IOL parameters											
			anterior radius of curvature ($n = 10$)			central thickness ($n = 20$)			posterior radius of curvature ($n = 10$)		
Serial No.	labelled focal length (mm)	labelled power (D)	SD (μm)	100 · SD/Mean (%)	SEM (μm)	SD (μm)	100 ·SD/Mean (%)	SEM (μm)	SD (μm)	100 ·SD/Mean (%)	SEM (μm)
1633502/014	166.667	6.0	242.3	0.74	76.6	12.9	1.91	2.9	247.7	0.53	78.3
1821118/043	80.000	12.5	48.3	0.28	15.3	13.4	2.15	3.0	29.2	0.13	9.2
1821702/037	74.074	13.5	34.5	0.21	10.9	8.4	1.29	1.9	56.2	0.28	17.8
1707208/088	71.429	14.0	36.5	0.24	11.5	10.0	1.55	2.2	29.6	0.15	9.4
1711707/015	68.966	14.5	25.6	0.17	8.1	9.3	1.36	2.1	32.4	0.17	10.2
1633508/041	66.667	15.0	14.4	0.10	4.5	5.8	0.81	1.3	35.5	0.19	11.2
1634105/011	64.516	15.5	49.0	0.35	15.5	16.4	2.26	3.7	20.2	0.11	6.4
1627514/059	62.500	16.0	20.0	0.15	6.3	23.3	3.16	5.2	28.2	0.16	8.9
1631113/006	60.606	16.5	18.7	0.15	5.9	6.0	0.80	1.3	17.3	0.10	5.5
1700804/075	58.824	17.0	11.0	0.09	3.5	7.7	1.00	1.7	10.2	0.06	3.2
1701013/069	57.143	17.5	23.9	0.20	7.6	6.4	0.79	1.4	22.6	0.14	7.1
1705130/052	55.556	18.0	47.1	0.41	14.9	5.8	0.70	1.3	65.1	0.40	20.6
1635304/039	54.054	18.5	12.1	0.10	3.8	6.2	0.75	1.4	17.2	0.11	5.4
1712210/026	54.054	18.5	9.3	0.08	3.0	11.2	1.37	2.5	19.6	0.13	6.2
1810627/029	51.282	19.5	13.4	0.12	4.2	5.8	0.67	1.3	17.5	0.12	5.5
1703801/007	50.000	20.0	10.1	0.10	3.2	12.1	1.40	2.7	12.4	0.09	3.9
1719007/004	50.000	20.0	51.9	0.48	16.4	9.0	1.04	2.0	285.3	2.03	90.2
1800217/021	50.000	20.0	13.0	0.12	4.1	8.7	0.96*	2.0	19.7	0.14	6.2
1719113/045	46.512	21.5	12.6	0.13	4.0	8.1	0.89	1.8	16.7	0.13	5.3
1719422/011	45.455	22.0	17.2	0.18	5.4	4.4	0.48	1.0	16.6	0.13	5.2
1811215/063	44.444	22.5	8.9	0.09	2.8	5.3	0.58	1.2	17.3	0.14	5.5
1706003/047	43.478	23.0	10.8	0.12	3.4	11.4	1.24	2.5	26.1	0.21	8.3
1710723/075	41.667	24.0	13.1	0.15	4.1	5.4	0.58	1.2	13.1	0.11	4.1
1716613/027	40.000	25.0	5.5	0.06	1.7	5.0	0.51	1.1	9.7	0.09	3.1
1702909/082	39.216	25.5	14.6	0.17	4.6	5.7	0.57	1.3	25.0	0.23	7.9
1702914/070	38.462	26.0	17.0	0.21	5.4	7.4	0.72	1.6	13.3	0.12	4.2
1631902/024	37.037	27.0	4.5	0.06	1.4	4.9	0.47	1.1	7.6	0.07	2.4
1813812/069	35.714	28.0	10.9	0.14	3.5	14.2	1.32	3.2	6.3	0.06	2.0
1704803/025	35.088	28.5	10.1	0.13	3.2	5.3	0.49	1.2	9.0	0.09	2.9
1627501/003	34.483	29.0	16.3	0.22	5.2	5.3	0.48	1.2	7.3	0.08	2.3
1627501/001	34.483	29.0	20.9	0.28	6.6	4.4	0.39*	1.0	5.5	0.06	1.7
1630414/007	33.333	30.0	4.7	0.07	1.5	11.2	0.99	2.5	12.6	0.14	4.0
1630414/008	33.333	30.0	8.5	0.12	2.7	7.1	0.63	1.6	13.3	0.12*	4.2
		Mean ($n = 33$)	26.0	0.19	8.2	8.6	1.04	1.9	35.3	0.21	11.2

TABLE 2.4: Test-retest repeatability of the Akreos Adapt AO (Bausch and Lomb) IOL. Asterisks* mark data that is influenced by calculation with suspected outlier mean values. SD is standard deviation. SEM is standard error of the mean.

Shape factor

Using the mean radius of curvature data reported in Table 2.2, the shape factor of each IOL was calculated using the Coddington equation (Eq. 1.2). IOL serial number 1630414/008 was excluded from this analysis as its posterior radius of curvature value is erroneous. All other remaining IOLs were analyzed, the shape factor (q) ranges in value from a minimum of 0.117 to a maximum of 0.173, with mean value of 0.135. The shape factor is important for many clinical reasons previously described including PCO prevention and stability of ELP across a dioptric series. Concerning imaging quality the shape factor is a fundamental parameter of the IOL design [192] and [193]. Shape factor is a classical method used to control spherical aberration. The *best form* Coddington shape factor minimizes spherical aberration of a singlet lens, considering a specific conjugate ratio, by satisfying

$$q = \frac{r_2 + r_1}{r_2 - r_1} = \frac{2(n^2 - 1)}{n + 2} \cdot \frac{i + o}{i - o} \tag{2.7}$$

where r_1 is the apical radius of curvature of the anterior surface of the lens (meters) and r_2 is the apical radius of curvature of the posterior surface of the lens (meters), i is the image distance (meters) and o is the object distance (meters).

Conclusions and future improvements

The metrology experiment was successful in providing a reliable method for modelling the Akreos Adapt AO (Bausch and Lomb) IOL. In the labelled power range from 12.5 D to 30.0 D it is recommended to model the apical anterior radius of curvature, central thickness and apical posterior radius of curvature using Eqs. 2.1 to 2.3. In the labelled power range from 6.0 D to 12.5 D, it is recommended to model these parameters using Eqs. 2.4 to 2.6. The IOL is also supplied in the 0 D to 6.0 D power range and over this range Eqs. 2.4 to 2.6 may be used to extrapolate IOL parameters with caution. The IOL refractive index was verified, although the method used is dependent upon the accuracy of the labelled dioptric power. A value of 1.4580 is recommended for pseudophakic eye modelling under standard conditions of temperature 35°C ± 2°C and wavelength 546 nm ± 10 nm. However, the benefit of any effort to increase the precision to which the refractive index of an IOL optic material is known, is limited by the precision to which the aqueous humor of refractive index is known. The test-retest repeatability in metrology data indicates excellent consistency of the experimental results.

The main limitation of the study concerns the difficulty in capturing reliable interferograms in the autocollimated position. Temperamental quality of the interferograms was difficult to overcome and laborious raytracing analysis required preliminary calculation of saline depth, IOL radius of curvature, and beam coverage of the IOL before the Z_0^4 coefficient could be analyzed, distinguishing between residual IOL surface aberration and the spherical aberration artifact introduced by the air/saline interface, and then finally rescaled to a consistent pupil size for comparison across the dioptric series. The resulting data (not presented) possessed an inconsistent pattern that could not be interpreted sensibly. To address this issue, data collection would need to be repeated with a revised protocol aimed at increasing the contrast and stability of the interferograms, and at improving the IOL mounting. The suggested modifications are described below.

Suggested improvements to the experiment design include;

- Modifying the interferometer to allow the reference beam irradiance to be varied so as to match the returned signal irradiance from the test beam. The measurement beam irradiance is relatively low owing to the modest refractive index differential at the saline/IOL interface (1.333 to 1.4580) compared to the more typical measurement of an air/glass interface for which the reference beam irradiance is optimised. By obtaining a closer match between the reference and measurement irradiance, the interferogram fringe contrast will increase. Vibration control of the interferometer could also be improved by the use of a dampening table.

- Improved IOL mounting is essential in any future repeated experiment. Rotation control (tilt about z axis) is necessary to relate the measurements of the anterior and posterior surfaces with each other. It is absolutely necessary for metrology of toric IOL designs and for measuring non rotationally symmetric HOAs. Although the IOL was always initially positioned at a consistent position, in the absence of a mechanical brace, rotation occurred. By mechanically bracing the haptics on at least 2 sides, this issue could be corrected, simply and effectively.

- The range of the micrometer stage limited the dioptric range of IOLs measurable and should be increased in any future experiment repetition. With a large enough range it would become possible to measure the confocal position, providing information regarding how the IOL surfaces are aligned with each other. In the current study, it was necessary to assume that the IOL surfaces are centered and

untilted with respect to each other as there was no simultaneous mutual metrology. Another significant benefit from measurement of the confocal position is determination of vertex focal length, which could then be used to directly infer a refractive index value for the IOL material.

- To better mimic *in situ* conditions, the bath should use BSS instead of saline. The bath should also be temperature controlled at 35°C, provided that evaporation was acceptably controlled at this temperature. Additionally, the refractive index of the BSS should be measured independently at this temperature and for the specific wavelength used by the interferometer.

- Measurement of a greater range of IOLs is preferable, particularly regarding studies of reproducibility in manufacturing. The IOLs are a significant consumable expense for the financial limits of the study.

Although there are some areas of limitation in the current metrology study, overall it was successful. The gold standard method for IOL metrology must combine the ability to measure IOL surface topography, central thickness, and wavefront aberration of a transmitted beam. Without measurement of all three of these parameters, the IOL modelling is incomplete, typically relying on assumptions regarding; centration and alignment of the IOL surfaces with respect to each other, and the refractive index of the IOL material. Metrology methods other than interferometry, such as Hartmann-Shack wavefront sensing, may be better suited to the measurement of IOLs.

2.3 Protocol for biometry data collection

Introduction

Biometric data was collected on a cohort of subjects undergoing routine cataract surgery with phacoemulsification and *in-the-bag* implantation with an Akreos Adapt AO (Bausch and Lomb) IOL. Anterior corneal topography elevation data using Placido disc technology (Atlas 9000, Carl Zeiss Meditec), autorefraction/autokeratometry (ARK-510A, Nidek), and segmented axial length data using optical low coherence reflectometry (Lenstar 900, Haag-Streit) was collected on both eyes of each subject prior to surgery.

The same measurements were repeated approximately 3 weeks post-operatively with additional measurements of wavefront aberrometry (Zywave, Bausch and Lomb) to quantify the refractive outcome. The experiment aims were to investigate changes in anterior corneal topography due to cataract surgery and to develop models for predicting the stabilized IOL axial depth using pre-surgery biometry data. A thorough understanding of both topics is essential in working towards personalised eye modelling of cataract surgery and simulating customised intraocular lens designs (see Ch. 3).

Subject selection

After examination and diagnosis of cataract requiring phacoemulsification and IOL implantation surgery by Dr Eamonn O'Donoghue, volunteers were invited to participate in the study. The investigation was approved of the Ethics Board of National University of Ireland Galway and volunteers gave written informed consent to participate in the study. No age, gender, or general health exclusion criteria were applied. Subjects with a history of previous ocular surgery or eye disease were excluded. Subjects unable to cooperate sufficiently to allow reliable biometry measurements were excluded. No exclusion criteria relate to the post-surgery refractive goal, although nearly all subjects had a refractive goal of near emmetropia and any exceptions are highlighted in the data reporting and analysis. The range and quartile distributions of the subjects' pre-surgery refractive error and age are reported in Table 2.5.

	Pre-surgery refractive error		Age
Statistic	Best Sphere (D)	Cylinder (D)	(years)
Minimum	-23.88	0.00	32
Quartile 1	-1.00	0.75	68
Quartile 2	+0.88	1.25	75
Quartile 3	+2.00	1.75	80
Maximum	+10.75	6.75	98

TABLE 2.5: The range and quartile distribution of subjects' pre-surgery refractive error and age.

Protocol

The experiment protocol was based on advanced clinical measurements associated with IOL power calculation and assessment of the refractive outcome. All instruments used

were commercially manufactured, providing rapid measurement with good patient comfort. All instruments possessed a chin rest and forehead rest only (no bite-bars were used). Measurements were performed pre-surgery and then repeated approximately 3 weeks post-surgery to allow sufficient wound healing and stabilization of the IOL position. The measurements typically lasted 30 minutes and were performed on both eyes regardless of which eye was undergoing cataract surgery. Data concerning the fellow non-surgical eye is used in the analysis as a control data set. In some cases of dense cataract or posterior subcapsular cataract, measurements with low coherence reflectometry (LCR) failed, necessitating axial length measurement with ultrasonography. These cases are marked in the reported data and although excluded from analysis regarding IOL axial depth, they are still included in analysis regarding corneal topography. For such cases, topical anesthesia required for ultrasonography was only instilled after all other biometry measurements had been performed. Nearly all measurements were made under natural pupil conditions, any exceptions are reported in the data. In cases of dry eye, a low viscosity lubricant was instilled and allowed to disperse over the cornea before measurements were performed. This was primarily necessary during corneal topography and wavefront aberrometry measurements.

At each instrument station, the same procedure was followed. The subject was seated and then aligned with the instrument. The subject was asked to look at the fixation target, to blink, and then to hold their eye still for a few seconds while the measurement was performed. The fellow eye was occluded if the subject preferred and also if judged clinically helpful to improve fixation of the eye under measurement. Most measurements only lasted a few seconds and subjects were reminded that they may pause measurements and rest whenever required. Several repeated measurements (without the subject removing their head from the chin/forehead rest) were performed to ensure that suitably reliable data was obtained. The number of measurements depended on the instrument; regarding LCR, corneal topography, autorefraction/autokeratometry, and wavefront aberrometry the number of measurements were 5, 1, 3, and 5, respectively.

After processing the repeated measurements, a single value for each parameter was exported for use in the final data analysis. The internal software of biometry instruments generally possesses only rudimentary capability regarding assessment of data quality and operator supervision is essential whenever permitted by internal software. Concerning the Lenstar and ARK-510A, the instrument software allows operator manipulation of the

data processing so all measurements were reviewed by the operator and any unreliable data was excluded. Following the operator's review of data quality, the mean value for each parameter was exported. The Zywave instrument software does not allow operator supervision (apart from a pass/fail control regarding pupil edge detection) and the 'best' 3 out of the 5 captured measurements are used by the internal software to generate a single data set for export. Concerning the Atlas corneal topographer, operator supervision is not permitted by the instrument software and as only one measurement was performed, averaging process are not relevant for this data type and the elevation data file is exported directly. In cases of unreliable data as judged by the internal instrument software or by the operator's clinical judgment, the data was discarded and new measurements were performed.

Surgical details

All surgeries were performed by the same ophthalmologist (Dr Eamonn O'Donoghue) and all biometry measurements were performed by the same clinician (Matthew Sheehan). Biometry data was collected prospectively; however the investigation did not interfere with Dr O'Donoghue's established routine pattern of surgery, choice of IOL design, choice of IOL power calculation formula, or IOL power selection. The surgery technique used a clear corneal incision 2.85 mm in size and one auxiliary manipulation port was also created. The incision location varied from subject to subject as determined by access considerations and the orientation of any significant (> 1 D) corneal astigmatism. The incision location data was recorded and is considered by the corneal shape data analysis. The auxiliary port was 0.5 mm in size, always orientated perpendicular to the main incision, and positioned at the limbus. Dr Eamonn O'Donoghue is left handed, although his position with respect to the eye undergoing surgery was adjusted such that the default orientation of the corneal incision was truly at the 12 o'clock meridian. The cataract was accessed through a continuous curvilinear capsulorhexis of typically 4.5 mm diameter created manually. Two different phacoemusification machines were used, an Infiniti (Alcon) and Premiere (Storz), as surgeries took place at two different hospitals. The IOLs were supplied unfolded and all IOLs were folded by Dr O'Donoghue immediately prior to implantation using the Akreos single use insertion device (AI-28 Bausch and Lomb). The implantation location for all IOLs was inside the capsular bag. In cases

without adequate capsular support, a Morcher tension ring was implanted and these exceptions are noted in the reported data. In some cases the corneal wound was secured with a suture; these cases are marked in the reported data and although excluded from analysis regarding corneal topography, they are still included in analysis regarding IOL axial depth. Topical anesthetic (Proxymetacaine hydrochloride 0.5%) was used during the surgery with ancillary anesthetic action from the viscoelastic material (Visthesia - Lidocaine hydrochloride 1% and Sodium hyaluronate 1%) and combination corticosteroid and dual antibiotics (Maxitrol - Polymyxin B sulphate, Neomycin sulphate, and Dextramethasone) with a dosage regime of four times per day for two weeks was used post-operatively.

Subject details

Table 2.6 presents a summary of the subject and biometry details of the experiment. Pre-surgery biometry measurements were performed on 221 enrolled subjects; however by the closure of the data collection period, only 137 subjects could be considered valid (both pre-surgery and post-surgery data collected), with the majority (79) of subjects excluded due to time constraints and a small number (5) excluded due to medical or clinical reasons. The age range of the valid subjects spans from 32 to 98 years, with a mean age of approximately 75 years. This late adult age is typical for cataract and combined with differences in life expectancy and utilization of health care services between the sexes, it is also typical to observe a higher proportion of female subjects (89 females, 48 males). This should not be interpreted as a difference in the incidence rate of cataract between the sexes. Of the 137 valid subjects, 24 subjects only contributed one valid eye to the study while 113 subjects contributed two valid eyes to the study, making a sample size of 250 valid eyes in total for the study. The total number of eyes in the control group (non-surgical) is about one quarter of the sample size of surgical eyes. Roughly 1/5 of subjects contributed one surgical eye, 2/5 of subjects contributed one surgical eye and one non-surgical eye, and 2/5 of subjects contributed two surgical eyes.

The mean healing period from the date of surgery to the date of post-operative examination was approximately 37 days. This review period of about a month was selected to allow sufficient time for healing and yet prevent loss of subjects to recall. All eyes in the study were quiet and settled at the post-surgery examination. Subjects were instructed to discontinued their anti-inflammatory and antibiotic eye drops 2 weeks after

the surgery, meaning that in vast majority of cases, the eye was also allowed a period of about 1 week to settle following the discontinuation of eye drops. All eyes included in the study were quite and calm at the post-operative examination with the implant position seeming quite stable.

For subjects in the lower quartile of the healing period, it is arguable that their relatively brief healing period may introduce uncertainty regarding stability of the IOL axial position, corneal topography and refractive outcome. These subjects perhaps should have been recalled to a later appointment date to repeat the post-operative examination. This concern may be heightened for subjects with systemic diseases known to reduce healing ability such as diabetes. In my opinion, the study included a representative percentage of patients with non insulin-dependent diabetes mellitus (NIDDM).

The subgroup of patients contributing 2 surgical eyes to the study allowed rudimentary analysis of this issue, as their first eye to undergo surgery was measured over 2 different healing intervals. Regarding stability of the IOL axial position, corneal topography and best sphere defocus refractive outcome, it seems that the mean review period was adequate but that the minimum review period may be associated with slight instability. As with any experiment of this nature, a compromise exists between what is ideal regarding data quality and what is practical in a clinical environment with real patients, many of whom are elderly.

In the lower aspect of Table 2.6 the relatively infrequent incidence of situations requiring a capsular tension ring (0.53%) or corneal suture (1.60%) are reported, by contrast the occurrence of failure of LCR measurement is much higher for both surgical (6.42%) and non-surgical (3.17%) subgroups. This failure due to a low SNR is a known issue for LCR and PCI technologies and becomes more prevalent with maturity/density of cataract. We feel the sample from this study represents current (2011) trends of a fairly typical cataract grade presenting to private ophthalmology clinics in Ireland. The asymmetry in the LCR failure rate between the surgical and non-surgical groups is an artifact owing to the reason that, all things being equal, an ophthalmologist will typically elect to perform cataract surgery on the most advanced cataract first, thus in many cases the less mature cataract in the fellow eye was allocated to the control group. As a side note, the suitability of PCI/LCR technology suffers another limitation when considering mobility issues in a cataract population (e.g. wheelchair-bound patients, etc). Our

study found that the failure rate of LCR increased to approximately 14% when mobility issues preventing measurement are included, further emphasizing the advantages of an ultrasonography instrument's portability.

The 6th division in Table 2.6 reports a summary count regarding pseudophakic LCR measurements. At the post-surgery examination, LCR measurement was successfully performed on all 187 surgical eyes; however, significant inter-subject variation exists regarding if the measurement could detect a signal from the IOL. The breakdown of numbers describes the count of eyes that in which no signal from the IOL was detected (10), a signal from one IOL surface was detected (138), and when a signal from both IOL surfaces was detected (39). This variation does not represent malfunction of the LCR instrument in any way; it simply illustrates the influence of inter-subject variation regarding *in situ* IOL alignment. In cases when no signal was detected, the pupil was dilated with 1% Tropicamide and the measurement was repeated - this occasionally resulted in an IOL signal being detected. The failure rate of pre-surgery LCR measurement in the presence of dense cataract, combined with the inconsistent ability of the LCR to detect the IOL position in the pseudophakic eye, means that analysis of the axial depth of the implanted IOL is restricted to a smaller sample size (165 surgical eyes) compared to the data set relating to the corneal topography (184 surgical eyes, 63 non-surgical eyes) topic.

At the post-surgery examination regarding the refraction measurement, autorefraction measurements were successfully performed on all valid eyes, however temperamental operation of the wavefront sensor, meant that in some instances reliable aberrometry could not be performed. The temperamental operation of the wavefront aberrometer can be attributed to the age of the personal computer controlling the instrument (approximately 10 years old) and should not be interpreted to describe the performance of the Zywave instrument in general. The refraction data therefore contains some redundancy, but at least as a minimum, the refractive state of each eye can be described in sphero-cylindrical terms. This aspect of the data is used in Chapter 3 to assess the performance of personalised eye modelling.

Subject and Biometry data summary			
no. subjects enrolled	221 (89 males, 132 females)		
no. subjects excluded due to medical or clinical reasons	5		
no. subjects excluded due to time constraints	79		
no. of valid subjects	137 (48 males, 89 females)		
age range (years)	32 to 98 (mean 74.8)		
no. of subjects contributing one surgical eye	24		
no. of subjects contributing one surgical eye and one non-surgical eye	63		
no. of subjects contributing two surgical eyes	50		
	OD	OS	BE
no. of excluded eyes (although fellow eye included)	12	12	24
no. eyes valid	125	125	250
no. of surgical eyes	88	99	187
no. of non-surgical (control) eyes	37	26	63
minimum healing period (days)	10	10	10
maximum healing period (days)	164	129	164
mean healing period (days)	34.7	39.8	37.3
no. surgical eyes requiring a capsular tension ring	1	0	1
no. surgical eyes requiring a corneal suture	2	1	3
no. surgical eyes LCR failed (requiring ultrasonography)	7	5	12
no. non-surgical control eyes LCR failed (requiring ultrasonography)	0	2	2
no. eyes with no signal pseudophakic LCR data	8	2	10
no. eyes with single signal pseudophakic LCR data	58	80	138
no. eyes with double signal pseudophakic LCR data	22	17	39
no. of surgical eyes with reliable autorefraction data	88	99	187
no. of surgical eyes with reliable abberrometry data	70	86	156
no. of surgical eyes with reliable autokeratometry data (ARK-510A)	79	84	163
no. of control eyes with reliable autokeratometry data (ARK-510A)	37	26	63
no. of surgical eyes with reliable autokeratometry data (Lenstar)	86	97	183
no. of control eyes with reliable autokeratometry data (Lenstar)	3	7	10
no. of surgical eyes with reliable corneal topography data (Atlas)	87	97	184
no. of control eyes with reliable corneal topography data (Atlas)	37	26	63

TABLE 2.6: Summary of subject and biometry details. OD is right eye, OS is left eye, BE is both eyes.

2.4 Analysis - Anterior corneal topography changes due to cataract surgery

To model the pseudophakic eye it is widely accepted that the effect of surgery on corneal shape should be considered. It is conceivable that the posterior corneal shape changes as a result of cataract surgery; however as the anterior surface contributes roughly 10 times more optical power, it is reasonable to limit consideration to the anterior cornea and approximate the posterior surface as unchanged. The effect of surgery is likely to depend on factors such as the length of the incision [194], the incision architecture [195], incision

orientation [196], incision proximity to the corneal centre and other factors influencing biomechanical properties such as corneal thickness [197] and age.

The main goal of this study was to analyze the effect of modern small-incision cataract surgery (specifically phacoemulsification with a 2.85 mm clear corneal incision) on corneal shape. During analysis, the pre-surgery and post-surgery corneal data was always paired with the same eye. Attention must be given to the eye under consideration (OD or OS) as this influences the coordinate system used for some descriptors, and also to the orientation of the incision, which influences the predicted change in corneal shape due to surgery.

A control non-surgical group was also analyzed with paired measurements of the same eye to gauge what variation could be expected in a repeated corneal shape measurement without intervening cataract surgery. As the control group eyes were either non-cataractous, or if cataractous they were generally less visually debilitating than for the fellow eye, this group likely had better fixation ability. Thus the reliability of the corneal topography alignment may have a biased advantage for this group.

Corneal shape data was recorded using 3 different instruments during the experiment; the Lenstar autokeratometry, the ARK-510A autokeratometry, and the Atlas corneal topography measurements. All three data sets were analyzed by comparing paired (post-surgery and pre-surgery) measurements of the same eye. The control subject group consists of non surgical eyes and these measurements are also paired across the same period of typically 3 weeks. The Atlas data set is considered superior to the autokeratometry due to its greater sampling density, measurement over a greater area, and the ability of the elevation data to represent shapes with greater detail than the sphero-cylindrical approximation used by the Lenstar and the ARK-510A instruments. Due to the differences in the exported data, the Lenstar and the Nidek data sets are analyzed using power vectors [198], whereas the Atlas elevation data set is analyzed by fitting the surface elevation with Zernike polynomials [149].

The use of power vectors is appropriate for the autokeratometry data sets because this data is already approximated to a sphero-cylindrical surface by the internal software of the instrument. Happily the power vector terms resemble the 2nd order Zernike polynomial terms and allow comparisons to be made with the Atlas data set through methods of least-squares fitting or paraxial curvature matching [199].

Zernike polynomials were selected for use to describe the Atlas elevation data file because they are well-known in the optic and ophthalmic industry, they offer a comparable description to power vectors (by the 2nd order terms or by paraxial curvature matching), and because they are suitable for use in defining the corneal surface in the Zemax raytracing software, which is the program selected for generating the personalised eye models. It is unclear if Zernike polynomials are the optimal set of basis functions for describing the corneal shape, especially regarding unusual corneas such as in keratoconus, post corneal refractive surgery or post penetrating keratoplasty, however, they are generally accepted as an appropriate first-choice in many applications [200]. The elevation data exported from the Atlas is fitted with Zernike polynomials (to 28 terms over a 6 mm diameter) in Matlab software using an ordinary least-squares method [201].

The autokeratometry data sets (Lenstar and ARK-510A) were analyzed by transforming the two principle radius of curvature values into power vectors M, J_{45} and J_{180}. A thorough description of power vectors and their potential use is given by Thibos *et al.* [198] and examples of their use in describing corneal shape is given by Barsky *et al.* [202] and Read *et al.* [203]. The equations required to transform the corneal shape descriptors from sphero-cylindrical form to power vectors are;

$$J_{45} = \frac{-C}{2} \, sin\, 2\theta \tag{2.8}$$

$$M = S + \frac{C}{2} \tag{2.9}$$

$$J_{180} = \frac{-C}{2} \, cos\, 2\theta \tag{2.10}$$

where corneal shape is represented in sphero-cylindrical form with a negative cylinder value. The sphero-cylinder format is $\pm\, sphere/-cylinder\,@\,meridian$ where S is sphere, C is cylinder, and θ is the meridian associated with the cylinder.

The principle radius of curvature values were first converted into a sphero-cylindrical format before being decomposed into power vectors according to Eqs. 2.8 to 2.10. The power vectors M, J_{45} and J_{180} are determined for the pre-surgery measurement and

the post-surgery measurement. The data is paired so that the pre-surgery power vector values are subtracted from the post-surgery values for each surgical eye to give the *difference* data set. The control group data set is also paired by subtracting the earlier measurement values from the later measurement values without any interceding surgery. The time between measurements of the control group is similar to that for the surgical group (typically 3 weeks).

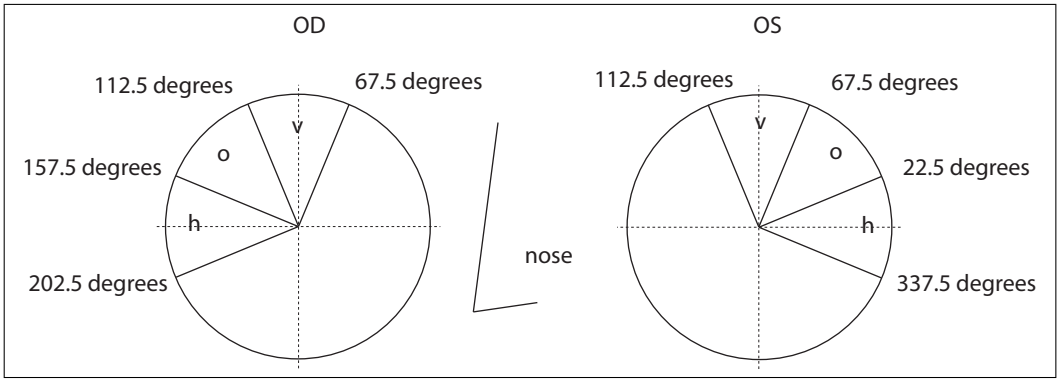

FIGURE 2.6: The coordinate system used to designate the orientation of the clear corneal incision into 3 subclasses of vertical (v), oblique (o) and horizontal (h).

Before further analysis, the *difference* data sets are grouped according to eye (left or right) and also according to the incision orientation. Three arbitrary subgroups are used to describe the incision orientation as vertical (between 67.5 degrees to 112.5 degrees), oblique (112.5 degrees to 157.5 degrees), or horizontal (157.5 degrees to 202.5 degrees) for the right eye as schematically displayed in Fig. 2.6. The incision subgrouping for the left eye uses a coordinate system with symmetry to the vertical axis as shown in Fig. 2.6. The subgrouping of left or right eye is relevant because the power vector J_{45} is not symmetric with the vertical axis, and therefore before pooling the left eye data with the right eye data, the J_{45} term is multiplied by -1. Accordingly, all results presented should be interpreted in regard to the right eye although the experiment was based on measurements of both eyes. Finally, a mean value for the *difference* data set is calculated for the 4 subgroups; vertical incision, oblique incision, horizontal incision, and control (non-surgical). The *mean difference* data set is then converted from power vectors M, J_{45} and J_{180} back into sphero-cylindrical format and principle radius of curvature values. This is done solely to describe the results in a format that clinicians are familiar with and requires the use of a reference cornea - arbitrarily modelled as a spherical surface with a 7.70 mm radius of curvature. The equations required to transform the power vectors into a sphero-cylindrical format are;

$$C = -2\sqrt{J_{45}^2 + J_{180}^2} \tag{2.11}$$

$$S = M - \frac{C}{2} \tag{2.12}$$

$$\theta = \frac{arctan\,(J_{45}/J_{180})}{2} \tag{2.13}$$

with the following logical tests applied to Eq. 2.13

$$\begin{array}{llllll}
\text{If } J_{180} < 0, & & & \text{then} & \text{meridian} = \theta + 90 \text{ degrees} \\
\text{If } J_{180} = 0, & \text{and} & \text{if } J_{45} < 0, & \text{then} & \text{meridian} = 135 \text{ degrees} \\
\text{If } J_{180} = 0, & \text{and} & \text{if } J_{45} > 0, & \text{then} & \text{meridian} = 45 \text{ degrees} \\
\text{If } J_{180} > 0, & \text{and} & \text{if } J_{45} \leq 0, & \text{then} & \text{meridian} = \theta + 180 \text{ degrees} \\
\text{If } J_{180} > 0, & \text{and} & \text{if } J_{45} > 0, & \text{then} & \text{meridian} = \theta
\end{array} \tag{2.14}$$

The raw autokeratometry data exported from both the Lenstar and the ARK-510A consists of the two principal radius of curvature values with units of millimeters and reported with a precision of 2 decimal places. The Lenstar data is an average value of 5 measurements and the ARK-510A data set is an average value of 3 measurements. Because the radius of curvature values were exported (as opposed to dioptric power), the potential for ambiguity regarding the value used for effective refractive index for the cornea by the instrument is avoided.

To analyse the Atlas elevation data it was fitted with Zernike polynomials. The Matlab code written for this operation was verified by comparison and agreement with Matlab code independently written by a colleague (Tim de Jong). The Matlab code was also verified by 2 other methods as below.

Firstly, the Zernike coefficients fitted by the Matlab code were compared to the Zernike coefficients fitted by the internal software of the Atlas instrument and displayed on screen. After accounting for the different nomenclature of the two systems (e.g. single index vs double index), perfect agreement (100%) is observed for up to 36 coefficients

(7th order) fitted over a 10 mm diameter. The Atlas software only displays the fitted Zernike coefficient to a precision of 1 μm, and therefore most coefficients have a value of zero that is not helpful when attempting to make a rigorous comparison. Because the Atlas-fitted coefficients are not exportable (except as a screen capture), the data must be manually transcribed (an onerous task) and thus the case study was limited to only a few eyes. Of the eyes that were investigated; glass hemispheres of known radius of curvature (r = 6.15 mm, r = 8.00 mm and r = 9.65 mm), and both OD and OS of subject 1002, all cases demonstrated 100% agreement.

As a second anecdotal verification, Atlas corneal topography measurements were performed on glass hemispheres of known radius of curvature (r = 6.15 mm, r = 8.00 mm and r = 9.65 mm) and the .DAT file generated by the Matlab function was imported to Zemax and used to define a Zernike sag surface. When spherical surfaces of r = 6.15 mm, r = 8.00 mm and r = 9.65 mm are overlaid using the Zemax lens editor, excellent agreement is observed between all three paired surfaces over a 8 mm diameter. This step verifies the generation of the .DAT file in addition to the Zernike polynomial fitting.

When fitting a surface with Zernike polynomials it is arguable how many terms should be used, and to what diameter the fitting should be applied. For artificial 'cornea' test surfaces, the use of a large fitting diameter (e.g. 8 mm) is reasonable because generally a full complement of data exists. However, for real eyes, the choice of a more conservative fitting diameter is more appropriate. The superior aspect of corneal topography data is often very restricted by ptosis of the upper lid, especially in subjects of the typical cataract age group.

To select an appropriate fitting diameter, a typical elevation data file was fitted using each combination of diameter (10 mm, 8 mm, 6 mm) and fitting order (28 terms, 36 terms, 45 terms, 55 terms, 66 terms). As the Zernike polynomials are orthogonal (at least in the continuous domain), the fitting order should have no effect on the coefficient value. However, it was observed that when the fitting diameter was large (10 mm and 8 mm) significant variation was observed in the value of a coefficient (e.g. 26.8% variation in the Z4 defocus coefficient) as the fitting order was varied from 28 terms to 66 terms.

Fitting over large diameters (> 6 mm) for the typical Atlas elevation file of a cataract patient displayed unstable coefficient values. As the fitting order changed, the value of an individual coefficient fluctuated highly. We postulate that this is due to an extrapolation

problem as few data points exist beyond the 6 mm diameter, especially in the superior region. Combined with the fact that the fitting operation is an over-determined problem and no unique solution exists. By selecting a more conservative diameter over which to fit the Zernike polynomials, the coefficients become much more stable with respect to fitting order. That is - the coefficients start to show orthogonality. Note that this stabilization is not just an absolute decrease in noise (as commensurate with a smaller fitting diameter), it is a relative (percentage) decrease in instability. Compare the 26.8% variation in the Z4 defocus coefficient as the fitting order was varied from 28 terms to 66 terms for a 10 mm diameter to a variation less than 0.3% for a 6 mm diameter.

As this experiment concerned eyes without corneal disease and with no history of previous ocular surgery, it is unsurprising that the corneal topography data showed negligible structure above 28 Zernike terms (6th order). After preliminary investigations of fitting with a higher number of terms (36, 45, 55, and 66), it was decided to fit the corneal topography data to 28 terms. To select the optimal fitting order, it is possible to perform an F-test [204] on each elevation file. Although we selected to fit corneal topography with 28 terms, a greater number of terms may be necessary if considering patients with unusual corneal shape such as those who have previously undergone refractive surgery.

For the reasons discussed above, the Atlas elevation data set was fitted with Zernike polynomials over a 6 mm diameter using 28 terms (6th order). The Matlab code developed during this work starts by importing and reading the Atlas elevation file (.CSV file). The elevation data is fitted with Zernike polynomials using an ordinary least-squares method. The Matlab function then outputs the Zernike coefficients for analysis (.CSV file) and it also creates a data file (.DAT file) suitable for creating a Zernike sag surface in the Zemax ray-tracing program. These .DAT files are imported into Zemax when creating personalised pseudophakic eye models (see Ch. 3) to define the anterior corneal surface, after first applying the predicted influence of the cataract surgery. This predicted effect on corneal shape is largely taken from the results of Table 2.12.

In ophthalmic and vision science fields, double-indexed Zernike polynomials have been recommended for use in describing aberrations as defined in standards [39, 40] and previously described in Section 1.6. In this work the corneal topography elevation data file is fitted with Zernike polynomials, however we have elected to use the format described by Noll [149] as this is the format necessary for creating a Zernike sag surface in the

Zemax ray-tracing program. Noll's format differs from the standards [39, 40] regarding the sign for z axis and regarding the listing order (indexing) of the Zernike polynomials. In the coordinate system of this work, the positive z represents *away* from the observer. For example, the defocus term fitted to the corneal topography is positive, and a positive *differential* value represents steepening of the cornea. Noll's format defines the angle theta (θ) counterclockwise from the positive x axis. Table 2.7 defines the Zernike polynomials in polar coordinates using Noll's format. Before pooling data from left and right eyes, it is necessary to convert any Zernike function that lacks symmetry with the vertical axis. These functions are marked with an asterisk (*) in Table 2.7 and the corresponding coefficients for all left eyes were multiplied by -1 to change the sign of the left eye data set before pooling it with the right eye data set. Accordingly, all results presented should be interpreted in regard to the right eye although the experiment was based on measurements of both eyes.

Zernike Polynomials (Noll's format)			
Z	Order	Polynomial	OD/OS
$Z1$	0	1	
$Z2$	1	$2\rho\cos\theta$	*
$Z3$	1	$2\rho\sin\theta$	
$Z4$	2	$\sqrt{3}(2\rho^2-1)$	
$Z5$	2	$\sqrt{6}\rho^2\sin 2\theta$	*
$Z6$	2	$\sqrt{6}\rho^2\cos 2\theta$	
$Z7$	3	$\sqrt{8}(3\rho^3-2\rho)\sin\theta$	
$Z8$	3	$\sqrt{8}(3\rho^3-2\rho)\cos\theta$	*
$Z9$	3	$\sqrt{8}\rho^3\sin 3\theta$	
$Z10$	3	$\sqrt{8}\rho^3\cos 3\theta$	*
$Z11$	4	$\sqrt{5}(6\rho^4-6\rho^2+1)$	
$Z12$	4	$\sqrt{10}(4\rho^4-3\rho^2)\cos 2\theta$	
$Z13$	4	$\sqrt{10}(4\rho^4-3\rho^2)\sin 2\theta$	*
$Z14$	4	$\sqrt{10}\rho^4\cos 4\theta$	
$Z15$	4	$\sqrt{10}\rho^4\sin 4\theta$	*
$Z16$	5	$\sqrt{12}(10\rho^5-12\rho^3+3\rho)\cos\theta$	*
$Z17$	5	$\sqrt{12}(10\rho^5-12\rho^3+3\rho)\sin\theta$	
$Z18$	5	$\sqrt{12}(5\rho^5-4\rho^3)\cos 3\theta$	*
$Z19$	5	$\sqrt{12}(5\rho^5-4\rho^3)\sin 3\theta$	
$Z20$	5	$\sqrt{12}\rho^5\cos 5\theta$	*
$Z21$	5	$\sqrt{12}\rho^5\sin 5\theta$	

TABLE 2.7: List of Zernike polynomials in Noll's right-handed polar coordinate system. Functions lacking symmetry to the vertical axis requiring conversion from OS to OD before pooling data are marked with an asterisk(*).

To convert the Zernike coefficients into an equivalent curvature metric, it is possible to use either a least-squares fitting or a paraxial curvature matching method (approximated by some finite number of terms) as described by Thibos *et al.* [199]. Preliminary results suggested that, for this particular application, the least-squares fitting method was more reliable than the curvature-matching method due to noisy higher-order terms in the dataset and so the former was used. The equations necessary to convert the Zernike coefficients using curvature matching (abbreviated to the first 28 Zernike terms) are given in Eqs. 2.15 to 2.17. To employ the least-squares fitting method, the same expressions (Eqs. 2.15 to 2.17) are used, except that the numerator in each expression is truncated to the first term.

$$M = \frac{-c_4 4\sqrt{3} + c_{11} 12\sqrt{5} - c_{22} 24\sqrt{7}}{r^2} \tag{2.15}$$

$$J_{45} = \frac{-c_5 2\sqrt{6} + c_{13} 6\sqrt{10} - c_{23} 12\sqrt{14}}{r^2} \tag{2.16}$$

$$J_{180} = \frac{-c_6 2\sqrt{6} + c_{12} 6\sqrt{10} - c_{24} 12\sqrt{14}}{r^2} \tag{2.17}$$

By using Eqs. 2.15 to 2.17 and 2.11 to 2.14, the Zernike polynomials fitted to the corneal topography data can be represented in power vector and also sphero-cylindrical notation. Attention must be given to the units at each conversion stage as the terms M, J_{45} and J_{180} in Eqs. 2.15 to 2.17 are curvature values with units of meters^{-1} and to convert differential curvature values to differential radius of curvature values it is necessary to use a nominal radius of curvature value (7.70 mm) as demonstrated in Eq. 2.18. Also note that the meaning of the sign changes when converting units from curvature to radius of curvature. A positive value for ΔC for the power vector M represents steepening, while a negative value for Δr for the power vector M represents steepening.

$$\Delta r = \frac{1}{\Delta C + \dfrac{1}{0.0077}} - 0.0077 \tag{2.18}$$

where ΔC is the differential curvature value (in terms of M, J_{45} and J_{180}) and Δr is the differential radius of curvature value (in terms of M, J_{45} and J_{180}).

The mean change in coefficient results presented in Table 2.12 are converted into power vectors for three different parameters (curvature, radius of curvature, nominal power) in Table 2.13. These results are then re-expressed in Table 2.14 as nominal post-surgery values of radius of curvature, principle power, and change in refractive error in sphero-cylinder format because this more readily interpreted by clinicians.

2.5 Results - Anterior corneal topography changes due to cataract surgery

Mean paired difference in anterior corneal shape - Lenstar autokeratometry data					
Incision	Mean difference	M	J_{45}	J_{180}	sphero/cylinder @ meridian
vertical	radius of curvature (mm)	0.0013	0.0041	0.0275	+0.0292 / -0.0557 @ 4.20
($n = 115$)	nominal power (D)	-0.008	-0.023	-0.156	
oblique	radius of curvature (mm)	0.0048	0.0208	-0.0041	+0.0260 / -0.0425 @ 50.54
($n = 25$)	nominal power (D)	-0.027	-0.118	0.023	
horizontal	radius of curvature (mm)	-0.0092	-0.0088	-0.0348	+0.0267 / -0.0717 @ 97.07
($n = 43$)	nominal power (D)	0.052	0.050	0.199	
control	radius of curvature (mm)	0.0120	0.0116	0.0160	+0.0317 / -0.0395 @ 17.94
($n = 10$)	nominal power (D)	-0.068	-0.066	-0.091	

TABLE 2.8: Mean change in Lenstar autokeratometry data for 3 surgical subgroups based on incision orientation and 1 control (non-surgical) subgroup. Calculation of dioptric power requires the assumption of a nominal spherical cornea (radius of curvature 7.70 mm) and an effective refractive index of 1.3375. Results from both eyes are pooled using a right eye format.

In Tables 2.8 to 2.11 for both sets of autokeratometry data (Lenstar and ARK510-A) and in Tables 2.12 to 2.14 for the topography (Atlas) data, the control group displays the smallest amount of corneal shape change as expected. It was anticipated that the greatest shape change would occur in either the oblique of the horizontal incision subgroups, which is also observed. It is known that all eyes in these subgroups possessed significant corneal astigmatism and that the surgeon was attempting to induce compensatory astigmatism with the incision in all eyes of these subgroups. By contrast, the vertical incision orientation is the surgeon's default preference, so it is known that this subgroup includes eyes in which the surgeon intended to induce *no* topography change, as well as eyes in which the surgeon *did* intend to induce a topography change.

The results from all 3 instruments are in good agreement. The topography (Atlas) data set might be expected to be more sensitive to the change in corneal shape because the

Nominal anterior corneal shape and induced refractive error - Lenstar autokeratometry data		
Incision	Parameter	Nominal post-surgery values
vertical	radius of curvature (mm)	7.7292 / 7.6735 @ 4.20
($n = 115$)	principal powers (D)	43.666 / 43.983 @ 4.20
	refractive error change (D)	+0.151 / -0.317 x 94.20
oblique	radius of curvature (mm)	7.7260 / 7.6836 @ 50.54
($n = 25$)	principal powers (D)	43.683 / 43.925 @ 50.54
	refractive error change (D)	+0.094 / -0.242 x 140.54
horizontal	radius of curvature (mm)	7.7267 / 7.6550 @ 97.07
($n = 43$)	principal powers (D)	43.680 / 44.089 @ 97.07
	refractive error change (D)	+0.258 / -0.409 x 7.07
control	radius of curvature (mm)	7.7317 / 7.6923 @ 17.94
($n = 10$)	principal powers (D)	43.651 / 43.875 @ 17.94
	refractive error change (D)	+0.044 / -0.224 x 107.94

TABLE 2.9: Nominal post-surgery anterior corneal shape using Lenstar autokeratometry data. Calculations assume a pre-surgery spherical cornea (radius of curvature 7.70 mm $\sim$ 43.83 D) and an effective refractive index of 1.3375. Refractive error values are relative to the *corneal* plane rather than the *spectacle* plane. Results from both eyes are pooled using a right eye format.

Mean paired difference in anterior corneal shape - ARK 510A autokeratometry data					
Incision	Mean difference	M	J_{45}	J_{180}	sphero/cylinder @ meridian
vertical	radius of curvature (mm)	0.0033	0.0039	0.0146	+0.0184 / -0.0303 @ 7.43
($n = 96$)	nominal power (D)	-0.019	-0.022	-0.083	
oblique	radius of curvature (mm)	-0.0013	0.0307	-0.0027	+0.0294 / -0.0616 @ 47.56
($n = 26$)	nominal power (D)	0.008	-0.174	0.016	
horizontal	radius of curvature (mm)	0.0006	-0.0090	-0.0270	+0.0291 / -0.0569 @ 99.22
($n = 41$)	nominal power (D)	-0.003	0.051	0.154	
control	radius of curvature (mm)	-0.0076	-0.0055	-0.0066	+0.0010 / -0.0172 @ 109.92
($n = 63$)	nominal power (D)	0.043	0.031	0.038	

TABLE 2.10: Mean change in ARK 510A autokeratometry data for 3 surgical sub-groups based on incision orientation and 1 control (non-surgical) subgroup. Calculation of dioptric power requires the assumption of a nominal spherical cornea (radius of curvature 7.70 mm) and an effective refractive index of 1.3375. Results from both eyes are pooled using a right eye format.

fitting diameter (6 mm) is much larger and proximal to the incision compared to the central 3 mm measurement zone used in autokeratometry. The control group provides a measure of naturally occurring variation due to repeated measurement over a similar time period as the surgical eye and provides a similar match for subject age and gender as these eyes come from the same primary patient group. The meridian of astigmatic flattening closely aligns with the orientation of the incision for all 3 surgical sub-groups and all 3 instrument data sets. The meridian of astigmatic flattening in the control group appears randomly orientated, as expected. In agreement with the literature [195,

Nominal anterior corneal shape and induced refractive error - ARK 510A autokeratometry data		
Incision	Parameter	Nominal post-surgery values
vertical ($n = 96$)	radius of curvature (mm)	7.7184 / 7.6881 @ 7.43
	principal powers (D)	43.726 / 43.899 @ 7.43
	refractive error change (D)	+0.068 / -0.172 x 97.43
oblique ($n = 26$)	radius of curvature (mm)	7.7294 / 7.6679 @ 47.56
	principal powers (D)	43.664 / 44.015 @ 47.56
	refractive error change (D)	+0.184 / -0.351 x 137.56
horizontal ($n = 41$)	radius of curvature (mm)	7.7291 / 7.6722 @ 99.22
	principal powers (D)	43.666 / 43.990 @ 99.22
	refractive error change (D)	+0.159 / -0.324 x 9.22
control ($n = 63$)	radius of curvature (mm)	7.7010 / 7.6838 @ 109.92
	principal powers (D)	43.825 / 43.923 @ 109.92
	refractive error change (D)	+0.092 / -0.098 x 19.92

TABLE 2.11: Nominal post-surgery anterior corneal shape using ARK 510A autokeratometry data. Calculations assume a pre-surgery spherical cornea (radius of curvature 7.70 mm $\sim$ 43.83 D) and an effective refractive index of 1.3375. Refractive error values are relative to the *corneal* plane rather than the *spectacle* plane. Results from both eyes are pooled using a right eye format.

Atlas data - mean difference in Zernike coefficient (μm) for 6 mm diameter.										
Incision	Z2	Z3	Z4	Z5	Z6	Z7	Z8	Z9	Z10	Z11
vertical ($n = 112$)	-0.119	-0.034	-0.169	0.121	0.908	0.000	-0.012	0.472	-0.072	-0.018
oblique ($n = 20$)	-0.310	0.264	0.092	0.818	-0.097	0.088	-0.073	-0.252	-0.046	-0.023
horizontal ($n = 40$)	0.305	-0.249	0.607	-0.258	-1.092	-0.029	0.089	0.027	0.447	0.042
control ($n = 63$)	-0.103	0.010	0.006	-0.067	0.010	-0.006	-0.042	0.031	0.084	-0.010

TABLE 2.12: Mean change in Atlas corneal topography data fitted with Zernike polynomials (fitted to 28 terms, 6 mm diameter) for 3 surgical subgroups based on incision orientation and 1 control (non-surgical) subgroup. Results from both eyes are pooled using a right eye format.

196, 205, 206, 207, 208, 209, 210, 211], the results of all 3 instruments suggest that the incision orientation should be recommended along the steepest corneal meridian as the incision will induce flattening along this meridian.

Table 2.12 displays the mean difference in the fitted Zernike coefficients. This is the most important set of results in this section as these mean difference values are used in Chapter 3 to predict each individual eye's post-surgery anterior corneal shape from their pre-surgery topography measurement. For the sake of being concise, Table 2.12 only reports the mean coefficient difference for the 1st to 3rd order terms plus the spherical-like aberration term ($Z11$). It is important not to exclude the 1st order terms from analysis ($Z2$ and $Z3$) as is often done when analyzing wavefront data. As we are

Mean paired difference in anterior corneal shape - Atlas corneal topography data (6 mm diameter)					
Incision	Mean difference	M	J_{45}	J_{180}	sphero/cylinder@meridian
vertical	curvature (m^{-1})	0.1300	-0.0660	-0.4942	
($n = 112$)	radius of curvature (mm)	-0.0077	0.0039	0.0294	0.0220 / -0.0594 @ 3.79
	power (D)	0.044	-0.022	-0.167	
oblique	curvature (m^{-1})	-0.0708	-0.4452	0.0528	
($n = 20$)	radius of curvature (mm)	0.0042	0.0265	-0.0031	0.0309 / -0.0533 @ 48.37
	power (D)	-0.024	-0.150	0.018	
horizontal	curvature (m^{-1})	-0.4671	0.1404	0.5943	
($n = 40$)	radius of curvature (mm)	0.0278	-0.0083	-0.0351	0.0638 / -0.0721 @ 96.67
	power (D)	-0.158	0.047	0.201	
control	curvature (m^{-1})	-0.0047	0.0365	-0.0056	
($n = 63$)	radius of curvature (mm)	0.0003	-0.0022	0.0003	0.0025 / -0.0044 @ 139.37
	power (D)	-0.002	0.012	-0.002	

TABLE 2.13: Mean change in Atlas corneal topography data for 3 surgical subgroups based on incision orientation and 1 control (non-surgical) subgroup. The radius of curvature and power parameters represent nominal values, their calculation requires the assumption of a pre-surgery spherical cornea (radius of curvature 7.70 mm) and an effective refractive index of 1.3375. Results from both eyes are pooled using a right eye format.

Nominal anterior corneal shape and induced refractive error - Atlas corneal topography data (6 mm diameter)		
Incision	Parameter	Nominal post-surgery values
vertical	radius of curvature (mm)	7.7220 / 7.6626 @ 3.79
($n = 112$)	principal powers (D)	43.706 / 44.045 @ 3.79
	refractive error change	+0.214 / -0.339 x 93.79
oblique	radius of curvature (mm)	7.7309 / 7.6775 @ 48.37
($n = 20$)	principal powers (D)	43.656 / 43.959 @ 48.37
	refractive error change	+0.128 / -0.303 x 138.37
horizontal	radius of curvature (mm)	7.7638 / 7.6917 @ 96.67
($n = 40$)	principal powers (D)	43.471 / 43.878 @ 96.67
	refractive error change	+0.047 / -0.407 x 6.67
control	radius of curvature (mm)	7.7025 / 7.6981 @ 139.37
($n = 63$)	principal powers (D)	43.817 / 43.842 @ 139.37
	refractive error change	+0.011 / -0.025 x 49.37

TABLE 2.14: Nominal post-surgery anterior corneal shape using Atlas corneal topography data. Calculations assume a pre-surgery spherical cornea (radius of curvature 7.70 mm $\sim$ 43.83 D) and an effective refractive index of 1.3375. Refractive error values are relative to the *corneal* plane rather than the *spectacle* plane. Results from both eyes are pooled using a right eye format.

dealing with corneal elevation data, the 1st order terms do **not** simply represent image translation in the xy plane as they do regarding wavefront analysis. Not withstanding, variation in $Z2$ and $Z3$ can be attributed to variation in subject fixation associated with the reduced acuity of cataractous subjects. Without any definitive pattern of change consistent with the incision orientation, and given that the magnitude of change is approximately less than 3 times that of the control group, the change observed in the $Z2$ and $Z3$ terms should be to attributed to fixation variation.

Table 2.12 illustrates the superior detail achieved by describing the corneal shape change with topography data compared to autokeratometry data. Several terms beyond from the 2nd order show significant magnitude of change. For the 3rd-order terms, the change in the trefoil terms ($Z9$ and $Z10$) seems more dominant than that of the coma terms ($Z7$ and $Z8$). The angular frequency of the trefoil terms (3) makes them good candidates to display effects from the main surgical incision. To explain this finding, we argue that the effect of the incision is localised to some degree and its influence decreases with distance from the incision site. Due to the position of the upper lid in an aged subject, the 6 mm fitting diameter is more likely to mask the superior region such that each topography measurement includes more data points located along the horizontal mid-band compared to the superior region. This may make the coma terms, with an angular frequency of 1, more susceptible to a *masking* effect compared to the trefoil terms, with an angular frequency of 3. Topography data sets that contain more data sampling points located along the horizontal region compared to the vertical region may make accurate measurement of vertical coma ($Z7$) particularly difficult. Another possibility is that a comatic topography change is simply not induced by the cataract surgery. The change in the coma terms ($Z7$ and $Z8$) are relatively small in all incision subgroups, with the magnitude of change is approximately less than twice that of the control group.

It is sensible to analyze the change in the defocus term ($Z4$) and the spherical-like term ($Z11$) together. These functions are rotationally symmetric and theoretically these functions should be independent of incision orientation. Therefore, the pattern displayed by the incision subgroups for these terms is not intuitively understood. The horizontal subgroup shows a *steepening* of the $Z4$ and $Z11$ terms (positive change in coefficient value). Meanwhile the vertical and oblique incision subgroup show much reduced magnitude of change and indeed the vertical subgroup has a negative coefficient sign showing a *flattening* of these terms. Slight differences in the subgroups incision proximity rather

than incision orientation may perhaps be responsible for these results. As previously described, the horizontal and oblique subgroups contain only patients in whom the surgeon intended to induce a topography change, whereas the vertical subgroup being the default preference of the surgeon, contains a percentage of patients in whom the surgeon intended to induce no topography change. It is possible that, on average, the clear corneal incision is more proximal to the corneal centre in the horizontal and oblique subgroups than in the vertical subgroup. Over a 6 mm fitting diameter this may tenuously explain the small amount of flattening observed in the vertical subgroup and the greater amount of steepening observed in the horizontal subgroup.

Summary

The corneal shape change measured by the 3 different instruments all display the same general pattern regarding the change in 2nd order astigmatism terms. The combined typical results of all 3 instruments is reported below relevant to the surgically induced change in radius of curvature as described by power vectors for the right eye.

- vertical incision $\Delta J_{180} \approx +0.024$ mm
- oblique incision $\Delta J_{45} \approx +0.026$ mm
- horizontal incision $\Delta J_{180} \approx -0.032$ mm
- control no incision $\Delta J_{45} \approx +0.001$ mm and $\Delta J_{180} \approx +0.003$ mm

To interpret the corneal shape data in Tables 2.8, 2.10, and 2.13, some examples are provided below, relating to radius of curvature as described by power vectors for the right eye.

- ΔM positive value describes flattening.
- ΔM negative value describes steepening.
- ΔJ_{45} positive value describes steepening @ 45 meridian, flattening @ 135 meridian.
- ΔJ_{45} negative value describes steepening @ 135 meridian, flattening @ 45 meridian.
- ΔJ_{180} positive value describes steepening @ 180 meridian, flattening @ 90 meridian.

- ΔJ_{180} negative value describes steepening @ 90 meridian, flattening @ 180 meridian.

The corneal shape change as measured by the Atlas corneal topographer and fitted with Zernike polynomials (28 terms, 6 mm diameter) using Noll's notation [149] follows a general pattern as reported below relevant to change in Zernike coefficient for the right eye.

- vertical incision ΔZ6 $\approx +0.94\,\mu$m and ΔZ9 $\approx +0.46\,\mu$m
- oblique incision ΔZ5 $\approx +0.94\,\mu$m and ΔZ9 $\approx -0.15\,\mu$m and ΔZ10 $\approx -0.15\,\mu$m
- horizontal incision ΔZ6 $\approx -0.94\,\mu$m and ΔZ10 $\approx +0.46\,\mu$m
- control no incision ΔZ5,ΔZ6 $\approx +0.04\,\mu m$, ΔZ9,ΔZ10 $\approx +0.06\,\mu$m

A significant change in the defocus coefficient ($Z4$) for the horizontal subgroup was found, but this pattern was not present in other subgroups and at the moment we can not interpret this finding to our satisfaction or explain why this should occur. As such, this finding should not be considered representative of cataract surgery until it is investigated further. Age related influences were not investigated in this study and this is another suggested area for continuing research.

One of the features of modern small incision clear corneal incision cataract surgery is it's reduced influence on corneal topography. However, the surgery's effect is non-negligible, as evidenced by the changes in refractive error of a typical eye reported in Tables 2.9, 2.11 and 2.14, in consideration that refractive error is clinically measured with a precision of 0.25 D. For an experienced surgeon using a 2.85 mm clear corneal incision, the surgically induced anterior corneal topography change is significantly greater than the repeatability level of instruments measuring corneal shape, as evidenced by comparison against the control subgroup reported in Tables 2.9, 2.11 and 2.14). The results of this study are used in Chapter 3 when generating the personalized pseudophakic eye models from pre-surgery biometry data. The predicted shape change is applied to the pre-surgery corneal topography data before being imported into the ray-tracing software.

2.6 Analysis - The axial depth of the intraocular lens *in situ*

To model the required IOL power using ray-tracing it is critical to predict accurately the geometrical position of the IOL following healing and stabilization, which has a dominant influence on defocus and retinal image quality. This prediction of the axial depth of the IOL was one of the main goals of the experiment; we wanted to find the optimal model using pre-surgery parameters for predicting the position of the IOL. Subjects that could not be reliably measured by the low coherence reflectometry (LCR) technique at both pre-surgery and post-surgery examinations were excluded from analysis. All data analysis was performed using paired pre-surgery and post-surgery measurements of the same eye. There is no control group relevant to this aspect of the study.

Performing an LCR measurement on a pseudophakic eye can have one of three different possible outcomes regarding IOL detection; no surfaces detected, one surface detected, or both surfaces detected. If no surfaces were detected, the eye was excluded from the study. If both surfaces were detected, the eye was included in the study. If only one surface was detected, the eye was included in the study, but two issues must first be resolved: which surface is responsible for creating the observed signal? and what value should be used to approximate the central thickness of the IOL?

Figure 2.7 shows an example of the LCR data for the pre-surgery cataractous and post-surgery pseudophakic conditions. To determine if a *single* signal belongs to the anterior or posterior surface of the IOL, the growth in the ACD was calculated for each possibility. The growth in the ACD is calculated by subtracting the post-surgery axial distance separating the posterior corneal surface and the 'anterior' IOL surface from the pre-surgery axial distance separating the posterior corneal surface and the anterior cataractous lens surface. The values for each possibility (designating the signal's origin as the anterior IOL surface or the posterior surface) are then plotted against the cataractous lens thickness; as it is reasonable to assume that the growth in ACD should be related to cataractous lens thickness by some degree. Figure 2.8 shows a plot of growth in ACD verses cataract thickness for the three data series, dual signal (green squares), single signal designated as originating from the posterior IOL surface (orange circles), and single signal designated as originating from the anterior IOL surface (red triangles). By

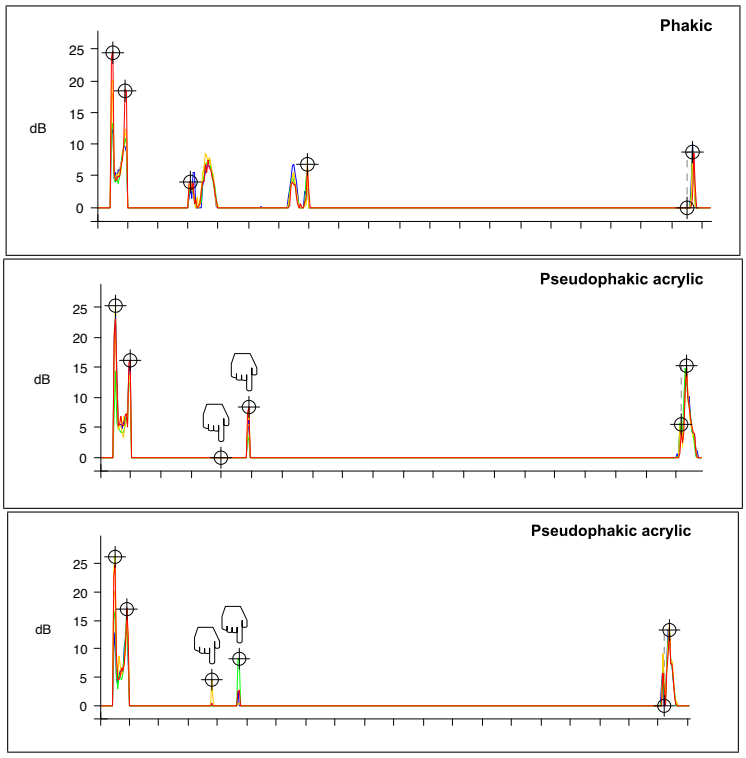

FIGURE 2.7: Three examples of the graphical display of segmented axial length data of the Lenstar. The top image is of a cataractous eye. The middle image is of a pseudophakic eye with a single IOL signal. The bottom image is of a pseudophakic eye with dual IOL signal.

also displaying results from the *dual* signal measurements on the same plot, an obvious trend is observed and for all *single* signal measurements and it can be confidently argued the signal belongs to the posterior IOL surface. Following this analysis, the *single* signal measurements are modified using the Lenstar software that allows a graphical user-designation of the ocular surfaces. Each measurement is modified by manually assigning the *single* signal to the posterior IOL surface and to position the marker for the anterior IOL surface at a distance equal to the central thickness value obtained by evaluating either Eq. 2.2 or 2.5 as appropriate (as the implanted IOL power is known).

After modifying the LCR data to account for *single* signal measurements, the pre-surgery biometry data was analyzed to the investigate possible methods of predicting the post-surgery geometric axial position of the IOL. Only the pre-surgery biometry data of the Lenstar instrument is used (no biometry data from the ARK-510A or the Atlas instruments are used). The parameters investigated by this study are; the central corneal thickness, the anterior chamber depth, the cataractous lens thickness, the axial length of the eye, the corneal principal radius of curvature values, and the white to white horizontal distance. The possible relationship between these parameters and the observed

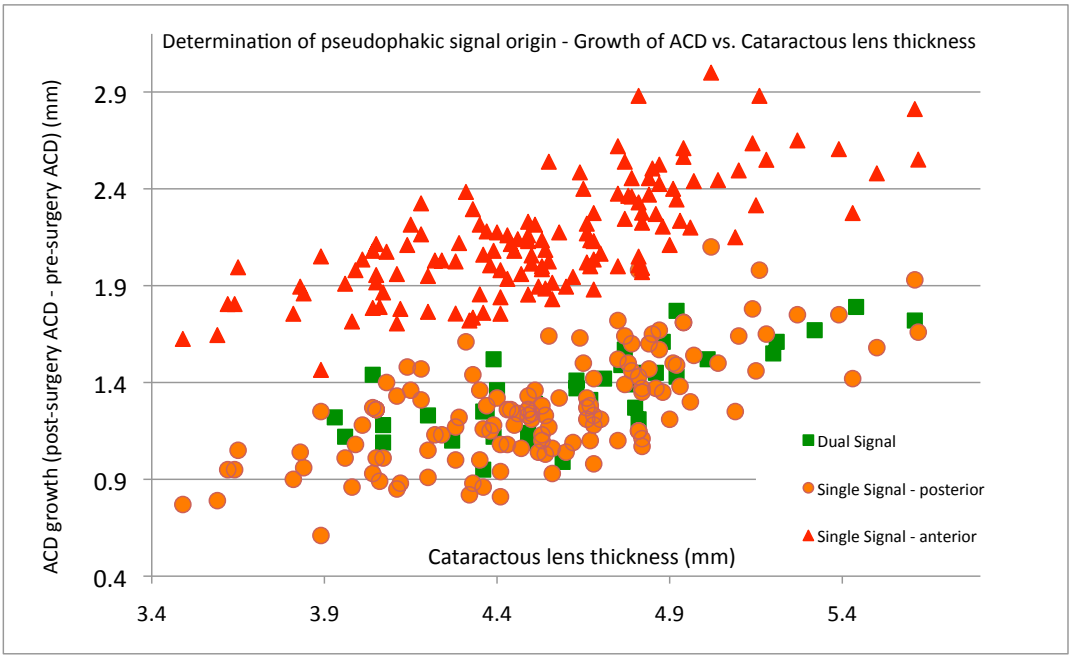

FIGURE 2.8: A plot of growth in ACD verses cataractous lens thickness for three data series, dual pseudophakic signal (green squares), single pseudophakic signal designated as originating from the posterior IOL surface (orange circles) and single pseudophakic signal designated as originating from the anterior IOL surface (red triangles).

axial depth of the IOL were investigated using multiple linear regression methods. To decrease bias in the IOL position owing to the IOL shape and thickness itself, the IOL position was calculated as the geometrical midpoint of its two surfaces, i.e. the IOL depth is described as the axial distance between the posterior cornea and the point midway between the anterior and posterior IOL surfaces. This reference plane at the midpoint between the IOL surfaces should improve the consistency of the axial depth prediction across the IOL dioptric range.

Initial modelling

Before describing the various models investigated, it is appropriate to examine a plot of the change in IOL depth (relative to the mean IOL depth) verses the normalized change in each biometry parameter (relative to the mean parameter value). These plots are shown in Figs. 2.9 to 2.14 and illustrate the generally noisy and indistinct relationship between each parameter and the IOL depth. In fact, the only parameter that displays an obvious and strong relationship with the IOL depth is the anterior chamber depth (Fig. 2.10).

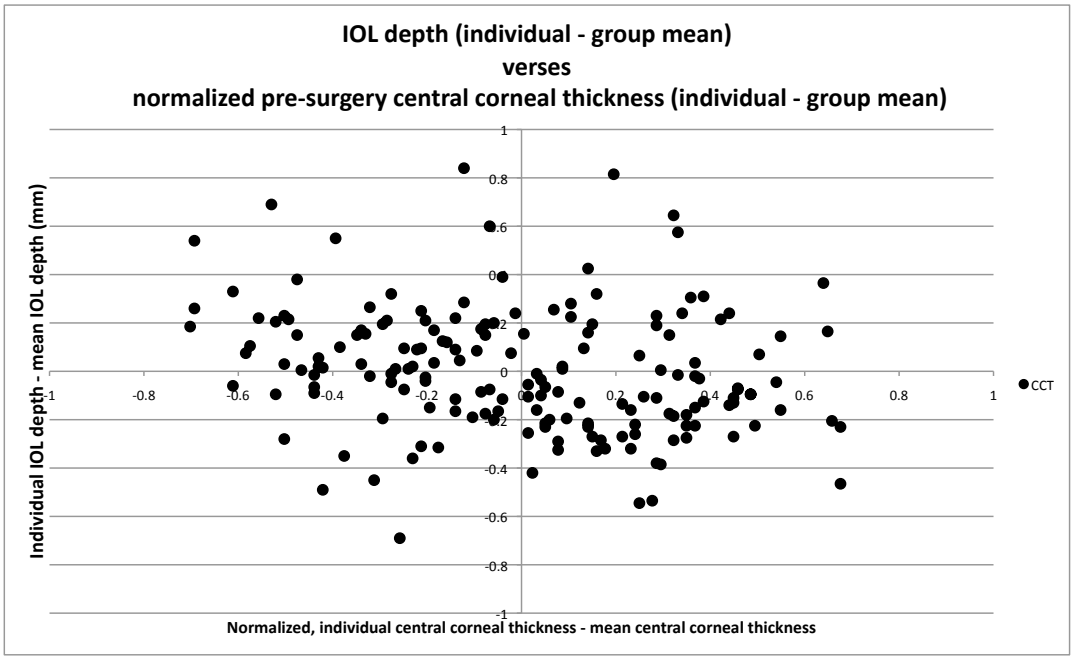

FIGURE 2.9: A plot of difference in IOL depth (individual - mean) verses the normalized difference in pre-surgery central corneal thickness (individual - mean). Difference values are normalized by dividing by 3 standard deviations.

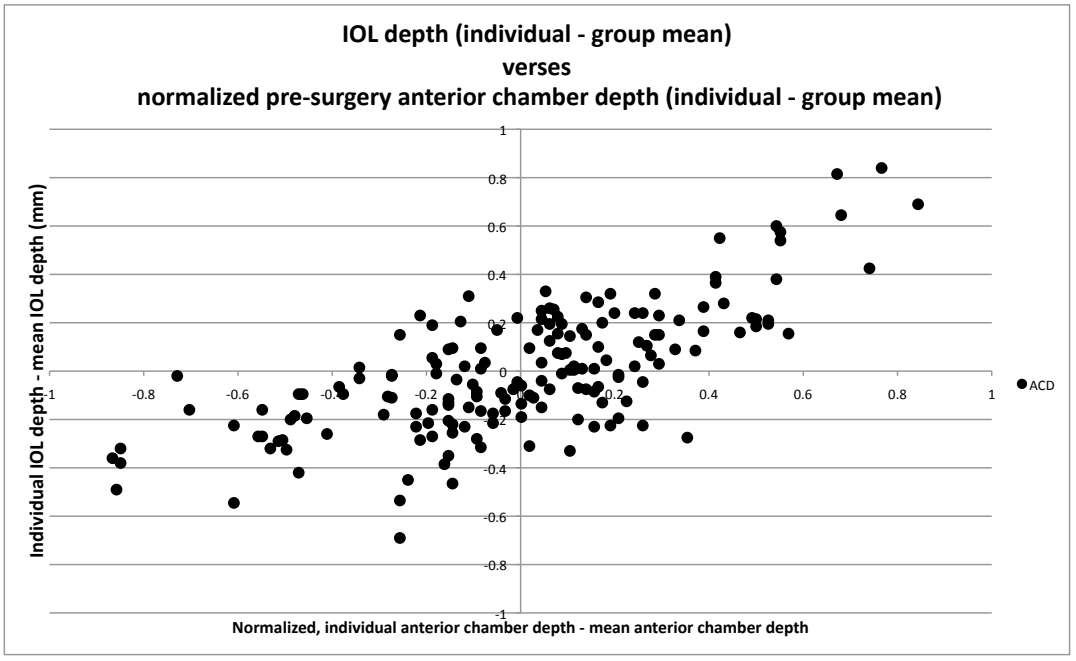

FIGURE 2.10: A plot of difference in IOL depth (individual - mean) verses the normalized difference in pre-surgery anterior chamber depth (individual - mean). Difference values are normalized by dividing by 3 standard deviations.

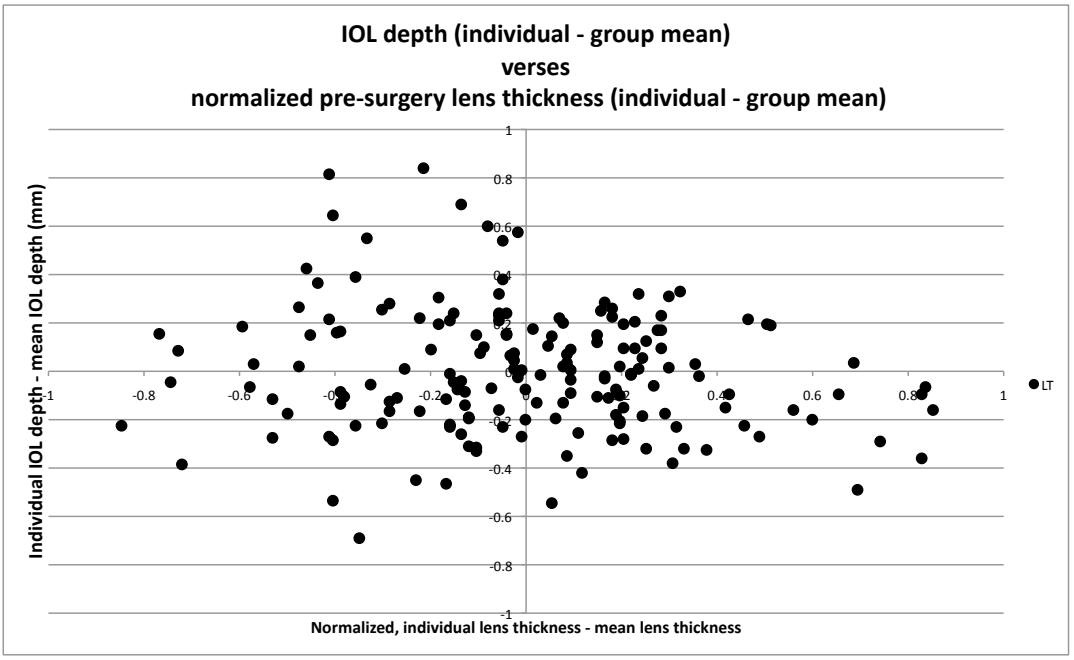

FIGURE 2.11: A plot of difference in IOL depth (individual - mean) verses the normalized difference in pre-surgery lens thickness (individual - mean). Difference values are normalized by dividing by 3 standard deviations.

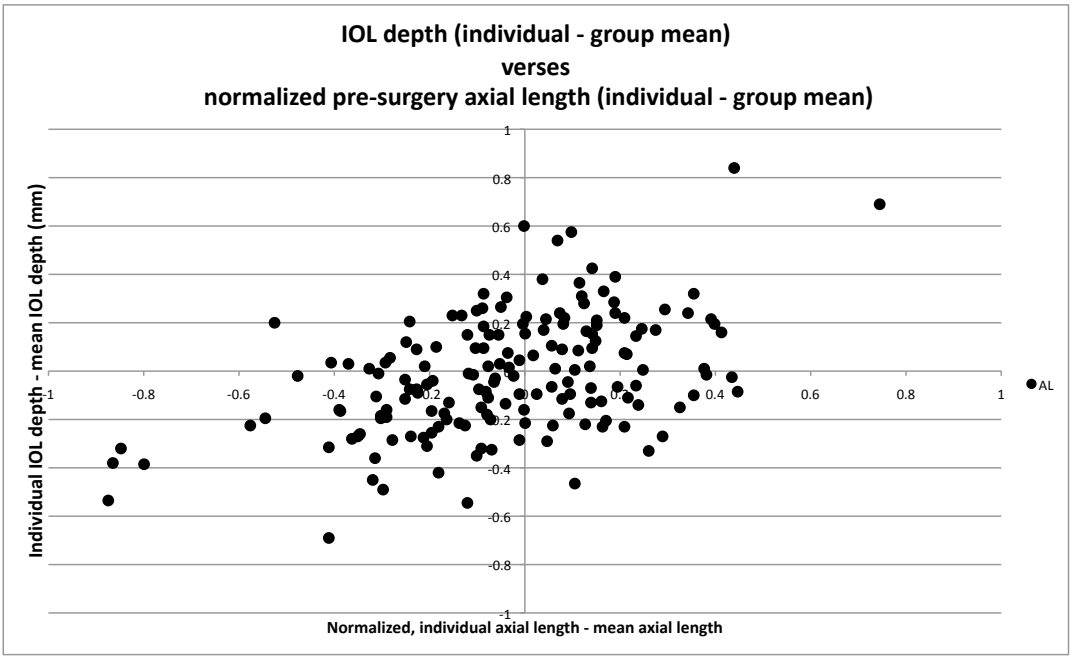

FIGURE 2.12: A plot of difference in IOL depth (individual - mean) verses the normalized difference in pre-surgery axial length (individual - mean). Difference values are normalized by dividing by 3 standard deviations.

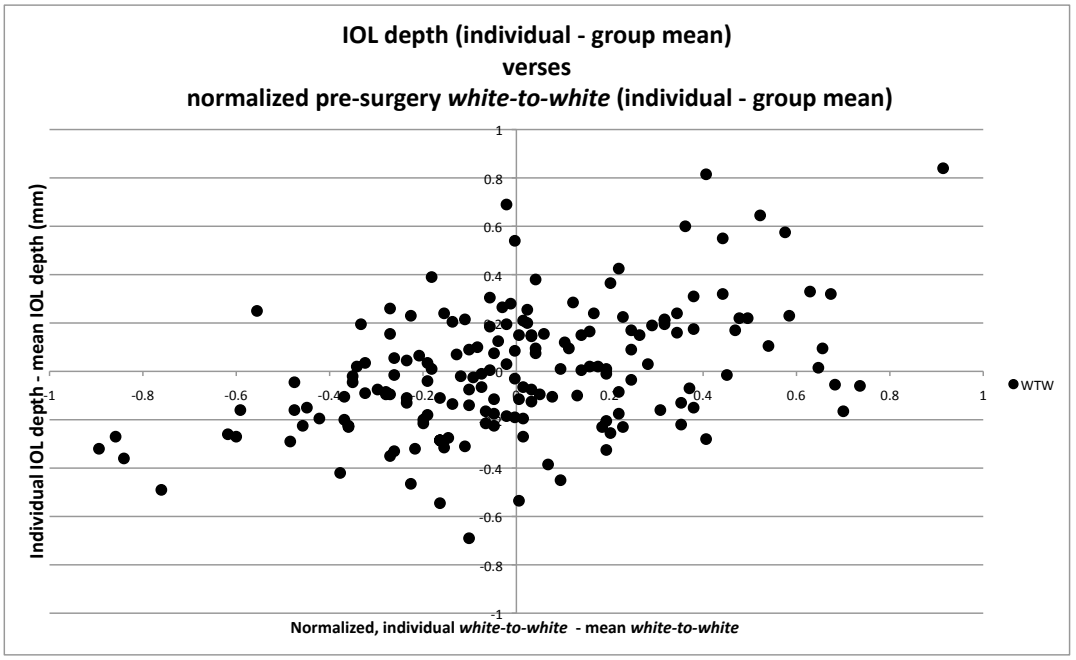

FIGURE 2.13: A plot of difference in IOL depth (individual - mean) verses the normalized difference in pre-surgery *white-to-white* (individual - mean). Difference values are normalized by dividing by 3 standard deviations.

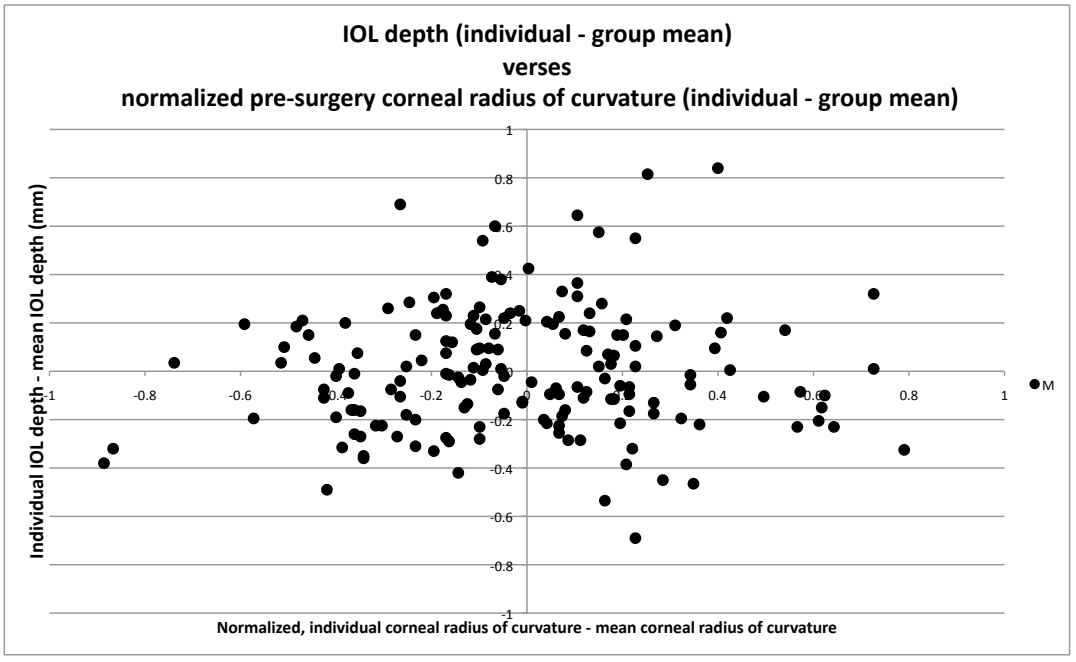

FIGURE 2.14: A plot of difference in IOL depth (individual - mean) verses the normalized difference in pre-surgery corneal radius of curvature (individual - mean). The power vector M is used to describe the anterior corneal radius of curvature, which is equivalent to *mean K* used by clinicians. Difference values are normalized by dividing by 3 standard deviations.

Multiple regression analysis (a least-squares method) was performed, initially using all previously listed parameters (central corneal thickness, ACD, etc) as independent variables. Care was taken to avoid redundancy of independent variables, known as collinearity. For example, it is inappropriate to use both corneal principal radius of curvature values, colloquially referred to as *K minimum* and *K maximum* values by clinicians. Instead it is more appropriate to describe the corneal shape using power vectors (as previously defined in Eqs. 2.8 to 2.10), which are orthogonal.

The t statistic was calculated for each regression model. Any parameter with an absolute value of the coefficient (m_n) divided by the estimated standard error (se_n) less than the critical t statistic may be considered to posses low importance in its ability to contribute to the prediction of IOL depth, for that particular model. Accordingly, the central corneal thickness parameter and the corneal astigmatism power vectors J_{45} and J_{180} were excluded from the regression models quite early during the study as they contributed little advantage (if any) towards the prediction of the IOL depth. To calculate the critical t statistic, a significance level of $\alpha = 0.005$ was used with a two-tailed distribution. The degrees of freedom for the calculation of t is varied according to the number of parameters used by each model.

Numerous multiple linear regression models in the form of Eq. 2.19 were investigated,

$$y = m_1\, x_1 + m_2\, x_2 + ... + m_n\, x_n + c \tag{2.19}$$

where y is the IOL depth, m_n is the coefficient of the independent variable x_n, and c is the y-intercept constant.

A multiple logarithmic regression model in the form of Eq. 2.20 was also investigated,

$$y = a\,(b_1^{x_1} \cdot b_2^{x_2} \cdot ..... \cdot b_n^{x_n}) \tag{2.20}$$

where y is the IOL depth, b_n is the base raised to the power of the independent variable x_n, and a is the coefficient. However, the logarithmic regression model was ill-conditioned and did not improve the sum of the squares of the residuals (SSE). In fact, it showed a worsening of the SSE value (3.50); hence logarithmic regression modelling was abandoned in preference for the superior stability of multiple linear regression models (Eq. 2.19).

For the sake of being succinct, a representative selection of models and a brief description of its unique features or potential relationships being explored are reported in Table 2.15. When comparing regression models of differing numbers of independent variables, the correlation coefficient (R^2) is an inappropriate metric to use. Instead the sum of the squares of the residuals (SSE) is used because it is a fairer metric by which to compare models with differing numbers of independent variables. Thus, rather than report the R^2 values in Table 2.15, the sum of the squares of the residuals are emphasized. Later, when presenting our final selected model the correlation coefficient (R^2) is reported and a full discussion of this model is given.

	Case study examples of linear regression models for the prediction of IOL depth.								
Let	x_1 be the central corneal thickness								
	x_2 be the anterior chamber depth								
	x_3 be the cataractous lens thickness								
	x_4 be the axial length								
	x_5 be the *white to white* distance								
	x_6 be the corneal radius of curvature, power vector M								
	x_7 be the corneal radius of curvature, power vector J_{45}								
	x_8 be the corneal radius of curvature, power vector J_{180}								
	x_9 be the corneal height according to Eq.E.5								
	m_n is the coefficient of parameter n								
	se_n is the estimated standard error of parameter n								
	t_c is the critical t statistic of the model								
Model A	$y = m_1x_1 + m_2x_2 + m_3x_3 + m_4x_4 + m_5x_5 + m_6x_6 + m_7x_7 + m_8x_8 + c$								
	SSE = 3.55		$t_c = 2.23$						
$m_n .... c$	0.000	0.490	0.212	0.040	0.134	-0.197	-0.197	-0.013	1.034
se_n	0.000	0.050	0.037	0.011	0.040	0.058	0.167	0.110	0.495
$t = \lvert m_n/se_n \rvert$	0.15	9.81	5.77	3.75	3.36	3.40	1.18	0.12	
Comments									
Values of $t < t_c$ suggest that the parameters central corneal thickness, and power vectors J_{45}, and J_{180} for corneal radius of curvature are not useful in the prediction of IOL position.									
Model B	$y = m_2x_2 + m_3x_3 + m_4x_4 + m_5x_5 + m_6x_6 + c$								
	SSE = 3.58		$t_c = 2.36$						
$m_n .... c$	0.492	0.211	0.041	0.133	-0.200	1.092			
se_n	0.049	0.036	0.011	0.039	0.055	0.461			
$t = \lvert m_n/se_n \rvert$	10.06	5.87	3.82	3.42	3.64				
Comments									

Continued on next page

Table 2.15 – continued from previous page

Case study examples of linear regression models for the prediction of IOL depth.

By removing the parameters of central corneal thickness, and power vectors J_{45}, and J_{180} for corneal radius of curvature only a minimal increase in the SSE value is observed compared to Model A.

Model C	$y = m_2x_2^2 + c$										
	SSE = 5.37		$t_c = 3.18$								
$m_n .... c$	0.096	3.676									
se_n	0.007	0.047									
$t = \lvert m_n/se_n \rvert$	13.967										

Comments

Because the anterior chamber depth shows the strongest relationship with the IOL depth (see Figs. 2.9 - 2.14), this model investigated the possibility of using the square of the ACD value as the sole independent variable.

Model D	$y = m_2x_2^2 + m_3x_3^2 + m_4x_4^2 + m_5x_5^2 + m_6x_6^2 + m_2x_2 + m_3x_3 + m_4x_4 + m_5x_5 + m_6x_6 + c$										
	SSE = 3.21		$t_c = 2.18$								
$m_n .... c$	0.221	-0.041	-0.001	0.033	-0.103	-0.639	0.571	0.102	-0.650	1.439	-0.780
se_n	0.063	0.047	0.003	0.059	0.110	0.332	0.426	0.163	1.440	1.733	10.245
$t = \lvert m_n/se_n \rvert$	3.523	0.883	0.399	0.554	0.939	1.926	1.338	0.622	0.452	0.830	

Comments

The intention of this model was to compare each parameter as linear terms and also as a square of each parameter. By comparing like-for-like it can be argued that the squared terms of the parameters anterior chamber depth, white to white, and mean corneal radius of curvature, have stronger relationships than their linear counterparts. By contrast, the linear terms for lens thickness and axial length show stronger relationships than their squared counterparts.

Model E	$y = m_2x_2^2 + m_3x_3 + m_4x_4 + m_5x_5^2 + m_6x_6^2 + c$					
	SSE = 3.33		$t_c = 2.36$			
$m_n .... c$	0.101	0.214	0.036	0.006	-0.012	1.687
se_n	0.009	0.034	0.010	0.002	0.003	0.284
$t = \lvert m_n/se_n \rvert$	10.959	6.258	3.527	3.738	3.429	

Comments

This model investigates the combination of linear and squared terms according to the t statistic comparison discussed by Model D. This model has a very similar SSE value as that of Model D.

Model F	$y = m_2x_2^2 + m_3x_3 + m_4x_4 + m_5x_5^2 + c$				
	SSE = 3.56		$t_c = 2.45$		
$m_n .... c$	0.114	0.255	0.021	0.003	1.415
se_n	0.009	0.033	0.010	0.001	0.282
$t = \lvert m_n/se_n \rvert$	13.370	7.737	2.217	2.348	

Comments

This model is based on Model E, except the parameter for corneal radius of curvature is not used.

Continued on next page

Table 2.15 – continued from previous page

Case study examples of linear regression models for the prediction of IOL depth.

Considering that post-refractive surgery patients have a modified corneal shape, to avoid spurious predictions of IOL depth in these patients, perhaps the corneal shape should not be used by the model. The SSE value increases slightly as a result from 3.33 to 3.56.

Model G $y = m_2x_2 + m_3x_3 + m_4x_4 + m_5x_5 + c$

SSE = 3.86 $t_c = 2.45$

$m_n .... c$	0.567	0.258	0.025	0.065	0.333
se_n	0.046	0.035	0.010	0.035	0.426
$t = \lvert m_n/se_n \rvert$	12.346	7.379	2.445	1.855	

Comments

This model is based on Model B, except the parameter for corneal radius of curvature is not used. The model considers that post-refractive surgery patients have a modified corneal shape and to avoid spurious predictions of IOL depth in these patients, perhaps the corneal shape should not be used by the model. The SSE value increases slightly as a result from 3.58 to 3.86.

Model H $y = m_2x_2 + m_3x_3 + m_4x_4 + m_5(x_5/2)^2 + m_6(x_6^{-1}) + c$

SSE = 3.57 $t_c = 2.36$

$m_n .... c$	0.493	0.211	0.041	0.022	12.217	-1.251
se_n	0.048	0.036	0.011	0.006	3.340	0.610
$t = \lvert m_n/se_n \rvert$	10.179	5.864	3.819	3.507	3.658	

Comments

Knowing that the corneal shape is approximately spherical, the purpose of this model was to investigate if the sag of the cornea was helpful in predicting IOL depth. The sag of a spherical surface can be approximated by $s = 0.5 \cdot c\rho^2$ where c is curvature and ρ is the radial distance from the apex. Note the modifications to the terms for white to white (x_5) and corneal radius of curvature (x_6) to achieve this pseudo-representation of sag. Also note the risk of collinearity with the ACD term.

Model I $y = m_2x_2 + m_3x_3 + m_4x_4 + m_5x_5 + m_6x_6 + m_9x_9 + c$

SSE = 3.57 $t = 2.31$

$m_n .... c$	0.487	0.211	0.041	0.436	-0.480	-0.484	1.020
se_n	0.049	0.036	0.011	0.460	0.428	0.733	0.475
$t = \lvert m_n/se_n \rvert$	9.875	5.839	3.829	0.947	1.122	0.661	

Similar to Model H, this model approximates the anterior chamber as a section of a sphere.

A *corneal height* parameter is calculated according to Eq. E.5 derived in Appendix E.

The t statistic of 0.661 suggests this idea is not worthwhile pursuing. The SSE value is approximately equal to that of Model B.

TABLE 2.15: Selected case studies of linear regression models investigated for prediction IOL depth from pre-surgery biometry data.

Only a representative sample of the models investigated are reported in Table 2.15; to exhaustively list the details of all models investigated would not offer any additional insight. The number of models one may evaluate is only limited by one's imagination, especially if non-linear combinations of terms are considered. Many models with higher order polynomials and non-linear terms were investigated, but all only marginally reduced the SSE value below that of Model B in Table 2.15, if at all. The plots of Figs. 2.9 to 2.14 do not suggest any strong relationships other than linear and it can be argued that fitting higher-order and non-linear models to this data will produce outcomes dominated by noise; failing to represent the true trends in the data.

In other models investigated each parameter was *weighted* according to it's reliability, as judged by personal clinical opinion. For example, it could be argued that within the interferometry data subset, anterior chamber depth is more reliably known than lens thickness, which in turn is more reliably known than axial length. This occurs because as interferometry measurements progress deeper into the eye, the greater any errors (such as regarding the assumed refractive index values) will affect the measured outcome. Other reliability ranking might suggest that interferometry data (anterior chamber depth, lens thickness, axial length) is known to a higher precision than measurements based on edge-detection of an enface image (the white to white measurement), or, that the corneal radius of curvature is the least reliable parameter due to the potential for extreme values associated with previous refractive surgery and/or poor tear quality. This methodology of weighting parameters according to perceived reliability offered no improvement in the SSE value and was abandoned.

In any model, but there should be a connection between the model and the physical reality of the situation. There should be a real, physical, plausible reason why a particular relationship should exist between the independent variables and the IOL depth. I specifically wanted to avoid modeling high-order polynomials or non-linear terms that lacked a physical basis to explain why that relationship may exist, apart from to argue *'it gives a better SSE value.'* From the plots in Figs. 2.9 to 2.14, there is no evidence to argue the case for any high order polynomial relationship. The investigations outlined above satisfied me that the most appropriate relationship to use was generally linear-shaped, at least over the normal range of biometry values.

At a basic level it is reasonable to argue that;

- A greater anterior chamber depth should correspond to a larger eye, and therefore a greater IOL depth, and vice-versa regarding lesser values.
- A greater axial length should correspond to a larger eye, and therefore a greater IOL depth, and vice-versa regarding lesser values.
- A greater white to white distance should correspond to a larger eye, and therefore a greater IOL depth, and vice-versa regarding lesser values.
- For a given WTW value, a lesser corneal radius of curvature value should correspond to greater sag of the anterior chamber, and therefore a greater IOL depth, and vice-versa regarding greater values.

However, it is debatable how the lens thickness should correspond to IOL depth. From one point of view, a greater lens thickness should correspond to a larger eye and therefore a greater IOL depth. From an alternative point of view, it could be argued that a greater lens thickness in a cataract population (assuming no accommodation) is likely to represent age-related crystalline lens thickening rather than a truly larger eye. As it is known that this thickening predominantly effects the anterior lens vertex position (i.e. the crystalline lens thickens mainly in the anterior direction) [212], perhaps this is associated with an anterior shift in the equatorial plane of the capsular bag and the associated mechanical structures of the zonules and ciliary body. This argument would support a model of greater lens thickness corresponding to a lesser IOL depth.

During the modelling process, the idea developed that the model should be resilient to corruption by extreme values for corneal shape, specifically with the circumstance of previous refractive surgery in mind. This initially began with investigations that excluded the corneal radius of curvature parameter from the model (see Table 2.15, Models F and G); however this was not entirely satisfactory. Although there is only a moderate increase in the SSE value with this approach, why should the model disadvantage the prediction of a typical patient just to benefit the atypical (e.g. previous refractive surgery) patient ? This issue was better addressed by a model that allowed the corneal shape parameter to influence IOL depth, but within an envelope restricting the influence of extreme values for corneal shape.

Preliminary investigations regarding this concept applied a cubic root function of the form

$$y = m_2\, x_2 + m_3\, x_3 + m_4\, x_4 + m_5\, x_5 + m_6\, x_6^{1/3} + c \tag{2.21}$$

and then progressed to rationalizing the same argument for all parameters, allowing the model to be stable in the event of atypical values or mis-readings of *any* biometry parameter as below;

$$y = m_2\, x_2^{1/3} + m_3\, x_3^{1/3} + m_4\, x_4^{1/3} + m_5\, x_5^{1/3} + m_6\, x_6^{1/3} + c \tag{2.22}$$

For the models described in Eqs. 2.21 and 2.22 it is preferable to normalize the range of each independent variable and set the midpoint of that range equal to zero. In this way, the value for the y-intercept c can directly correspond to the population mean IOL depth. This gives the model flexibility in that if a complete set of biometry variables are unavailable (e.g. white to white measurement failed but all other parameters were reliably measured), the expression can still be partially evaluated. The method for normalizing and setting the midpoint of the domain of each independent variable is explained in detail below regarding sigmoid functions, which constitute the final selected model for prediction IOL depth.

The cubic root models described in Eqs. 2.21 and 2.22 were not ideal because the middle part of the function is not 'linear' enough and the tail ends of the functions do not asymptote quickly enough. Models using a fifth root function ($x_n^{1/5}$) applied to the independent variables were investigated but they still suffered similar behavior issues as cubic root models (Eqs. 2.21 and 2.22). The qualities of sigmoid functions are better suited to our application; they provide a linear range in the middle part of the function and asymptote as quickly or slowly as desired, by setting an appropriate value for the constant k. Our final model investigated for predicting IOL depth was based on the linear combination of a series of sigmoid functions. This model is described below and we recommend its use in preference to all preliminary models presented in Table 2.15 and Eqs. 2.19 to 2.22.

Final selected model

We propose that the geometrical IOL depth (d) can be approximated by the linear sum

of sigmoid functions (d_n) and a constant (c);

$$d = \Sigma\, d_1 + d_2 + d_3 + d_4 + d_5 + c \tag{2.23}$$

Each sigmoid function (d_n) is dependent on a single biometry parameter; anterior chamber depth, lens thickness, axial length, white to white, or mean anterior corneal radius of curvature. The sigmoid function (d_n) for each biometry parameter is normalized and its range midpoint is set equal to zero. As previously described, this arrangement allows the y-intercept constant (c) to represent the population mean IOL depth and allows the partial evaluation of Eq. 2.23 in the absence of a complete biometry data set without risking a large error penalty compared to alternative methods for predicting IOL depth. For the symmetric sigmoid functions investigated (logistic and tanh), the mean of each function is zero. Note that this arrangement also means that both d and the constituent d_n functions posses a sigmoid shape.

Within the sigmoid family we investigated the logistic function (Eq. 2.24), the hyperbolic tangent (tanh) function (Eq. 2.25), and the Gompertz function (Eq. 2.26).

We used the logistic function in the following form

$$d = \frac{d_{amp}}{1 + e^{-k(x-x_m)\cdot\alpha/3\sigma}} - \frac{d_{amp}}{2} \tag{2.24}$$

where d is the difference in IOL depth compared to the population mean, e is Euler's number, σ_n is the standard deviation of the independent variable, α is the normalisation factor for the sigmoid function, x is the value of the independent variable. The x_m term is set equal to the mean of the independent variable. The constant k determines the curvature of the function and is set equal to 1. The value d_{amp} defines the amplitude of the function and is determined by a multiple linear regression (least squares) method.

We used the tanh function in the following form

$$d = d_{amp} \cdot \tanh\left(k(x - x_m) \cdot \pi \cdot \alpha/3\sigma\right) \tag{2.25}$$

where all symbols are as defined above. Evaluating the tanh function requires the conversion of the normalized independent variable to radians by multiplying by π.

We used the Gompertz function in the following form

$$d = d_{amp}\, e^{-e^{-k(x-x_m)\cdot\alpha/3\sigma}} - \frac{d_{amp}}{2} \tag{2.26}$$

where all symbols are as defined above.

A plot of the 3 sigmoid functions (Eqs. 2.24 to 2.26) investigated is displayed in Fig. 2.15. The independent variable is normalised so the shape of all 3 functions can be appreciated on a single graph. A helpful discussion of the sigmoid family of functions is given by Yin *et al.* [213] and Birch [214].

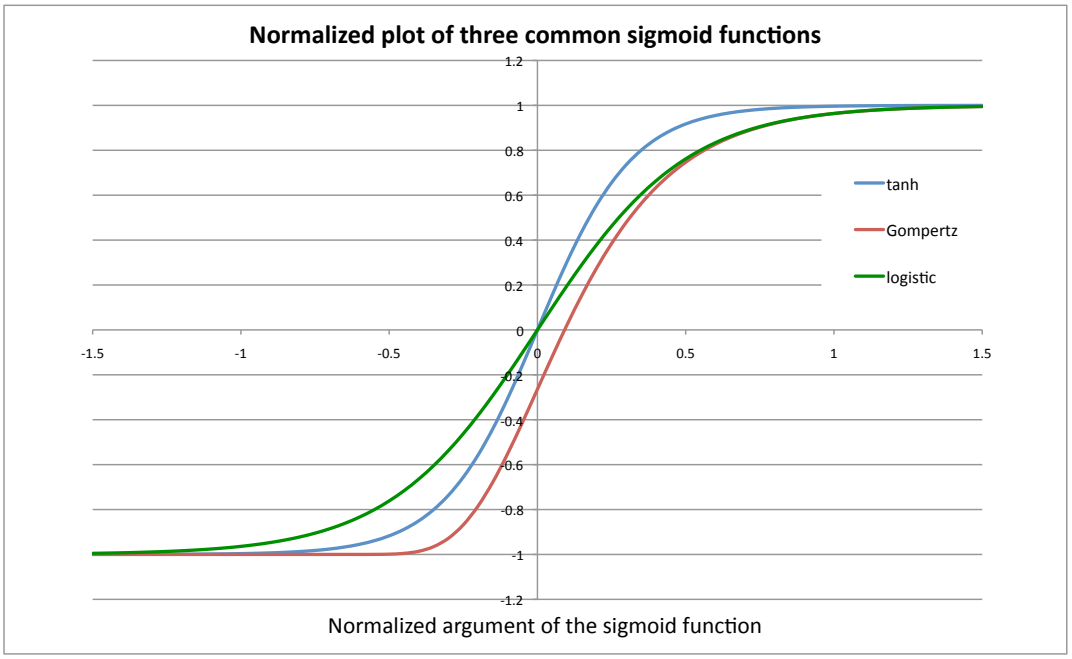

FIGURE 2.15: A plot of three different sigmoid functions; the logistic function, the tanh function, and the Gompertz function. The generalized form of each function has been modified to suit our application, including a normalization process. The value for the constant determining curvature of the function (k) is set to unity ($k = 1$), the value for x_m is set equal to zero, σ is set equal to 1/3 for all functions, while the value for α is set equal to 1, 4, and 4, for the tanh, Gompertz, and logistic functions, respectively.

Multiple linear regression was used to solve the value for d_{amp} for each parameter (anterior chamber depth, lens thickness, axial length, white-to-white, mean anterior corneal radius of curvature) using the logistic function model according to (Eqs. 2.23 and 2.24). A plot of the residual fitting error of this model is shown in Fig. 2.16 and raised mild concerns of possessing non-random features; the plot suggests that the model overestimates when the IOL depth is lesser and underestimates when the IOL depth is greater. This prompted us to investigate 'steeper' logistic functions by altering the values of the

constants k and α. We also investigated modelling with the inherently steeper tanh function (Eqs. 2.23 and 2.26) and the asymmetric Gompertz function (Eqs. 2.23 and 2.26). The asymmetry of the Gompertz function offers a potentially useful modality if a more abrupt limit to the IOL position is observed when the IOL depth is small and a more gradual asymptote when the IOL depth is great. Note that this normalized function has a y-intercept equal to $2/e - 1$, compared to the logistic and tanh functions that intercept at zero.

All of these variations (in constants for curvature (k) and normalization (α)), and alternative sigmoid functions (logistic, tanh, and Gompertz functions) failed to significantly change the distribution of the plot of residual error verses observed IOL depth. All variations and alternative models performed similarly in regard to the SSE value. We conclude that for the given data set, all three sigmoid functions investigated performed similarly and any one of these would be suitable to use in modelling the IOL depth. The details of the logistic model are presented below as our recommended model.

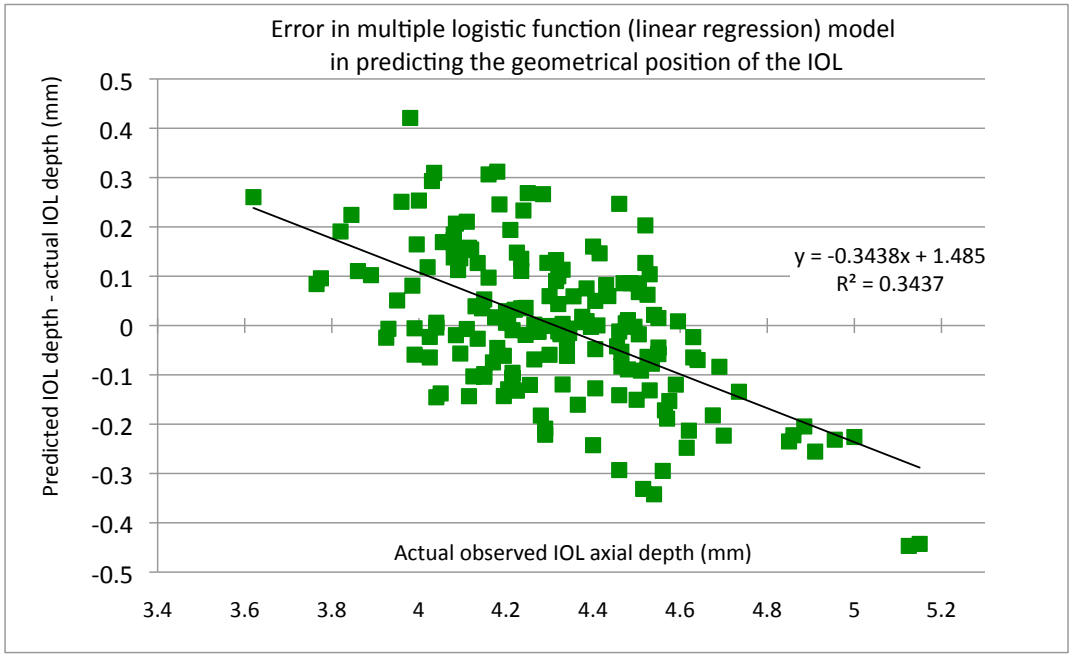

FIGURE 2.16: A plot of residual error in prediction of IOL depth using a model based on the linear combination of multiple logistic functions.

The selected model is the linear combination of logistic functions and a constant y-intercept as already described by Eqs. 2.23 and 2.24. Each individual parameter is related to the IOL depth by its own logistic function. The y-intercept constant represents the mean IOL depth of the population. The model is flexible in so much as; if certain

parameter unknown or unreliable its logistic function (d_n) can be excluded from Eq. 2.23 and the expression can still be evaluated with minimal risk of spurious results compared to alternative methods for predicting IOL depth.

The value for the constants k and α influence the sigmoid curvature and normalisation. There values are chosen arbitrarily but restricted by the need to minimize the SSE value (by fitting over the middle 'linear' range of the function) and to produce a model that will be robust in the presence of atypical values and reach its asymptote quickly enough for values beyond those typically observed. We select values of $k = 1$ and $\alpha = 4$ for the logistic function. This ensures that the asymptote occurs at about 3 standard deviations of the independent variable (x). The normalisation also requires setting x_m equal to the mean value for each parameter. If a data sample is small and bias is suspected, use of the median value for x_m may be more appropriate. However, in our data set optimal results were achieved using mean values for x_m. Rather than repeating the description of each constituent logistic function as separate equations, the values for all variables used by our model are listed in Table 2.16, and the logistic function for the anterior chamber depth parameter is displayed Eq. 2.27 as an example.

Values used in the multiple logistic model of IOL depth						
Parameter	d_{amp} (mm)	k	t_m (mm)	σ_t (mm)	$3 \cdot \sigma_t$ (mm)	α
Description	amplitude	curvature	mean value	st. deviation (σ)	normalisation	
anterior chamber depth	0.701	1	2.538	0.388	1.164	4
lens thickness	0.315	1	4.562	0.422	1.265	4
axial length	0.284	1	23.367	1.375	4.125	4
white to white	0.246	1	12.094	0.374	1.123	4
mean anterior corneal radius of curvature	-0.227	1	7.758	0.261	0.782	4
The y-intercept (c) in Eq. 2.23 represents the mean population IOL depth of 4.31 mm						

TABLE 2.16: Values of all parameters used in the multiple logistic model of IOL depth.

$$d_1 = \frac{0.701}{1 + e^{-1 \cdot (x - 2.538) \cdot (4/1.164)}} - \frac{0.701}{2} \tag{2.27}$$

Figure 2.17 shows a plot of all 5 constituent logistic functions used to model IOL depth, displayed on the one graph. The strong influence of the anterior chamber depth parameter on the prediction of IOL depth is obvious. The magnitude of the effect of the other

biometry parameters differ slightly from each other. Their ranking in order from greatest to least influence is; lens thickness, axial length, white to white, and mean anterior corneal radius of curvature.

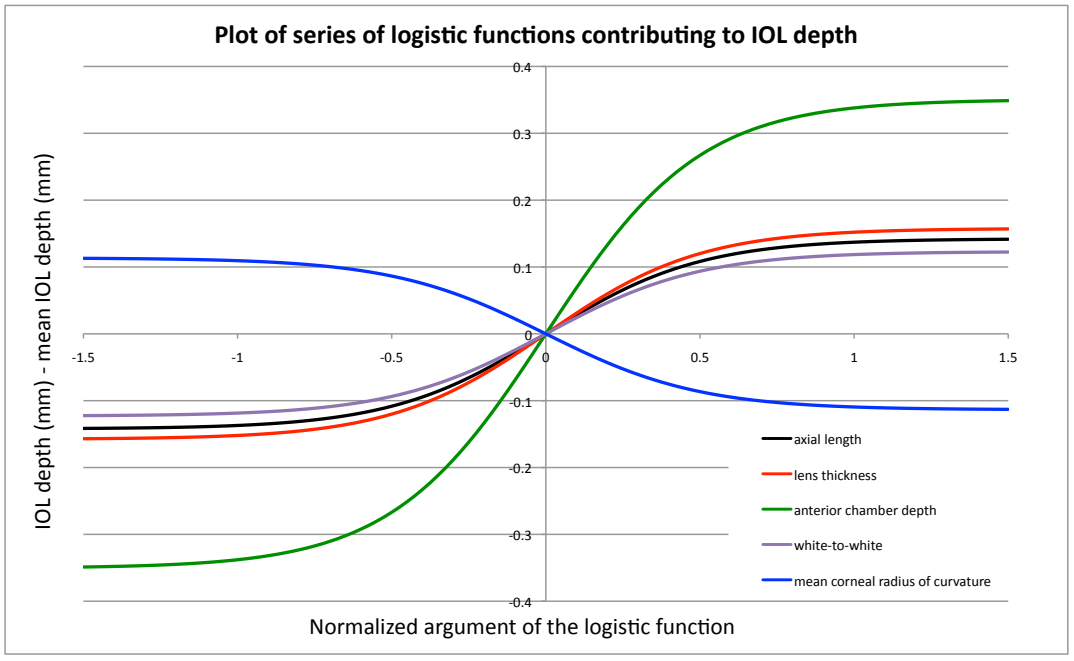

FIGURE 2.17: A plot of the modelled contribution of each parameter to the IOL depth using normalized logistic functions. The range of each parameter is normalized by dividing by 3 standard deviations.

The specific values for d_{amp} and c reported in Table 2.16 are only valid for the specific IOL used in this experiment (Akreos Adapt AO), however the same methodology as described in deriving this model can be applied to any consistent data set in order to determine the values of d_{amp} and c for *any* IOL design. The mean (x_m), standard deviation (σ), and constant k values are **not** IOL-specific and may be used in replicating the model to predict the IOL depth of other IOL designs. A plot of the residuals (predicted IOL depth - observed IOL depth) plotted against the observed IOL depth was previously presented in Fig. 2.16. A plot of the observed IOL depth verses the IOL depth predicted by our model is given in Fig. 2.18. The correlation coefficient (R^2) for this plot is 0.66, the sum of the squares of the residuals for this model is 3.94 mm^2, and the sample size (n) was 174. This SSE value is comparatively higher than that of Model B (3.58) reported in Table 2.15. However, we argue this is an acceptable compromise as the multiple logistic model (Eqs. 2.23 and 2.24) offers greater stability in the event of atypical biometry (e.g. a previous refractive surgery patient) or accidental biometry mis-readings. A linear regression line is displayed in Fig. 2.18 although at the extremes of the domain the data

departs from a linear relationship and is somewhat suggestive of a sigmoidal relationship itself.

Alternative formulas for predicting the IOL depth generally have been developed using multiple linear regression techniques, considering various combinations of biometry parameters [3, 64, 134, 146, 215, 216]. The use of a multiple logistic model has not previously been described to the best of our knowledge, although a method using neural networks has been previously reported [217] and such networks are associated with sigmoid functions.

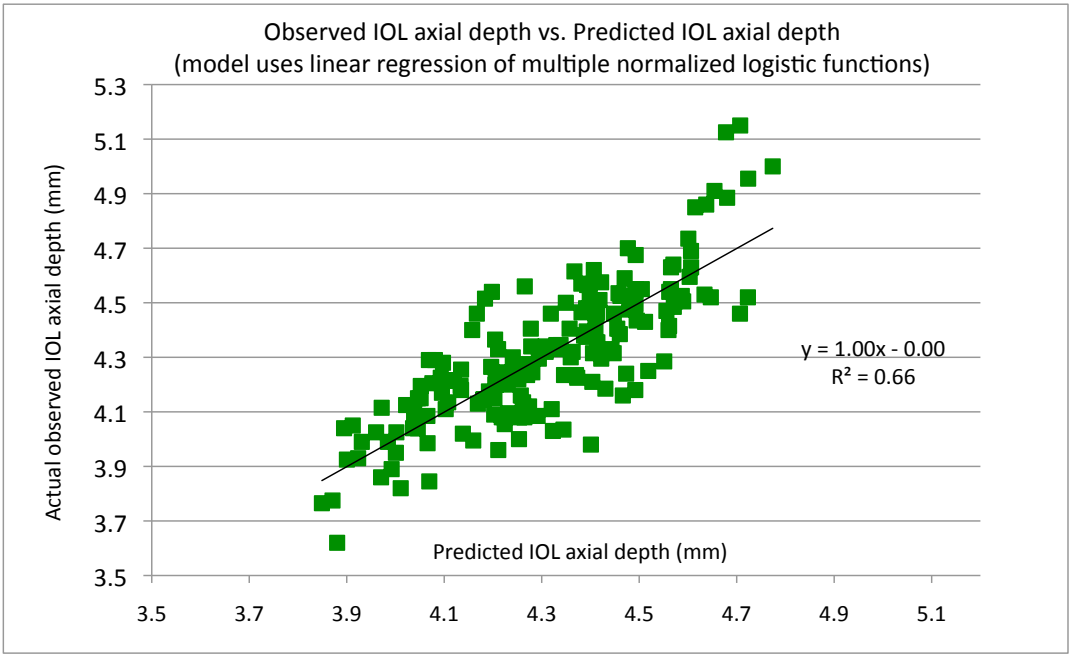

FIGURE 2.18: A plot of the observed IOL depth verses the IOL depth predicted by the model using normalized logistic functions with independent variables from Lenstar pre-surgery biometry parameters.

Future investigations may consider using corneal topography biometry data in place of the autokeratometry data set used in this study (all biometry parameters in this study were measured using the Lenstar). However, given the mild relationship between corneal shape and IOL depth, it is not anticipated that such a substitution would significantly improve the prediction of IOL depth. It is possible, if not likely, that if a longer review period (mean 37 days) was used in the experiment, the IOL position may stabilize further and a model optimized for such a data set may be more accurate. The selected multiple logistic model described above is used to predict IOL depth in the personalised eye modelling work (Chapter 3).

Chapter 3

Personalised Eye Modelling

This chapter reports on the crux of this work; bringing together the results of the experiments and data analysis presented in Chapter 2 and using this knowledge to perform personalised pseudophakic eye modelling on ray-tracing software. As subjects were also examined following cataract surgery, the predictions of the personalised eye model and a current industry-standard formula (SRK/T) are compared against the observed actual refractive outcome. For the sake of being concise, comparison of performance is restricted to the personalised eye model and the SRK/T formula, which is considered representative of all other modern formulas (Holladay, Holladay II, Hoffer Q, Olsen, Haigis, etc.).

The ray-tracing method allows the simulation of higher-order monochromatic aberration correction and investigation of any associated improvement in retinal image quality. In doing so, the required optimal topography of a customized IOL can be determined, which is conceptually equivalent to a very detailed IOL design or *prescription*. A case study example of this technique is reported later in Section 3.6. As previously emphasized, any associated potential visual benefit derived from IOL design customization requires consideration of psychophysical and visual perception issues beyond the scope of this work.

Numerous scientists have contributed to the development and promotion of personalised eye models using ray-tracing software as a tool for IOL power calculation and investigation of optical performance of novel IOL designs [60, 61, 64, 65, 146, 187, 218, 219,

220, 221, 222]. Our work is a continuation of these efforts towards establishing the personalised eye modelling technique and assessing both its utility and limitations.

3.1 Performance of the SRK II and SRK/T formulas

A revised A constant was back-calculated from the biometry data of valid subjects (184 eyes), according to the method recommended by Retzlaff *et al.* [223] as described in Section 1.5.5 and using Eqs. 1.21 to 1.34. Using the personalised A constant and associated *offset* value, the predicted refractive error was then re-evaluated for both the SRK II and SRK/T formulas. A *best sphere* calculation is used, as is the consensus approach when considering a *defocus only* IOL design (as this work does). Results of the optimization, along with analysis of the performance of the re-evaluated personalised SRK II and SRK/T formulas are reported in Table 3.1. The principal metric against which the personalised ray-tracing eye model and SRK/T formula will be compared, is the standard error of the estimate. It is calculated by $\sqrt{SSE/n}$, where SSE is the sum of the squares of the difference between the predicted *best sphere* refractive error and the observed actual *best sphere* refractive error, and n is the sample size. The optimised SRK/T standard error of the estimate is 0.56 D, which is superior to the SRK II formula (0.70 D), as expected.

Figure 3.1 shows a plot of the residuals of the SRK II and SRK/T formulas when applying the personalised A constant (118.826) and associated *offset* (2.144 mm) values and re-evaluating the refractive error prediction. The spread of residuals is better confined by the SRK/T formula. Note the SRK/T mean residual is not zero; this is because the method recommended by Retzlaff *et al.* [223] actually optimizes the A constant rather than the *offset*, and hence the SRK II formula has a mean residual of zero (-0.02 D), but the SRK/T formula (-0.27 D) does not.

In the bottom division of Table 3.1 the *offset* of the SRK/T formula itself is optimised, rather than relying on the legacy relationship linking the SRK/T formula with the SRK II formula via Eq. 1.32. All four performance metrics show improvement with reduced values for the sum of the squares of the residuals, the standard error of the estimate, and the mean of the absolute of the residuals. This method produces a mean residual of zero (0.00 D), an improved standard error of the estimate (0.50 D), and is a superior

technique for optimizing the SRK/T formula compared to the approach described by Retzlaff *et al.* [223]. Figure 3.2 shows a plot of the residuals of the SRK/T formulas when applying the personalised *offset* (1.950 mm) value and re-evaluating the refractive error prediction.

Accuracy of the personalised SRK II and SRK/T formulas	
manufacturer-nominated A constant	118.0
manufacturer-nominated ACD constant	4.96 mm
personalised SRK II A constant	118.826
personalised SRK/T ACD constant	5.48 mm
personalised SRK/T *offset* (includes central corneal thickness)	2.144 mm
sample size, number of eyes (n)	184
SRKII mean residual	-0.02 D
SRKII sum of the squares of the residuals	91.41 D
SRKII standard error of the estimate	0.70 D
SRKII mean of the absolute of the residuals	0.51 D
SRK/T mean residual	-0.27 D
SRK/T sum of the squares of the residuals	57.84 D
SRK/T standard error of the estimate	0.56 D
SRK/T mean of the absolute of the residuals	0.42 D
if the offset of the SRK/T formula is optimised, then....	
personalised SRK/T *offset* (includes central corneal thickness)	1.950 mm
equivalent personalised SRK/T A constant	118.515
SRK/T mean residual	0.00 D
SRK/T sum of the squares of the residuals	46.46 D
SRK/T standard error of the estimate	0.50 D
SRK/T mean of the absolute of the residuals	0.39 D

TABLE 3.1: Summary of results following optimization of constants used by the SRK II and SRK/T formulas. The *residual* is the actual refractive error - target refractive error (diopters).

Evaluating Eqs. 1.22 and 1.23, the mean corneal height of our biometry data sample is 3.159 mm, which differs from the original SRK/T published data set mean value of 3.336 mm. Accordingly, the ACD constant (d_0) optimised following the method of Retzlaff *et al.* [223], using Eq. 1.31, for our data set is 5.480 mm, while the mean ELP (d) as calculated using Eq. 1.32 for the same data set is 5.303 mm. These differences are not errors, nor do they indicate bias in our sample, they are simply a consequence of the relationships and definitions declared by the SRK/T formula. Applying the SRK/T expression for corneal width (Eq. 1.23), our biometry data set has a mean value of 12.45 mm, as compared to the directly measured mean white-to-white value of 12.09 mm.

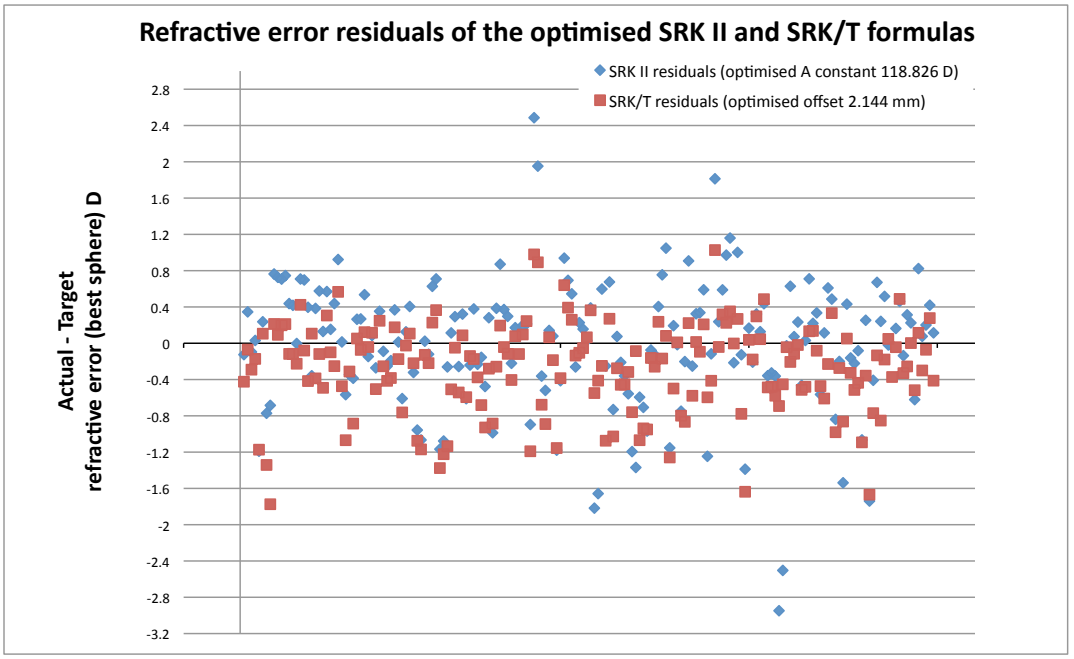

FIGURE 3.1: A plot of the *best sphere* residual error (actual - target refractive error) (diopters) for the SRK II and SRK/T formulas using an optimised A constant, which is then converted to an *offset* value according to the method of Retzlaff *et al.* [210].

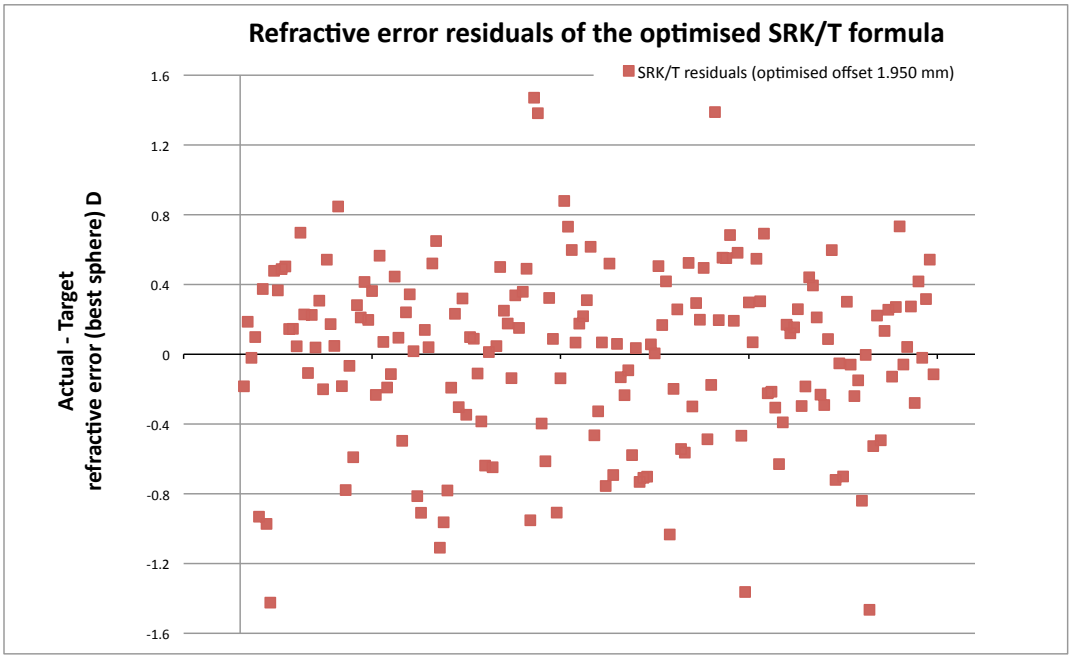

FIGURE 3.2: A plot of the *best sphere* residual error (actual - target refractive error) (diopters) for the SRK/T formula optimized using the *offset* rather than the A constant.

3.2 Preliminary evaluation and refinement

A paraxial thick lens approach was used to preliminarily evaluate the personalised eye models. This first crude modelling was helpful because it allowed rapid and straightforward calculation of the predicted *best sphere* refractive error. It also allowed parameter values to be manipulated and their effects to be readily observed over the whole collection of eyes. The results of this preliminary modelling were useful for verification and testing of the ray-tracing models (generated later in Section 3.3) for any mistakes or oversights. Preliminary modelling was performed by evaluating Eq. 3.1 with Lenstar pre-surgery biometry data and IOL metrology data. Details of the values selected for each parameter of the preliminary model (Eq. 3.1) are the same as those described later for the ray-tracing eye model in Section 3.3, except that anterior corneal shape is taken from the Lenstar autokeratometry measurement. Equation 3.1 can be derived using a step-vergence geometrical optics approach similar to that demonstrated in Appendix B. Each horizontal bar represents a division operation, separating numerator from the denominator.

$$
R = \cfrac{n_o}{\cfrac{n_o}{\cfrac{n_c}{\cfrac{n_c}{\cfrac{n_a}{\cfrac{n_a}{\cfrac{n_i}{\cfrac{n_i}{\cfrac{n_v}{t_v} - \cfrac{n_v - n_i}{r_{ip}}} + t_i} - \cfrac{n_i - n_a}{r_{ia}}} + t_a} - \cfrac{n_a - n_c}{r_{cp}}} + t_c} - \cfrac{n_c - n_o}{r_{ca}}} + t_s} \tag{3.1}
$$

where R is the predicted refractive error, n_0, n_c, n_a, n_i, n_v are the refractive indices of the air, cornea, aqueous humor, IOL, and vitreous, respectively, r_{ca}, r_{cp} are the radius of curvature of the anterior and posterior corneal surfaces, respectively, t_c is the central corneal thickness, t_s is the axial distance from the spectacle plane to the anterior corneal vertex, t_a is the axial distance from the posterior corneal vertex to the anterior IOL vertex, t_v is the axial distance from the posterior IOL vertex to the retina, t_i is the IOL

central thickness, and r_{ia}, r_{ip} are the radius of curvature of the anterior and posterior IOL surfaces, respectively. All distances have units of meters and all powers have units of diopters. A typical sign convention is followed; distances measured from the surface vertex in the direction that light is traveling are positive. For example, convex surfaces (such as the corneal surfaces) have a positive radius of curvature. Note the sign of the refractive error describes the spectacle lens power required to focus light on the retina when viewing a target at infinity.

The results of this preliminary eye modelling are presented in Table 3.2. In the first division of Table 3.2, the performance of the model is reported for its initial evaluation without any parameter manipulation. In the second division of Table 3.2, the performance is reported after increasing the distance from the posterior IOL vertex to the retina (t_v) by $300\,\mu m$. The reason for this adjustment is to attempt to *undo* the manipulation performed by the Lenstar software. The Lenstar actually measures a signal thought to predominately originate from the RPE. However, the axial length value is then converted *'in an axial length dependent manner'* [224] to report the depth as if measured to the ILM for the sake of agreement with historical optical biometry [225]. It seems that the Lenstar software makes this data manipulation for reasons of desired continuity with the IOL Master (Zeiss Meditec) and the historically developed IOL power calculations. As the manufacturer does not disclose the equation used to perform this adjustment, we estimate it with a constant of $300\,\mu m$, based on a compromise between histological and OCT normal values [226, 227, 228, 229].

The dramatic improvement following this modification is observed for the prediction accuracy (mean residual improves from -0.87 D to -0.05 D). A similarly pronounced improvement is shown in all three measures of the spread of the residuals. The standard error of the estimate improves from 1.04 D to 0.53 D.

In the third division of Table 3.2, the thick lens model's performance is reported after optimizing the distance from the posterior corneal vertex to the anterior IOL vertex (t_a in Eq. 3.1) with the addition of a constant. In this way, the axial depth of the IOL is still predicted using the normalised logistic functions (Eqs. 2.23, 2.24, Table 2.16), except that the value for the constant c is manipulated. This optimisation technique corresponds with methods used by modern industry-standard formulas, insofar as all

consistent bias[1] of the model is attributed to a single parameter (the IOL axial depth), rather than any other parameter in the model.

For our data set we found a mean optimized value of $t_a = 3.825$ mm, suggesting that the optimized value of the constant c used in Eq. 2.23 to predict IOL depth with a series of normalised logistic functions should be 4.275 mm, instead of the biometry-derived value of 4.31 mm reported in Table 2.16; a difference of 35 microns. Comparing the second and third devisions of Table 3.2, similar performance is observed in the metrics describing the spread of the residuals. By optimizing the IOL depth, the mean residual value improves slightly from -0.05 D to 0.00 D.

Accuracy of the paraxial thick lens step-vergence personalised eye model	
sample size, number of eyes (n) 184	spectacle plane distance (t_s) 12 mm
if the model is evaluated without any modification....	
mean residual	-0.87 D
sum of the squares of the residuals	199.27 D
standard error of the estimate	1.04 D
mean of the absolute of the residuals	0.88 D
if the vitreous thickness is increased by $300\,\mu m$*, then....*	
mean residual	-0.05 D
sum of the squares of the residuals	51.24 D
standard error of the estimate	0.53 D
mean of the absolute of the residuals	0.40 D
if the constant c in the prediction of IOL depth (Eq. 2.23) is modified, then....	
mean residual	0.00 D
sum of the squares of the residuals	50.18 D
standard error of the estimate	0.52 D
mean of the absolute of the residuals	0.41 D
if the measured post-surgery axial depth of the IOL is known, then....*	
mean residual	-0.01 D
sum of the squares of the residuals	38.09 D
standard error of the estimate	0.47 D
mean of the absolute of the residuals	0.37 D

TABLE 3.2: Summary of results for preliminary personalised eye modelling using a paraxial step-vergence equation. Asterisk * indicates that the same size of this sub group is slightly reduced, to $n = 174$ due to no IOL signal being detected by the Lenstar when 10 of the eyes were examined post-surgery.

Historically, a common approach to error analysis of IOL power prediction formulas has been to attribute all consistent bias to the parameter describing IOL axial depth, such that the mean of the difference between the actual and predicted refractive error equals

[1]The consistency of bias, or otherwise, is assessed with respect to the difference between the *actual* and *target* stabilized refractive error. Note that refractive error is not linearly related to all individual parameters of the model.

zero for a sufficiently large data set collected under uniform conditions. Olsen argues that if the post-surgery axial depth of the IOL is known exactly, then all consistent bias in the refractive error prediction is accounted for [3]. While it is a reasonable premise to argue that IOL depth is the parameter with the greatest uncertainty, it does not seem reasonable to dismiss the potential contributions that other parameters in the model may impart towards this bias. To investigate if other parameters in the model might be contributing, and to what degree, the refractive error prediction was re-analyzed (Eq. 3.1) using the actual post-surgery IOL depth (measured with the Lenstar) for each individual eye, instead of the predicted value from the normalised logistic functions (Eqs. 2.23, 2.24, Table 2.16). The performance of this final evaluation is reported in the fourth division of Table 3.2.

Overall, the results of this work (Table 3.2) supports the findings of Kriechbaum *et al.* [215] and Preussner *et al.* [146]; close agreement is observed between the measured mean IOL position, predicted mean IOL position, and optimised[2] mean IOL position. However, the predicted refractive error an individual eye shows a typically error of approximately 0.50 D, and this magnitude of error largely persists, even when the measured post-surgery IOL axial position is known to the model. Comparing division three and four of Table 3.2, the mean residual remains very stable, only changing from 0.00 D to -0.01 D. This provides reassurance that the value of $300\,\mu m$ added to the reported axial length, is a fairly accurate approximation for *undoing* the original Lenstar software modification, at least for a typical eye.

Even with *state-of-the-art* biometry data, analysed using a thick lens optical formula, that has been optimised for the same data set, the standard error of the estimate is still clinically and subjectively significant (0.47 D). The values reported in division four of Table 3.2 suggests that a noise floor, perhaps due to random biological variation, may exist, at least within the accuracy levels of current biometry technology. However, this study was preliminary; in Sections 3.3 and 3.5 we investigate if this noise floor can be reduced by using a ray-tracing model, instead of a thick lens paraxial model.

Continuing the analysis of the optimized preliminary model reported in the fourth division of Table 3.2, the residuals of the refractive error (actual -target) were plotted against several model parameters, to investigate if any pattern of bias might be observed (Figs.

[2]Optimised by minimizing the refractive error residuals (i.e. *actual* - target refractive error).

3.3 to 3.5). Any bias may then be attributed to the appropriate parameter by *optimization*. Recognition of systematic errors is difficult due to their combination with random errors and the fact that refractive error is not linearly related to all parameters of the model. To simplify this study, only subject-specific parameters (i.e. biometry of axial length, corneal shape, and measured IOL depth) were investigated, and subject-invariant parameters assumed from population norms (i.e. refractive index of the media, ratio of anterior to posterior corneal topography, and IOL shape) were not.

Figures 3.4 and 3.5 show no pattern of bias associated with the mean anterior corneal radius of curvature (R^2 0.01) or the measured post-surgery axial IOL depth (R^2 0.02). However, the axial length parameter (Fig. 3.3), suggests a weak pattern of systematic error. Arguably, this may not be a significant finding as the correlation coefficient is still quite low (R^2 0.13). This effect is most likely due to the fact that a constant correction of retinal thickness ($300\,\mu m$) is applied to the model, whereas the original modification by the Lenstar software is dependent on axial length. If thought significant, it may be addressed by further modification of the axial length data.

The results plotted in Figs. 3.3 to 3.5 show a constriction of the spread of the residuals on one side of each plot. This tapering feature does not indicate bias, it is expected behaviour; the tolerance of the predicted refractive error calculation becomes more forgiving as axial length increases, corneal power increases (i.e. radius of curvature decreases), and IOL axial depth increases.

Analysis of the preliminary eye model provided the opportunity to refine the methodology used to create the personalised ray-tracing eye models. The results of this study assisted decisions regarding, which parameters in the model are contributing systematic errors, and this analysis should lead to improved *optimisation* decisions. Note, that conventional *optimisation* methods used by industry-standard formulas rely on a normal distribution of the residuals (target refractive error - residual refractive error) for accuracy. The same is true for the personalised eye model.

3.3 Procedure for creating personalised eye models

Personalised eye models were simulated on Zemax ray-tracing software for 184 eyes using pre-surgery biometry data collected during the experiment described in Section

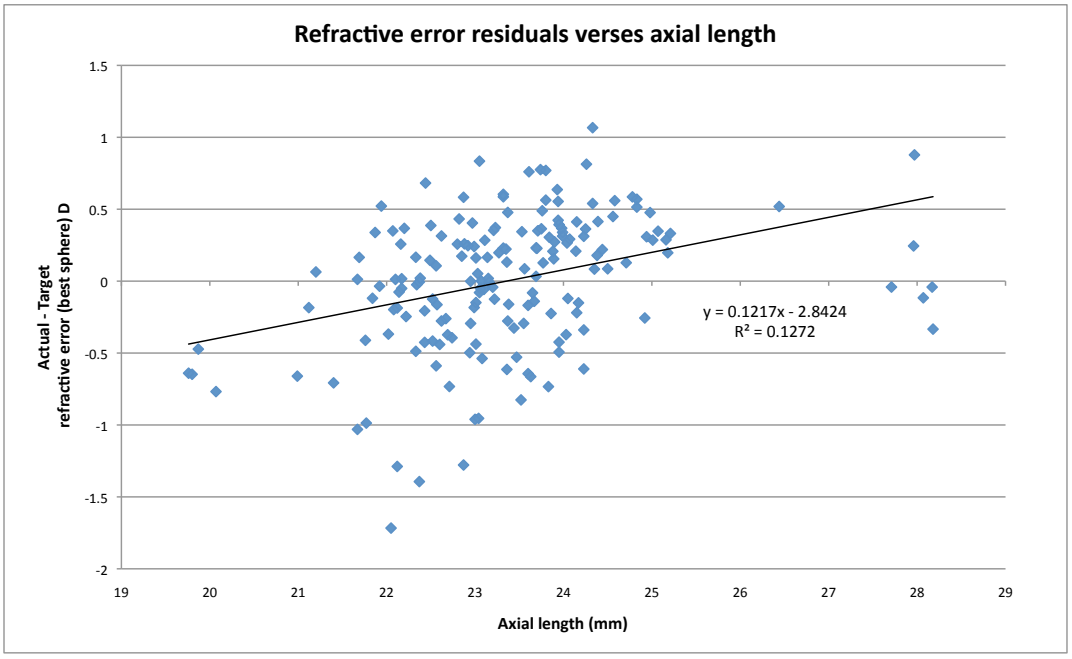

FIGURE 3.3: A plot of the *best sphere* residual error (actual - target refractive error) (diopters) against axial length.

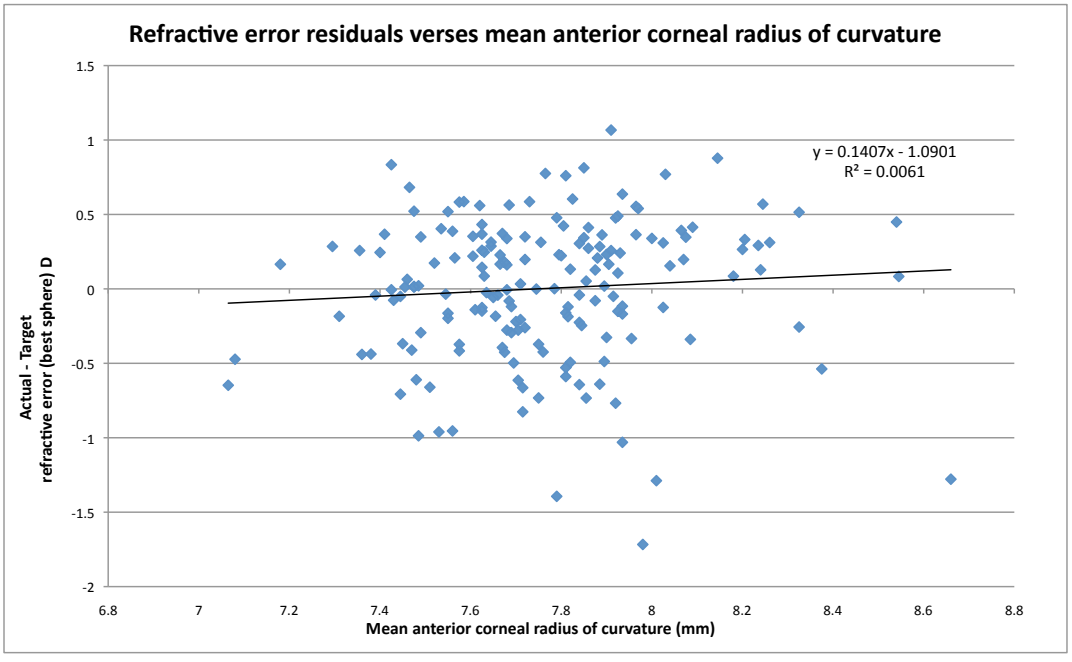

FIGURE 3.4: A plot of the *best sphere* residual error (actual - target refractive error) (diopters) against mean anterior corneal radius of curvature.

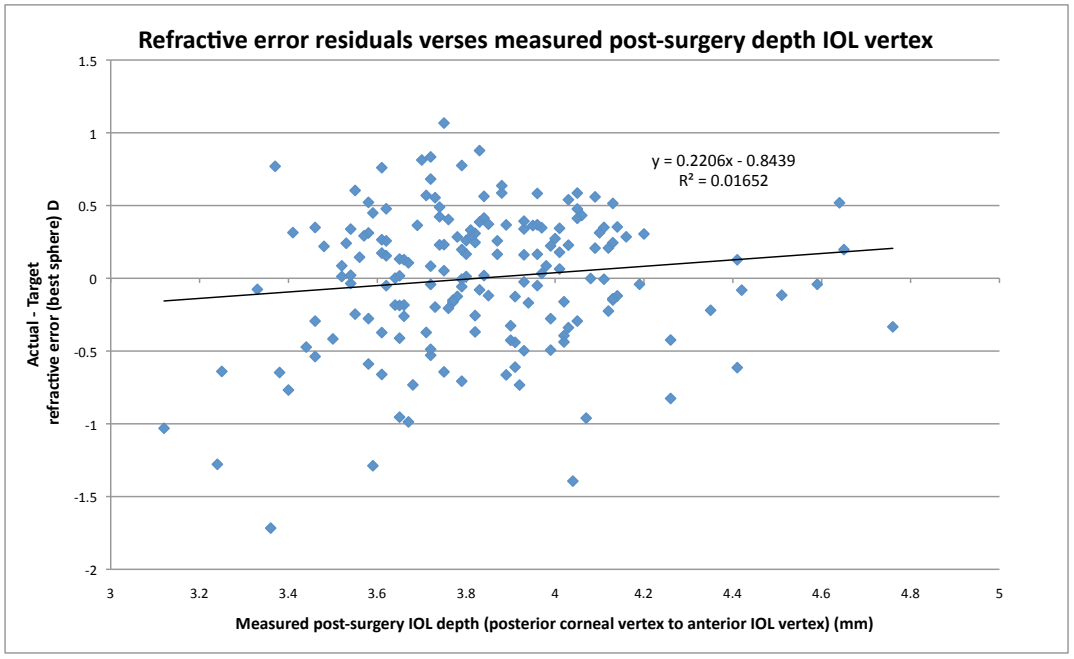

FIGURE 3.5: A plot of the *best sphere* residual error (actual - target refractive error) (diopters) against measured post-surgery axial IOL depth.

2.3, using the results and analysis reported in Sections 2.4 to 2.6, while the parameters of the implanted IOL were determined using the metrology results presented in Section 2.2. This following section describes how the eye model parameters were determined and any pre-processing performed on the biometry data before its incorporation into the model. Tocci [230] presents a useful introductory tutorial on eye modelling with the Zemax ray-tracing program. Another tutorial by Hill [231] is useful for those who have not previously used the Zemax programing language (.ZPL file), which allows user-created macros to automate repetitive tasks; this is particularly useful when analyzing a large data set such as our study of 184 eyes.

Reference axis

A selection of the most commonly used ocular axes are outlined in Section 1.3.2. As the Lenstar employs the visual axis[3] [224] for subject alignment and measurement of intra-ocular distances, it is convenient to use this same axis as a reference while generating the personalised eye model. Once the personalised eye model is established in the ray-tracing program, refractive error and wavefront analysis may then be assessed along alternative axes such as the line of sight, which has the advantage of using the principle

[3]We interpret this to be a correct statement and the Lenstar manual [213] purports this. However, disconcertingly, other product information from the manufacturer uses the term 'visual axis' interchangeably with the term 'line of sight' [214].

ray of the fixating eye as a reference and is the measurement axis used by most wavefront sensors, including the Zywave. Note that no ocular axis is perfectly static and unchanged following cataract surgery, as such any decision regarding selection of a reference axis is bound by this error constraint.

Refractive indices and chromatic dispersion

Within the literature there is a lack of direct empirical measurements of refractive index and dispersion for the human ocular media across the visible spectrum. The relatively few studies regarding this topic are not entirely appropriate for our application as they primarily concern; the tear film [24], the crystalline lens [25, 232], non-human animals [233, 234, 235, 236], or the infrared region of the spectrum [23, 237, 238, 239].

We adopt a *cherry-picking* method to discuss selection of the most appropriate refractive index and dispersion values from the data of Sivak and Mandelman [236], Patel *et al.* [240], and Zhao and Mainster [71]. The Abbe values selected for the media (apart from the IOL) correspond to the combined data of Navarro *et al.* [241] and Le Grand/Polack [242] as fitted to the Cauchy equation by Atchison and Smith [243]; although note that these values are not based on direct empirical refractive index measurements of isolated individual ocular media.

Anterior corneal surface

Elevation data from an Atlas corneal topography measurement was exported and fitted with Zernike polynomials using 28 terms over a 6 mm diameter using a Matlab script and an ordinary least squares method. To predict the effects of cataract surgery on corneal shape, certain coefficients are manipulated by the addition/subtraction of amounts specified in the final summary of Section 2.5 according to the incision location. The $Z2$ and $Z3$ tip/tilt coefficients of the fitted Zernike polynomials are set equal to zero. These terms are susceptible to large variations dependent upon the accuracy of the subject's fixation. During the corneal topography measurement, the subject is attempting to fixate a small target at a finite distance, without refractive error correction, with an eye possessing visual acuity typically worse than 6/12 due to cataract. For these reasons, and also because only one corneal topography measurement was performed, nullifying the $Z2$ and $Z3$ coefficients is a reasonable data modification. A *Zernike standard sag* Zemax surface type is used. The gross corneal shape must be represented as a radius of

curvature value in Zemax, with the smaller topographical fluctuations being described by the Zernike coefficients. If this rule is not followed, the parabasal Zemax calculations become erroneous. The necessary curvature can be calculated from the fitted Zernike coefficients using a curvature matching technique (Eq. 3.2).

$$C = \frac{\alpha_4 \, 4\sqrt{3} \; - \; \alpha_{11} \, 12\sqrt{5} \; + \; \alpha_{22} \, 24\sqrt{7}}{r^2} \tag{3.2}$$

where C is curvature (m^{-1}), α_4, α_{11}, α_{22} and the coefficients of the fitted Zernike polynomials $Z4$, $Z11$, $Z22$, respectively, as defined by Noll's format (Table 2.7), and fitted over radius (r) . All coefficients and radius units are meters.

The corneal topography data was measured with respect to the videokeratometric axis and this is approximated as coaxial with the visual axis. Therefore, no decentration or tip/tilt is applied to either corneal surface when incorporated into the model. We argue the error resulting from this approximation is likely to be of the same order of magnitude as the change in orientation of the visual axis itself due to cataract extraction and replacement with an IOL of uncertain centration and tip/tilt alignment.

An alternative possibility would be to use the Lenstar autokeratometry data to simulate the anterior corneal surface. The Lenstar spatial sampling is not as high as that of the Atlas, and it measures over a smaller area than the Atlas. However, it does offer the distinction of improved data continuity, insofar that the autokeratometry is referenced to the visual axis [224] as opposed to the videokeratometric axis. However, neither of these axes necessarily intercept the cornea at its apex[4] [244], and as such, description and reconstruction of the corneal shape is prone to false representation in either case [31].

The tear film is not included in the model; it is assumed approximately uniformly thick over the central 6 mm diameter region, with identical anterior and posterior topography (equal to that of the anterior cornea topography). As it is a thin (approximately 7 μm) [245], parallel-cap shaped volume, the amount of aberrations induced are negligible. Not withstanding, the tear film is tri-laminar, with each layer possessing different optical properties [24, 245].

[4] A seemingly common misconception, and cause for erroneous terminology use.

Central corneal thickness

The axial corneal thickness value is taken from the mean of 5 measurements performed on the Lenstar. The refractive index of the cornea is typically quoted as 1.376 in the literature [31, 246] and although a reference wavelength is almost never specified, it is reasonable to infer correspondence to the peak spectral sensitivity of the standard photopic observer (555 nm). Atchison and Smith [31] describe that each corneal layer possesses different optical properties but that the overall refractive index value is dominated by the stromal value. Patel *et al.* [240] report a study of human corneal refractive index in the visible spectrum for 10 eyes but unfortunately no other experimental data for comparison/verification of their results was found in the literature. Liou and Brennan [247] highlight the lack of direct experimental data regarding the human corneal refractive index in the visible spectrum (and also for the refractive index of the aqueous and vitreous); oxymoronically their *'anatomically accurate'* eye model employs refractive index values cited from Gullstrand's schematic eye, due to the scant alternatives. Our model also suffers from this issue, and a refractive index of 1.376 is assumed in reference to a 555 nm wavelength. The Abbe value of the cornea is estimated as 55.48 [243].

Posterior corneal surface

The posterior corneal shape is estimated using the average posterior : anterior ratios with respect to corneal radius of curvature (0.81) and asphericity (0.53) as reported by Dubbelman [138] for the 62 year age group, which is approximately a decade younger than our subject group. These ratios are evaluated using the same anterior corneal topography measurement (Atlas) described previously. For previous refractive surgery subjects an alternative method is recommended;

- the mean values reported by Dubbelman [138] should be used for posterior radius of curvature (6.40 mm) and posterior corneal asphericity (0.62). Essentially this approximates that the virgin eye possessed a typical corneal shape and that refractive surgery had negligible effect on the posterior corneal shape.
- Or preferably, if the subject's virgin anterior corneal shape is known, the Dubbleman ratio may be applied to these values to estimate the posterior corneal shape.

To evaluate the Dubbelman ratios, the anterior cornea is fitted with the general equation for a conicoid;

$$z = \frac{cr^2}{1 + \sqrt{1 - (1+k)c^2\,r^2}} \tag{3.3}$$

where z is the corneal height (m), c is the apical curvature (m^{-1}), k is the conic constant, and r is the radial distance from the apex (m). Note that Eq. 3.3 is defined using a format with symbols consistent with that used by the Zemax ray tracing program. Some clarification is necessary because the same symbol (k) is used by Dubbelman [138] to define 'asphericity' regarding a parameter that may be called 'form factor' (p) by others [31]. A value of 1 needs to be subtracted from the 'asphericity' values given by Dubbelman before they can be interpreted properly by the Zemax program as the 'conic constant' (k). Also note that the Dubbelman ratios need to be adjusted to account for this change in terminology.

If direct measurements of posterior corneal shape are available, for example from Scheimpflug photography or OCT measurements, then use of these data sets would be preferable, provided that the images were corrected for optical and geometrical distortion.

A *Zernike standard sag* Zemax surface type is used to define the radius of curvature and conic constant. A *pickup* allows the Zernike astigmatism parameters to replicate that of the anterior surface, and hence preserves Dubbelman's ratios in all meridians.

Anterior chamber depth to iris

Most eye models reported in the literature (personalised and non-personalised) use a value of 1.336 for the refractive index of the aqueous humor, consistent with the work of Gullstrand [111]. There is limited experimental data reporting empirical measurements of the refractive index of the human aqueous humor. Sivak and Mandelman [236] report measurements for cows, pigs and cats, amongst other animals. Considering a combination of both pig and cow data, one might postulate a refractive index value of 1.3352 for the 555 nm wavelength as an acceptable estimate. However, specifying refractive index to such high precision is notional as the accuracy of such experimental measurements are an overriding constraint, affected by numerous influences such as temperature. Unfortunately, due to the insufficient and inappropriate data available, we elect to follow convention, and estimate the refractive index of the aqueous as 1.336, with an Abbe value of 50.37 [243].

The axial depth of the iris plane is set midway between the anterior vertex of the pre-surgery cataractous lens and the predicted location of the anterior vertex of the IOL. This rule to designate the iris depth is speculative; it is not based on any quantitative assessment of biometric data. No distinction is made between the anterior or posterior iris plane as the iris is modelled with negligible thickness.

Pupil size, shape, thickness and position

Although it is known that anatomically the iris is slightly bowed, has a typical thickness of approximately 400 μm, and a tapered edge profile [248]; for the sake of simplicity, the iris is modelled as a flat surface (infinite radius of curvature) of negligible thickness. This approximation is acceptable in our application, as the true iris edge thickness is unlikely to influence image quality, except for extremely wide field angles.

The pupil shape is approximated as a circle, with its diameter and centration values determined by the mean of 5 measurements performed on the Lenstar. Individual decentration values are used by the personalised eye model. By contrast, generic eye models might typically use a constant 0.5 mm nasal decentration of the pupil from the optical axis, based on population mean values [247]. The pupil diameter value is intended to be representative of the pupil size under ambient luminance conditions. A *standard* Zemax surface type is used and the pupil decentration (xy) is created with a preceding coordinate break surface type. A subsequent coordinate break uses a *pickup* to reset the alignment. As the Lenstar measures the size of the entrance pupil (and not the aperture diaphragm), a trivial pre-processing calculation is performed to account for the magnification difference in size, typically 13% [31]. This adjustment is not performed by the Lenstar internal software [224]. The coordinate break takes into account the change of sign for the horizontal decentration of right/left eyes.

For analysis of the ray-tracing model prediction of refractive error, the biometry-measured pupil size is used if refractive error data measured using the wavefront sensor (Zywave) is available. In circumstances where only the autorefraction (ARK - 510A) data is available to evaluate the model, the pupil size must be conditioned by the aperture limits of the autorefractor. In this case, the lower and upper bounds for pupil diameter are set at a 2 mm and 4 mm, respectively, in correspondence to the limiting aperture of the autorefractor [249].

IOL axial depth

The IOL axial depth is predicted using a linear combination of normalised logistic functions as described in Section 2.6. Equations 2.23 and 2.24 describe these functions and the values of their associated parameters are reported in Table 2.16. The value for the constant c is taken from the thick lens model optimization (4.275 mm), before being *re-optimized* for the ray-tracing model. As this model predicts the axial depth to the mid point of the IOL, the anterior and posterior surfaces are set equi-distant from this point.

IOL alignment, shape and central thickness

The IOL alignment is assumed ideal (no tip, tilt, or decentration error) for this work. Future studies may simulate various amounts of IOL misalignment to assess the optical performance of customised designs under real-word conditions.

A *standard* Zemax surface type is suitable for elementary investigations. In this work we use a *standard* surface type regarding the prediction of refractive error of a standard (non-customized) IOL. Various other Zemax surface types are useful when investigating novel IOL designs, or when optimizing the IOL surface to correct the monochromatic aberrations. For example, a *biconic* surface type is used in the case study (Section 3.6) to create a toroidal-like surface, with the ability to apply different asphericities to each principal meridian.

In the thick lens approximation (Eq. 3.1), the IOL shape was modelled by spherical surfaces, with radius of curvature and central thickness values determined from Eqs. 2.1 to 2.6. This is an acknowledged approximation, as the Akreos Adapt AO is known to possess an aspheric surface design. To address this limitation, the IOL design was investigated with ray-tracing for six dioptric powers (19 to 24 D, in 1D steps) in an aberration-free convergent beam path, in a medium with a refractive index of 1.336. The beam convergence was set at typical levels, relevant to each specific IOL power. The focal plane was positioned such that the defocus error was zero. The anterior IOL surface was the aperture stop. The asphericity of the anterior surface of the IOL was then optimised using a zero spherical aberration merit function. The results for the optimised conic constants showed a mean value of -0.30, trending to -0.33 for the lower dioptric powers (19 D), and towards -0.27 for the higher dioptric powers (24 D). Accordingly, these values were incorporated into the representation of the IOL in the

ray-tracing model. Note that the posterior IOL surface is assumed spheric, and that the values are only indicative of this particular IOL design (Akreos Adapt AO).

The refractive index of the IOL is modelled as 1.4580, which is in agreement with the manufacturer-stated value regarding *in vivo* conditions at 35°C as reported in Table 2.1 and confirmed by the analysis reported in Table 2.3. The primary wavelength used by the eye model (555 nm) differs slightly from the reference wavelength of IOL standards (546 nm) [66].

Due to the lack of published chromatic dispersion data for the Akreos Adapt AO material, an estimated Abbe value of 55 is used, following the work of Zhao and Mainster [71]. Although Zhao and Mainster did not characterize the Akreos Adapt AO, they did perform measurements on the AMO Acrylic IOL (Tecnis ZA9003), which has a refractive index similar to that of the Akreos Adapt AO (1.47 compared to 1.458) and is from the same general family of IOL materials (acrylics). As the Tecnis ZA9003 material is hydrophobic, while the Akreos Adapt AO material is hydrophilic, this difference may affect the accuracy of the deduced Abbe value.

The capsular bag is not included in the model; it is assumed to be completely absent from the pupil region on the anterior side, while the optical properties of the posterior capsule are assumed negligible owing to its uniformity and thinness.

Vitreous chamber

The length of the vitreous chamber is taken from the mean of 5 measurements performed on the Lenstar. The vitreous length is found by subtracting the central corneal thickness, the predicted depth of the IOL anterior vertex, and the IOL central thickness, from the axial length.

The Lenstar manual states;

'Since the device measures up to the retinal pigmented epithelium, the reading displayed is adjusted to the internal limiting membrane either automatically, in an axial length dependent manner or manually.' [224]

Therefore, as the photoreceptors are adjacent to the RPE, it is necessary to readjust the axial length value to try and undo the Lenstar software's original manipulation. As the manufacturer does not disclose the equation applied, a constant value of 300 μm is

added to the vitreous thickness. This issue is an example of the need for compatibility with the historical legacies of instruments and methods, hindering the development of new methods.

The actual thickness of the sensory retina is expected to vary under influences such as age, ametropia, and the presence of retinal disease (particularly glaucoma which is known to cause thinning of the nerve fiber layer). The Lenstar adjustment 'in an axial length dependent manner' may roughly incorporate the effect of axial ametropia, however the influence of age, retinal disease, and individual anatomical variation on retinal thickness are currently disregarded by biometry instruments. The reason for the retinal thickness adjustment is solely to support legacy instruments and IOL power calculation formulas, and to this purpose the actual thickness of an individual's retinal thickness needn't be known, because such information was not used (or indeed available) during the development of these formulas. For personalised ray-tracing eye modelling, an individual's variation in retinal thickness contributes useful information in cases reliant on ultrasonography measurements of axial length. However, as the distance from the RPE to the photoreceptors is relatively consistent between subjects, an individual's variation in retinal thickness may be superfluous in cases of optical interferometry measurement, provided the axial length data was reported without a retinal thickness manipulation.

The scant availability of empirical measurements of refractive index for the human vitreous means that this value is simply assumed from Gullstrand's model, as is the convention. The refractive index of the vitreous is estimated as 1.336 ($\lambda = 555$ nm), with an Abbe value of 51.30.

Retina

The retinal shape is modelled as a *standard* Zemax surface type with a radius of curvature of -12 mm. This value follows the work of Escudero-Sanz and Navarro [250], although note this value is not based on direct anatomical measurements. This parameter value is a constant; however, in the future it may be possible to personalise this value based on an individual eye's biometry data. Liou and Brennan [247] highlight the lack of experimental data regarding retinal shape. Some progress is recently been made in this area regarding the foveal pit contour [251] but not for the larger macula region as a whole.

3.4 Optimization and merit functions

For many applications of personalised eye models, consideration must be given to detailed issues such as; the field angle under investigation (i.e. the angular size of the object being critically viewed), the spatial frequency content of the object, the spectral frequency of the object, how to weight the various constituent wavelengths to account for the spectral sensitivity of the eye, how to weight the pupil function to account for the Stiles-Crawford effect, and what merit function, or combination of merit functions, should be used to assess retinal image quality. Many classical merit functions are mostly relevant for a near diffraction-limited optical systems and are not particularly well suited to describing a population sample of eyes, who's retinal image quality can vary across a range of blur levels. A more coarse metric (such as refractive error) is better suited to the ophthalmic situation.

In the first instance, the performance of the personalised ray-tracing model is evaluated by investigating its accuracy in predicting the post cataract surgery refractive error. Thus, for this initial application, incorporation of the features and considerations listed above is unnecessary. Other researchers have previously described suitable strategies to address these issues, and to take full advantage of the utilities possible with ray-tracing software [60, 61, 64, 221, 222]. The work reported here has been analyzed using the personalised ray-tracing model in perhaps its most simplified form. The purpose being primarily one of validation; ray-tracing with real biometry data must be first proven reliable in consideration of the second-order terms (defocus and astigmatism), before it's predictions of higher-order terms can be interpreted and accepted with confidence.

The model was evaluated under the following arrangement. The ZPL script reads and loads all parameters that the model will require from a previously prepared text file. An on-axis point source is positioned at the front focal plane of a positive powered paraxial lens. The resulting collimated beam then propagates 12 millimeters to the anterior corneal vertex. The wavefront enters the eye and is refracted to focus near the fovea. The paraxial lens induces no aberration to the wavefront, but the unique aspects of the eye do, and the resulting retinal image is blurred. The ZPL then runs an optimisation of the distance between the object point source and the paraxial lens. In this way, reminiscent of a Badal optometer. The optimisation reduces the image (retinal) blur using the default Zemax merit function. By simple calculation, the defocus (*best sphere*

refractive error) of the eye is found according to Eq. 3.4.

$$R = \frac{1}{f} - \frac{1}{d} \tag{3.4}$$

where R is refractive error in diopters, f is the focal length of the paraxial lens in meters, and d is the optimised distance separating the point source from the paraxial lens, in meters. The paraxial lens must be quite highly powered. Its power sets the upper limit of hyperopia the model can describe, while the 12 millimeter distance from the paraxial lens to the eye sets the limit of myopia measurable. The way that the Zemax software performs optimisation, also makes it important that this lens be highly powered. Otherwise, the perturbation step size of the optimisation algorithm may not find the true global minimum. This arrangement; defining the paraxial lens focal length as fixed, while the object distance is the solved variable is a simple way to let the optimisation program cross over from searching in a hyperopic domain into a myopic domain. The vice-versa arrangement (fixed object distance, variable focal length) is not suitable as to change sign (swap from myopic space to hyperopic space), as the focal length must pass through a zero value which creates a strong discontinuity.

The model assumes monochromatic light ($\lambda = 555$ nm). No compensation is made for the Stiles-Crawford effect. No assumptions are necessary regarding the spatial frequency of the scene that the eye is observing. Refractive error is described relative to an infinitely distant fixation target, as by definition. Slight errors result from the difference between the planes of reference used by, the model and autorefractometer (spectacle plane), and the wavefront sensor data (pupil plane). As all eyes are near-emmetropic, this error is relatively small. At the end of each optimisation the ZPL script reports the distance value (d) (as well as other results such as Zernike wavefront aberrations). It then resets the point source object back to the null position at the front focal plane of the paraxial lens, before proceeding through to analyze the next eye model in the data set.

3.5 Performance of Personalised Eye Model

The refractive error predicted by the ray-tracing model was compared to the actual observed refractive error. All of the methods for analysis are the same as that applied to the SRK/T and thick lens models described earlier, except that for five eyes, corneal

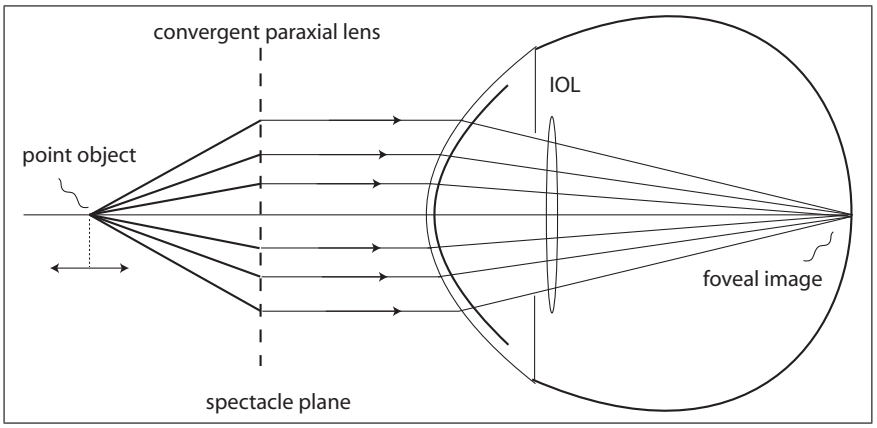

FIGURE 3.6: Schematic layout of the evaluation method of the ray-tracing personalised eye model.

topography measurement was not possible, and so the sample size is reduced. One important feature of real ray-tracing compared to calculations in the paraxial domain, is the sensitivity of the system to pupil size. It is essential to exactly match, the pupil size of the model with that used by the instrument providing the refractive error measurement (Zywave and ARK-510A).

Following the results of the preliminary eye model reported in Section 3.2, the ray-tracing model was refined by adding a constant to the vitreous thickness, and investigating if the constant c in Eq. 2.23 for prediction of IOL depth, required any adjustment from its default value of 4.31 mm.

The results of the first division of Table 3.3 are reported after correcting the Lenstar modification of axial length from the retinal pigmented epithelium (RPE) to the inner limiting membrane (ILM), by adding a constant distance of $200\,\mu m$. This value is remarkably different to the $300\,\mu m$ constant used in the thick lens model. This difference can be explained by the additional contribution of asphericity of surfaces in the model, affecting the ray-tracing model position of minimum blur by inducing positive spherical aberration.

It was not necessary to shift the IOL depth significantly to optimise the refractive error prediction once the *undoing* of the retinal thickness adjustment was performed. The prediction of the IOL depth using the linear combination of normalized functions (with $c = 4.31$) seemed quite successful. Instead, it became apparent that the corneal topography data from the Atlas was a more deleterious source of error. The corneal elevation data was re-analyzed using a lower number of Zernike fitting terms and fitting over smaller

diameters. Combinations of conservative fitting orders and diameters (e.g. 15 Zernike terms over a 4 mm diameter) did not greatly improve the model's predictive ability. This suggests the blame lay in the *single* measurement of one topography image, and the fact that the Placido disc technique is susceptible to tear film disturbances. From the results in the second division of Table 3.3, it is apparent that by substituting the Lenstar auto keratometry data into the model, in place of the Atlas topography[5], a slight improvement in all three metrics for the spread of the residuals is observed.

One of the most exciting features of the ray-tracing model, not considered in any way by the paraxial formulas, is the ability to investigate pupil decentration. Before investigating the characteristics of the ray-tracing model, it was assumed a great sensitivity would be imparted by this parameter. However, this was not observed, at least when considering the mean monochromatic defocus as reported here. Decentering the pupil under monochromatic conditions did not impart significant changes in *best sphere* refractive error or optical power in the eye. Other metrics such as HOAs, the point spread function as measured by RMS spot size, or transverse chromatic aberration under chromatic simulation, are likely to have much greater sensitivity in portraying the influence of a decentered pupil.

Another possible explanation is that the pupil decentration itself represents an emmetropization process. Just as the eye adjusts its axial length and corneal curvature during growth stages to generally trend towards an evolutionary ideal, perhaps the pupil centration is also representing not just an idiosyncrasy, but a unique parameter which has taken up a centration with respect to the other ocular surfaces, in an effort to balance and complement each other to the benefit of the overall goal, of improved vision. The ray-tracing model showed negligible effects on average when the pupil decentration was considered. The third division of Table 3.3 shows identical values to those reported in division two; setting the pupil on the visual axis or decentering it seems to have minimal effect on monochromatic defocus refractive error.

The spread of the residuals (actual refractive error - predicted refractive error) for the ray tracing model are plotted in Fig. 3.7. In the same plot, the residuals of the optimised SRK/T formula are shown to provide a gauge and comparison. The performance of both methods, at least in this study, seem of similar reliability regarding the ability to predict

[5]The Atlas data is still used to generate a conic constant value.

the refractive error (and indirectly, optimal IOL power). The ray-tracing method does provide greater amounts of information, although it also requires greater resources to be dedicated to biometry measurement and analysis.

Accuracy of the ray-tracing personalised eye model	
sample size, number of eyes (n)	179*
if the model is optimised using a retinal thickness value of 200 microns, and $c = 4.31$....	
mean residual	0.03 D
sum of the squares of the residuals	74.09 D
standard error of the estimate	0.64 D
mean of the absolute of the residuals	0.51 D
if the Atlas topography data is replaced with Lenstar autokeratometry data....	
mean residual	0.02 D
sum of the squares of the residuals	51.26 D
standard error of the estimate	0.53 D
mean of the absolute of the residuals	0.42 D
if using the Lenstar autokeratometry data, but pupil decentration is set to zero.....	
mean residual	0.02 D
sum of the squares of the residuals	51.26 D
standard error of the estimate	0.53 D
mean of the absolute of the residuals	0.42 D

TABLE 3.3: Summary of results for the ray-tracing personalised eye model compared to the post-surgery refractive error actually observed. Asterisk * indicates the sample size is lower than that of the SRK/T study due to absent Atlas data for five eyes.

3.6 Case study of customized IOL design

Personalised ray-tracing eye models, along with psychophysical experiments using adaptive optics vision simulators [252], are fundamental investigative tools for developing decision-making criteria concerning what HOAs an IOL should attempt to correct, for each individual eye. Each aberration mode is present in differing amounts for each individual eye [41, 253]. The deleterious effects on vision for each aberration mode are not equal. Furthermore, the tolerances for alignment and positioning of the IOL vary, depending upon which aberrations are being corrected. IOL designs with HOA correction are known to be more sensitive to tilt, decentration, and axial depth errors. However, for typical values and typical combinations of these misalignments, their optical performance is theoretically superior to that of a defocus-only IOL correction [221, 222, 254].

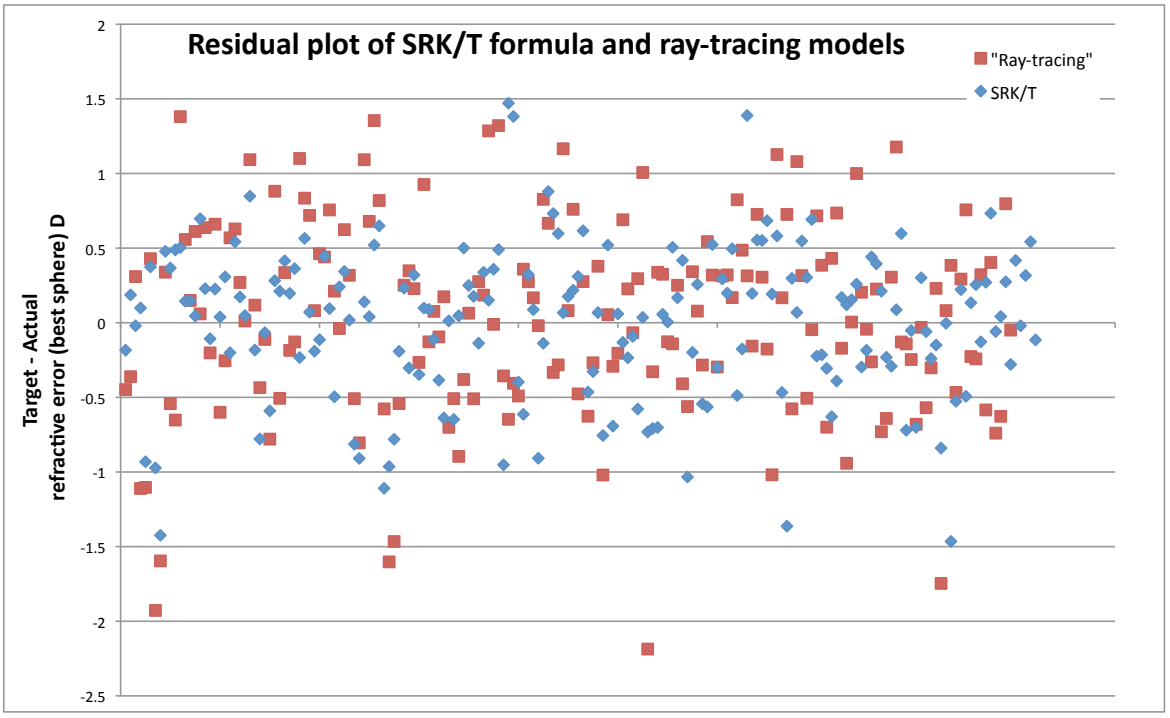

FIGURE 3.7: A plot of the *best sphere* residual error (target -actual refractive error) (diopters) for the optimized SRK/T formula and the optimized ray-tracing model. Note that the sample sizes differ from 184 (SRK/T) to 179 (ray-tracing).

The relatively large magnitude of spherical aberration (relative to other HOAs) amongst the population [41], and the fact that it is a rotationally symmetric aberration, makes its tailored correction a likely goal of any future trials of customized IOLs. The benefit of HOA correction is dependent on the elimination, or near elimination, of the second-order aberrations of defocus and astigmatism.

From the data set, an eye with typical axial length, corneal shape, pupil size, and refractive outcome was selected to study in regard to customisation of the IOL design. For this eye, a case study of three IOL designs were modelled;

- defocus correcting
- defocus and astigmatism correcting
- defocus, astigmatism, and spherical aberration correcting

The results of the spot diagrams are shown in Figs. 3.8 to 3.8. While the wavefront Zernike coefficients (units of waves) are reported in Table 3.4.

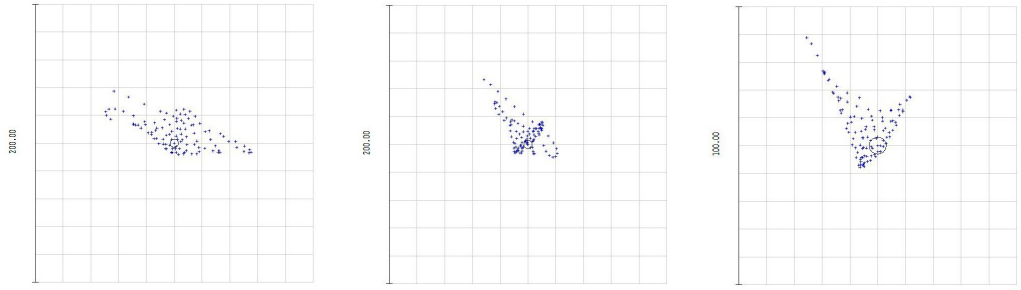

FIGURE 3.8: The spot diagram of a spherical, toroidal, and biconic IOL design, each optimized for the same typical eye. The Airy disc is marked as a black circle for reference.

Case study aberrations of three different IOL designs for a typical eye			
	IOL designs for a typical eye		
Zernike Polynomial	Spherical	Toroid	Biconic
Z 4	0.358	0.007	0.000
Z 5	-0.617	-0.617	-0.621
Z 6	0.901	0.002	-0.028
Z 7	-0.204	-0.203	-0.205
Z 8	0.085	0.086	0.077
Z 9	0.025	0.024	0.021
Z 10	-0.043	-0.042	-0.046
Z 11	0.155	0.156	0.006
RMS (to principal ray) (waves)	1.341	0.924	0.911
RMS (to centroid) (waves)	1.183	0.678	0.662
Variance (waves squared)	1.400	0.460	0.438

TABLE 3.4: Summary of Zernike coefficients for the ray-tracing personalised eye model, showing a step-wise reduction in aberration as the design of the IOL becomes personalised.

3.7 Assumptions and limitations

Only a single Atlas corneal topography measurement was recorded at each pre and post surgery examination. Thus, the personalised eye models are somewhat susceptible to measurement error and other noise such as tear film fluctuations. When planning the experiment protocol, the inclusion of the two autokeratometry measurements, and time constraints were factors in the decision to perform only one corneal topography measurement. If time had permitted multiple measurements of corneal topography, then each elevation data file could be fitted with Zernike polynomials, with the mean coefficient of all trials being used to simulate the corneal surface. This is a preferable approach, and it is recommended for any future experiments regardless of the instrument technology (e.g. OCT, Scheimpflug photography, or Placido disc).

As the posterior corneal surface accounts for nearly 10% of the refractive power of the cornea, its *direct* measurement should be the goal of any eye characterization. The posterior corneal shape was estimated by using a population mean correlation with the anterior corneal shape, rather than by direct measurement of both surfaces. This limitation was due to the unavailability of our preferred topographer (Pentacam, Oculus). As highlighted in the work of Dubbleman *et al.* [255], the correlation of asphericity between the two surfaces is not always reliable. For eye modelling, direct measurement of the posterior corneal shape is recommended whenever possible.

When measuring biometry of a pseudophakic eye, the Lenstar software only allows user-control to designate the IOL material as either; silicone, acrylic, PMMA, or default. As the IOL used in the study was the Akreos Adapt AO, the *acrylic* setting was selected. However, a more widely used acrylic material is the Acrysof (Alcon) [106], which has a much higher refractive index (1.55) compared to the Akreos Adapt AO (1.458). As such, if the time of flight calculations of the Lenstar software assume a refractive index biased towards the more popular 1.55 value, then the position of the IOL midpoint may be underestimated, typically by approximately 30 microns. Note that the true anterior IOL vertex location is unaffected by this error; however, in the vast majority of cases, only a signal from the posterior IOL surface was observed, and the data set is therefore prone to this potential error.

The retinal surface topography is approximated with a radius of curvature of -12 mm and is not measured for individual eyes. This does not influence the results of our initial study, as a single on-axis field angle (point source at the fovea) was considered, however, retinal curvature does affect image quality when finite object sizes or off-axis field points are considered.

Following completion of the clinical data collection, we became aware of an additional measurement capability of the Lenstar. The manufacturer purports that *'with an additional 10 second step, the user can obtain exact retinal thickness at the point of the patients line of sight.'* [225]. Perhaps this extra data could have assisted in tailoring a retinal thickness correction value for each individual eye, rather than employing the constant $300\,\mu m$ value ? It is tempting to presume that the Lenstar software uses this value for its correction of axial length from the RPE to the ILM. However, it is also possible that the two calculations are not linked in this way by the instrument software.

The refractive index and chromatic dispersion values of the media are assumed from Gullstrand [111] according to convention. This approach is based on consensus rather than direct experimental measurements and is a source of potential error.

In the work reported here, monochromatic light was used, and so chromatic dispersion was not invoked by the ray-tracing program. However, chromatic dispersion is an important consideration for many other scenarios and applications that one may investigate with the ray-tracing eye model. The model has declared Abbe values of the ocular media for this future purpose.

There is no scientific dictum specifying what size diameter corneal topography measurements should be employed when creating an eye model. During the planning stages of the experiment, it was anticipated that corneal topography data would be fitted over an 8 mm diameter. This protocol was modified to a 6 mm diameter after preliminary analysis found that most topography measurements were incomplete with very sparse sampling at diameters greater than 6 mm. All absent data points were peripheral, mostly in the superior region, typically obstructed due to the upper lid ptosis of the elderly age group. For previous refractive surgery patients, a smaller fitting diameter risks the full magnitude of HOAs not being represented by the model. Thus, the goal is to find a compromise; obtaining the most *reliable* corneal topography description over the *greatest* area.

The basis functions used to fit the corneal topography are partially set by the exported data format of the instrument. For example, the cartesian sampling reported by the Pentacam (Oculus) lends itself to generation of *grid sag* surfaces with bicubic spline interpolation in the Zemax software (zonal reconstruction). By contrast, the polar sampling reported by the Atlas lends itself to generation of a *Zernike standard sag* surface in the Zemax program (modal reconstruction). Particularly for atypical corneas, modal reconstruction using basis functions fitted to the corneal topography elevation with a finite number of polynomials, will unavoidably smooth the data to some degree.

There is no scientific dictum concerning which basis functions to use for describing the corneal surface. Zernike polynomials are a commonly used set of basis functions, but they are not without their limitations [152].

The corneal topography instrument itself performs discrete sampling at a finite number of locations, although it is generally thought that modern technologies describe typical corneal shape with reasonable accuracy. The issue of selecting the most appropriate basis functions to represent the corneal surfaces becomes a moot point if the internal software of the topographer does not provide true raw elevation data in its exported files. In this case, it may be best to match the basis functions describing the surface in the ray-tracing program, to that used by the topographer (if known).

Future work may extend the analysis of this data set, to include comparison of other modern formulas (e.g. Holladay, Holladay II, Hoffer Q, Hagis, Olsen), not included here for the sake of being concise. The SRK/T performance is considered representative of the modern formulas, especially for typical eyes.

All of the measured parameters of the eye model contain errors and uncertainty. Further reading is recommended for details regarding; the stability of aberrations and corneal topography [256], accuracy and repeatability of the Zywave wavefront sensor [257], accuracy and repeatability of the Atlas corneal topographer [258], manufacturer-claimed accuracy, repeatability and dynamic range specifications for the ARK-510A auto-refractor/autokeratometer [249], and the Lenstar biometer [224].

Summary

The main question this work has attempted to address is;

Can the personalised ray-tracing eye model predict the post-surgery defocus refractive error with any greater reliability than current industry-standard formulas? and if not, what are the main issues?

Generally it seems the prediction performance is similar for ray-tracing and the industry-standard formulas. The main limitations for personalised ray-tracing eye models are;

- the accuracy in predicting the stabilized axial depth of the IOL, at least insomuch as this parameter can be considered static in the absence of accommodative effort,
- the accuracy of the refractive error (the metric by which the ray-tracing model is judged), as measured by autorefractors, wavefront sensors, or subjective techniques,

- the accuracy in measurement or prediction of the posterior corneal shape,
- the accuracy and precision of assumed refractive indices of the ocular media.

These four issues are also prime sources of error for the industry-standard formulas [126]. However, we expect that a ray-tracing methodology is better able to take advantage and capitalize on any future advancements that may be realized regarding these four areas.

Our results showed ray-tracing performed similarly to the SRK/T formula when considering a biometry data set of *normal* eyes. We propose the advantages of the ray-tracing methodology would become more pronounced when applied to a data set of *abnormal* eyes.

Some researchers suggest the prediction of IOL axial depth may be improved if pre-surgery biometry measurements of the cataractous lens shape were known, especially concerning the peripheral areas near the lens equator (not just within the apical zone). Lens shape in this region is difficult to measure *in vivo* by any technique. OCT offers capabilities for analyzing the anterior cataractous lens shape, but becomes far less reliable regarding the posterior lens shape, particularly in cases of moderate to dense cataract. For Scheimpflug photography the task of imaging the anterior cataract lens shape is achievable, but even in the case of a transparent crystalline lens, imaging the posterior surface is only possible at acute angles, due to the depth of this surface and the observation angle constraint set by the pupil size. Scheimpflug imaging of the posterior crystalline lens is possible, but the severe geometrical distortion induced by the acute angles required, leads to a significant lose of resolution with respect to the z dimension. Let alone the reliability issues encountered when cataractous lenses are considered.

If the posterior cataractous lens shape is an important parameter for predicting the IOL position, then ultrasound technologies may be more reliable in the cataractous eye, even though in most other applications, acoustic resolution is inferior to optical. Additionally, if the peripheral lens shape near the equator is important, then ultrasound becomes an even more attractive solution owing to its ability to image through the iris. By contrast, optical technologies are limited to image within the maximum dilated pupil size, which may not be sufficient, particularly within an elderly patient group. Other imaging modalities such as MRI may be technically capable of imaging the cataractous lens shape in high resolution, but this solution is prohibitively expensive.

One final suggestion is to predict information about the cataractous lens shape by avoiding phacometry altogether, and to instead model the lens shape indirectly from the phakic refractive error measurement. If the cataract density is mild enough to permit accurate refraction (or wavefront aberration) measurement, then a personalised *phakic* eye model can be simulated with ray-tracing software. Combined with other typical pre-surgery biometry measurements (segmented axial length, anterior/posterior corneal topography), the cataractous lens shape may be *optimized* (from some initial seed value based on population norms), such that the model generates the same refractive error as that measured clinically. Admittedly, the estimated refractive index of the cataractous lens may be fairly noisy, given the large individual variation that can occur, especially with nuclear sclerotic cataract development. Even so, such *phakic* personalised eye modelling on ray-tracing software may provide useful information about the cataractous lens shape, which in turn may provide information about the equatorial plane of the cataractous lens, and lead to improved accuracy in prediction of the stabilized axial position of an implanted IOL.

Chapter 4

Conclusions

4.1 Areas of success

This thesis reports a detailed methodology for measuring ocular biometry and IOL metrology data required for generation of personalised eye models and determination of the optimal IOL power/design required following cataract extraction. A laboratory-based study of IOL metrology was performed to characterize the geometrical properties of the Akreos Adapt AO (Bausch and Lomb) IOL. A clinic-based study of patients undergoing cataract surgery was performed and analysis of this data was presented with specific attention given to the prediction of:

- anterior corneal shape changes due to cataract surgery, and
- methods to predict the geometrical axial position of the stabilized IOL.

The steps required to combine this knowledge and create personalised eye models on ray-tracing software were presented with an emphasis on comparison of performance regarding the accuracy of the defocus refractive error prediction verses that of a current industry-standard method (SRK/T formula). A case study was presented to demonstrate some of the useful features of personalised eye models, especially regarding simulation of IOL designs intended to correct the monochromatic aberrations of the eye. Original ideas such as *a method to predict the IOL axial depth using a linear combination of normalised logistic functions*, and new findings such as *quantitative results describing the typical change in anterior corneal topography following cataract surgery* were

developed. Our work to characterize the Akreos Adapt AO (Bausch and Lomb) apical shape and central thickness represents the first public disclosure of these geometrical parameters that we are aware of.

Historically, schematic eye models were based on mean population values and broadly classified as either paraxial or finite. The topic of personalised eye modelling is a developing area of interest within the literature [60, 61, 62, 63, 64, 146, 218, 220] and provides a powerful and feature-rich modality to investigators and researchers. The personalised eye model is a tool which complements the large amount of work that has already been dedicated to the development of generic non-customized eye models [65, 111, 241, 242, 247, 250, 259, 260, 261, 262, 263, 264, 265, 266] and statistical eye models [267, 268]. Ray-tracing personalised eye models allow simulation of IOL designs *optimized* according to a specific quality metric (e.g. RMS spot size). It is a powerful tool for comparison and characterization of novel IOL designs.

The overall aim of this work was to investigate personalised eye models using ray-tracing techniques, with a hypothesis that IOL power prediction by current industry-standard formulas, based on paraxial thin lens approximations, may be improved upon. The work was carried out with a view to future developments, in anticipation that atypical eyes (such as those having undergone previous refractive surgery), might benefit from a customized IOL design correcting the higher-order aberrations of the eye. The prescription for such a customized IOL may be derived from ray-tracing personalised eye models.

4.2 Areas of limitation

Personalised eye modelling should particularly benefit cataract patients with high amounts of HOAs (e.g. post refractive surgery, post corneal graft, pellucid marginal degeneration, or keratoconic patients), extreme values of axial length and corneal power, large pupils, or atypical combinations of values (e.g. a short eye with a flat cornea). Ray-tracing is a more scientifically rigorous approach to the issue of IOL power calculation than is currently used by the industry-standard formulas. Although, for typical eyes, the paraxial approximation for IOL power calculation may be considered adequate for many applications.

Many inter-related and complex optical phenomena and visual processes make it difficult to know if the correction of monochromatic HOAs with a customized IOL design will result in improved visual performance under real-world conditions. Some of the difficulties and challenges of such a task include; the temporal fluctuations of the ocular aberrations, neural processing issues, neural adaptation [269], scatter [57], diffraction, interaction with chromatic aberrations, subjective tolerance to blur (especially under binocular viewing conditions), tear film fluctuations, and age-related pupil miosis. These effects may negate, or partially negate, the benefits of HOA correction with a customized IOL. Additionally, there are many other manufacturing, verification, surgical, logistical, and commercial challenges associated with the development of customised IOLs.

Particularly for typical eyes with near-median biometry values and low amounts of corneal HOAs, the visual outcome may not necessarily be enhanced by use of a customized IOL design. In such circumstances, the cost-to-benefit considerations may preclude the use of a customized IOL design, however this does not prohibit the use of personalised ray-tracing eye models to determine the optimal generic IOL design or power.

4.3 Future research opportunities

Various modalities for HOA correction in the eye are being investigated, such as intraocular lenses [252], contact lenses [270] and refractive surgery [185]. In addition to the application investigated here (modelling the pseudophakic eye with an *in-the-bag* type IOL), personalised ray-tracing eye models may be applied to;

- Modelling the pseudophakic eye with other various types of IOLs, e.g. angle-supported, sulcus-sutured, iris-supported, add-on/piggy-back.
- Modelling the eye with various phakic-IOL types, e.g. phakic angle-supported, phakic sulcus-supported, phakic iris-supported.
- Ablation pattern design for refractive surgeries such as personalised LASIK and PRK.
- Other studies of the phakic eye, e.g. myopia development, the delivery of laser therapy to the retina, design of new technologies for ocular imaging, etc.

Dynamic aberration correction might also be possible in the future with adaptive devices [271].

Action in several areas will assist the development of personalised ray-tracing models for IOL design;

- Call for geometry to be disclosed for all IOL designs, especially those in high use.
- Call for disclosure of the refractive indices used by optical biometry instruments (IOL Master and Lenstar) regarding time-of-flight calculations.
- Call for disclosure of equations used by optical biometry instruments (IOL Master and Lenstar) regarding time-of-flight calculations and manipulations.
- Call for segmented axial length data measured by optical interferometry to be reported without a 'retinal thickness' manipulation.
- Call for further studies of the refractive indices of the human ocular media, over the visible and infrared spectrum.
- Call for further studies of phacometry and the development of instruments for topographical phacometry. Phacometry data may be a useful parameter for improving the prediction of the stabilized IOL axial depth.
- Call for further studies measuring the IOL depth, tilt, and decentration, particularly regarding how these parameters change during the healing and stabilization period. There is little data available concerning the medium to long term (months and years) IOL axial position. Such information regarding stability/fluctuation of the IOL position would be valuable in fields of IOL design and necessary late interventions such as Nd YAG laser capsulotomy.
- Call for development of novel methods for prediction of the stabilized IOL axial depth.
- Call for biometry instrument manufacturers to remove obsolete formulas from their software, e.g. the SRK II formula. Both instrument manufacturers and IOL manufacturers must underline the need to depart from limited traditional formulas that are still in widespread use.

If progress can be made in these areas; faster, more accurate, and more confident development could be achieved in the field of personalised ray-tracing eye modelling and customized IOL design.

Personalised ray-tracing eye models, in partnership with psychophysical experiments, can address the following topic;

Given the errors in biometry measurements and uncertainty in the stabilized IOL position and alignment, which HOAs should an IOL design attempt to correct ?

If HOA correction by customized IOLs is attempted, consideration must be given to the choice of which aberrations to correct, and by what amount. Research is continuing to establish how visual performance is affected by different aberration modes of equal wavefront variance [41, 272, 273]. In general, modes with lower angular frequency terms seem to be more deleterious on visual performance than higher angular frequency terms [274]. Spherical and coma aberration modes are thus attractive candidates for personalised IOL correction.

If development eventually proceeds to clinical trials of customized IOL designs, we suggest initial efforts should attempt to correct defocus, astigmatism and spherical aberration, before attempting the correction of other HOAs. Candidates for such hypothetical trials should posses large amounts of corneal spherical aberration. Furthermore, to improve the resilience of retinal image quality in the event of IOL misalignment and other perturbations, the hypothetical candidates should require a low defocus correction (i.e. they should posses a longer than average axial length and/or a higher than average corneal power). An associated future research topic is: Do previous *myopic* or *hyperopic* refractive surgery patients possess greater amounts of HOAs, and which of these groups are most likely to benefit visually from a customized IOL design ?

The method presented for the prediction of IOL axial depth using a linear combination of normalised logistic functions may be expanded upon in the future, if other biometry parameters are found to improve the prediction (e.g. cataractous lens shape). The addition of new logistic functions to the linear series is allowable, and facilitated by its arrangement.

The increasing prevalence of myopia, particularly evident in Asia as associated with greater access to education, greater amounts of near work, and greater population urbanization, will likely coincide with increased affluence and access to ophthalmic services within these populations. It is reasonable to anticipate that such factors will drive continued popularity of corneal refractive surgery and therefore reinforces the importance of developing a methodology to determine the optimal IOL design for such surgically-altered eyes.

Increasing access to both corneal refractive surgery and cataract surgery amongst the population strengthens assertions promoting that biometry measurements should be performed early. That is *i*) before corneal refractive surgery, and *ii*) before cataract maturity prevents optical interferometry measurement and would otherwise later require ultrasonic measurement of axial length. Such data could be banked until such time in the future if/when proceeding with cataract surgery this data would be a valuable planning asset.

4.4 Conclusions

Development of a personalised IOL is an *of-the-moment* idea; during the 1990s there was a large increase in the popularity of corneal refractive surgeries and this generation of patients are now approaching later life and require cataract operations. The standard IOL power formulas and generic IOL designs do not provide consistently successful outcomes for these patients because they rely on models too simplistic to deal with highly aberrated corneas, extreme values of corneal power and axial length, or atypical combinations of such.

This work combined laboratory techniques (performing IOL metrology) and clinical measurements on subjects (performing biometry measurements), which were then used to simulate personalized eye models on ray-tracing software.

Ray-tracing of any optical system will provide more detailed and more accurate information than equations based on the paraxial approximation; provided that an ideal scenario is applied, where all parameters in the optical system are known with reasonable accuracy. In the real-life scenario, the parameters of the system are not all known accurately, and indeed natural biological variation may limit the accuracy level to which

some parameters can be known. If we consider two optical models (one paraxial and the other ray-tracing), each receiving the same input data, with all of its associated errors and uncertainty, each will produce a different result, and there are three possible outcomes;

1. The errors of the input data may be sufficiently low, such that the ray-tracing model provides greater types of information and more accurate information than the paraxial model.
2. The errors of the input data may be moderate, such that the ray-tracing model provides greater types of information, but with a similar accuracy to that of the paraxial model.
3. The errors of the input data may be high, such that, although the ray-tracing model provides greater types of information than the paraxial model, the accuracy of this information is unreliable.

In this third case, there is no motivation to proceed with the extra effort required to measure and include the additional parameters and complexity required by the personalised ray-tracing model. In this situation, the extra parameters (measured for each individual eye) are so unreliable (compared to their estimation with a population norm), that the advantages of theoretical accuracy associated with ray-tracing, is overwhelmed by the errors, and no benefit is realised. This third case seems disproven by our results.

The purpose of this work was to take steps towards determining if the errors of the input data are low enough, that the ray-tracing model can demonstrate superior performance to that of the paraxial model. Or, if the errors of the input data are moderate, and no significant advantage can be achieved by the use of ray-tracing. Our results suggest there is sufficient reason to pursue personalised eye modelling and ray-tracing. With anticipated future advancements in biometry technology, the potential for superior performance of personalised ray-tracing eye models is strong. Correspondingly, scientific motivation and enthusiasm for this technique should remain strong.

Personalised eye modelling by ray-tracing techniques has the potential to benefit many people by improving the visual outcome of cataract patients through improved IOL design and selection process. Current technology used to treat cataract is highly sophisticated and involves remarkable skills. By contrast, IOL power calculation methods are

somewhat rudimentary and offer the opportunity for revision and improvement. In the future, IOLs may be customized to correct HOAs for a specific patient according to a design generated and analyzed with a personalised ray-tracing eye model.

Appendices

Appendix A

Approximation of Corneal Power

Within the paraxial approximation, the power of a spherical surface can be described by,

$$F = \frac{n' - n}{r} \tag{A.1}$$

where F is the power of a spherical surface (units of diopters), r is the radius of curvature of the surface (units of meters), n is the refractive index of the first media, and n' is the refractive index of the second media.

Conventional keratometers and Placido disc technologies are based on analyzing the virtual image of a known object, after it's reflection off the anterior cornea (Purkinji image I). Historically, the direct measurement of the posterior corneal shape was a difficult task due to the close position of the two corneal surfaces, the close position of their centers of curvature, and the vast disparity in the intensity of their reflections (Purkinji images I and II). Direct measurement of the posterior corneal radius of curvature (which for keratometers and Placido disc technologies entails resolving Purkinji image II separately from I) was generally abandoned in the clinical environment, and instead it is estimated from the anterior corneal radius of curvature value. This estimation relies on the high correlation exhibited between the two curvature values. In the literature it is often suggested that Gullstrand's exact schematic model eye, which proposes the two curvature values are related by a ratio of approximately 0.883, is useful for this purpose although others have reported perhaps more accurate population values [138].

Let

n_e be the equivalent corneal refractive index,

n_c be the physiological corneal refractive index,

n_a be the refractive index of aqueous,

n_o be the refractive index of air,

r_a be the anterior corneal radius of curvature, and

r_p be the posterior corneal radius of curvature.

Within the paraxial approximation, assuming the corneal surfaces are spherical, assuming a thick lens system, and also assuming that the tear film is a parallel-pipette meniscus lens of zero power, we start by expressing the corneal power (K) as a function of the anterior corneal power (K_1), the posterior corneal power (K_2), the central corneal thickness (t) and the corneal refractive index (n_{cor}):

$$K = K_1 + K_2 - \frac{t}{n_c} \cdot K_1 \cdot K_2 \tag{A.2}$$

after substituting with Eq. A.1, Eq. A.2 becomes

$$\frac{n_e - n_o}{r_a} = \frac{n_c - n_o}{r_a} + \frac{n_a - n_c}{r_p} - \frac{t}{n_c} \cdot \frac{n_c - n_o}{r_a} \cdot \frac{n_a - n_c}{r_p} \tag{A.3}$$

Given

$$n_c = 1.376 \qquad n_a = 1.336 \qquad n_o = 1.000 \tag{A.4}$$

Eq. A.3 becomes

$$\frac{n_e - 1.000}{r_a} = \frac{0.376}{r_a} + \frac{-0.04}{r_p} - \frac{t}{1.376} \cdot \frac{0.376}{r_a} \cdot \frac{-0.04}{r_p} \tag{A.5}$$

and with re-arranging and simplifying Eq. A.5 becomes,

$$n_e = 1.376 - \frac{r_a}{r_p} \cdot 0.04 + \frac{t}{r_p} \cdot \frac{0.01504}{1.376} \tag{A.6}$$

From Gullstrand's schematic eye we estimate values of

$$r_p = 6.8 \times 10^{-3} \qquad r_a = 7.7 \times 10^{-3} \qquad t = 5 \times 10^{-4} \tag{A.7}$$

where all units are meters.

Then, Eq. A.6 evaluates to

$$n_e = 1.376 - \frac{7.7}{6.8} \cdot 0.04 + \frac{0.5}{6.8} \cdot \frac{0.01504}{1.376} \tag{A.8}$$

and finally the equivalent corneal refractive index is evaluated as

$$n_e = 1.3315 \tag{A.9}$$

Accordingly, keratometers estimate corneal power (K), accounting for the combined power of both the anterior and posterior corneal surfaces, from their measured value of anterior corneal radius of curvature (r_a), by using the following simplified expression

$$K = \frac{n_e - n_o}{r_a} = \frac{0.3315}{r_a} \quad . \tag{A.10}$$

The preceding derivation relies on Gullstrand's ratio of 6.8/7.7 for corneal radius of curvature (posterior : anterior), a posterior radius of curvature of 6.8 mm and a central corneal thickness of 0.5 mm. The value of $n_e = 1.3375$ used by many biometry instruments seems to be a choice based on convenience as this results in a value of 7.5 mm for anterior corneal radius of curvature converting to a corneal power of exactly 45.00 D [3]. Historically there was only modest motivation for a precise and accurate knowledge of K and thus the approximations described above, inherently persists in many biometry instruments still in use today. Modern commercial OCT and Scheimpflug technologies allow convenient simultaneous measurement of both pachymetry (corneal thickness) and the posterior corneal shape in a clinical environment. The known inter-subject variation in the three parameters estimated (Eq. A.7) [137, 138] flags the possibility of improving IOL power calculations by addressing this issue, through the direct measurement of these parameters, regardless of the IOL power prediction methodology employed.

Appendix B

Geometrical Optics Approach

Clinically it is useful for practitioners to understand the relationship between IOL power and refractive error, primarily because refractive error is a universally used and well-understood metric of visual state, whereas IOL power is not. These two parameters are inversely proportional and often approximated by Eq. 1.7. In the following section we will derive the geometrical optics equation (Eq. 1.4) using the step-vergence method, then continue on to derive an expression relating the change in IOL power to refractive error. The system is treated as sphero-cylindrical system composed of three thin lenses (the spectacle lens, the corneal lens, and the IOL), and the calculation can be applied to each principle meridian in turn.

Let us consider a wavefront from infinity is incident at the spectacle plane. The wavefront vergence at the spectacle plane is zero ($V_1 = 0$). The refractive error (R) relates to the focal length of the spectacles (f_s) by

$$R = \frac{n_o}{f_s} \tag{B.1}$$

The wavefront vergence at the spectacle plane (V_2) is

$$V_2 = V_1 + R = 0 + \frac{n_o}{f_s} \tag{B.2}$$

Then step to the corneal plane, which is a distance (b) from the spectacle plane. The wavefront vergence at the corneal plane (V_3) is

$$V_3 = \frac{n_o}{f_s - b} \tag{B.3}$$

then consider the power from the cornea (K)

$$K = \frac{n_a}{f_c} \tag{B.4}$$

so after corneal surface, the wavefront vergence (V_4) is

$$V_4 = \frac{n_o}{f_s - b} + \frac{n_a}{f_c} \tag{B.5}$$

then step to the IOL plane, which is a distance (d) from the cornea. The wavefront vergence at the IOL plane (V_5) is

$$V_5 = \frac{n_a}{\dfrac{n_a}{\dfrac{n_o}{f_s - b} + \dfrac{n_a}{f_c}} - d} \tag{B.6}$$

then adding the power of the IOL (P) gives

$$V_6 = \frac{n_a}{\dfrac{n_a}{\dfrac{n_o}{f_s - b} + \dfrac{n_a}{f_c}} - d} + P \tag{B.7}$$

This wavefront of vergence (V_6) must focus on the retina. The retina is a distance ($l - d$) from the IOL plane, therefore

$$\frac{n_a}{\dfrac{n_a}{\dfrac{n_o}{f_s - b} + \dfrac{n_a}{f_c}} - d} + P = \frac{n_v}{l - d} \tag{B.8}$$

Rearranging to solve for IOL power gives

$$P = \frac{n_v}{l-d} - \frac{n_a}{\frac{n_a}{\frac{n_o}{f_s - b} + \frac{n_a}{f_c}} - d} \tag{B.9}$$

Since the back vertex distance (b) between spectacles and the cornea is usually 12-15 mm, and we a considering the near-emmetropic case of moderate refractive errors (say $f_s > 1000$ mm), we can make the approximation that

$$b << f_s \tag{B.10}$$

then we can re-write Eq. B.4 as

$$V_3 \approx \frac{n_o}{f_s} = R \tag{B.11}$$

Now we can simply add the refractive correction provided by the spectacles (R) to the corneal lens (K) and Eq. B.9 becomes

$$P_a \approx \frac{n_v}{l-d} - \frac{n_a}{\frac{n_a}{K+R} - d} \tag{B.12}$$

As an aside let us take the chance to re-express and solve for refractive error accurately from Eq. B.8 and approximately from Eq. B.12

$$R = \frac{n_o}{\frac{n_o}{\frac{n_a}{\frac{n_a}{\frac{n_v}{l-d} - P} + d} - K} + b} \approx \frac{n_a}{\frac{n_a}{\frac{n_v}{l-d} - P} + d} - K \tag{B.13}$$

Now if the target is for emmetropia as it normally is, then we set the refractive error to zero ($f_s = \infty$), and Eq. B.9 becomes

$$P_e = \frac{n_v}{l-d} - \frac{n_a}{\frac{n_a}{K} - d} \tag{B.14}$$

which is equivalent to Eq. 1.4. Now if we define the change in IOL power (ΔP) as the difference between the implanted power (P_i) and the power required for emmetropia (P_e)

$$\Delta P = P_e - P_i \tag{B.15}$$

then

$$\Delta P \approx \frac{n_v}{l-d} - \frac{n_a}{\frac{n_a}{K} - d} - \frac{n_v}{l-d} + \frac{n_a}{\frac{n_a}{K+R} - d} \tag{B.16}$$

then

$$\Delta P \approx \frac{n_a}{\frac{n_a}{K+R} - d} - \frac{n_a}{\frac{n_a}{K} - d} \tag{B.17}$$

So we can see, that under this approximation the relationship between ΔP and R is dependent on K and d. If we choose some typical values for $R = 1$ D, $K = 45$ D and $d = 4$ mm then we get

$$\Delta P = P_e - P_i \approx 1.34\, R \tag{B.18}$$

which is in reasonable agreement with the factor of 1.25 suggested by the SRK II formula (Eq. 1.12), but highlights the discrepancy of the factor of ~ 1.5 suggested by the earlier SRK formula (Eq. 1.7). Equations B.17 and B.18 provide a background and an example calculation, useful in understanding how the change in IOL power from the default emmetropic predicted value effects the expected refractive error. Note that Eq. B.18 is

only valid for the near-emmetropic state and with assumed values for corneal power and ELP. It requires assumptions of paraxial optics, sphero-cylindrical surfaces, thin lenses, a near-emmetropic pseudophakic eye, and typical values for corneal power and ELP of a posterior chamber IOL.

Appendix C

IOL power calculation formula

Thijssen's formula

$$P = \frac{n_v}{l - d - t\dfrac{n_a}{n_i}} - \frac{n_a}{\dfrac{n_a}{K} - d - t} \tag{C.1}$$

where t is the central IOL thickness

Colenbrander's formula

$$P = \frac{n_v}{l - d - 5 \cdot 10^{-5}} - \frac{n_a}{\dfrac{n_a}{K} - d - 5 \cdot 10^{-5}} \tag{C.2}$$

Fyodorov's formula

$$P = \frac{n_v - l\,K}{(l - d)\left(1 - \dfrac{Kd}{n_a}\right)} \tag{C.3}$$

van der Heijde's formula

$$P = \frac{n_v}{l - d} - \frac{1}{\dfrac{1}{K} - \dfrac{d}{n_a}} \tag{C.4}$$

Binkhorst's formula (which assumes $n_e = n_v = n_a = 4/3$)

$$P = \frac{n_v(4r - l)}{(l - d)(4r - d)} \tag{C.5}$$

Appendix D

Derivation of Holladay I formula

Proof that Holladay I Eq. 1.18 is equivalent to the geometrical optics equation (Eq. B.9) under the assumption that $n_{vit} = n_{aq}$. A paraxial sphero-cylindrical system composed of three thin lenses (the spectacle lens, the cornea, and the IOL) is assumed, and we begin with the geometrical optics equation (Eq. B.9) derived using paraxial step-vergence formula and treating the system as 3 thin lenses (the spectacle lens, the corneal lens and the IOL).

$$P = \frac{n_v}{l-d} - \frac{n_a}{\dfrac{n_a}{\dfrac{n_o}{f_s - b} + \dfrac{n_a}{f_c}} - d} \tag{D.1}$$

$$f_c = \frac{n_a}{K} = \frac{n_a\, r}{n_e - n_o} \tag{D.2}$$

where r is the anterior corneal radius of curvature

$$P = \frac{n_v}{l-d} - \frac{n_a}{\dfrac{n_a}{\dfrac{n_o}{f_s - b} + \dfrac{n_e - n_o}{r}} - d} \tag{D.3}$$

Given that the refractive index of air is $n_o = 1.000$

$$P = \frac{n_v}{l-d} - \frac{n_a}{\frac{n_a r(f_s - b)}{r + (n_e - 1)(f_s - b)} - d} \tag{D.4}$$

$$P = \frac{n_v}{l-d} - \frac{n_a}{\frac{n_a r(f_s - b) - d[r + (n_e - 1)(f_s - b)]}{r + (n_e - 1)(f_s - b)}} \tag{D.5}$$

$$P = \frac{n_v}{l-d} - \frac{n_a[r + (n_e - 1)(f_s - b)]}{n_a r(f_s - b) - d[r + (n_e - 1)(f_s - b)]} \tag{D.6}$$

$$P = \frac{n_v[n_a r(f_s - b) - d[r + (n_e - 1)(f_s - b)]] - (l-d)[n_a[r + (n_e - 1)(f_s - b)]]}{(l-d)[n_a r(f_s - b) - d[r + (n_e - 1)(f_s - b)]]} \tag{D.7}$$

given $f_s = n_o/R$

$$P = \frac{n_v[(n_a r - dn_e + d) - R(n_a rb + dr - n_e db + db)] - (l-d)[n_a[r + (n_e - 1)(f_s - b)]]}{(l-d)(n_a r - dn_e + d) - R(n_a rb + dr - n_e db + db)} \tag{D.8}$$

and assuming $n_v = n_a$

$$P = \frac{n_v[(n_a r - dn_e + d) - R(n_a rb + dr - n_e db + db) - (l-d)[r + (n_e - 1)(f_s - b)]]}{(l-d)(n_a r - dn_e + d) - R(n_a rb + dr - n_e db + db)} \tag{D.9}$$

$$P = \frac{n_v[(n_a r - dn_e + d) - R(n_a rb + dr - n_e db + db) - R(lr - ln_e b + lb - dr + n_e db - db) - (ln_e - l - dn_e + d)]}{(l-d)(n_a r - dn_e + d) - R(n_a rb + dr - n_e db + db)} \tag{D.10}$$

$$P = \frac{n_v[n_a r - dn_e + d - ln_e + l + dn_e - d - R(n_a rb + dr - n_e db + db + lr - ln_e b + lb - dr + n_e db - db)]}{(l-d)(n_a r - dn_e + d) - R(n_a rb + dr - n_e db + db)} \tag{D.11}$$

$$P = \frac{n_v[n_a r - n_e l + l - R(n_a rb + lr - n_e lb + lb)]}{(l-d)(n_a r - n_e d + d) - R(n_a rb + dr - n_e db + db)} \tag{D.12}$$

and if we use Holladay's default value of $n_e = 4/3$

$$P = \frac{n_v[n_a r - l/3 - R(n_a rb + lr - lb/3)]}{(l-d)(n_a r - d/3) - R(n_a rb + dr - db/3)} \tag{D.13}$$

which is equivalent to Holladay's Eq. 1.18

Appendix E

The corneal height formula

The corneal height formula regards the cornea as a section of a sphere, the base of which forms a plane at the level of the anterior iris.

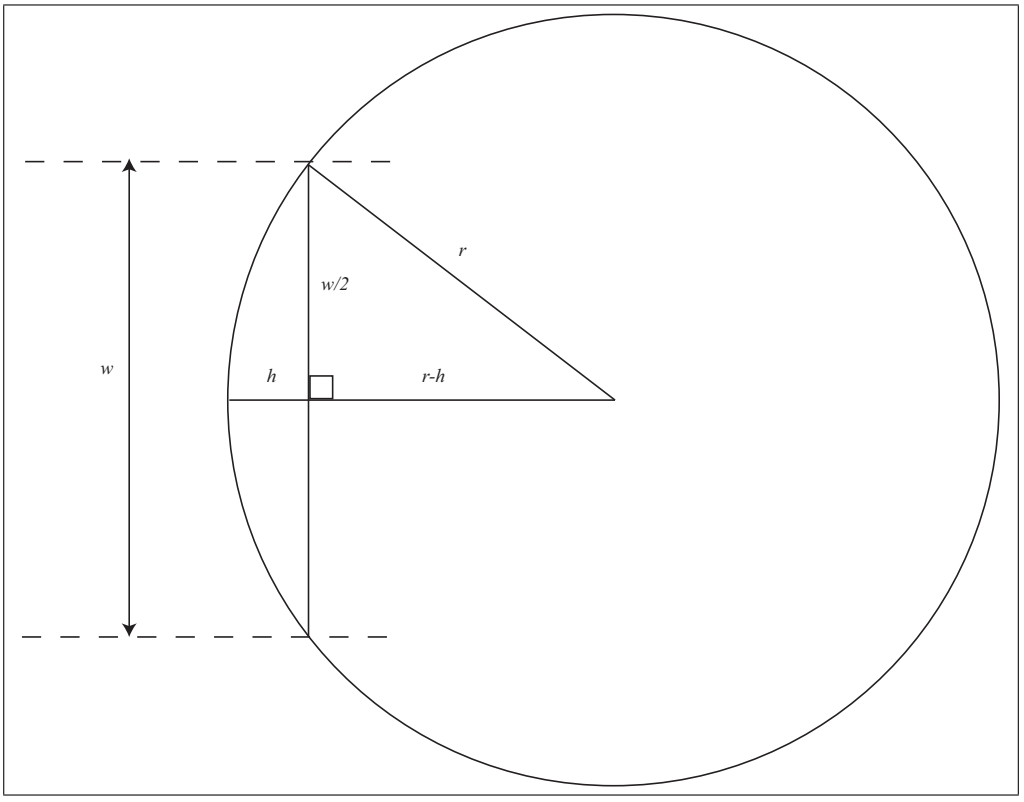

FIGURE E.1: A circle, representing a meridional section through the center of a sphere. A segment is demarked and the sag is used to represent the corneal height.

Beginning with Pythagorus theorem for the right-angled triangle we can say

$$(r-h)^2 + \left(\frac{w}{2}\right)^2 = r^2 \tag{E.1}$$

Expands to

$$r^2 - 2rh + h^2 + \left(\frac{w}{2}\right)^2 = r^2 \tag{E.2}$$

Re-arranging to the general form of the quadratic equation

$$h^2 - 2rh + \left(\frac{w}{2}\right)^2 = 0 \tag{E.3}$$

And solving with the general solution for the quadratic equation gives

$$h = \frac{2r \pm \sqrt{(-2r)^2 - 4\left(\frac{w}{2}\right)^2}}{2} \tag{E.4}$$

which simplifies to

$$h = r - \sqrt{r^2 - \left(\frac{w}{2}\right)^2} \tag{E.5}$$

where we eliminate the plus/minus operation by selecting the root that makes physical sense. Note that if the *white-to-white* is not measured clinically, then the corneal width parameter in Eq. E.5 is usually instead estimated by proportionality with axial length. Equation E.5 is the formula used by Fyodorov and Olsen. Holladay developed a slight variation in this formula (see Eq. 1.14) by accounting for typical corneal asphericity and the steeper curvature of the posterior corneal compared to the anterior.

Appendix F

Derivation of the personalised ACD constant

Proof that Hoffer Q formula (Eq. 1.36) used to find the *personalised ACD constant* is a re-arrangement of the geometrical optics equation (Eq. B.9) under the assumption that $n_{vit} = n_{aq} = 1.336$. A paraxial sphero-cylindrical system composed of three thin lenses (the spectacle lens, the cornea, and the IOL) is assumed.

Let

$$R_{rm} = \frac{R_r}{1 - 0.012R_r} \tag{F.1}$$

and

$$\eta = \frac{n_a}{K + R_{rm}} \tag{F.2}$$

and

$$\kappa = d + 5 \cdot 10^{-5} \tag{F.3}$$

Begining with the geometrical optics equation (Eq. B.9)

$$P = \frac{n_v}{l - d} - \frac{n_a}{\dfrac{n_a}{\dfrac{n_o}{f_s - b} + \dfrac{n_a}{f_c}} - d} \tag{F.4}$$

Using the default value of $b = 12$ mm, and knowing $n_o = 1$, we substitute making use of the refractive error at the corneal plane (R_{rm}) as declared in Eq. F.1

$$P = \frac{n_v}{l-d} - \frac{n_a}{\dfrac{n_a}{R_{rm} + \dfrac{n_a}{f_c}} - d} \tag{F.5}$$

Knowing that $K = n_a/f_c$

$$P = \frac{n_v}{l-d} - \frac{n_a}{\dfrac{n_a}{R_{rm} + K} - d} \tag{F.6}$$

To this generic version of the geometrical optics solution, we follow Colenbrander's arrangement (Eq. C.2), which differs from the generic version (Eq. B.9) by including a 50 micron distance to account for the distance between the IOL vertex and it's second principal plane (a convex-plano IOL design was considered by Colenbrander in determining his formula and Hoffer also used a convex-plano design in his study of the Hoffer Q formula). Thus, we have

$$P = \frac{n_v}{l-d-5\cdot 10^{-5}} - \frac{n_a}{\dfrac{n_a}{R_{rm} + K} - d - 5\cdot 10^{-5}} \tag{F.7}$$

Let us substitute the previously declared parameters η (Eq. F.2) and κ (Eq. F.3), and use the specific subscript for implanted IOL power as this equation will be applied to a retrospective case series.

$$P_i = \frac{n_v}{l-\kappa} - \frac{n_a}{\eta - \kappa} \tag{F.8}$$

Given that $n_v = n_a = 1.336$, we can simplify by removing the specific subscript for refractive index

$$P_i = \frac{n}{l-\kappa} - \frac{n}{\eta - \kappa} \tag{F.9}$$

Rearranging becomes

$$P_i(l-\kappa)(\eta-\kappa) = n(\eta - \kappa - l + \kappa) \tag{F.10}$$

simplifying and further rearranging

$$(l-\kappa)(\eta-\kappa)=\frac{n(\eta-l)}{P_i} \tag{F.11}$$

expanding the left-hand side and setting the expression equal to zero

$$0=l\,\eta-l\,\kappa-\kappa\,\eta+\kappa^2-\frac{n(\eta-l)}{P_i} \tag{F.12}$$

and by grouping terms we see the general form of the quadratic equation, made more distinct by the use of some extraneous brackets

$$0=\kappa^2+(-l-\eta)\kappa+\left(l\,\eta-\frac{n(\eta-l)}{P_i}\right) \tag{F.13}$$

and solving using the general solution for the quadratic equation

$$\kappa=\frac{-(-l-\eta)\pm\sqrt{(-l-\eta)^2-4\cdot\left(l\,\eta-\dfrac{n(\eta-l)}{P_i}\right)}}{2} \tag{F.14}$$

and remove brackets to simplify

$$\kappa=\frac{l+\eta\pm\sqrt{(-l-\eta)^2-4l\,\eta+\dfrac{4n(\eta-l)}{P_i}}}{2} \tag{F.15}$$

In the next step we examine the first term inside the square root, which is $(-l-\eta)^2$ and can be expanded to show

$$(-l-\eta)^2=l^2+2l\eta+\eta^2 \tag{F.16}$$

whereas the term $(l-\eta)^2$ and can be expanded to show

$$(l-\eta)^2=l^2-2l\eta+\eta^2 \tag{F.17}$$

From Eqs. F.16 and F.17 we can state

$$(-l-\eta)^2=(l-\eta)^2+4l\eta \tag{F.18}$$

From the relationship in Eq. F.18, we can see that the term $(-l-\eta)^2$ in Eq. F.15 can be replaced with $(l-\eta)^2+4l\eta$, which gives

$$\kappa = \frac{l+\eta \pm \sqrt{(l-\eta)^2+4l\eta-4l\,\eta+\dfrac{4n(\eta-l)}{P_i}}}{2} \tag{F.19}$$

where it becomes obvious that the $4l\eta$ terms cancel each other. Now, after having made use of the abbreviations, replace κ as declared in Eq. F.3 and η as declared in Eq. F.2,

$$d = \frac{l+\dfrac{n_a}{K+R_{rm}} \pm \sqrt{\left(l-\dfrac{n_a}{K+R_{rm}}\right)^2+\dfrac{4n\left(\dfrac{n_a}{K+R_{rm}}-l\right)}{P_i}}}{2} - 5\cdot 10^{-5} \tag{F.20}$$

and we can remove the $\pm$ symbol by selecting to subtract the positive solution to the square root. Also the refractive index term is replaced by the default value ($n_v = n_a = 1.336$) as previously explained

$$d_p = \frac{l+\dfrac{1.336}{K+R_{rm}} - \sqrt{\left(l-\dfrac{1.336}{K+R_{rm}}\right)^2+\dfrac{4\cdot 1.336[(1.336/(K+R_{rm}))-l]}{P_i}}}{2} - 5\cdot 10^{-5} \tag{F.21}$$

which is equivalent to the solution given in the original Hoffer Q publication (Eq. 1.36), and it is also equivalent to the solution used by the Holladay I formula, with the exception of the $5\cdot 10^{-5}$ term, and except that the refractive error at the spectacle plane is used, rather than at the corneal plane (an abbreviation that improves the aesthetics of the Hoffer version). In the Holladay I solution for personalising the surgeon factor (Eqs. 1.16), the term immediately on the right hand side of the equality symbol represents the personalised ELP value, and it is intentionally presented in the form of the general solution to the quadratic equation.

Bibliography

[1] World Health Organisation. Prevention of blindness and deafness. Global initiative for the elimination of avoidable blindness. WHO document WHO/PBL/97.61 Rev2. Technical report, Geneva: WHO, 2000.

[2] David J Apple and John Sims. Harold Ridley and the invention of the Intraocular Lens. *Surv Ophthalmol*, 40(4):279–292, January-February 1996.

[3] H John Shammas, editor. *Intraocular lens power calculations*. SLACK Incorporated, 6900 Grove Road, Thorofare, NJ 08086, 2003.

[4] Greg Munton. A short history of cataract surgery. *CE Optometry*, 4(2):45–88, 2001.

[5] Marvin L Kwitko and Charles D Kelman, editors. *The history of modern cataract surgery*. Kugler Publications, The Hague, The Netherlands, 1998.

[6] David J Apple. A pioneer in the quest to eradicate world blindness. *Bulletin of the World Health Organization*, 81(10):756–757, 2003.

[7] Harold Ridley. Intraocular acrylic lenses after cataract extraction. *Lancet*, 259 (6699):118–21, 19 January 1952.

[8] D Peter Choyce. The uses of acrylic anterior chamber implants illustrated by cases shown. In *Proceedings of the Royal Society of Medicine*, volume 54, pages 849–56. Royal Society of Medicine, October 1961.

[9] Alan E A Ridgway. Intraocular lens implants. In W Neil Charman, editor, *Visual optics and instrumentation*, volume 1 of *Vision and visual dysfunction*, chapter 7, pages 121–137. CRC Press, Boca Raton, FL 33487, 1991.

[10] Dermot Pierse and H N O'Donoghue. Alpha-chymotrypsin in cataract surgery. *Br Med J*, 2(5213):1629–33, December 1960.

[11] Joaquin Barraquer. Enzymatic zonulolysis. In *Proceedings of the Royal Society of Medicine*, volume 52, pages 973–82. Royal Society of Medicine, November 1959.

[12] Tedeusz Krwawicz. Intracapsular extraction of intumescent cataract by application of low temperature. *Br J Ophthalmol*, 45(4):279–83, April 1961.

[13] Charles D Kelman. Phacoemulsification and aspiration. A new technique of cataract removal. A preliminary report. *Am J Ophthalmol*, 64(1):23–35, July 1967.

[14] Howard V Gimbel and Thomas Neuhann. Continuous curvilinear capsulorhexis. *J Cataract Refract Surg*, 17(1):110–1, 1991.

[15] David V Leaming. Practice styles and preferences of ASCRS members–2003 survey. *J Cataract Refract Surg*, 30(4):892–900, April 2004.

[16] David V. Leaming. Snapshots (guest editorial). *J Cataract Refract Surg*, 32(9): 1401–2, September 2006.

[17] Jaime Tejedor and Juan Murube. Choosing the location of corneal incision based on preexisting astigmatism in phacoemulsification. *Am J Ophthalmol*, 139(5):767–76, May 2005.

[18] David Spalton and Elsie Chan. Latest developments in intraocular lenses. *CET - Optometry Today*, 9 October:28–34, 2009.

[19] Pammal T Ashwin, Sunil Shah, and James S Wolffsohn. Advances in cataract surgery. *Clin Exp Optom*, 92(4):333–42, July 2009.

[20] Alan H Tunnacliffe and J G Hirst. *Introduction to visual optics*. The Association of British Dispensing Opticians, Canterbury, 4th edition, 2007.

[21] Douglas Coster. *Cornea - Fundamentals of clinical ophthalmology*. BMJ Books, London, 2002.

[22] Lisa Battat, Angelo Macri, Dilek Dursun, and Stephen C Pflugfelder. Effects of laser in situ keratomileusis on tear production, clearance, and the ocular surface. *Ophthalmology*, 108(7):1230–5, Jul 2001.

[23] Young L Kim, Joseph T Walsh, Jr, Thomas K Goldstick, and Matthew R Glucksberg. Variation of corneal refractive index with hydration. *Phys Med Biol*, 49(5): 859–68, Mar 2004.

[24] Barry A Clark and Leo G Carney. Refractive index and reflectance of the anterior surface of the cornea. *Am J Optom Arch Am Acad Optom*, 48(4):333–43, April 1971.

[25] Catherine E Jones, David A Atchison, Roger Meder, and James M Pope. Refractive index distribution and optical properties of the isolated human lens measured using Magnetic Resonance Imaging (MRI). *Vision Res*, 45(18):2352–66, August 2005.

[26] Pablo Artal, Antonio Guirao, Esther Berrio, and David R Williams. Compensation of corneal aberrations by the internal optics in the human eye. *J Vis*, 1(1):1–8, 2001.

[27] Pablo Artal and Antonio Guirao. Contributions of the cornea and the lens to the aberrations of the human eye. *Opt Lett*, 23(21):1713–5, November 1998.

[28] William Tasman and Edward A. Jaeger, editors. *The Wills Eye Hospital Atlas of Clinical Ophthalmology*. Lippincott Williams & Wilkins, Philadelphia, 2nd edition, 2001.

[29] Jack J Kanski. *Clinical ophthalmology - a systematic approach*. Butterworth Heinemann, Edinburgh, 5th edition, 2003.

[30] John W Heath and Barbara Young. *Wheater's functional histology*. Churchill Livingstone, Edinburgh, 4th edition, 2000.

[31] David A Atchison and George Smith. *Optics of the human eye*. Butterworth-Heinemann, Oxford, 2000.

[32] L R Loper. The relationship between angle lambda and the residual astigmatism of the eye. *Am J Optom & Arch Am Acad Optom*, 36:365–377, 1959.

[33] Gunter K. Von Noorden. *Burian and Von Noorden's binocular vision and ocular motility*. C. V. Mosby, St. Louis, 3rd edition, 1985.

[34] Authur Bradley and Larry N Thibos. Modeling off-axis vision - I: The optical effects of decentering visual targets or the eye's entrance pupil. In E Peli, editor,

Vision models for target detection and resolution, pages 313–337. World Scientific Press, 1995.

[35] Heidi Hofer, Pablo Artal, Ben Singer, Juan Luis Aragón, and David R Williams. Dynamics of the eye's wave aberration. *J Opt Soc Am A*, 18(3):497–506, March 2001.

[36] Junzhong Liang and David R Williams. Aberrations and retinal image quality of the normal human eye. *J Opt Soc Am A*, 14(11):2873–2883, November 1997.

[37] Trusit Dave. Automated refraction - design and applications. *Optometry Today*, pages 28–32, June 2004.

[38] Walter T Welford. *Aberrations of optical systems*. Adam Hilger, Bristol, 1989.

[39] American National Standards Institute. ANSI Z80.28 American National Standard for Ophthalmics: Methods for reporting optical aberrations of the eye, 2004.

[40] International Organization for Standardization. ISO 24157 International standard: Ophthalmic optics and instruments, Reporting aberrations of the human eye, 2008.

[41] Larry N Thibos, Xin Hong, Arthur Bradley, and Xu Cheng. Statistical variation of aberration structure and image quality in a normal population of healthy eyes. *J Opt Soc Am A*, 19(12):2329–2349, December 2002.

[42] Junzhong Liang, Bernhard Grimm, Stefan Goelz, and Josef F Bille. Objective measurement of wave aberrations of the human eye with the use of a Hartmann-Shack wave-front sensor. *J Opt Soc Am A*, 11(7):1949–57, July 1994.

[43] Karen M Hampson. Adaptive optics and vision. *J Mod Optics*, 55(21):3425–67, 2008.

[44] Susana Marcos, Stephen A. Burns, Esther Moreno-Barriusop, and Rafael Navarro. A new approach to the study of ocular chromatic aberrations. *Vision Res*, 39: 4309–4323, 1999.

[45] Peter A Howarth, Xiaoxiao X Zhang, Arthur Bradley, David L Still, and Larry N Thibos. Does the chromatic aberration of the eye vary with age ? *J Opt Soc Am A*, 5(12):2087–92, December 1988.

[46] Michael H Freeman and Christopher C Hull. *Optics*. Butterworth Heinemann, Edinburgh, 2003.

[47] Arthur Bradley, Xiaoxiao Zhang, and Larry N Thibos. Achromatizing the human eye. *Optom Vis Sci*, 68(8):608–16, 1991.

[48] Fergus W Campbell and Roland W Gubisch. The effect of chromatic aberration on visual acuity. *J Physiol*, 192:345–358, 1967.

[49] Arthur Bradley. Perceptual manifestations of imperfect optics in the human eye: attempts to correct for ocular chromatic aberration. *Optom Vis Sci*, 69(7):515–521, 1992.

[50] Norberto López-Gil and Robert Montés-Micó. New intraocular lens for achromatizing the human eye. *J Cataract Refract Surg*, 33(7):1296–302, July 2007.

[51] Pablo Artal, Silvestre Manzanera, Patricia Piers, and Henk Weeber. Visual effect of the combined correction of spherical and longitudinal chromatic aberrations. *Opt Express*, 18(2):1637–48, January 2010.

[52] Eugene Hecht and Alfred Zajac. *Optics*. Addison-Wesley, Reading, Massachusetts, 4th edition, 1979.

[53] Geun-Young Yoon and David R. Williams. Visual performance after correcting the monochromatic and chromatic aberrations of the eye. *J Opt Soc Am A*, 19(2): 266–276, February 2002.

[54] Austin Roorda. Making the most of AO for vision science. In *CfAO summer school for adaptive optics*, pages 1 – 15. Santa Cruz: Center for Adaptive Optics, 2005.

[55] Thomas O Salmon, Larry N Thibos, and Arthur Bradley. Comparison of the eye's wave-front aberration measured psychophysically and with the Shack-Hartmann wave-front sensor. *J Opt Soc Am A*, 15(9):2457–65, September 1998.

[56] Trusit Dave. Wavefront aberrometry - current theories and concepts. *Optometry Today*, pages 41–5, November 2004.

[57] Michael J Cox, David A Atchison, and Dion H Scott. Scatter and its implications for the measurement of optical image quality in human eyes. *Optom Vis Sci*, 80 (1):58–68, January 2003.

[58] National Research Council. *Emergent techniques for assessment of visual performance*. The National Academies Press, Washington, 1985.

[59] W N Charman and N Chateau. The prospects for super-acuity: limits to visual performance after correction of monochromatic ocular aberration. *Ophthalmic Physiol Opt*, 23(6):479–93, Nov 2003.

[60] P Rosales and S Marcos. Customized computer models of eyes with intraocular lenses. *Opt Express*, 15(5):2204–18, Mar 2007.

[61] Paul-Rolf Preussner, Jochen Wahl, Hedro Lahdo, Burkhard Dick, and Oliver Findl. Ray tracing for intraocular lens calculation. *J Cataract Refract Surg*, 28(8):1412–9, August 2002.

[62] Huanqing Q Guo, Zhaoqi Q Wang, Qiuling L Zhao, Wei Quan, and Yan Wang. Individual eye model based on wavefront aberration. *Optik*, 116(2):80–5, 2005.

[63] Rafael Navarro, Luis González, and Jos L Hernández-Matamoros. On the prediction of optical aberrations by personalized eye models. *Optom Vis Sci*, 83(6): 371–81, June 2006.

[64] Carmen Canovas and Pablo Artal. Customized eye models for determining optimized intraocular lenses power. *Biomed Opt Express*, 2(6):1649–62, June 2011.

[65] Stefano Giovanzana. *A virtual environment for modeling and analysis of human eye*. PhD thesis, Mechanical Engineering, University di Padova, 2011.

[66] International Organization for Standardization. ISO 11979 European Standard: Ophthalmic implants - Intraocular lenses, 2006.

[67] Jim Schwiegerling. Recent developments in pseudophakic dysphotopsia. *Curr Opin Ophthalmol*, 17(1):27–30, Feburary 2006.

[68] Myron Yanoff and Jay S. Duker, editors. *Ophthalmology*. Mosby Elsevier Inc, St. Louis, 3rd edition, 2009.

[69] Michel Renard, Michel Delmelle, and Albert Galand. Buoyancy of human and intraocular lenses in air and in aqueous humor. *Graefes Arch Clin Exp Ophthalmol*, 223(4):205–6, 1985.

[70] Stefka N Kasarova, Nina G Sultanova, and Ivan D Nikolov. Temperature dependence of refractive characteristics of optical plastics. In *Journal of Physics: Conference Series 16 ISCMP: Progress in Solid State and Molecular Electronics, Ionics and Photonics. No 012028.*, volume 253. Institute of Physics Publishing, 2010.

[71] Huawei Zhao and Martin A Mainster. The effect of chromatic dispersion on pseudophakic optical performance. *Br J Ophthalmol*, 91(9):1225–9, September 2007.

[72] S G Lipson, H L Lipson, and D S Tannhauser. *Optical physics*. Cambridge University Press, Cambridge, 3rd edition, 1995.

[73] Edward A Boettner and J Reimer Wolter. Transmission of the ocular media. *Invest Ophthalmol Vis Sci*, 1(6):776–783, 1962.

[74] Tom H Margrain, Mike Boulton, John Marshall, and David H Sliney. Do blue light filters confer protection against age-related macular degeneration? *Prog Retin Eye Res*, 23(5):523–31, September 2004.

[75] Yuichi Yokoyama, Hidetoshi Iwamoto, and Akio Yamanaka. Blue light-filtering foldable acrylic intraocular lens. *J Artif Organs*, 9(2):71–6, 2006.

[76] Martin A Mainster. Violet and blue light blocking intraocular lenses: photoprotection versus photoreception. *Br J Ophthalmol*, 90(6):784–92, June 2006.

[77] Liliana Werner, Nick Mamalis, Natalya Romaniv, Jonathan Haymore, Brian Haugen, Brian Hunter, and Scott Stevens. New photochromic foldable intraocular lens: preliminary study of feasibility and biocompatibility. *J Cataract Refract Surg*, 32 (7):1214–21, July 2006.

[78] Claudette Abela-Formanek, Michael Amon, Gebtraud Schild, Jörg Schauersberger, Georg Heinze, and Andreas Kruger. Uveal and capsular biocompatibility of hydrophilic acrylic, hydrophobic acrylic, and silicone intraocular lenses. *J Cataract Refract Surg*, 28(1):50–61, January 2002.

[79] Thomas J Newland, Mark L McDermott, Dean Eliott, Linda D Hazlett, David J Apple, Richard J Lambert, and Ronald P Barrett. Experimental neodymium:YAG laser damage to acrylic, poly(methyl methacrylate), and silicone intraocular lens materials. *J Cataract Refract Surg*, 25(1):72–6, January 1999.

[80] Stella N Arthur, Qun Peng, Marcela Escobar-Gomez, and David J Apple. Silicone oil adherence to silicone intraocular lenses. *Int Ophthalmol Clin*, 41(3):33–45, 2001.

[81] Aylin Yaman, A Osman Saatci, Sulen Sarioğlu, F Hakan Oner, and Ismet Durak. Interaction with intraocular lens materials: Does heavy silicone oil act like silicone oil ? *J Cataract Refract Surg*, 33(1):127–9, January 2007.

[82] Joseph R Davis, editor. *Handbook of materials for medical devices*. ASM International, 2003.

[83] Christos Haritoglou, Alice Yu, Wolfgang Freyer, Siegfried G Priglinger, Claudia Alge, Kirsten Eibl, Christian A May, Ulrich Welge-Luessen, and Anselm Kampik. An evaluation of novel vital dyes for intraocular surgery. *Invest Ophthalmol Vis Sci*, 46(9):3315–22, September 2005.

[84] Anna M Beasley, Gerd U Auffarth, and Andreas F von Recum. Intraocular lens implants: a biocompatibility review. *J Invest Surg*, 9(6):399–413, November-December 1996.

[85] Graham D Barrett, Harold Beasley, Olfeo J Lorenzetti, and A Rosenthal. Multicenter trial of an intraocular hydrogel lens implant. *J Cataract Refract Surg*, 13 (6):621–6, November 1987.

[86] Thomas R Mazzocco and B M Davidson. Insertion technique and clinical experience with silicone lenses. In Thomas R Mazzocco, George M Rajacich, and Edward Epstein, editors, *Soft implant lenses in cataract surgery*, pages 97–106. SLACK Incorporated, 1986.

[87] Jerry A Fogle, J E Blaydes, K J Fritz, Stephen H Blaydes, Thomas R Mazzocco, Robert L Peiffer, C Cook, and E Wright. Clinicopathologic observations of a silicone posterior chamber lens in a primate model. *J Cataract Refract Surg*, 12 (3):281–4, May 1986.

[88] Douglas D Koch. Issues in new foldable IOL designs. *J Cataract Refract Surg*, 28 (7):1083–4, July 2002.

[89] Kim T Doan, Randall J Olson, and Nick Mamalis. Survey of intraocular lens material and design. *Curr Opin Ophthalmol*, 13(1):24–9, Feburary 2002.

[90] David F Chang, Samuel Masket, Kevin M Miller, Rosa Braga-Mele, Brian C Little, Nick Mamalis, Thomas A Oetting, Mark Packer, and ASCRS Cataract Clinical Committee. Complications of sulcus placement of single-piece acrylic intraocular lenses: Recommendations for backup IOL implantation following posterior capsule rupture. *J Cataract Refract Surg*, 35(8):1445–58, August 2009.

[91] Michael D Wagoner, Terry A Cox, Reginald George Ariyasu, Deborah S Jacobs, Carol L Karp, and American Academy of Ophthalmology. Intraocular lens implantation in the absence of capsular support: A report by the American Academy of Ophthalmology. *Ophthalmology*, 110(4):840–59, April 2003.

[92] Richard J Duffey and David Leaming. Trends in refractive surgery in the United States. *J Cataract Refract Surg*, 30(8):1781–5, August 2004.

[93] Mark Chehade and Mark J Elder. Intraocular lens materials and styles: A review. *Aust N Z J Ophthalmol*, 25(4):255–63, November 1997.

[94] Daniel M Schwartz. Light-adjustable lens. *Trans Am Ophthalmol Soc*, 101:417–36, 2003.

[95] Okihiro Nishi and Kayo Nishi. Accommodation amplitude after lens refilling with injectable silicone by sealing the capsule with a plug in primates. *Arch Ophthalmol*, 116(10):1358–61, October 1998.

[96] Daniele Tognetto, Giorgia Sanguinetti, Paolo Sirotti, Paolo Cecchini, Luana Marcucci, Enzo Ballone, and Giuseppe Ravalico. Analysis of the optical quality of intraocular lenses. *Invest Ophthalmol Vis Sci*, 45(8):2682–2690, August 2004.

[97] Liliana Werner. Biocompatibility of intraocular lens materials. *Curr Opin Ophthalmol*, 19(1):41, 2008.

[98] H Burkhard Dick, Andreas Frohn, Albert J Augustin, Beate Wolters, Tadeusz Pakula, and Norbert Pfeiffer. Physicochemical surface properties of various intraocular lenses. *Ophthalmic Res*, 33(6):303–9, November-December 2001.

[99] Mana Tehrani, H Burkhard Dick, Beate Wolters, Tadeusz Pakula, and Evan Wolf. Material properties of various intraocular lenses in an experimental study. *Ophthalmologica*, 218(1):57–63, January-February 2004.

[100] Daniele Tognetto, Lisa Toto, Enzo Ballone, and Giuseppe Ravalico. Biocompatibility of hydrophilic intraocular lenses. *J Cataract Refract Surg*, 28(4):644–51, April 2002.

[101] Akira Miyata and Shigeo Yaguchi. Equilibrium water content and glistenings in acrylic intraocular lenses. *J Cataract Refract Surg*, 30(8):1768–72, August 2004.

[102] Daniele Tognetto, Lisa Toto, Giorgia Sanguinetti, and Giuseppe Ravalico. Glistenings in foldable intraocular lenses. *J Cataract Refract Surg*, 28(7):1211–6, Jul 2002.

[103] Eva Mönestam and Anders Behndig. Impact on visual function from light scattering and glistenings in intraocular lenses, a long-term study. *Acta Ophthalmol*, 89(8):724–8, December 2011.

[104] Joseph Colin, Isabelle Orignac, and David Touboul. Glistenings in a large series of hydrophobic acrylic intraocular lenses. *J Cataract Refract Surg*, 35(12):2121–6, December 2009.

[105] Namrata Sharma, Rajesh Sinha, and Rasik B Vajpayee. Phaco profile intraocular lenses: Deigns, materials and types. In Rasik B Vajpayee, Namrata Sharma, Suresh K Pandey, and Jeewan S. Titiyal, editors, *Phacoemulsification Surgery*, chapter 22, pages 194–203. Jaypee Brothers Medical Publishers, 2005.

[106] Market Scope. Comprehensive report on the global IOL market. Technical report, Market Scope, May 2011.

[107] David A Atchison. Optical design of intraocular lenses. I. On-axis performance. *Optom Vis Sci*, 66(8):492–506, August 1989.

[108] David A Atchison. Optical design of intraocular lenses. II. Off-axis performance. *Optom Vis Sci*, 66(9):579–90, September 1989.

[109] David A Atchison. Optical design of intraocular lenses. III. On-axis performance in the presence of lens displacement. *Optom Vis Sci*, 66(10):671–81, October 1989.

[110] Jay C Erie, Mark H Bandhauer, and Jay W McLaren. Analysis of postoperative glare and intraocular lens design. *J Cataract Refract Surg*, 27(4):614–21, April 2001.

[111] Albert Gullstrand. Helmholtz's treatise on physiological optics. English translation (1924) edited by J.P.C Southall, Optical Society of America, 1909.

[112] G Beiko. Personalized correction of spherical aberration in cataract surgery. Presented at The AAO Annual Meeting October 18, Chicago, IL., 2005.

[113] Robert Montés-Micó, Teresa Ferrar-Blasco, and Alejandro Cerviño. Analysis of the possible benefits of aspheric intraocular lenses: Review of the literature. *J Cataract Refract Surg*, 35:172–181, January 2009.

[114] Mayank A Nanavaty, David J Spalton, James Boyce, Shouvik Saha, and John Marshall. Wavefront aberrations, depth of focus, and contrast sensitivity with aspheric and spherical intraocular lenses: Fellow-eye study. *J Cataract Refract Surg*, 35:663–671, April 2009.

[115] Stefan Pieh, Werner Fiala, Andre Malz, and Wilhelm Stork. In vitro strehl ratios with spherical, aberration-free, average, and customized spherical aberration-correcting intraocular lenses. *Invest Ophthalmol Vis Sci*, 50(3):1264–1270, March 2009.

[116] Kamilla R Johannsdottir and Lew B Stelmach. Monovision: A review of the scientific literature. *Optom Vis Sci*, 78(9):646–51, September 2001.

[117] Fuxiang Zhang, Alan Sugar, Gordon Jacobsen, and Melissa Collins. Visual function and patient satisfaction: Comparison between bilateral diffractive multifocal intraocular lenses and monovision pseudophakia. *J Cataract Refract Surg*, 37(3): 446–53, March 2011.

[118] Stephen S Lane, Mike Morris, Lee Nordan, Mark Packer, Nicholas Tarantino, and R. Bruce Wallace. Multifocal intraocular lenses. *Ophthalmol Clin N Am*, 19(1): 89–105, March 2006.

[119] Staar Surgical. On the forefront of refractive technology, 2011. URL `http://www.staar.com/html/iol.html`.

[120] Alessandro Franchini, Barbara Zamma Gallarati, and Eleonora Vaccari. Analysis of stray-light effects related to intraocular lens edge design. *J Cataract Refract Surg*, 30(7):1531–6, July 2004.

[121] William B Trattler, Jeffrey C Whitsett, and Piero A Simone. Negative dysphotopsia after intraocular lens implantation irrespective of design and material. *J Cataract Refract Surg*, 31(4):841–5, April 2005.

[122] Charles R Munnerlyn. Lasers in ophthalmology: past, present and future. *J Mod Optics*, 50(15-17):2351–60, 2003.

[123] Jin-Wei Cheng, Rui-Li Wei, Ji-Ping Cai, Gui-Lin Xi, Huang Zhu, You Li, and Xiao-Ye Ma. Efficacy of different intraocular lens materials and optic edge designs in preventing posterior capsular opacification: A meta-analysis. *Am J Ophthalmol*, 143(3):428–36, March 2007.

[124] Suresh K Pandey, David J Apple, Liliana Werner, Anthony J Maloof, and E John Milverton. Posterior capsule opacification: a review of the aetiopathogenesis, experimental and clinical studies and factors for prevention. *Indian J Ophthalmol*, 52(2):99–112, June 2004.

[125] Andrew Coombes and Helen Seward. Posterior capsular opacification prevention: IOL design and material. *Br J Ophthalmol*, 83:640–1, 1999.

[126] N E Sverker Norrby. Sources of error in intraocular lens power calculation. *J Cataract Refract Surg*, 34(3):368–76, March 2008.

[127] S N Fedorov, A I Kolinko, and A I Kolinko. A method of calculating the optical power of the intraocular lens. *Vestn Oftalmol*, 80(4):27–31, 1967.

[128] M C Colenbrander. Calculation of the power of an iris clip lens for distant vision. *Br J Ophthalmol*, 57(10):735–40, October 1973.

[129] R D Binkhorst. Intraocular lens power. *Int Ophthalmol Clin*, 19(3):83–94, 1979.

[130] J M Thijssen. The emmetropic and the iseikonic implant lens: Computer calculation of the refractive power and its accuracy. *Ophthalmologica*, 171(6):467–86, 1975.

[131] Svyataslav N Fyodorov, Miles A Galin, and A Linksz. Calculation of the optical power of intraocular lenses. *Invest Ophthalmol*, 14(8):625–8, August 1975.

[132] G L van der Heijde. The optical correction of unilateral aphakia. *Trans Sect Ophthalmol Am Acad Ophthalmol Otolaryngol*, 81(1):OP80–8, 1976.

[133] R D Binkhorst. The optical design of intraocular lens implants. *Ophthalmic Surg*, 6(3):17–31, 1975.

[134] N E Sverker Norrby and Gabor Koranyi. Prediction of intraocular lens power using the lens haptic plane concept. *J Cataract Refract Surg*, 23(2):254–9, March 1997.

[135] Donald R Sanders and Manus C Kraff. Improvement of intraocular lens power calculation using empirical data. *J Am Intraocul Implant Soc*, 6(3):263–7, July 1980.

[136] Thomas Olsen. On the calculation of power from curvature of the cornea. *Br J Ophthalmol*, 70(2):152–4, Feburary 1986.

[137] Mark C M Dunne, Jonathon M Royston, and Derek A Barnes. Normal variations of the posterior corneal surface. *Acta Ophthalmol (Copenh)*, 70(2):255–61, April 1992.

[138] Michiel Dubbelman, Henk A Weeber, Rob G L van der Heijde, and Hennie J Völker-Dieben. Radius and asphericity of the posterior corneal surface determined by corrected Scheimpflug photography. *Acta Ophthalmol Scand*, 80(4):379–83, August 2002.

[139] Jack T Holladay, Thomas C Prager, Thomas Y Chandler, Kathryn H Musgrove, John W Lewis, and Richard S Ruiz. A three-part system for refining intraocular lens power calculations. *J Cataract Refract Surg*, 14(1):17–24, January 1988.

[140] Wolfgang Drexler, Oliver Findl, Rupert Menapace, Georg Rainer, Clemens Vass, Christoph K Hitzenberger, and Adolf F Fercher. Partial coherence interferometry: A novel approach to biometry in cataract surgery. *Am J Ophthalmol*, 126(4): 524–34, October 1998.

[141] Christoph K Hitzenberger. Optical measurement of the axial eye length by laser Doppler interferometry. *Invest Ophthalmol Vis Sci*, 32(3):616–24, March 1991.

[142] Charles Campbell. Reconstruction of the corneal shape with the mastervue corneal topography system. *Optom Vis Sci*, 74(11):899–905, November 1997.

[143] Kenneth J Hoffer. The Hoffer Q formula: A comparison of theoretic and regression formulas. *J Cataract Refract Surg*, 19(6):700–12, November 1993.

[144] Giacomo Savini, Kenneth J Hoffer, and Zanini Maurizio. IOL power calculations after LASIK and PRK. *Cataract & Refractive Surgery Today Europe*, April:37–44, 2007.

[145] Kenneth J Hoffer. Intraocular lens power calculation after previous laser refractive surgery. *J Cataract Refract Surg*, 35(4):759–65, April 2009.

[146] Paul-Rolf Preussner, Jochen Wahl, Daniela Weitzel, Silke Berthold, Katharina Kriechbaum, and Oliver Findl. Predicting postoperative intraocular lens position and refraction. *J Cataract Refract Surg*, 30(10):2077–83, October 2004.

[147] Jack T Holladay. International intraocular lens registry. *J Cataract Refract Surg*, 25(1):128–36, January 1999.

[148] Jack Holladay. International intraocular lens registry, 2011. URL `www.docholladay.com/search.aspx`.

[149] Robert J Noll. Zernike polynomials and atmospheric turbulence. *J Opt Soc Am*, 66(3):207–11, 1976.

[150] Virendra N Mahajan. Zernike polynomials and optical aberrations. *Appl Opt*, 34 (34):8060–2, December 1995.

[151] Daniel Malacara, editor. *Optical Shop Testing*. John Wiley and Sons, New York, 2nd edition, 1992.

[152] Michael K Smolek and Stephen D Klyce. Zernike polynomial fitting fails to represent all visually significant corneal aberrations. *Invest Ophthalmol Vis Sci*, 44 (11):4676–81, November 2003.

[153] Enrique J. Fernández, Angelika Unterhuber, Pedro M. Prieto, Boris Hermann, Wolfgang Drexler, and Pablo Artal. Ocular aberrations as a function of wavelength in the near infrared measured with a femtosecond laser. *Opt Express*, 13(2):400–49, January 2005.

[154] Lourdes Llorente, Luis Diaz-Santana, David Lara-Saucedo, and Susana Marcos. Aberrations of the human eye in visible and near infrared illumination. *Optom Vis Sci*, 80(1):26–35, January 2003.

[155] D B Henson. Optical methods for measurement of ocular parameters. In W Neil Charman, editor, *Visual optics and instrumentation*, volume 1 of *Vision and visual dysfunction*, chapter 17, pages 371–399. CRC Press, Boca Raton, FL 33487, 1991.

[156] N Brown. Slit-image photography. *Trans Ophthalmol Soc UK*, 89:397–408, 1970.

[157] Patricia Rosales and Susana Marcos. Pentacam Scheimpflug quantitative imaging of the crystalline lens and intraocular lens. *J Refract Surg*, 25(5):421–8, May 2009.

[158] Wolfgang Drexler and James G Fujimoto. State-of-the-art retinal optical coherence tomography. *Prog Retin Eye Res*, 27(1):45–88, January 2008.

[159] J A Izatt and M A Choma. Theory of optical coherence tomography. In Wolfgang Drexler and James G Fujimoto, editors, *Optical coherence tomography - technology and applications*, chapter 2, pages 47–72. Springer, 2008.

[160] Joseph M. Schmitt. Optical coherence tomography (OCT): a review. *IEEE J Sel Topics Quantum Electron*, 5(4):1205–1215, July/August 1999.

[161] Marco Ruggeri, Stephen R Uhlhorn, Carolina De Freitas, Arthur Ho, Fabrice Manns, and Jean-Marie Parel. Imaging and full-length biometry of the eye during accommodation using spectral domain oct with an optical switch. *Biomed Opt Express*, 3(7):1506–20, July 2012.

[162] Aristides Konstantopoulos, Parwez Hossain, and David F Anderson. Recent advances in ophthalmic anterior segment imaging: A new era for ophthalmic diagnosis? *Br J Ophthalmol*, 91(4):551–7, April 2007.

[163] Spiricon Inc. *Hartmann wavefront analyser tutorial*. Spiricon Inc., Logan, 2004.

[164] David A Atchison. Recent advances in measurement of monochromatic aberrations of human eyes. *Clin Exp Optom*, 88(1):5–27, January 2005.

[165] M Tscherning. Die monochromatischen aberrationen des menschlichen auges. *Z Psychol Physiol Sinne*, 6:456–471, 1894.

[166] Bradford Howland. Use of crossed cylinder lens in photographic lens evaluation. *Appl Opt*, 7(8):1587–600, August 1968.

[167] Howard C Howland and Bradford Howland. A subjective method for the measurement of monochromatic aberrations of the eye. *J Opt Soc Am*, 67(11):1508–18, November 1977.

[168] Glyn Walsh, W Neil Charman, and Howard C Howland. Objective technique for the determination of monochromatic aberrations of the human eye. *J Opt Soc Am A*, 1(9):987–92, September 1984.

[169] Michael Mrochen, Maik Kaemmerer, Peter Mierdel, Hans Eberhard Krinke, and Theo Seiler. Principles of Tscherning aberrometry. *J Refract Surg*, 16:S570–S571, 2000.

[170] Peter Mierdel, Maik Kaemmerer, Michael Mrochen, Hans Eberhard Krinke, and Theo Seiler. Ocular optical aberrometer for clinical use. *J Biomed Opt*, 6(2):200–4, April 2001.

[171] Alexandre Ivanoff. About the spherical aberration of the eye. *J Opt Soc Am*, 46 (10):901–3, October 1956.

[172] M S Smirnov. Measurement of the wave aberration of the human eye. *Biofizika*, 6:776–95, 1961.

[173] Robert H Webb, C Murray Penney, and Keith P Thompson. Measurement of ocular local wavefront distortion with a spatially resolved refractometer. *Appl Opt*, 31(19):3678–86, July 1992.

[174] Rafael Navarro and M Angeles Losada. Aberrations and relative efficiency of light pencils in the living human eye. *Optom Vis Sci*, 74(7):540–7, July 1997.

[175] Vasyl V Molebny, Sophia I Panagopoulou, Sergiy V Molebny, Youssef S Wakil, and Ioannis G Pallikaris. Principles of ray tracing aberrometry. *J Refract Surg*, 16(5):S572–5, September/October 2000.

[176] Vasyl V Molebny, Ioannis G Pallikaris, Leonidas P Naoumidis, Igor H Chyzh, Sergiy V Molebny, and Vyacheslav M Sokurenko. Retina ray-tracing technique for eye-refraction mapping. In Pascal O Rol, Karen M Joos, and Fabrice Manns, editors, *Ophthalmic Technologies VII*, volume 2971, pages 175–83. SPIE Press, 26 May 1997.

[177] Francois Roddier. Curvature sensing and compensation: a new concept in adaptive optics. *Appl Opt*, 27:1223–5, 1988.

[178] Roberto Ragazzoni. Pupil plane wavefront sensing with an oscillating prism. *J Mod Optics*, 43:289–93, 1996.

[179] Ignacio Iglesias, Roberto Ragazzoni, Yves Julien, and Pablo Artal. Extended source pyramid wave-front sensor for the human eye. *Opt Express*, 10(9):419–28, May 2002.

[180] Scott MacRae and Masanao Fujieda. Slit skiascopic-guided ablation using the Nidek laser. *J Refract Surg*, 16:S576–S580, September/October 2000.

[181] Warren J Smith. *Modern Optical Engineering*, chapter The Foucault Test, pages 557, 588–592. McGraw-Hill, San Francisco, 3rd edition, 2000.

[182] Jim Schwiegerling and Daniel R. Neal. Historical development of the Shack-Hartmann wavefront sensor. In J E Harvey and R B Hooker, editors, *Robert Shannon and Roland Shack: Legends in Applied Optics*, pages 132–139. SPIE Press, Bellingham WA, 2005.

[183] Mark A A Neil, Martin J Booth, and Tony Wilson. New modal wave-front sensor: a theoretical analysis. *J Opt Soc Am A*, 17(6):1098–107, June 2000.

[184] Harilaos S Ginis, Sotiris Plainis, and Aristofanis I Pallikaris. Variability of wave-front aberration measurements in small pupil sizes using a clinical Shack-Hartmann aberrometer. *BioMed Central Ophthalmology*, 4(1):1–15, 2004.

[185] Susana Marcos, Sergio Barbero, Lourdes Llorente, and Jesus Merayo-Lloves. Optical response to LASIK surgery for myopia from total and corneal aberration measurements. *Invest Ophthalmol Vis Sci*, 42(13):3349–56, December 2001.

[186] Jens Einighammer, Theo Oltrup, Elisabeth Feudner, Thomas Bende, and Benedikt Jean. Customized aspheric intraocular lenses calculated with real ray tracing. *J Cataract Refract Surg*, 35:1984–1994, 2009.

[187] Okulix. Okulix ray-tracing application, February 2012. URL `http://okulix.de`.

[188] Bausch and Lomb. Akreos AO Adapt product information sheet, 2011.

[189] Masahiko Daimon and Akira Masumura. Measurement of the refractive index of distilled water from the near-infrared region to the ultraviolet region. *Appl Opt*, 46(18):3811–20, June 2007.

[190] Refractive index, Februrary 2012. URL `http://refractiveindex.info`.

[191] George M Hale and Marvin R Querry. Optical constants of water in the 200-nm to 200-microm wavelength region. *Appl Opt*, 12(3):555–63, March 1973.

[192] K Takei, S Hommura, and H Okajima. Optimum form of posterior chamber intraocular lenses to minimize aberrational astigmatism. *Jpn J Ophthalmol*, 39 (4):390–401, 1995.

[193] Min-shan Jiang and J T Lin and Chuan-qing Zhou and Qiu-shi Ren. Aspherical optics design for minimal spherical aberration in vision correction of human eyes. In Pantazis Z Mouroulis, Warren J Smith, and R Barry Johnson, editors, *Current Developments in Lens Design and Optical Engineering IX,*, volume 7060, pages 1–7. 706013, SPIE, 2008.

[194] S W Samuelson, D D Koch, and C C Kuglen. Determination of maximal incision length for true small-incision surgery. *Ophthalmic Surg*, 22(4):204–7, April 1991.

[195] G Beltrame, M L Salvetat, M Chizzolini, and G Driussi. Corneal topographic changes induced by different oblique cataract incisions. *J Cataract Refract Surg*, 27(5):720–7, May 2001.

[196] G Rainer, R Menapace, C Vass, D Annen, O Findl, and K Schmetterer. Corneal shape changes after temporal and superolateral 3.0 mm clear corneal incisions. *J Cataract Refract Surg*, 25(8):1121–6, August 1999.

[197] Se Joon Woo and Jin-Hak Lee. Effect of central corneal thickness on surgically induced astigmatism in cataract surgery. *J Cataract Refract Surg*, 29(12):2401–6, December 2003.

[198] Larry N Thibos, William Wheeler, and Douglas G Horner. Power vectors: An application of Fourier analysis to the description and statistical analysis of refractive error. *Optom Vis Sci*, 74(6):367–5, 1997.

[199] Larry N Thibos, Xin Hong, Arthur Bradley, and Raymond A Applegate. Accuracy and precision of objective refraction from wavefront aberrations. *J Vis*, 4:329–351, April 2004.

[200] Jim Schwiegerling, John E Greivenkamp, and Joseph M Miller. Representation of videokeratoscopic height data with Zernike polynomials. *J Opt Soc Am A*, 12(10): 2105–13, October 1995.

[201] Robert K Tyson and Benjamin W Frazier. *Field guide to adaptive optics*. SPIE field guides. SPIE Press, Bellingham WA, 2004.

[202] Brian A Barsky, Stanley A Klein, and Daniel D Garcia. Gaussian power with cylinder vector field representation for corneal topography maps. *Optom Vis Sci*, 74(11):917–25, November 1997.

[203] Scott A Read, Michael J Collins, D Robert Iskander, and Brett A Davis. Corneal topography with Scheimpflug imaging and videokeratography: Comparative study of normal eyes. *J Cataract Refract Surg*, 35(6):1072–81, June 2009.

[204] David A Atchison and Dion H Scott. Monochromatic aberrations of human eyes in the horizontal visual field. *J Opt Soc Am A*, 19(11):2180–2183, 2002.

[205] Yannick Nochez, Samuel Majzoub, and Pierre-Jean Pisella. Corneal aberration integrity after microincision cataract surgery: prerequisite condition for prediction of total ocular aberrations. *Br J Ophthalmol*, 94(5):661–3, May 2010.

[206] İzzet Can, Hasan Ali Bayhan, Hale Çelik, and Başak Bostanc Ceran. Comparison of corneal aberrations after biaxial microincision and microcoaxial cataract surgeries: a prospective study. *Curr Eye Res*, 37(1):18–24, January 2012.

[207] Ke Yao, Xiajing Tang, and Panpan Ye. Corneal astigmatism, high order aberrations, and optical quality after cataract surgery: microincision versus small incision. *J Refract Surg*, 22(9 Suppl):S1079–82, November 2006.

[208] Bassam Elkady, Jorge L Alió, Dolores Ortiz, and Raúl Montalbán. Corneal aberrations after microincision cataract surgery. *J Cataract Refract Surg*, 34(1):40–5, January 2008.

[209] Antonio Guirao, Jaime Tejedor, and Pablo Artal. Corneal aberrations before and after small-incision cataract surgery. *Invest Ophthalmol Vis Sci*, 45(12):4312–9, December 2004.

[210] Susana Marcos, Patricia Rosales, Lourdes Llorente, and Ignacio Jiménez-Alfaro. Change in corneal aberrations after cataract surgery with 2 types of aspherical intraocular lenses. *J Cataract Refract Surg*, 33(2):217–26, Feburary 2007.

[211] Yannick Nochez, Anne Favard, Samuel Majzoub, and Pierre-Jean Pisella. Measurement of corneal aberrations for customisation of intraocular lens asphericity: impact on quality of vision after micro-incision cataract surgery. *Br J Ophthalmol*, 94(4):440–4, April 2010.

[212] P N Farnsworth and S E Shyne. Anterior zonular shifts with age. *Exp Eye Res*, 28(3):291–7, March 1979.

[213] Xinyou Yin, Jan Goudriaan, Egbert A Lantinga, Jan Vos, and Huub J Spiertz. A flexible sigmoid function of determinate growth. *Ann Bot*, 91(3):361–71, Feburary 2003.

[214] CPD Birch. A new generalized logistic sigmoid growth equation compared with the richards growth equation. *Annals of Botany*, 83(6):713–723, June 1999.

[215] Katharina Kriechbaum, Oliver Findl, Paul Rolf Preussner, Christina Köppl, Jochen Wahl, and Wolfgang Drexler. Determining postoperative anterior chamber depth. *J Cataract Refract Surg*, 29(11):2122–6, November 2003.

[216] Thomas Olsen. Prediction of intraocular lens position after cataract extraction. *J Cataract Refract Surg*, 12(4):376–9, July 1986.

[217] Oliver Findl, Walter Struhal, Georg Dorffner, and Wolfgang Drexler. Analysis of nonlinear systems to estimate intraocular lens position after cataract surgery. *J Cataract Refract Surg*, 30(4):863–6, April 2004.

[218] Juan Tabernero, Patricia Piers, Antonio Benito, Manuel Redondo, and Pablo Artal. Predicting the optical performance of eyes implanted with IOLs to correct spherical aberration. *Invest Ophthalmol Vis Sci*, 47(10):4651–8, October 2006.

[219] Haiying Jin, Tanja Rabsilber, Angela Ehmer, Andreas F Borkenstein, Il-Joo Limberger, Haike Guo, and Gerd U Auffarth. Comparison of ray-tracing method and

thin-lens formula in intraocular lens power calculations. *J Cataract Refract Surg*, 35(4):650–62, April 2009.

[220] William J Dupps, Jr. Intraocular lens calculations: call for more deterministic models. *J Cataract Refract Surg*, 36(9):1447–8, September 2010.

[221] Huanqing Guo, Alexander V Goncharov, and Chris Dainty. Comparison of retinal image quality with spherical and customized aspheric intraocular lenses. *Biomed Opt Express*, 3(4):681–91, April 2012.

[222] Huanqing Guo, Alexander Goncharov, and Chris Dainty. Intraocular lens implantation position sensitivity as a function of refractive error. *Ophthal Physiol Opt*, 32(2):117–124, 2012.

[223] John A Retzlaff, Donald R Sanders, and Manus C Kraff. Development of the SRK/T intraocular lens implant power calculation formula. *J Cataract Refract Surg*, 16(3):333–40, May 1990.

[224] Haag-Streit International. Instructions for use. Biometer LENSTAR LS 900. English edition. Downloaded on 22/5/2012 from http://www.haag-streit-usa.com, April 2012.

[225] Haag-Streit International. Precision measurements. Downloaded on 22/5/2012 from http://www.haag-streit-usa.com/mylenstar/measurements.aspx, April 2012.

[226] Richard S Snell and Michael A Lemp. *Clinical anatomy of the eye*. Blackwell Publishing Ltd, Oxford, 2nd edition, 1998.

[227] Z Yang and S Du. Histological measurement of human retinal thickness. *J Tongji Med Univ*, 19(3):246–8, 1999.

[228] Annie Chan, Jay S Duker, Tony H Ko, James G Fujimoto, and Joel S Schuman. Normal macular thickness measurements in healthy eyes using stratus optical coherence tomography. *Arch Ophthalmol*, 124(2):193–8, Feburary 2006.

[229] B Alamouti and J Funk. Retinal thickness decreases with age: an OCT study. *Br J Ophthalmol*, 87(7):899–901, July 2003.

[230] Michael Tocci. How to model the human eye in ZEMAX. Downloaded from http://www.radiantzemax.com, Knowledgebase article No. 50117, April 2007.

[231] Dan Hill. How to automate keyboard and mouse actions with ZPL. Downloaded from http://www.radiantzemax.com, Knowledgebase article No. 50240, March 2012.

[232] Barbara K Pierscionek and Derek Y Chan. Refractive index gradient of human lenses. *Optom Vis Sci*, 66(12):822–9, December 1989.

[233] Barbara K Pierscionek. Surface refractive index of the eye lens determined with an optic fiber sensor. *J Opt Soc Am A*, 10(9):1867–71, September 1993.

[234] Barbara K Pierscionek. The refractive index along the optic axis of the bovine lens. *Eye*, 9:776–82, 1995.

[235] Melanie C Campbell. Measurement of refractive index in an intact crystalline lens. *Vision Res*, 24(5):409–15, 1984.

[236] J G Sivak and T Mandelman. Chromatic dispersion of the ocular media. *Vision Res*, 22(8):997–1003, 1982.

[237] Wolfgang Drexler, Christoph K Hitzenberger, Angela Baumgartner, Oliver Findl, Harald Sattmann, and Adolf F Fercher. Investigation of dispersion effects in ocular media by multiple wavelength partial coherence interferometry. *Exp Eye Res*, 66 (1):25–33, January 1998.

[238] D X Hammer, A J Welch, G D Noojin, R J Thomas, D J Stolarski, and B A Rockwell. Spectrally resolved white-light interferometry for measurement of ocular dispersion. *J Opt Soc Am A*, 16(9):2092–102, September 1999.

[239] Roger C Lin, Mark A Shure, Andrew M Rollins, Joseph A Izatt, and David Huang. Group index of the human cornea at 1.3-microm wavelength obtained in vitro by optical coherence domain reflectometry. *Opt Lett*, 29(1):83–5, January 2004.

[240] S Patel, J Marshall, and F W Fitzke, 3rd. Refractive index of the human corneal epithelium and stroma. *J Refract Surg*, 11(2):100–5, 1995.

[241] Rafael Navarro, J Santamaría, and J Bescós. Accommodation-dependent model of the human eye with aspherics. *J Opt Soc Am A*, 2(8):1273–81, August 1985.

[242] Y. Le Grand. Form and space vision. Revised translation (cited in Atchison & Smith 2005), 1967.

[243] David A Atchison and George Smith. Chromatic dispersions of the ocular media of human eyes. *J Opt Soc Am A Opt Image Sci Vis*, 22(1):29–37, January 2005.

[244] R B Mandell, C S Chiang, and S A Klein. Location of the major corneal reference points. *Optom Vis Sci*, 72(11):776–84, November 1995.

[245] D R Korb, editor. *The tear film - structure, function and clinical examination.* Butterworth Heinemann, Oxford, 2002.

[246] Ronald B Rabbetts. *Bennett and Rabbetts' Clinical Visual Optics.* Butterworth Heinemann, Edinburgh, 3rd edition, 1998.

[247] Hwey-Lan Liou and Noel A. Brennan. Anatomically accurate, finite model eye for optical modeling. *J Opt Soc Am A*, 14(8):1684–1695, August 1997.

[248] N Wang, M Lai, X Chen, and W Zhou. Quantitative real time measurement of iris configuration in living human eyes (original journal article in mandarin chinese). *Zhonghua Yan Ke Za Zhi (Chinese journal of ophthalmology)*, 34(5): 369–72, September 1998.

[249] Nidek Co Ltd. Autorefractor / Keratometer ARK-560A / 530A / 510A. product information sheet downloaded on 27 May 2012 from http://www.nidek-intl.com/products/examination/ark-560a.html, May 2012.

[250] Isabel Escudero-Sanz and Rafael Navarro. Off-axis aberrations of a wide-angle schematic eye model. *J Opt Soc Am A*, 16(8):1881–91, August 1999.

[251] Adam M Dubis, John T McAllister, and Joseph Carroll. Reconstructing foveal pit morphology from optical coherence tomography imaging. *Br J Ophthalmol*, 93(9): 1223–7, September 2009.

[252] Patricia A Piers, Enrique J Fernandez, Silvestre Manzanera, Sverker Norrby, and Pablo Artal. Adaptive optics simulation of intraocular lenses with modified spherical aberration. *Invest Ophthalmol Vis Sci*, 45(12):4601–10, December 2004.

[253] Jason Porter, Antonio Guirao, Ian G. Cox, and David R. Williams. Monochromatic aberrations of the human eye in a large population. *J Opt Soc Am A*, 18(8):1793–1803, August 2001.

[254] Timo Eppig, Katja Scholz, André Löffler, Arthur Messner, and Achim Langenbucher. Effect of decentration and tilt on the image quality of aspheric intraocular lens designs in a model eye. *J Cataract Refract Surg*, 35(6):1091–100, June 2009.

[255] Michiel Dubbelman, Victor Arni D P Sicam, and Rob G L Van der Heijde. The shape of the anterior and posterior surface of the aging human cornea. *Vision Res*, 46(6-7):993–1001, March 2006.

[256] Marco A Miranda, Clare O'Donnell, and Hema Radhakrishnan. Repeatability of corneal and ocular aberration measurements and changes in aberrations over one week. *Clin Exp Optom*, 92(3):253–266, 2009.

[257] Michael J Dobos, Michael D Twa, and Mark A Bullimore. An evaluation of the Bausch & Lomb Zywave aberrometer. *Clin Exp Optom*, 92(3):238–45, 2009.

[258] M Jeandervin and J Barr. Comparison of repeat videokeratography: repeatability and accuracy. *Optom Vis Sci*, 75(9):663–9, September 1998.

[259] W Lotmar. Theoretical eye model with aspherics. *J Opt Soc Am*, 61(11):1522–1529, November 1971.

[260] A C Kooijman. Light distribution on the retina of a wide-angle theoretical eye. *J Opt Soc Am*, 73(11):1544–50, November 1983.

[261] O Pomerantzeff, M Pankratov, G J Wang, and P Dufault. Wide-angle optical model of the eye. *Am J Optom Physiol Opt*, 61(3):166–76, March 1984.

[262] R Navarro, J Santamaría, and J Bescós. Accommodation-dependent model of the human eye with aspherics. *J Opt Soc Am A*, 2(8):1273–81, August 1985.

[263] David A Atchison. Optical models for human myopic eyes. *Vision Res*, 46(14): 2236–50, July 2006.

[264] Larry N Thibos, M Ye, X Zhang, and Arthur Bradley. The chromatic eye: a new reduced-eye model of ocular chromatic aberration in humans. *Appl Opt*, 31(19): 3594–600, July 1992.

[265] Sverker Norrby. The Dubbelman eye model analysed by ray tracing through aspheric surfaces. *Ophthalmic Physiol Opt*, 25(2):153–61, March 2005.

[266] Alexander V Goncharov and Chris Dainty. Wide-field schematic eye models with gradient-index lens. *J Opt Soc Am A*, 24(8):2157–74, August 2007.

[267] Larry N. Thibos, Arthur Bradley, and Xin Hong. A statistical model of the aberration structure of normal, well-corrected eyes. *Ophthal Physiol Opt*, 22(5):427–433, 2002.

[268] Larry N. Thibos. Retinal image quality for virtual eyes generated by a statistical model of ocular wavefront aberrations. *Ophthal Physiol Opt*, 29(3):288–291, 2009.

[269] Pablo Artal, Li Chen, Enrique J Fernández, Ben Singer, Silvestre Manzanera, and David R Williams. Adaptive optics for vision: the eye's adaptation to point spread function. *J Refract Surg*, 19(5):S585–7, 2003.

[270] Larry N Thibos, Xu Cheng, and Arthur Bradley. Design principles and limitations of wave-front guided contact lenses. *Eye Contact Lens*, 29(1 Suppl):S167–70; discussion S190–1, S192–4, January 2003.

[271] Gleb Vdovin, Mikhail Loktev, and Alexander Naumov. On the possibility of intraocular adaptive optics. *Opt Express*, 11(7):810–817, 2003.

[272] Jason D. Marsack, Larry N. Thibos, and Raymond A. Applegate. Metrics of optical quality derived from wave aberrations predict visual performance. *J Vision*, 4:322–328, April 2004.

[273] Xu Cheng, Arthur Bradley, and Larry N. Thibos. Predicting subjective judgment of best focus with objective image quality metrics. *J Vision*, 4:310–321, 2004.

[274] Jim Schwiegerling. Gaussian weighting of ocular wave-front measurements. *J Opt Soc Am A Opt Image Sci Vis*, 21(11):2065–72, November 2004.